Design and Calibration of Stress Sensors on 4H-SiC

by

Jun Chen

A dissertation submitted to the Graduate Faculty of
Auburn University
in partial fulfillment of the
requirements for the Degree of
Doctor of Philosophy

Auburn, Alabama
May 7, 2022

Keywords: Die Stresses, 4H-SiC Piezoresistive Stress Sensor, Stress Effect on FET,
Off-axis Effect, Elastic Properties

Approved by

Jeffrey C. Suhling, Co-chair, Quina Distinguished Professor of Mechanical Engineering
Richard C. Jaeger, Co-chair, Emeritus Professor of Electrical Engineering
Hareesh V. Tippur, McWane Professor of Mechanical Engineering
James S. Davidson, Gottlieb Professor of Civil Engineering

Abstract

Stresses in electronic packages due to thermal and mechanical loadings can cause premature mechanical failures such as fracture of die, severing of connections, die bond failure, solder fatigue, and encapsulant cracking. Therefore, there is a desire to have some type of non-intrusive measurement device compatible with current processing techniques to effectively detect and measure the stresses in electronic packages. Stress sensors integrated on silicon ICs represent a powerful tool for experimental evaluation of die stress distributions, but silicon's upper temperature range is limited by its relatively low bandgap energy. Stress sensors made with wide bandgap semiconductor such as 4H silicon carbide (4H-SiC) offer the advantage of much higher temperature operation and can be utilized to monitor stresses in high-voltage, high-power SiC devices and have applications in deep well drilling, geothermal plants, and automotive and aerospace systems, to name a few.

In this work, the basics of piezoresistive effect have been reviewed to help the understanding of the semiconductor stress sensors and the piezoresistive behavior of 4H-SiC material has been studied. The general expressions for the stress dependence of resistors and van der Pauw devices on standard 4H-SiC wafers have been established. The theoretical results delineate similarities and differences of sensor rosettes on 4H-SiC with respect to those commonly utilized on silicon. Stress sensors were proposed to detect in-plane normal stresses, shear stress and out-of-plane normal stress.

The lateral and transverse piezoresistive coefficients were calibrated using four-point bending method. Four-terminal van der Pauw devices have been demonstrated to be excellent vehicles for calibration of those piezoresistive coefficients of 4H-SiC, and experimental results for the coefficients of both p- and n-type 4H-SiC at various

temperatures have been presented. The calibration results of in-plane piezoresistive coefficients from resistors were also shown in this study. The out-of-plane piezoresistive coefficients were measured using the combination of four-point bending method and hydrostatic method. In general, measurements of the basic piezoresistive coefficients of the various resistive structures are relatively small (<100/TPa).

The theory for the stress dependence of NMOS transistors on 4H-SiC was developed. The stress model for NMOSFETs includes the classic mobility terms plus a new term describing changes in threshold voltage. The longitudinal and transverse piezoresistive coefficients for NMOSFETs were calibrated. It has been found that the developed model agrees well with the measurements.

Since the devices are usually fabricated on the tilted 4H-SiC wafer plane, this study also evaluated the impact of the off-axis wafer plane on 4H-SiC and silicon stress sensors. The off-axis angle of our test chips was measured with EBSD analysis, according to which the piezoresistive coefficients were developed for tilted wafer planes using coordinate transformation. The errors induced by such off-axis wafer were found to be highly dependent on the magnitude of fundamental piezoresistive coefficients and stress distributions on chips. A case study was performed to better illustrate the concept.

A study on elastic properties of 4H-SiC was conducted and 4H-SiC was confirmed to be a transversely isotropic material. The in-plane elastic modulus E_1, Poisson's ratio ν_{12} were characterized using strain gauge method, and the out-of-plane elastic modulus E_3 were measured with nanoindentation technique. The experimental results were compared with other studies.

Finally, the designed piezoresistive stress sensors were used to characterize the stresses on the die surface and finite element simulation was performed.

Acknowledgements

I would like to express my sincere gratitude to my advisor Dr. Jeffrey C. Suhling and co-advisor Dr. Richard C. Jaeger for their continuous support, excellence guidance, and encouragement throughout my study. I am grateful for getting the opportunity to work with them. I am deeply grateful to Dr. Hareesh V. Tippur and Dr. James S. Davidson for serving on my committee, providing guidance and valuable advice. I would like to thank Dr. Guofu Niu for his help in semiconductor devices and physics.

My sincere thanks go to Dr. Jordan C. Roberts, Mr. Drew Sellers, and Ms. Tamara Isaacs-smith for their continuous assistance in helping with the sample preparation for the experimental work. I would also like to thank my all colleagues, Dr. Quang Nguyen, Dr. Sudan Ahmed, Dr. Nianjun Fu, Dr. Promod Chowdhury, Dr. Mohammad Alam, Dr. Abdullah Fahim, Dr. Jing Wu, Dr. KM Rafidh Hasan, Mohd Aminul Hoque, Kamrul Hasan, Mohammad Ashraful Haq, Debabrata Mondal for their friendship and support.

I would also like to take this opportunity to gratefully thank my parents, Xinping Wang and Rongguang Chen. Without their support, encouragements, and sacrifices, I would not be what am I today.

TABLE OF CONTENTS

TABLE OF CONTENTS vi

LIST OF TABLES ix

Chapter 1 1

INTRODUCTION 1

Chapter 2 6

THEORETICAL BACKGROUND AND LITERATURE REVIEW 6

2.1 Piezoresistive effect 6

2.2 Piezoresistive Stress Sensors 11

2.3 Physical Properties of 4H-SiC 18

Chapter 3 26

DESIGN AND CALIBRATION OF RESISTIVE STRESS SENSORS ON 4H-SIC 26

3.1 Design of Resistive Sensors 26

3.2 Calibration Method 40

3.3 Calibration Results 48

3.4 Summary 62

Chapter 4 64

MECHANICAL STRESS EFFECTS ON NMOS FETs 64

4.1 Introduction 64

4.2 Review of MOSFET Characteristics 65

4.3 Piezoresistive Theory of FETs 70

4.4 Four-Element Sensor Rosette 73

4.5 Experimental Method 75

4.6 Experimental Results 76

4.7 Summary 89

Chapter 5 91

EVALUATION OF IMPACT OF FOUR-DEGREE OFF-AXIS WAFERS ON 4H-SiC STRESS SENSORS 91

5.1 Introduction 91

5.2 Epitaxial Growth of SiC 92

5.3 Off-axis Angle Measurement 94

5.4 Impact of Off-axis Wafers on Calibration 96

5.5 Impact of Off-axis Wafers on Measurements 103

5.5 Summary 107

Chapter 6 108

EVALUATION OF IMPACT OF FOUR-DEGREE OFF-AXIS WAFERS ON SILICON STRESS SENSORS 108

6.1 Introduction 108

6.2 Review of Basic Equations 108

6.3 Off-axis Wafer Plane Errors 112

6.4 A Case Study on Four-element Rosette on (100) Silicon 119

6.5 Summary and Conclusion 127

Chapter 7 129

STRESS-STRAIN RELATIONS OF 4H-SIC 129

7.1 Introduction 129

7.2 Stress-Strain Relations of 4H-SiC 130

7.3 General Coordinate Transformations 133

7.4 Elastic Properties on (0001) Plane 138

7.5 Four Point Bending Method 141

7.6 Strain Gauge Method 144

7.6 Nanoindentation Method 147

7.7 Elastic Properties Comparison 152

7.8 Summary and Conclusion 153

Chapter 8 154

DIE STRESS MEASUREMENT IN CERAMIC DIP PACKAGE USING VDP SENSORS 154

8.1 Experimental Procedure 154
8.2 Experimental Results 156
8.3 FEA Simulation 159
8.4 Summary.. 172
Chapter 9 174

SUMMARY AND FUTURE WORK.. 174
9.1 Summary.. 174
9.2 Recommendations for Future Work.. 176
REFERENCES 178

LIST OF TABLES

Table 2. 1: Physical Properties of Si and SiC at Room Temperature..............................21

Table 3. 1: Measured Values of Piezoresistive Coefficients at Room Temperature.........50

Table 3. 2: Measured Values of Piezoresistive Coefficients for p+- type VDP 54

Table 3. 3: Measured Values of Piezoresistive Coefficients for n+- type VDP 55

Table 3. 4: Measured Values of Piezoresistive Coefficients for n+- type VDP 59

Table 3. 5: Fundamental Piezoresistive Coefficients of p- type 4H-SiC..........................61

Table 4. 1: Piezoresistive Coefficient Results..87

Table 4. 2: Results of a Simultaneous Least Square Fit to Table 4.1 Data.......................88

Table 6. 1: Typical Piezoresistive Coefficient Values for Lightly Doped Silicon $(TPa)^{-1}$ 121

Table 6. 2: Material Properties..125

Table 7. 1: Extracted Elastic Modulus E_1 From 4PB method.......................................144

Table 7. 2: Material Properties Extracted by Strain Gauge Method 147

Table 7. 3: Modulus of 4H-SiC Extracted from Nanoindentation 151

Table 7. 4: Elastic Constants (C_{ij} in GPa)..152

Table 7. 5: Elastic Modulus (E_{ij} in GPa) and Poisson’s Ratio......................................152

Table 8.1: Normal Stress Difference vs. Temperature Data 157

LIST OF FIGURES

Figure 1.1: Piezoresistive Sensor Concept..3

Figure 2.1: Top and Side View of a Resistor Sensor. Reprinted from [29]......................12

Figure 2.2: Photomicrograph of Eight Elements Resistive Rosettes. Reprinted from [28] 13

Figure 2.3: Photomicrograph of Ten Elements Resistive Rosettes. Reprinted from [39] .13

Figure 2.4: n-type VDP Structure in a p-well. 15

Figure 2.5: Schematic of a Four Element VDP Rosette on (111) Silicon. Reprinted from [40]..15

Figure 2.6: Conceptual Layout of 0-90° PMOS and ±45° NMOS Stress Sensors on (100) Silicon. Reprinted from [43] 17

Figure 2.7: (a) p-type Out-of-plane Shear Stress Sensor and (b) the Device Sensitive to Out-of-plane Normal Stress. Reprinted from [46]. 18

Figure 2.8: Occupation Sites in Hexagonal Closed-packed System, Borrowed from [51]. 19

Figure 2.9: Schematic Structure of Popular Polytypes: (a) 3C-SiC, (b) 4H-SiC and (c) 6H-SiC, Borrowed from [51]. 20

Figure 2.10: Crystal Structure of cubic and hexagonal SiC..20

Figure 2.11:Gauge Factors vs. Temperatures. Reprinted From [57]...............................22

Figure 2.12: Cantilever beam for Piezoresistance Characterization, Reprinted From [58]. 23
Figure 2.13: Gauge Factors as a Function of Piezoresistor's Widths and Lengths. Reprinted From [58]. 23
Figure 2.14: Schematic Sketch of the Cantilever Beam Bending Experiment and the Gauge Factors. Reprinted From [60]. 24
Figure 2. 15: Schematic Sketch of the Cantilever Beam Bending Experiment and the Gauge factors. Reprinted From [61]. 25
Figure 3.1: Crystal Structure and Conventional Coordinate System For 4H-SiC 27
Figure 3.2: Coordinate Systems on (0001) Plane 28
Figure 3.3: Resistor Arbitrarily Orientated with Respect to the Wafer Axes 29
Figure 3.4: Four-element Rosette for In-plane Stress Measurement 31
Figure 3.5: Four-element Rosette for Out-of-Plane Stress Measurement 34
Figure 3.6: 0° and 45° VDP Devices 36
Figure 3.7: p and n VDP Device 39
Figure 3.8: Cantilever Beam Setup 41
Figure 3.9: Actual Four-point Bending Fixture with an Example Test Strip in Place 42
Figure 3.10: Schematic Sketch of Four-point Bending Method 43
Figure 3.11: Four-point Bending System in an Environmental Chamber 44
Figure 3.12: Flexible Circuit Approach 45
Figure 3.13: Hydrostatic Calibration System 46
Figure 3.14: A Wire-bonded Chip on Board for TCR and Hydrostatic Test 47

Figure 3.15: 4H-SiC Strip with Resistors 48

Figure 3.16: Normalized Resistance Change vs. Transverse Stress for a n^+ Resistor.......49

Figure 3.17: Normalized Resistance Change vs. Transverse Stress for a p^+ Resistor.......49

Figure 3.18: 4H-SiC Strip with VDP Device..52

Figure 3.19: Normalized Resistance Changes vs. Stress at 60 ℃..................................53

Figure 3.20: Diagonal Measurement Results at 60 ℃..53

Figure 3.21: Coefficient πD for p^+-type VDP vs. Temperature.......................................55

Figure 3.22: Coefficient πD for n^+-type VDP vs. Temperature.......................................56

Figure 3.23: Normalized Resistance Change of p^+-type VDP vs. Temperature...............58

Figure 3.24: Normalized Resistance Change of n^+-type VDP vs. Temperature...............58

Figure 3.25: An Example of Total and Temperature Induced ΔR/R for p-type VDP.......60

Figure 3.26: An Example of Pressure Induced ΔR/R vs. Pressure For p^+-type VDP 61

Figure 4.1: MOS FET Structure...66

Figure 4.2: Electron Concentration at the Surface vs. Surface Potential. Axes are Linear.

....67

Figure 4.3: Subthreshold Conduction in an NMOS Transistor with V_{TN} = 0.8V. Reprinted

from [81]. 68

Figure 4.4: Typical Set of Output Characteristics for an n-channel Enhancement Type FET.

....70

Figure 4.5: NMOS Drain Current Orientations in a Four-Element Rosette 74

Figure 4.6: Layout of the 10/1 Lateral NMOS Transistor 76

Figure 4.7: Semi-logarithmic Graph of the Turn-on Characteristic.................................77

Figure 4.8: Threshold Voltage versus Gate-source Voltage Extracted from Linear Region Measurements with V_{DS}=100 mV 77
Figure 4.9: Comparison of Measurements with Theory for Normalized Transconductance 79
Figure 4.10: A Linear Region Turn-on Characteristics for Three Levels of Uniaxial Stress (V_{DS}=0.25V)....................80
Figure 4.11: Expansion of the Region Between 15 and 20 Volts. 80
Figure 4.12: Example of Normalized Change in NMOS Channel Conductance vs. Applied Stress at V_{GS}= 2.5 V Yielding $\Xi_{12} = -868$ /TPa 82
Figure 4.13: Example of Normalized Change in NMOS Channel Conductance vs. Applied Stress at V_{GS}= 5 V Yielding $\Xi_{12} = -394$ /TPa 82
Figure 4.14: Example of Normalized Change in NMOS Channel Conductance vs. Applied Stress at V_{GS}= 7.5 V Yielding $\Xi_{12} = -263$ /TPa 83
Figure 4.15: Example of Normalized Change in NMOS Channel Conductance vs. Applied Stress at V_{GS}= 10 V Yielding $\Xi_{12} = -201$ /TPa 83
Figure 4.16: Example of Normalized Change in NMOS Channel Conductance vs. Applied Stress at V_{GS}= 12.5 V Yielding $\Xi_{12} = -169$ /TPa 84
Figure 4.17: Example of Normalized Change in NMOS Channel Conductance vs. Applied Stress at V_{GS}= 15 V Yielding $\Xi_{12} = -151$ /TPa 84
Figure 4.18: Example of Normalized Change in NMOS Channel Conductance vs. Applied Stress at V_{GS}= 17.5 V Yielding $\Xi_{12} = -137$ /TPa 85

Figure 4.19: Example of Normalized Change in NMOS Channel Conductance vs. Applied Stress at V_{GS}= 20 V Yielding $\Xi_{12} = -126$ /TPa 85

Figure 4.20: Example of Normalized Change in NMOS Channel Conductance vs. Applied Stress at V_{GS}= 22.5 V Yielding $\Xi_{12} = -118$ /TPa 86

Figure 4.21: Example of Normalized Change in NMOS Channel Conductance vs. Applied Stress at V_{GS}= 25 V Yielding $\Xi_{12} = -112$ /TPa 86

Figure 4.22: Comparison Between the Measured Values of First-Order Coefficients and the Theory in Eq. 4.20. 88

Figure 5.1: Off-axis SiC Wafer Cutting Orientation. 93

Figure 5.2: Schematic Illustration of Growth Modes and Stacking Sequences of SiC Layers Grown on (a) on-axis 6H-SiC (0001) and (b) off-axis 6H-SiC (0001). (c) Bond Configuration Near an Atomic Step and on the (0001) Terrace. Borrowed from [51]. 93

Figure 5.3: – Flow Chart of Experimental Procedure (Including ZEISS Crossbeam 550) 95

Figure 5.4: Typical EBSD Result for (100) Silicon 96

Figure 5.5: Untilted wafer plane 97

Figure 5.6: Tilted wafer plane..98

Figure 6.1: Wafer Coordinate System on the (001) Silicon...109

Figure 6.2: Wafer Coordinate System on the (111) Silicon...112

Figure 6.3: Untilted Wafer Plane for (100) Silicon...114

Figure 6.4: Tilted Wafer Plane for (100) Silicon 115

Figure 6.5: Untilted Wafer Plane for (111) Silicon...117

Figure 6.6: Tilted Wafer Plane for (111) Silicon 117

Figure 6.7: Piezoresistive Coefficients Matrices for Untilted and Tilted wafer plane. ...118

Figure 6.8: Four-Element Rosette on (100) Silicon 119

Figure 6.9: Plastic Ball Grid Array Package Model...124

Figure 6.10: Simulated Stress Distribution of ($\sigma'_{11} - \sigma'_{22}$)..125

Figure 6.11: Simulated Stress Distribution of σ'_{12} 126

Figure 6.12: Calculated Errors Plot for ($\sigma'_{11} - \sigma'_{22}$) Using Eq. 6.15 126

Figure 6.13: Calculated Errors Plot for σ'_{12} Using Eq. 6.16 127

Figure 7.1: Rotated Cartesian Coordinate System 134

Figure 7.2: Coordinate Systems for (0001) 4H-SiC Wafers...139

Figure 7.3: Test Strip Cut from SiC Wafer..141

Figure 7.4: Deflection of a Beam in a Four-Point Bending Fixture..............................142

Figure 7.5: F' vs. Displacement 143

Figure 7.6: Strain Gauges on SiC Strip 144

Figure 7.7: Uniaxial Stress vs. Axial Strain...145

Figure 7.8: Transverse Strain vs. Axial Strain 146

Figure 7.9: Typical Load-displacement Curve of Nanoindentation..............................148

Figure 7.10: SiC Chip Cut from the Strip...149

Figure 7.11: SiC Chip Embedded in Resins 150

Figure 7.12: Nanoindentation Load-Displacement Curve for 4H-SiC..........................151

Figure 8.1: Ceramic DIP Before Encapsulation..155

Figure 8.2: Ceramic DIP After Encapsulation 155

Figure 8.3: Schematic of the Encapsulated DIP (Cross Section) 155

Figure 8.4: VDP Sensor Locations 156

Figure 8.5: Normal Stress Difference vs. Temperature for p^+ VDP 157

Figure 8.6: Normal Stress Difference vs. Temperature for n^+ VDP 159

Figure 8.7: Quarter Model of Ceramic DIP 160

Figure 8.8: Dimensions of DIP in Millimeters..160

Figure 8.9: Meshed Quarter Model 161

Figure 8.10: Detailed View of Mesh Near the Chip..161

Figure 8. 11: The CTE of 4H-SiC, Reprinted From [125]...162

Figure 8.12: Elastic Modulus of Encapsulant at Different Temperatures 163

Figure 8.13: TMA Test Results for ME 525, Borrowed From [126]. 164

Figure 8.14: Simulation Results for σ'_{11} and σ'_{22} at 125 ℃ 165

Figure 8.15: Simulation Results for σ'_{11} and σ'_{22} at 100 ℃ 165

Figure 8.16: Simulation Results for σ'_{11} and σ'_{22} at 75 ℃ 166

Figure 8.17: Simulation Results for $\sigma'11$ and σ'_{22} at 50 ℃ 166

_Toc89871932Figure 8.18: Simulation Results for σ′11 and σ'_{22} at 25 ℃..................167

Figure 8.19: Stress Difference $(\sigma'_{11} - \sigma'_{22})$ Correlations at 125 ℃ 168

Figure 8.20: Stress Difference $(\sigma'_{11} - \sigma'_{22})$ Correlations at 100 ℃ 168

Figure 8.21: Stress Difference $(\sigma'_{11} - \sigma'_{22})$ Correlations at 75 ℃ 169

Figure 8.22: Stress Difference $(\sigma'_{11} - \sigma'_{22})$ Correlations at 50 ℃ 169

Figure 8.23: Stress Difference $(\sigma'_{11} - \sigma'_{22})$ Correlations at 25 ℃ 170

Figure 8.24: Comparison Between Simulation and Experimental Results for p^+ VDP ..171

Figure 8.25: Comparison Between Simulation and Experimental Results for n^+ VDP..171

Figure 8.26: Stress Distributions near the n^+ Sensor at 25℃..172

Chapter 1

INTRODUCTION

Silicon carbide (SiC) as a wide band gap semiconductor material is perfectly suited for power applications, thanks to its superior physical and electronic properties including higher thermal conductivity, lower leakage current, higher breakdown electric field, and higher operating frequency and temperature, etc. Having considered these advantages, much attention has been given to SiC [1]. To date, SiC power devices are widely and commercially available and they have been used in many areas, such as automotive, aerospace, and renewable energy industries [4].

SiC based electronics technology always tends to be higher power density, higher efficiency, lower cost, and more integrated systems [5]. Recent studies discuss the future of 3D packaging and integration of silicon carbide power modules and eliminating wire bonds for lower parasitics leads to a reduction in size of electronic components [7]. However, with continually shrinking of the component size and increasing power density, the structural reliability has become a concern.

During normal operation, power devices are expected to operate at high temperature and each power cycle (ON and OFF) will cause large variation of temperatures. Due to direct contact of materials with different coefficients of thermal expansion (CTE), the elements of packing are subjected to thermomechanical stresses. Because of thermal and mechanical loads, stresses in electronic packages may not only cause premature mechanical failures but also alteration of the function of the semiconductor devices. The

common stress related problems are fracture of the die, die bond failure, solder fatigue, severing of connections, and encapsulant cracking. Additionally, thermally induced stresses can be produced during packaging procedures such as encapsulant and die attachment, as well as during the application of the package in a thermally changing environment. Therefore, to better understand the failure mechanism and improve the reliability, stress analysis is of crucial importance in electronic industry.

Stress analysis of electronic packages can be conducted by using analytical, numerical, and experimental methods. Analytical approaches involve constructing well-understood equations and providing exact solutions, but it becomes hard to use for complex problems. Numerical methods often refer to finite element analysis and they are used for sophisticated situations. Although numerical solutions are approximate, in most cases, they have sufficient accuracy for engineering purposes. Experimental methods, giving real information about the behavior of structure, have included the use of test chips incorporating piezoresistive stress sensors (semiconductor strain gauges), and the use of optical techniques such as holographic interferometry, moiré interferometry, and photo elasticity [8],[9].

Piezoresistive stress sensors are a powerful tool for experimental structural analysis of electronic packages. Fig. 1.1 illustrates the basic application concepts. The structures of interest are semiconductor chips which are incorporated in electronic packages. The sensors are resistors that are conveniently fabricated into the surface of the die. Therefore, embedded sensors are not affected by the external environments like chemical, moisture, and contamination. Due to the piezoresistive effect, the stress induced resistance change

can be measured. If the piezoresistive sensors are calibrated over a wide temperature range, thermally induced stress range may be measured.

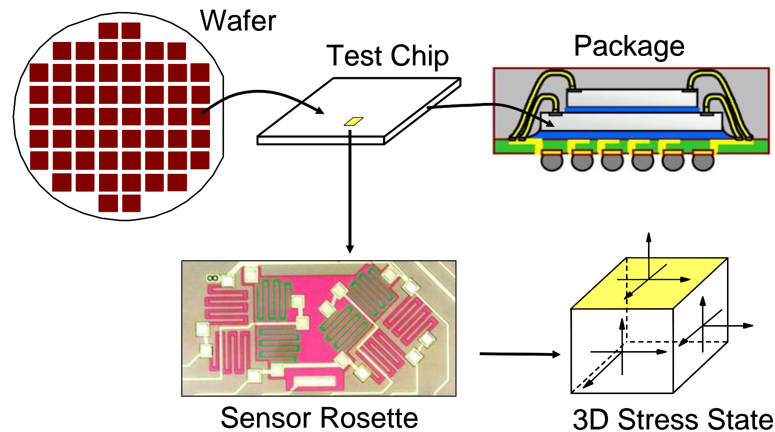

Figure 1.1: Piezoresistive Sensor Concept

In the past, silicon based piezoresistive stress sensors were widely utilized for qualifying of manufacturing processes, guiding material selection, and evaluating reliability. For instance, a full-field mapping of the stress distribution over the surface of a die can be obtained using specially designed test chips, which can be used to measure processing induced die stress as a function of various manufacturing variables. In this role, test chips can be used to guide material selection processes (e.g., encapsulants) [10],[11]. Additionally, embedded sensors can perform in-situ monitoring of stress at critical locations even within encapsulated packages, and can be useful for Prognostics and Health Monitoring (PHM) systems. PHM is a set of algorithms based on in-situ stress measurements, which can provide different level of prognostics, including failure detection,

diagnostics, and life-time prediction [12],[13]. Thus, for power electronics, stress sensors directly integrated on SiC chips are a promising tool for stress analysis and failure prediction.

In the microelectromechanical systems (MEMS) industry, comparing with other types of sensors, the piezoresistive sensor is cheaper and more durable, because of its simple structure. The linear resistance change with strain is critical for preventing distortion of output signal and makes the readout circuit very simple. Therefore, silicon piezoresistance has been extensively studied and used for various sensors such as pressure sensors, accelerometers, strain gauges, etc. However, when it comes to the harsh environments (high temperature, pressure, voltage, radiation, shock, moisture, corrosion, contamination), silicon piezoresistive sensors are ill-suited based on its material properties. For example, high temperature can cause p-n junction failure and current leakage for silicon-based devices. Also, degradation of mechanical properties such as lose of elasticity and plastic deformations have been reported for silicon exposed to extreme conditions [14].

In this case, the use of wide band-gap materials as sensors has raised a great deal of attention. With high elastic modulus, high breakdown voltage, high radiation, hardness, high chemical inertness, SiC is a promising candidate for developing MEMS devices for extreme conditions [15]-[17].

SiC exists in more than 200 different crystal structures, called polytypes. Most of the research and development has focused on three types: 3C, 4H and 6H. Among the polytypes, 4H polytype is the most common for electronic devices because of its excellent

material properties [18]. For instance, the band gap of 3C (2.3eV) and 6H (3.0eV) polytypes are significantly lower than that of 4H (3.23eV), which enables 4H-SiC to operate at higher temperature without breakdown [19]. The carrier mobility of 4H-SiC is higher than the others. In terms of MEMS applications, 4H-SiC possesses high chemical/oxidation resistance, high hardness, high elastic modulus, and large thermal conductivity, which are important for harsh environment applications.

In this work, the design and calibration of piezoresistive stress sensors on 4H-SiC are discussed. The stress sensors investigated in this research are resistors, van der Pauw structures (VDP), and field-effect transistors (FETs). Due to the fabrication limitations, the electronic devices are fabricated on the off-axis wafer plane of the 4H-SiC. The impact of such off-axis effect on the stress sensors are investigated. For subsequent stress analysis in electronic packaging, the mechanical properties such as elastic modulus and Poisson's ratio of 4H-SiC are characterized using strain gauge and nanoindentation methods. Finally, an example of stress analysis using stress sensors is presented.

Chapter 2

THEORETICAL BACKGROUND AND LITERATURE REVIEW

2.1 Piezoresistive effect

2.1.1 History

The word “piezoresistive” contains two words of different linguistic origin: “piezo” comes from Greek words meaning “to press, to squeeze” and “resistive” is derived from Latin words which means “to stop”. The piezoresistive effect is a change in electrical resistance of a metal or semiconductor when the material is stressed. The change of resistance in metal due to applied stress was first discovered by William Thomson (Lord Kelvin) in 1856 [20], followed by a vast number of studies. In 1876, Tomlinson measured direction dependent conductivity of metals under mechanical loads [21],[22]. Because of low sensitivity, the applications of piezoresistance in metals are very limited. In 1950, around a hundred years after the discovery of piezoresistance, Bardeen and Shockley proposed the theoretical formulation of deformation potentials and predicted large conductivity changes with strain in single crystal semiconductors [23]. In 1954, C. S. Smith, a researcher who was visiting Bell Laboratories, performed experimental measurements of the piezoresistive effect in silicon and germanium and reported ‘exceptionally large’ piezoresistive shear coefficients [24]. Since then, the piezoresistive effect in semiconductors has been intensively investigated.

Silicon strain gauges, with sensitivity more than fifty times higher than conventional metal strain gauges, were first reported by Mason and Thurston in 1957 [25]. With the advance of the micro fabrication technologies, especially after the invention of the 'planar' transistor in 1960 [26], mass production of silicon piezoresistive sensors was further developed.

Nowadays, many researchers have studied piezoresistive coefficients of silicon both analytically and experimentally, as a function of doping concentration and temperature and performance of piezoresistive sensors, including sensitivity, resolution, and bandwidth, are significantly improved by the modern fabrication processes and techniques.

2.1.2 Piezoresistive Fundamentals

The piezoresistive effect refers to the change of resistance due to mechanical stress or strain. The electrical resistance of an isotropic structure is a function of its dimensions and resistivity [27]:

$$R = \rho \frac{L}{Wt} \tag{2.1}$$

Where ρ is the resistivity, L is the length, W is the width, t is the thickness of the resistor. Under an applied stress, the resistance changes because of the dimension and resistance changes:

$$\partial R = \frac{L}{Wt}\partial\rho + \frac{\rho}{Wt}\partial L - \frac{\rho L}{W^2 t}\partial w - \frac{\rho L}{Wt^2}\partial t \tag{2.2}$$

The normalized resistance change can be obtained:

$$\frac{\partial R}{R} = \frac{\partial L}{L} - \frac{\partial W}{W} - \frac{\partial t}{t} + \frac{\partial \rho}{\rho}$$
$$= \varepsilon_L (1 + 2\nu) + \frac{\partial \rho}{\rho} \quad (2.3)$$

Where ε_L is the longitudinal strain, and ν is the Poisson's ratio.

The piezoresistive effect can be represented by the gauge factor (GF):

$$GF = \frac{\partial R / R}{\varepsilon_L} = (1 + 2\nu) + \frac{\partial \rho / \rho}{\varepsilon_L} \quad (2.4)$$

In metal strain sensors, the change of geometry dominates the GF, and the second term which presents resistivity change is negligible. Therefore, the GF for metals becomes

$$GF = \frac{\partial R / R}{\varepsilon_L} \simeq (1 + 2\nu) \quad (2.5)$$

However, for semiconductor sensors, the GF is primarily due to the resistivity changes which are related to the change in the number of free electrons and the change in mobility induced by the lattice deformation. Hence, the GF for semiconductors is

$$GF = \frac{\partial R / R}{\varepsilon_L} \simeq \frac{\partial \rho / \rho}{\varepsilon_L} \quad (2.6)$$

The resistance change $\partial R/R$ can also be expressed in terms of stress

$$\frac{\partial R}{R} \simeq \frac{\partial \rho}{\rho} = \pi_l \sigma_l \quad (2.7)$$

Where π_l and σ_l represent the piezoresistive coefficient and stress along longitudinal direction, respectively. Therefore, the relationship between the GF and piezoresistive coefficient can be given based on the Hook's law:

$$GF = \pi_l E \quad (2.8)$$

Where E is the elastic modulus.

2.1.3 Piezoresistive Tensor

In semiconductors, the piezoresistivity exhibits a large anisotropy, which means the change of resistivity depends on the orientation of electric field and mechanical loadings. In a cartesian coordinate system, the relationship between electric field $\overrightarrow{E_f}$ and current density $\vec{J}$ is

$$\begin{bmatrix} J_1 \\ J_2 \\ J_3 \end{bmatrix} = \begin{bmatrix} \rho_{11} & \rho_{12} & \rho_{13} \\ \rho_{12} & \rho_{22} & \rho_{23} \\ \rho_{13} & \rho_{23} & \rho_{33} \end{bmatrix} \begin{bmatrix} E_{f1} \\ E_{f2} \\ E_{f3} \end{bmatrix} \tag{2.9}$$

The resistivity tensor ρ is a second rank tensor. Since ρ is symmetric, there are only six independent components.

The applied stresses will change the value of resistivity components, which can be modeled using the series expansion [28].

$$\rho_{ij} = \rho_{ij}^0 + \Pi_{ijkl}\sigma_{kl} + \Lambda_{ijklmn}\sigma_{kl}\sigma_{mn} + \cdots \tag{2.10}$$

Where σ_{kl} represent stress components, ρ_{ij}^0 are the resistivity components for the stress free material and Π_{ijkl} and Λ_{ijklmn}, etc. are components for fourth, sixth, and higher order tensors which characterize the stress induced resistivity change. For sufficiently small stress levels, this relation is typically truncated so that the resistivity components are linearly related to the stress components

$$\begin{aligned} \rho_{ij} &= \rho_{ij}^0 + \Pi_{ijkl}\sigma_{kl} \\ \Delta\rho_{ij} &= \pi_{ijkl}\sigma_{kl} \end{aligned} \tag{2.11}$$

The relation in the above equation can be simplified by recognizing that the resistivity and stress tensors are symmetric($\rho_{ij} = \rho_{ji}$, $\sigma_{ij} = \sigma_{ji}$), therefore, the following relations are given

$$\Pi_{ijkl} = \Pi_{jikl} \qquad \Pi_{ijkl} = \Pi_{jilk} \tag{2.12}$$

To reduce the complexities of the index labels, the index pairs are replaced by single indices as

$$11 \sim 1 \quad 22 \sim 2 \quad 33 \sim 3 \qquad 13 \sim 4 \quad 23 \sim 5 \quad 12 \sim 6 \tag{2.13}$$

Hence, the expressions in Eq. 2.11 can be rewritten in indicial notations as

$$\rho_\alpha = \rho_\alpha^0 + \Pi_{\alpha\beta}\sigma_\beta \tag{2.14}$$

Where Greek indices take on the values 1,2, …, 6. Note that when $\beta \leq 3$, $\Pi_{\alpha\beta} = \Pi_{ijkl}$ and if $\beta > 3$, $\Pi_{\alpha\beta} = 2\Pi_{ijkl}$ (i.e., $\Pi_{11} = \Pi_{1111}$, $\Pi_{16} = 2\Pi_{1112}$), and more details can be found in [28]. A further notation simplification can be obtained by introduction of the so-called piezoresistive coefficients. They are defined by

$$\pi_{\alpha\beta} = \frac{\Pi_{\alpha\beta}}{\bar{\rho}} \tag{2.15}$$

where $\bar{\rho}$ is the mean unstressed resistivity

$$\bar{\rho} = \frac{\rho_{11}^0 + \rho_{22}^0 + \rho_{33}^0}{3} \tag{2.16}$$

Hence, Eq. 2.14 becomes

$$\frac{\Delta\rho_{\alpha}}{\bar{\rho}} = \pi_{\alpha\beta}\sigma_{\beta} \quad (2.17)$$

As we discussed previously, the resistance changes induced by geometry are negligible for semiconductors. Therefore, the relationship between resistance and stress is shown in Eq. 2.18 and the stress components can be evaluated by measuring resistance with known piezoresistive coefficients.

$$\frac{\Delta R}{R} \simeq \frac{\Delta\rho_{\alpha}}{\bar{\rho}} = \pi_{\alpha\beta}\sigma_{\beta} \quad (2.18)$$

2.2 Piezoresistive Stress Sensors

2.2.1 Resistive Rosettes

Piezoresistive stress sensors embedded on the die surface can characterize complex stresses developed in electronic packages. These sensors are mainly resistor sensors which are implanted or diffused in the surface of the die in suitable locations on the surface as shown in Fig. 2.1 [29]. In early 1980s, Texas instrument first reported characterization of silicon lattice stress in plastic encapsulated packages by using "diffused strain gauges" [30]-[32]. Two-element sensor rosettes with 0-90° orientations, capable of measuring in-plane normal stress on die surface on (100) silicon were used few researchers such as Spencer et al. [32], Edward et al. [31], Beaty et al. [33]. Four-element sensor rosettes with 0-±45°-90°, which can measure all three in-plane stress components, were studied by Natarajan et al. [34] on (100) silicon and Gee et al. [35],[36] on (111) silicon. The Suhling and Jaeger group have extensively studied embedded stress sensors and discovered optimized sensor rosette on the (111) silicon which can measure complete three-

dimensional (3D) state of stress. Fig 2.2 shows the top view of a 3D stress sensor, both n- and p-type sensing elements in 0-$\pm 45°$-90° configuration are used, and the serpentine pattern of each element provides an acceptable resistance level for measurement [28].

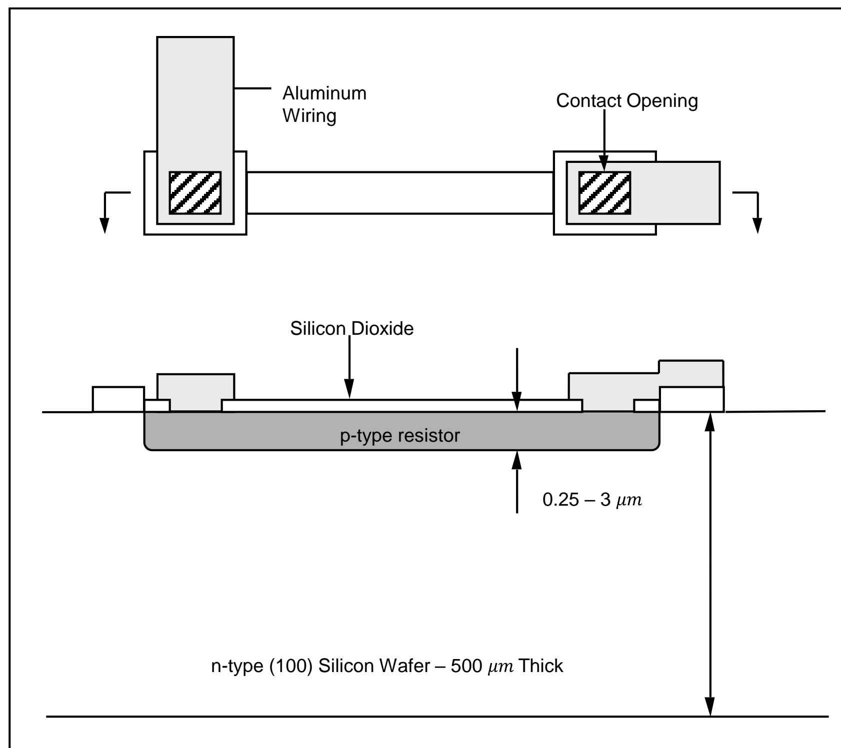

Figure 2.1: Top and Side View of a Resistor Sensor. Reprinted from [29].

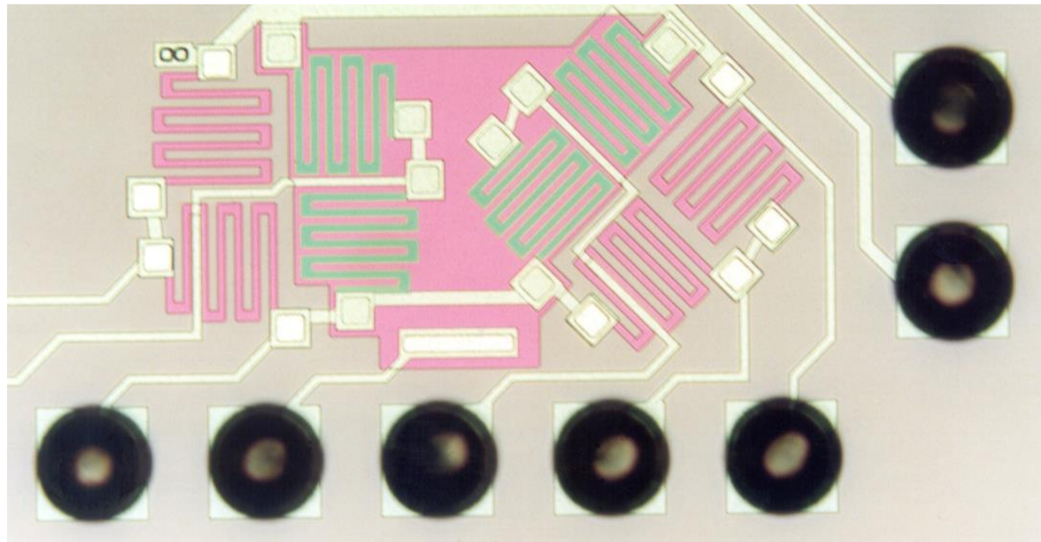

Figure 2.2: Photomicrograph of Eight Elements Resistive Rosettes. Reprinted from [28]

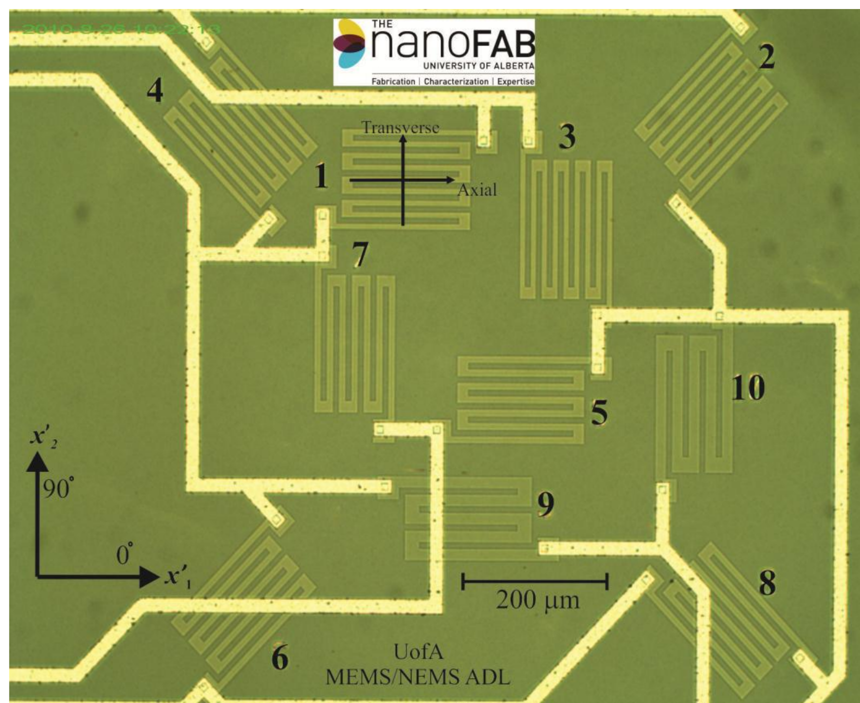

Figure 2.3: Photomicrograph of Ten Elements Resistive Rosettes. Reprinted from [39]

Tufte et al. [37],[38] discovered that the shear piezoresistive coefficient π_{44} of n-type silicon remains almost constant over most of the doping concentration range but starts to change rapidly at a concentration above $1 \times 10^{20}\ \mathrm{cm}^{-3}$. By using such concentration-dependent piezoresistive properties, Gharib et al. [39] introduced ten-element piezoresistive rosette which is able to measure 3D state of stress with temperature compensation.

2.2.2 Van der Pauw Stress Sensors

To achieve an acceptable unstressed reference resistance, the resistors are typically made using long serpentine conduction paths and cover a relatively large area on the die surface. Thus, they can only measure the average stresses over the region covered by all of the rosette elements. For critical areas such as near the corner of the die, the resistor rosettes are not optimal because of relatively large size. Another issue induced by large size is high leakage currents in p-n junction between the resistors and base. To overcome such limitations, an alternative approach for sensing rosettes was developed by Mian et al. [40] using Van der Pauw (VDP) structures. These structures are commonly used as test structures to measure sheet resistance. The VDP structure requires only one square of material (Fig. 2.4), and its characteristics are also size independent. Therefore, they can capture the stress in a small area without loss of sensitivity. If several VDP structure are arranged along proper orientations, 3D stress components can be extracted. In Fig. 2.5, four-element VDP rosette, containing both n- and p-type structures on (111) silicon, is capable of measuring all six stress components and four temperature compensated stress

components can be extracted. Moreover, VDP stress sensors can provide more than three times sensitivity than traditional resistor rosettes.

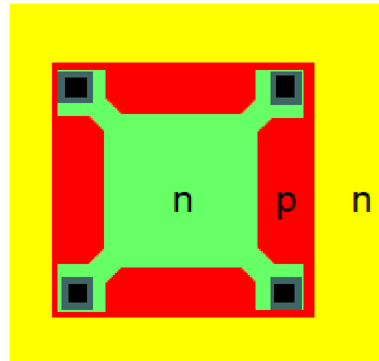

Figure 2.4: n-type VDP Structure in a p-well.

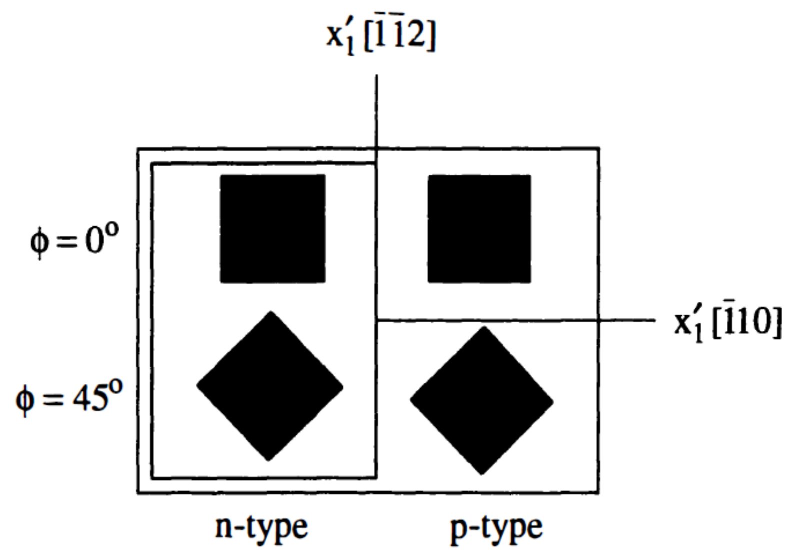

Figure 2.5: Schematic of a Four Element VDP Rosette on (111) Silicon. Reprinted from [40].

2.2.3 MOSFET Stress Sensors

In size limited applications, metal-oxide-semiconductor field-effect transistors (MOSFET) are excellent stress sensors because of their advantages of smaller size, high sensitivity due to lighter doping, operable in wide temperature range over the traditional resistor sensors. When a MOSFET is biased in either linear or saturation region of operation, its drain current is inversely proportional to its channel resistance. In this case, the MOSFET can be treated as a resistor whose resistance is a function of gate voltage. The application of stress can change the resistance of channel region and the piezoresistive behavior of MOS is similar to that of a resistor along the channel region [41],[42]. Hence, MOSFET sensor rosettes were developed as an alternative to the (100) sensing rosettes. Conceptual layout of the optimized PMOS and NMOS stress senor rosettes appear in Fig. 2.6 where the PMOS transistor pair measures the difference in the in-plane normal stress, and the NMOS pair measures in-plane shear stress [43]. Also, Bradley et al. showed that the stress sensitivity of the FET channel does not depend on the channel length and parasitic resistance is the reason for the observed reduction in piezoresistive coefficients of short-channel devices. Hussain et al. reported that the piezoresistive coefficients of PMOS and NMOS devices vary significantly with choice of operating point and are strongly correlated with the underlying value of channel mobility [44]. The stress sensitivity of the PMOS devices was demonstrated to be linearly dependent on both operating current and mobility, whereas the NMOS sensitivity increased more rapidly as the current was reduced and exhibited a quadratic relation to electron mobility. Jaeger et al. [45] proposed a simplified model which provides a continuous description of the MOSFET stress behavior from weak

though strong inversion in their recent work. They pointed out that the stress responses of individual NMOS and PMOS transistors are strongly affected by stress dependent changes in threshold voltage, particularly in moderate and weak inversion region.

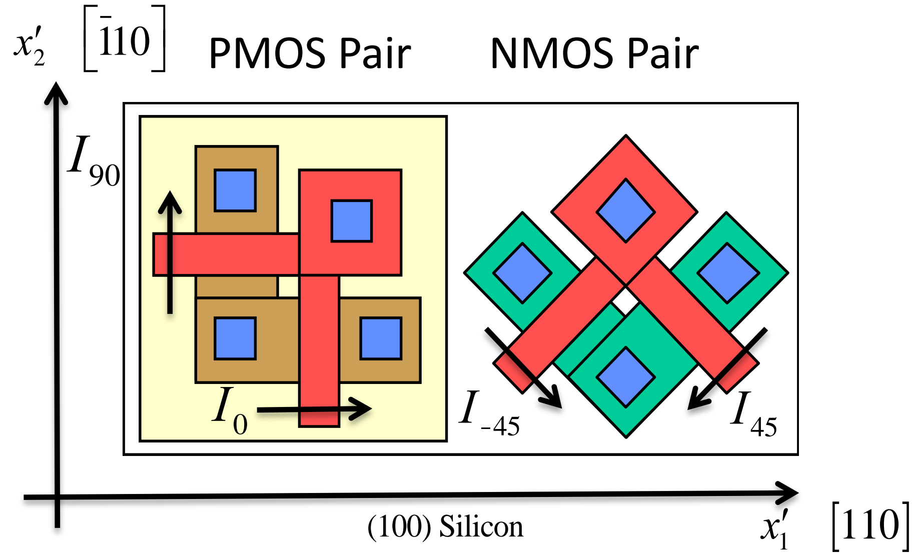

Figure 2.6: Conceptual Layout of 0-90° PMOS and ±45° NMOS Stress Sensors on (100) Silicon. Reprinted from [43]

Traditional MOSFET stress sensors measure two in-plane stress components ($\sigma_{11} - \sigma_{22}, \sigma_{12}$). Baumann et al. developed a MOSFET stress sensors that can extract three more stress components ($\sigma_{13}, \sigma_{23,} \sigma_{\Sigma} = \frac{\sigma_{11}+\sigma_{22}}{2} - \beta\sigma_{33}$). In Fig. 2.7, the vertical shear stress components can be obtained by using pseudo-hall contacts and the vertical resistance sensor can extract the sum of the three normal stresses in a temperature compensated manner [46].

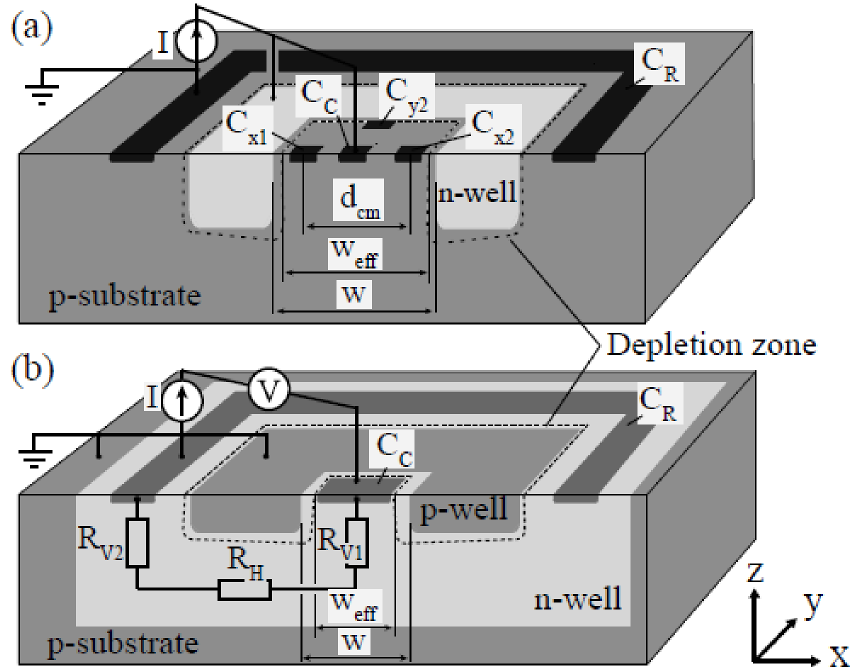

Figure 2.7: (a) p-type Out-of-plane Shear Stress Sensor and (b) the Device Sensitive to Out-of-plane Normal Stress. Reprinted from [46].

2.3 Physical Properties of 4H-SiC

2.3.1 Crystal Structure of SiC

Silicon carbide (SiC) exists in many different crystal structures, called polytypes. The polytypes are characterized by stacking consequence of atom layers [47]-[50]. For example, consider a hexagonal closed-packed system, shown in Fig. 2.8 [51]. If there are three possible sites (A,B, and C) and each site cannot directly stack on itself (the next top layer of "A" can only be "B" or "C"), there are infinite possible sequences in principle. For most materials, only one stacking structure is usually stable. However, SiC has more than 200 polytypes. Among these polytypes, only a few are used as electronic semiconductor

materials, including 3C-SiC, 4H-SiC, 6H-SiC, and 15R-SiC. Polytypes are represented by the number of bilayers in the unit cell and crystal system. As shown in Fig. 2.9, 3C-SiC is described by repeating sequence of ABC. Similarly, 4H- and 6H-SiC can be described by ABCB and ABCACB, respectively. "C", "H", "R" stands for cubic, hexagonal, and rhombohedral crystal structures. 3C-SiC is also called β-SiC, and other polytypes are called α-SiC. Fig. 2.10 shows the primitive cells and fundamental translation vectors of cubic and hexagonal SiC.

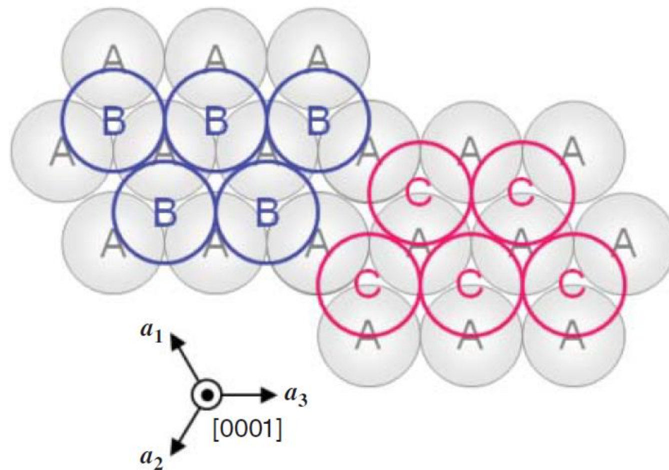

Figure 2.8: Occupation Sites in Hexagonal Closed-packed System, Borrowed from [51].

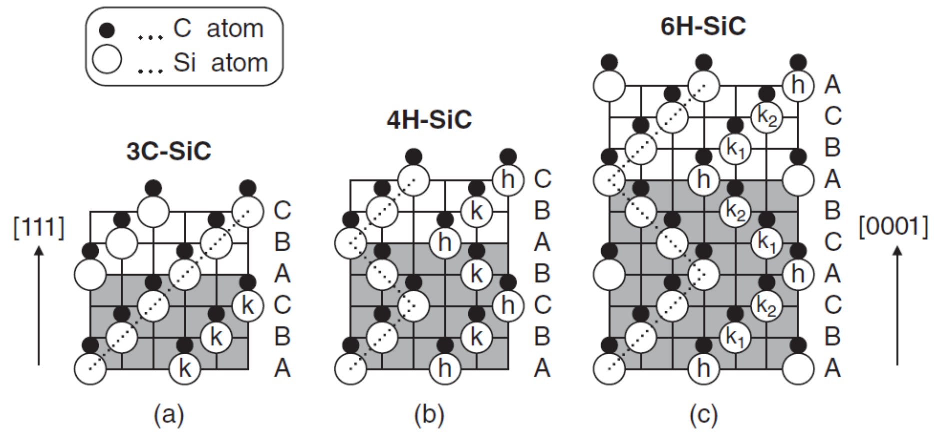

Figure 2.9: Schematic Structure of Popular Polytypes: (a) 3C-SiC, (b) 4H-SiC and (c) 6H-SiC, Borrowed from [51].

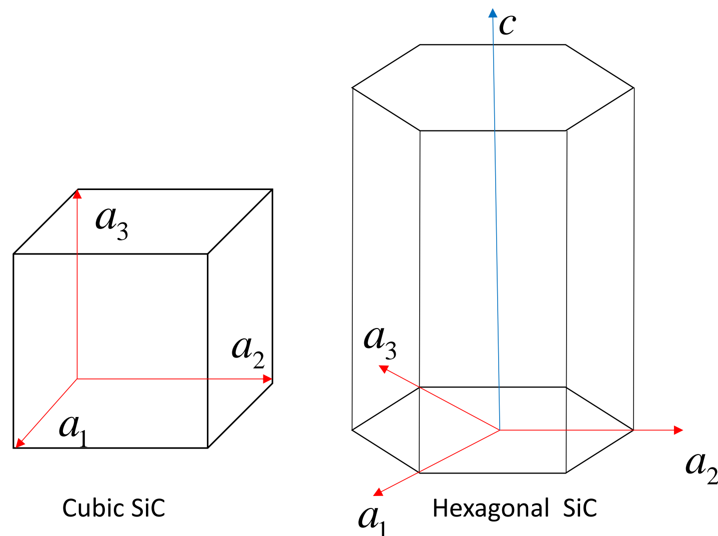

Figure 2.10: Crystal Structure of cubic and hexagonal SiC

2.3.2 Physical Properties of SiC

From Table 2.1 [52]-[56], silicon carbide polytypes have much higher bandgap and breakdown voltage than that of silicon whereas silicon has higher carrier mobility. 4H-SiC

possess the highest breakdown voltage and carrier mobility among these polytypes, which makes it an ideal material for electronic devices and high temperature applications. Also, silicon carbide polytypes possess higher hardness, stiffness, wear resistance and melting temperature, which are important for devices operating in harsh environment.

Properties	Si	3C-SiC	4H-SiC	6H-SiC
Bandgap (eV)	1.12	2.36	3.26	3.02
Breakdown Voltage (MV/cm)	0.3	1.4	2.2-2.8	1.7-3.0
Electron Mobility (cm^2/Vs)	1400	1000	1000-1200	100-450
Hole Mobility (cm^2/Vs)	470	40	120	100
Elastic Modulus (GPa)	130-170	330-384	400-550	440-500
Density (g/cm^3)	2.33	3.21	3.21	3.21
Mohs Hardness	6.5	9.2-9.3	9.2-9.3	9.2-9.3
Melting Point (K)	1690	3103	3103	3103
Thermal Conductivity (W/cmK)	1.3	3.6	4.9	4.9

Table 2.1: Physical Properties of Si and SiC at Room Temperature

2.3.3 Piezoresistive Effect of 4H-SiC

The fundamental piezoresistive coefficients or gauge factors (GFs) were studied experimentally and analytically by several groups. Nakamura et al. simulated the piezoresistivity of n-type SiC nano sheets using density functional theory [57]. As shown

in Fig. 2.11, The results show that the fundamental longitudinal and transverse GFs have similar magnitude but opposite sign and the sensitivity is decreasing with increasing temperature.

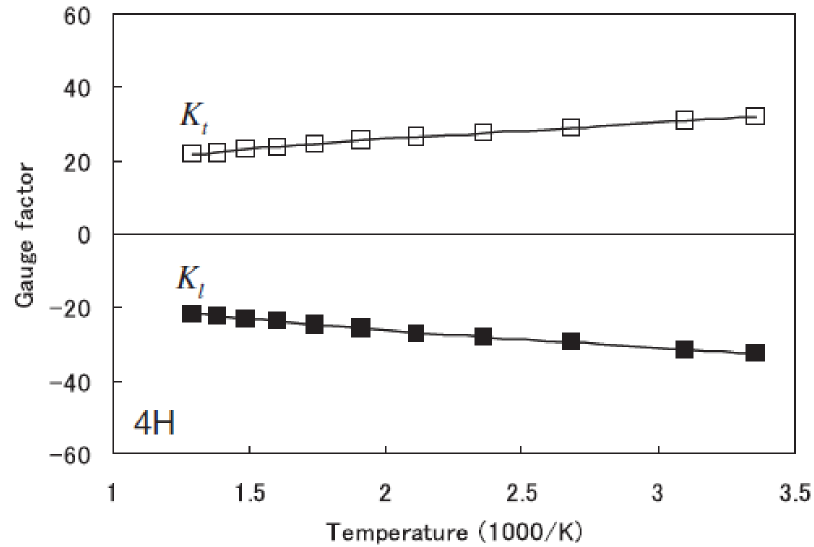

Figure 2.11:Gauge Factors vs. Temperatures. Reprinted From [57].

The experimental study on n-type 4H-SiC at room temperature were performed by Akiyama et al [58]. In Fig 2.12, the n-type piezoresistors were fabricated on p-type epilayer and cut from 4° off-axis wafers and stress were introduced by deflecting the free end of the cantilever. The results showed that the longitudinal GF is 5 to 20 and transverse GF is -5 to -10 depending on piezoresistor's width and length.

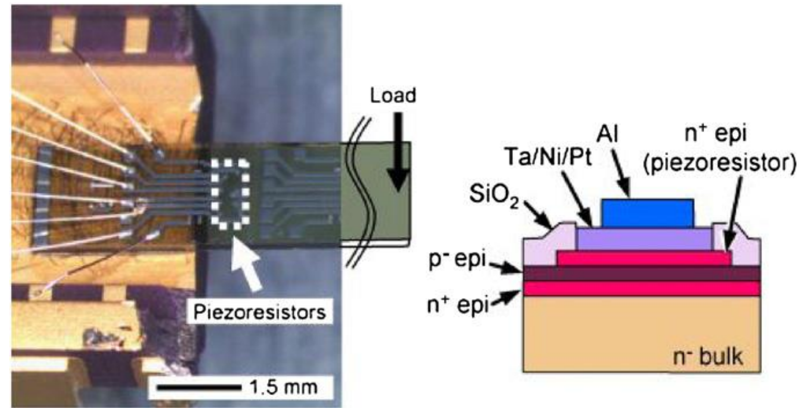

Figure 2.12: Cantilever beam for Piezoresistance Characterization, Reprinted From [58].

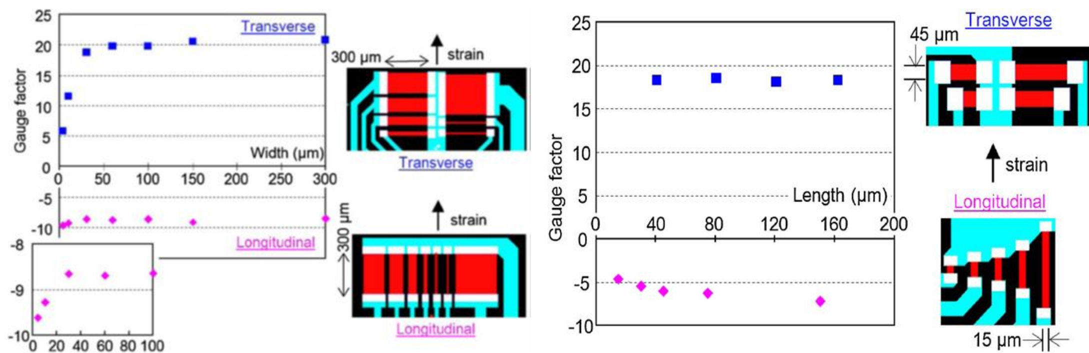

Figure 2.13: Gauge Factors as a Function of Piezoresistor's Widths and Lengths.

Reprinted From [58].

Okojie et al. [59] discovered that the n-type 4H-SiC pressure sensors start to recover its sensitivity at 400 ℃ and reaches values that are nearly equal to the temperature values at 800 ℃, which provides the promise of delivering room-temperature level sensitivity at the extremely high temperatures.

Nguyen et al. investigated the piezoresistivity of p-type 4H-SiC in their recent studies [60]-[61]. In Fig. 2.14, the GFs of 100 μm, 200 μm and 300 μm p-type piezoresistors were

characterized and the longitudinal and transverse GFs are around 31 and -27, respectively. The GFs at various temperatures (up to 600℃) were also characterized and they found that the longitudinal GF of p-type resistor at 600℃ decreases about 30% in comparison with the GF at room temperature (Fig. 2.15).

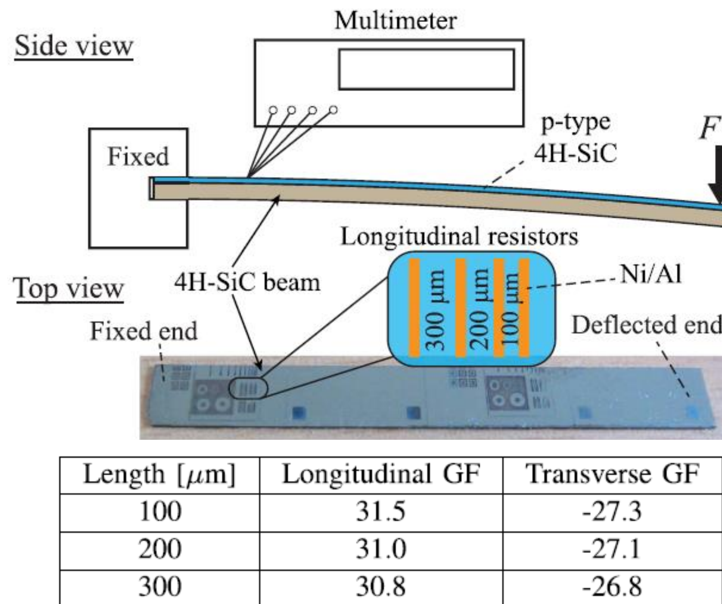

Length [μm]	Longitudinal GF	Transverse GF
100	31.5	-27.3
200	31.0	-27.1
300	30.8	-26.8

Figure 2.14: Schematic Sketch of the Cantilever Beam Bending Experiment and the Gauge Factors. Reprinted From [60].

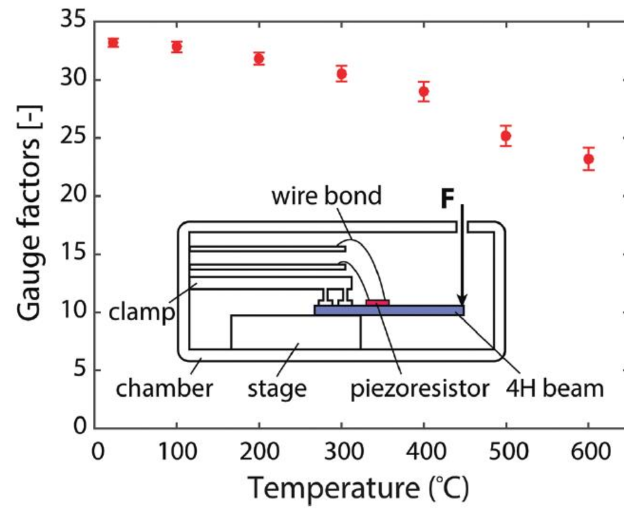

Figure 2. 15: Schematic Sketch of the Cantilever Beam Bending Experiment and the Gauge factors. Reprinted From [61].

Chapter 3

DESIGN AND CALIBRATION OF RESISTIVE STRESS SENSORS ON 4H-SIC

3.1 Design of Resistive Sensors

3.1.1 Introduction

Silicon has been one of the main materials used in piezoresistive stress sensors. However, Si based sensors are not capable of operating at high temperature due to its relatively low bandgap energy (1.12 eV). On the other hand, the bandgap of 4H-SiC is 3.23 eV, which can effectively reduce the number of electron-hole pairs generated in high temperature across the bandgap and improve the high temperature stability of SiC sensors. Therefore, 4H-SiC based stress sensors are capable of monitoring stress related “health issues” in packaged high-voltage, high power SiC devices, as well as applications including automotive and aerospace systems, deep well drilling, and geothermal applications, for example.

In this work, general expressions for the stress dependence of resistors and van der Pauw devices on 4H-SiC are established and the design of resistive rosettes and van der Pauw sensors are discussed. The fundamental piezoresistive coefficients of 4H-SiC were calibrated by using four points bending and hydrostatic method.

3.1.2 Piezoresistive Coefficients and Coordinate Systems for 4H-SiC Chip

As discussed in Chapter 2, the 4H-SiC has a hexagonal crystal structure. In Fig. 3.1, the top plane of the hexagonal structure ((0001) plane) is show on the right side and the a_1-a_2-a_3 represent the crystallographic axes of the 4H-SiC material. By using the symmetric

properties of crystals [62], the Cartesian coordinate system or conventional coordinate system x_1-x_2-x_3 are defined, so that the physic properties can be written in a concise form. The fundamental piezoresistive coefficient tensor in the conventional coordinate system is shown in Eq. 3.1. It can be seen that, there are six unique fundamental piezoresistive coefficients (i.e., π_{11}, π_{22}, π_{33} π_{13}, π_{31} and π_{44}) for 4H-SiC.

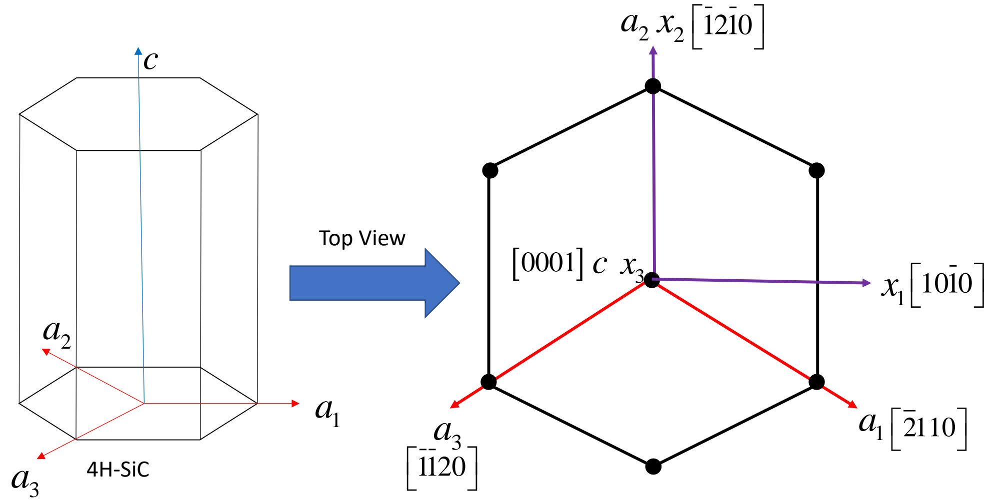

Figure 3.1: Crystal Structure and Conventional Coordinate System For 4H-SiC

$$[\pi] = \begin{bmatrix} \pi_{11} & \pi_{12} & \pi_{13} & 0 & 0 & 0 \\ \pi_{12} & \pi_{11} & \pi_{13} & 0 & 0 & 0 \\ \pi_{31} & \pi_{31} & \pi_{33} & 0 & 0 & 0 \\ 0 & 0 & 0 & \pi_{44} & 0 & 0 \\ 0 & 0 & 0 & 0 & \pi_{44} & 0 \\ 0 & 0 & 0 & 0 & 0 & \pi_{D} \end{bmatrix} \quad (3.1)$$

$$\pi_D = \pi_{11} - \pi_{12}$$

As shown in Fig. 3.2, the wafer coordinate system is defined: the surface of the wafer is a (0001) plane, and the x_2' and x_1' axes are parallel and perpendicular to the primary wafer flat, and x_3', x_3 and c axes are coincident and perpendicular to the wafer plane. These

axes are chosen so that the individual normal stresses are resolved in direction parallel to the edge of standard IC chips, and they also correspond to the orientation of most resistors and transistors in integrated circuits. In order to obtain the piezoresistive coefficient tensor in the wafer coordinate system, a coordinate transformation must be performed.

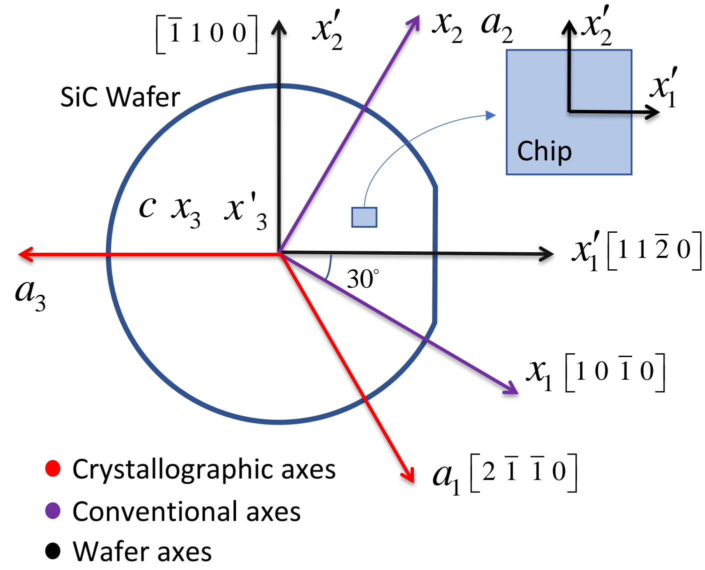

Figure 3.2: Coordinate Systems on (0001) Plane

The piezoresistive coefficient tensor in wafer (primed) coordinate system depends on the fundamental piezoresistive coefficient tensor and the angle between primed and unprimed coordinate systems as shown by Eq. 3.2.

$$[\pi'] = [T][\pi][T]^{-1} \tag{3.2}$$

where [T] is the transformation matrix and l, m, and n are the direction cosines of two coordinate systems.

$$
T = \begin{bmatrix}
l_1^2 & m_1^2 & n_1^2 & 2l_1n_1 & 2m_1n_1 & 2l_1m_1 \\
l_2^2 & m_2^2 & n_2^2 & 2l_2n_2 & 2m_2n_2 & 2l_2m_2 \\
l_3^2 & m_3^2 & n_3^2 & 2l_3n_3 & 2m_3n_3 & 2l_3m_3 \\
l_1l_3 & m_1m_3 & n_1n_3 & l_1n_3 + l_3n_1 & m_1n_3 + m_3n_1 & l_3m_1 + l_1m_3 \\
l_2l_3 & m_2m_3 & n_2n_3 & l_2n_3 + l_3n_2 & m_2n_3 + m_3n_2 & l_2m_3 + l_3m_2 \\
l_1l_2 & m_1m_2 & n_1n_2 & l_1n_2 + l_2n_1 & m_1n_2 + m_2n_1 & l_1m_2 + l_2m_1
\end{bmatrix} \quad (3.3)
$$

$$
\cos(x'_1, x_i) = l_i \quad \cos(x'_2, x_i) = m_i \quad \cos(x'_3, x_i) = n_i
$$

It has been found that the elements of piezoresistive coefficient tensor are identical ($[\pi]=[\pi']$) for rotations within the basal plane. Therefore, 4H-SiC is a transversely isotropic material. All the calculations have been performed symbolically using the mathematical software MATLAB®.

3.1.3 Resistive Rosettes

An arbitrarily orientated resistor on (0001) surface of the 4H-SiC is shown in Fig. 3.3. The angle between the resistor and x'_1 axis is ϕ.

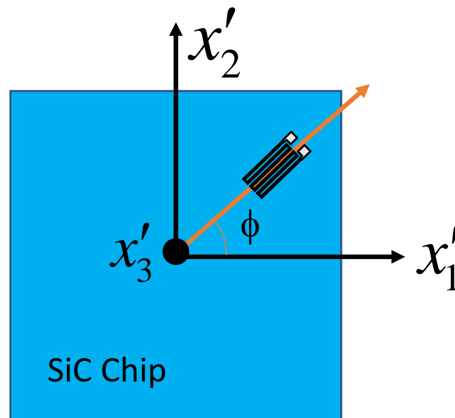

Figure 3.3: Resistor Arbitrarily Orientated with Respect to the Wafer Axes

For a given angle ϕ, the normalized change in resistance can be expressed in terms of the primed stress components (stress components in wafer coordinate system) using

$$\begin{aligned} \frac{\Delta R}{R} &= \frac{R(\alpha,T)-R(0,0)}{R(0,0)} \\ &= (\pi'_{1\alpha}\sigma'_{\alpha})\cos^2\phi + (\pi'_{2\alpha}\sigma'_{\alpha})\sin^2\phi \\ &+(\pi'_{6\alpha}\sigma'_{\alpha})\sin 2\phi + \left[\alpha_1\Delta T + \alpha_2\Delta T^2 + \cdots\right] \end{aligned} \tag{3.4}$$

where $\pi'_{1\alpha}$, $\pi'_{2\alpha}$, and $\pi'_{6\alpha}$ ($\alpha = 1,2,\ldots 6$) are temperature dependent piezoresistive coefficients in the wafer coordinate system, α_1, α_2, … are temperature coefficients of resistance, ΔT is the difference between the measurement temperature and reference temperature where the unstressed reference value of resistance R(0,0) is measured.

Since the transformed piezoresistive coefficients are equal to the fundamental piezoresistive coefficients, substitution of the unprimed values into Eq. 3.4 yields

$$\begin{aligned} \frac{\Delta R_\phi}{R_\phi} &= \left(\pi_{11}\sigma'_{11} + \pi_{12}\sigma'_{22}\right)\cos^2\phi + \left(\pi_{12}\sigma'_{11} + \pi_{11}\sigma'_{22}\right)\sin^2\phi \\ &+ \pi_D\sigma'_{12}\sin 2\phi + \pi_{13}\sigma'_{33} + \left[\alpha_1\Delta T + \alpha_2\Delta T^2 + \cdots\right] \end{aligned} \tag{3.5}$$

It can be seen that resistors on (0001) planes respond to only four of the six components of the stress state similar to the case for (100) silicon [28],[29]. Typical sensor rosettes similar to those on silicon consist of two or more resistors aligned at various angles relative to the primed axes as indicated in the four-element rosettes in Fig. 3.4.

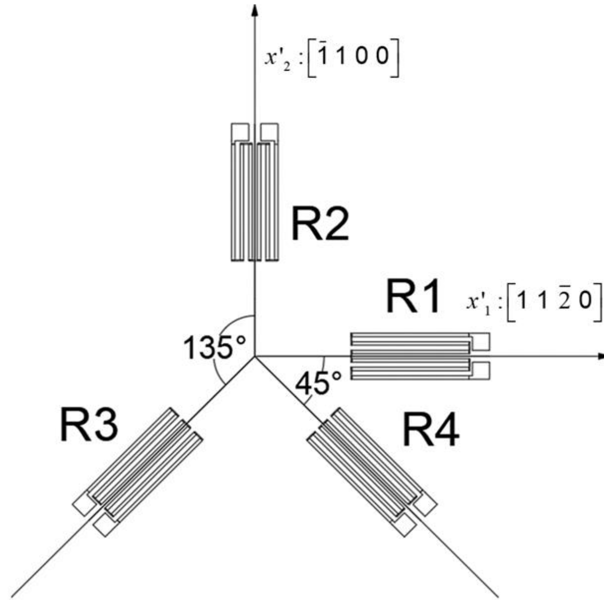

Figure 3.4: Four-element Rosette for In-plane Stress Measurement

Resistor change equations are found by expanding Eq. 3.5 for angles of 0, 90, +45 and -45 degrees as in Eq. 3.6.

$$\begin{aligned}
\frac{\Delta R_1}{R_1} &= \pi_{11}\sigma'_{11} + \pi_{12}\sigma'_{22} + \pi_{13}\sigma'_{33} + \left[\alpha_1\Delta T + \alpha_2\Delta T^2 + \cdots\right] \\
\frac{\Delta R_2}{R_2} &= \pi_{12}\sigma'_{11} + \pi_{11}\sigma'_{22} + \pi_{13}\sigma'_{33} + \left[\alpha_1\Delta T + \alpha_2\Delta T^2 + \cdots\right] \\
\frac{\Delta R_3}{R_3} &= \left(\frac{\pi_{11} + \pi_{12}}{2}\right)\sigma'_{11} + \left(\frac{\pi_{11} + \pi_{12}}{2}\right)\sigma'_{22} + \pi_{13}\sigma'_{33} \\
&\quad + \pi_D\sigma'_{12} + \left[\alpha_1\Delta T + \alpha_2\Delta T^2 + \cdots\right] \\
\frac{\Delta R_4}{R_4} &= \left(\frac{\pi_{11} + \pi_{12}}{2}\right)\sigma'_{11} + \left(\frac{\pi_{11} + \pi_{12}}{2}\right)\sigma'_{22} + \pi_{13}\sigma'_{33} \\
&\quad - \pi_D\sigma'_{12} + \left[\alpha_1\Delta T + \alpha_2\Delta T^2 + \cdots\right]
\end{aligned} \tag{3.6}$$

The four-element rosette is most often utilized because of the temperature compensation advantages (i.e., the $\alpha\Delta T$ terms cancel) that occur when subtracting the resistor changes from pairs of orthogonal resistors as demonstrated in Eq. 3.7.

$$\begin{aligned} &\frac{\Delta R_1}{R_1} - \frac{\Delta R_2}{R_2} = \pi_D(\sigma'_{11} - \sigma'_{22}) \\ &\frac{\Delta R_3}{R_3} - \frac{\Delta R_4}{R_4} = 2\pi_D\sigma'_{12} \\ &\pi_D = \pi_{11} - \pi_{12} \end{aligned} \tag{3.7}$$

Two temperature compensated quantities, the normal stress difference $(\sigma'_{11} - \sigma'_{22})$ and shear stress σ'_{12}, can be extracted using above equation. Note that the out-of-plane normal stress terms, $\pi_{33}\sigma'_{33}$, also cancel in Eq. 3.7 so that a free surface is not required for the stress extractions.

For the specific case of a free top surface $(\sigma'_{33} = 0)$ and careful control of temperature (ΔT= 0), the two individual normal stresses can be measured using either of the sum terms in Eq. 3.8 with Eq. 3.7.

$$\begin{gathered} \frac{\Delta R_1}{R_1} + \frac{\Delta R_2}{R_2} = \frac{\Delta R_3}{R_3} + \frac{\Delta R_4}{R_4} = \pi_S(\sigma'_{11} + \sigma'_{22}) \\ \pi_S = \pi_{11} + \pi_{12} \end{gathered} \tag{3.8}$$

Therefore,

$$\sigma'_{11} = \frac{1}{2}\left(\frac{\frac{\Delta R_0}{R_0} - \frac{\Delta R_{90}}{R_{90}}}{\pi_D} + \frac{\frac{\Delta R_0}{R_0} + \frac{\Delta R_{90}}{R_{90}}}{\pi_S} \right)$$

$$\sigma'_{22} = \frac{1}{2}\left(\frac{\frac{\Delta R_0}{R_0} + \frac{\Delta R_{90}}{R_{90}}}{\pi_S} - \frac{\frac{\Delta R_0}{R_0} - \frac{\Delta R_{90}}{R_{90}}}{\pi_D} \right) \tag{3.9}$$

In order to extract the in-plane stresses from the resistor change equations, we need values for π_{11} and π_{12} (π_S and π_D are sum and difference of π_{11} and π_{12}), which can be measured by using four-point bending method. Two in-plane piezoresistive coefficients π'_{11} and π'_{12} are often referred to as the longitudinal (π_L) and transverse (π_T) piezoresistive coefficients.

Now, three out of four stress components can be extracted by using the four-element single-polarity (either n-type or p-type) rosette. The out of plane normal stress σ'_{33} can be obtained by using dual-polarity (both n-type and p-type) rosettes because the piezoresistive coefficients of the n-type and p-type are different.

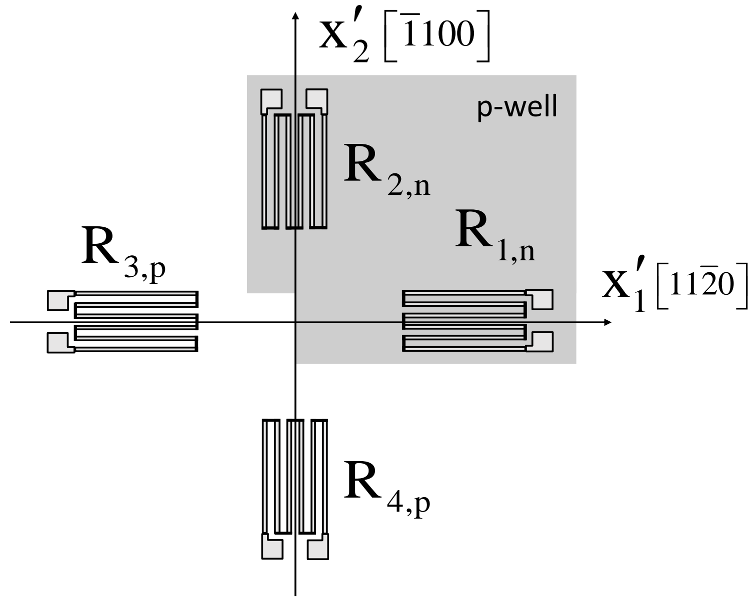

Figure 3.5: Four-element Rosette for Out-of-Plane Stress Measurement

The rosette contains a pair of n-type and a pair of p-type resistors directed at 0 and 90 degrees with respect to the x'_1-axis. Application of Eq. 3.5 to four orientations gives relations between resistance changes and the stresses at the rosette site (The second and higher order temperature terms are ignored).

$$\begin{aligned}
\frac{\Delta R_1}{R_1} &= \pi^{p}_{11}\sigma'_{11} + \pi^{p}_{12}\sigma'_{22} + \pi^{p}_{13}\sigma'_{33} + \alpha^{p}\Delta T \\
\frac{\Delta R_2}{R_2} &= \pi^{p}_{12}\sigma'_{11} + \pi^{p}_{11}\sigma'_{22} + \pi^{p}_{13}\sigma'_{33} + \alpha^{p}\Delta T \\
\frac{\Delta R_3}{R_3} &= \pi^{n}_{11}\sigma'_{11} + \pi^{n}_{12}\sigma'_{22} + \pi^{n}_{13}\sigma'_{33} + \alpha^{n}\Delta T \\
\frac{\Delta R_4}{R_4} &= \pi^{n}_{12}\sigma'_{11} + \pi^{n}_{11}\sigma'_{22} + \pi^{n}_{13}\sigma'_{33} + \alpha^{n}\Delta T
\end{aligned} \tag{3.10}$$

Direct combination of the expressions in Eq. 3.10 leads to the following resistance-stress expressions and the out-of-plane normal stress σ'_{33} can be obtained.

$$\sigma'_{33} = \frac{\pi_S^p \left[\frac{\Delta R_1}{R_1} + \frac{\Delta R_2}{R_2} - 2\alpha^n \Delta T \right] - \pi_S^n \left[\frac{\Delta R_3}{R_3} + \frac{\Delta R_4}{R_4} - 2\alpha^p \Delta T \right]}{2\left(\pi_S^p \pi_{13}^n - \pi_S^n \pi_{13}^p\right)}$$

$$\pi_S^p = \pi_{11}^p + \pi_{12}^p \qquad (3.11)$$

$$\pi_S^n = \pi_{11}^n + \pi_{12}^n$$

Evaluation of σ'_{33} requires measurement of the normalized resistance changes of the sensors and temperature change ΔT experienced by the sensing elements. The temperature coefficients of resistance (α) and piezoresistive coefficients (π_s and π_{13}) must also be known for each doping type. The value of π_{13} can be extracted by combining four-point bending and hydrostatic pressure method, which will be discussed with more details in later sections.

To increase the unstressed reference resistance value for measurement, the resistor rosettes are typically made using long serpentine conduction paths. Therefore, they are fairly large and they are not optimal for use in measuring stresses in critical areas such as near the corner of a die. To overcome the size limitation, alternate sensors such as van der Pauw and FET stress sensors are developed.

3.1.4 Van der Pauw Devices

The four-terminal resistive van der Pauw (VDP) device in Fig. 3.6 (a), commonly utilized for sheet resistance characterization, can also be used as a stress sensor [40][63][64]. The VDP structure requires only one square of material, and its characteristics are also size independent. Thus, such sensors can be made small enough to capture stress variation in a small area without any loss of sensitivity. Additionally, the

VDP measurements require four probes, ensuring Kelvin type measurements, thus nullifying the effect of probe-contact resistances. Moreover, the VDP stress sensors on silicon provides 3.16 times sensitivity than that of resistor rosette sensors.

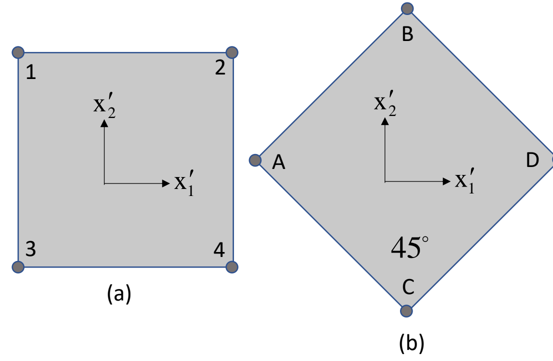

Figure 3.6: 0° and 45° VDP Devices

In Fig. 3.6 (a), the VDP sample has uniform thickness, and no isolated holes. The four electrical contacts 1,2,3, and 4 are located at four corners of the sample. Van der Pauw defined the resistance ($R_{12,34}$) of the sample as the potential difference V_4-V_3 between the contacts 4 and 3 per unit current through contacts 1 and 2. In this case, current enters the sample through contact 1 and leaves the sample through contact 2 and directs along x_1' direction, so that $R_{12,34}$ is defined as R_0 because angle between current direction and x_1' axis is 0 degree. Similarly, if the current directs along x_2' and the voltage between contacts 4 and 2 is measured, R_{90} can be calculated. For a symmetric structure in Fig. 3.6, the sheet resistance (R_S) is defined based on van der Pauw's theorem, so that

$$R_0 = \frac{V_{34}}{I_{12}} \qquad R_{90} = \frac{V_{24}}{I_{13}} \qquad R_S = \frac{\pi}{\ln(2)} \frac{V_{24}}{I_{13}} \tag{3.12}$$

R_{45} and R_{-45} requires another VDP device oriented at 45 degrees with respect to x_1' axis as in Fig. 3.6 (b).

According to Eq. 2.14, for fixed environmental conditions (i.e., temperature), the relationship between in-plane components of resistivity and stress is given by

$$\begin{aligned} \rho_{11}' &= \rho_0(1+\pi_{11}\sigma_{11}' + \pi_{12}\sigma_{22}' + \pi_{13}\sigma_{33}') \\ \rho_{22}' &= \rho_0(1+\pi_{12}\sigma_{11}' + \pi_{11}\sigma_{22}' + \pi_{13}\sigma_{33}') \\ \rho_{12}' &= \rho_0(\pi_D)\sigma_{12}' \end{aligned} \tag{3.13}$$

where $\rho_{\alpha\beta}'$ are resistivity components in primed coordinate system.

When there is no stress applied, $R_0= R_{90}$ for such a symmetric structure. Based on Eq. 3.13, the normalized resistance change in each direction can be obtained and difference of resistance change is shown in Eq. 3.14. More details can be found in [40].

$$\begin{aligned} \frac{\Delta R_0}{R_0} - \frac{\Delta R_{90}}{R_{90}} &= 3.157\pi_D\left(\sigma_{11}' - \sigma_{22}'\right) \\ \frac{\Delta R_{45}}{R_{45}} - \frac{\Delta R_{-45}}{R_{-45}} &= 6.314\pi_D\sigma_{12}' \\ \frac{\Delta R_0}{R_0} + \frac{\Delta R_{90}}{R_{90}} &= \frac{\Delta R_{45}}{R_{45}} + \frac{\Delta R_{-45}}{R_{-45}} \\ &= \pi_S\left(\sigma_{11}' + \sigma_{22}'\right) + 2\pi_{13}\sigma_{33}' + 2\alpha_1 T \end{aligned} \tag{3.14}$$

The VDP sensor exhibits similarities to resistive rosettes but provides a 3.157x greater sensitivity to the stress difference $(\sigma_{11}' - \sigma_{22}')$ and shear stress σ_{12}'. The sum of resistance changes can be used to exact the two individual in-plane normal stress in case of free top surface and well controlled temperature. Note that the important enhanced VDP sensitivity factors (3.157) appear in the difference, but not the sum, expressions. To measure the

temperature compensated stresses, four measurements are required to extract the difference of the resistance change. However, it has been proven that diagonal mode operation can yield the same results with only two measurements by using z-parameter analysis [64].

$$\begin{aligned}
\frac{\Delta R_{Diag}^{0/90}}{R_S} &= \frac{\Delta R_0}{R_0} - \frac{\Delta R_{90}}{R_{90}} \\
&= 3.157\pi_D\left(\sigma'_{11} - \sigma'_{22}\right) \\
\frac{\Delta R_{Diag}^{45/-45}}{R_S} &= \frac{\Delta R_{45}}{R_{45}} - \frac{\Delta R_{-45}}{R_{-45}} \\
&= 6.314\pi_D\sigma'_{12}
\end{aligned} \tag{3.15}$$

For the diagonal measurement, current is applied across one diagonal and voltage measured across another. (i.e. For 0-degree VDP, current enters the sample through contact 3 and leaves the sample through 2 and the voltage between contact 1 and 4 are measured.) The VDP structure can be any arbitrary shape, as long as the sample is two dimensional and solid (no holes), so that 0° and 45° VDP can be replaced by an eight-terminal square or round VDP.

Just like the resistive rosettes, the evaluation of out-of-plane normal stress σ'_{33} requires dual-polarity VDP rosette as in Fig. 3.7 and the normalized resistance changes in each device can be obtained (Eq. 3.16).

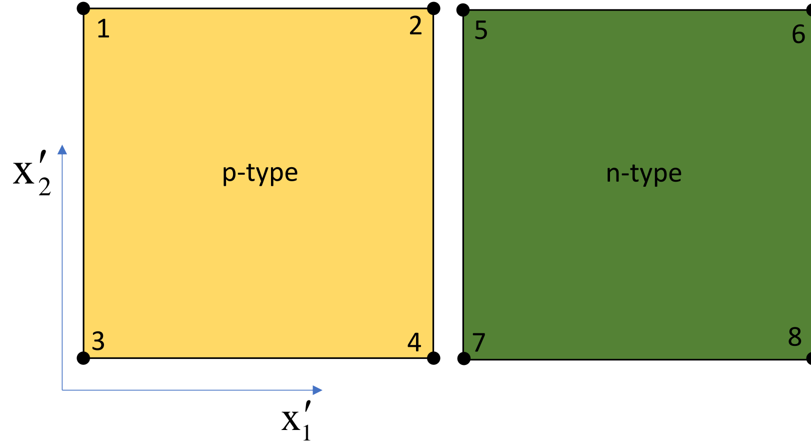

Figure 3.7: p and n VDP Device

$$\begin{aligned}
\frac{\Delta R_0^p}{R_0^p} &= \frac{1}{2}\pi_S^p\left(\sigma_{11}'+\sigma_{22}'\right)+\pi_{13}^p\sigma_{33}'+\frac{3.157}{2}\pi_D^p\left(\sigma_{11}'-\sigma_{22}'\right)+\alpha^p\Delta T \\
\frac{\Delta R_{90}^p}{R_{90}^p} &= \frac{1}{2}\pi_S^p\left(\sigma_{11}'+\sigma_{22}'\right)+\pi_{13}^p\sigma_{33}'-\frac{3.157}{2}\pi_D^p\left(\sigma_{11}'-\sigma_{22}'\right)+\alpha^p\Delta T \\
\frac{\Delta R_0^n}{R_0^n} &= \frac{1}{2}\pi_S^n\left(\sigma_{11}'+\sigma_{22}'\right)+\pi_{13}^n\sigma_{33}'+\frac{3.157}{2}\pi_D^n\left(\sigma_{11}'-\sigma_{22}'\right)+\alpha^n\Delta T \\
\frac{\Delta R_{90}^n}{R_{90}^n} &= \frac{1}{2}\pi_S^n\left(\sigma_{11}'+\sigma_{22}'\right)+\pi_{13}^n\sigma_{33}'-\frac{3.157}{2}\pi_D^n\left(\sigma_{11}'-\sigma_{22}'\right)+\alpha^n\Delta T
\end{aligned} \tag{3.16}$$

Combining the expressions in Eq. 3.16 yields Eq. 3.17,

$$\begin{gathered}
\sigma_{33}' = \frac{\pi_S^p\left[\frac{\Delta R_0}{R_0}+\frac{\Delta R_{90}}{R_{90}}-2\alpha^n\Delta T\right]-\pi_S^n\left[\frac{\Delta R_{45}}{R_{45}}+\frac{\Delta R_{-45}}{R_{-45}}-2\alpha^p\Delta T\right]}{2\left(\pi_S^p\pi_{13}^n-\pi_S^n\pi_{13}^p\right)} \\
\pi_S^p = \pi_{11}^p+\pi_{12}^p \\
\pi_S^n = \pi_{11}^n+\pi_{12}^n
\end{gathered} \tag{3.17}$$

It can be seen that resistive rosettes and VDP sensors have the same resistance-stress expressions when it comes to out-of-plane normal stress measurement.

3.2 Calibration Method

3.2.1 Introduction

To extract the stress state from the resistance changes measured with a sensor rosette, it is necessary to have accurate values of the piezoresistive coefficients. As discussed in previous sections, the values of π_{11}, π_{12} and π_{13} are required. These material constants relating the resistivity components to the stress components can be measured using controlled experiments where the resistance versus stress behavior is monitored. In this work, four-point bending and pressure vessel testing have been used to generate the uniaxial and triaxial calibration loadings. The in-plane piezoresistive coefficients π_{11} and π_{12} are measured using four-point bending method and the out-of-plane component π_{13} is extracted using hydrostatic pressure.

3.2.2 Four-point Bending Method

In general, there are two methods to apply uniaxial stress to the test sample: cantilever bending method and four-point bending method. For piezoresistive characterization, the cantilever method is not optimal when the actual size of the resistor is taken into account. For instance, the longitudinal resistor must extend over some finite length along the cantilever and the stress along the piezoresistor is not uniform as shown in Fig. 3.8.

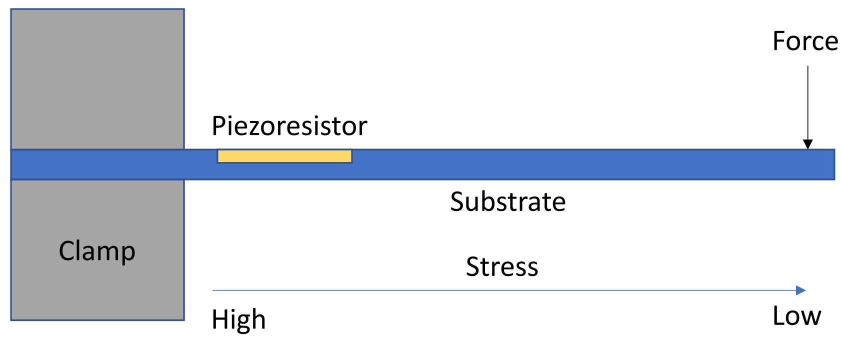

Figure 3.8: Cantilever Beam Setup

The four-point bending method, on the other hand, provides a constant bending moment or stress between two inner loading supports. In Fig. 3.9, a rectangular strip containing a row of chips is cut from a wafer and placed between the loading supports. By controlling the micrometer, the bottom supports move up and generate uniaxial stress. The reaction force F can be calculated from the output of the load-cell. The devices are probed through an opening in the top of the fixture, and the top surface of the strip represents a free surface (ignoring small probe forces). An HP-4146B semiconductor parameter analyzer connected to the probes is used to record the data.

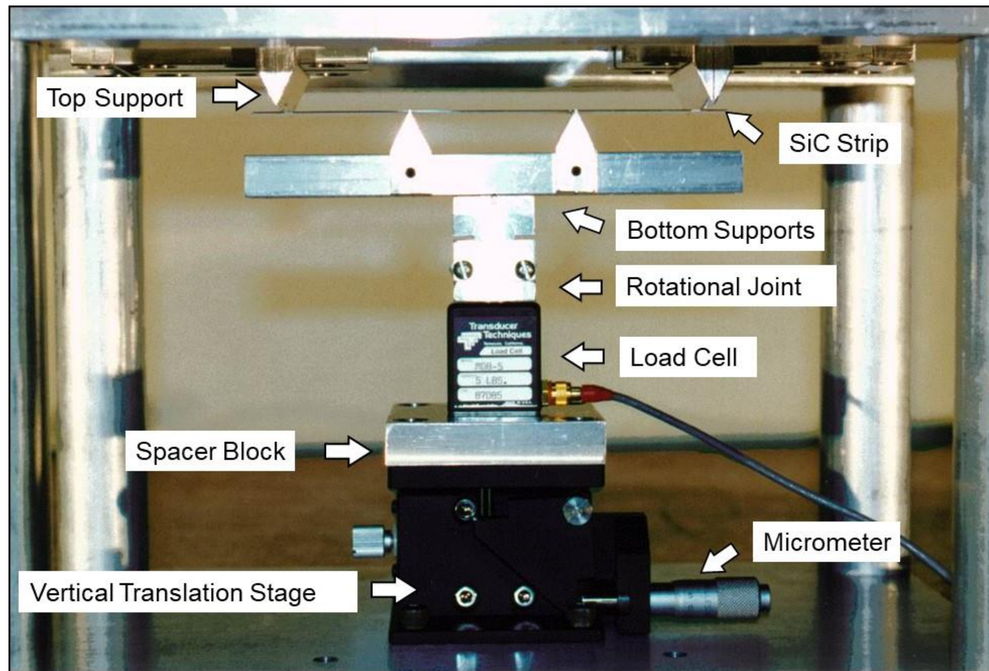

Figure 3.9: Actual Four-point Bending Fixture with an Example Test Strip in Place

The normal stress induced at points on the top surface of the strip that are between the bottom supports is given by

$$\sigma = \frac{3F(L-d)}{t^2 b} \tag{3.18}$$

Where F is the applied force, L is the distance between two top supports, L is the distance between two bottom supports, b and t are the width and thickness of the specimen, respectively.

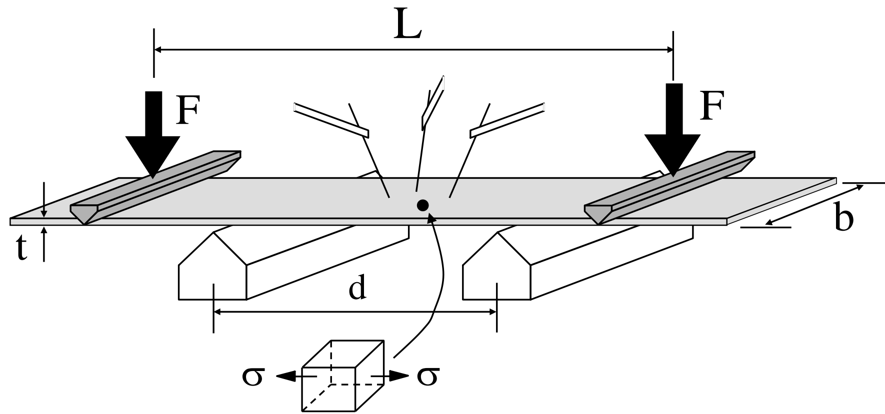

Figure 3.10: Schematic Sketch of Four-point Bending Method

The four-point bending setup mentioned above can make measurement at room temperature. For temperature dependent measurement, such four-point bending apparatus needs to be integrated into the environmental chamber. As shown in Fig. 3.11, by controlling the micrometer, force is applied to the bottom supports of the fixture through a low heat conductive ceramic rod penetrating the bottom side of the chamber. During experiments, the strip needs to be placed on the bottom supports inside the chamber and the traditional probing approach is not suitable in this case. Thus, a flex circuit approach shown in Fig. 3.12. is applied. The flexible circuit is attached to the center of the wafer strip with a thin and small piece of high-temperature double-sided tape to ensure good attachment under high-temperature and minimize stresses caused by CTE mismatch. Electrical connections between the strip and board utilize wire-bonding between bond pads on the strip and gold-plated copper trances on the flex. The tail of the flex circuit is inserted in a connector which is attached to an interface board connected to an interface box. HP

4146B semiconductor parameter analyzer connected to the interface box is used to record the data.

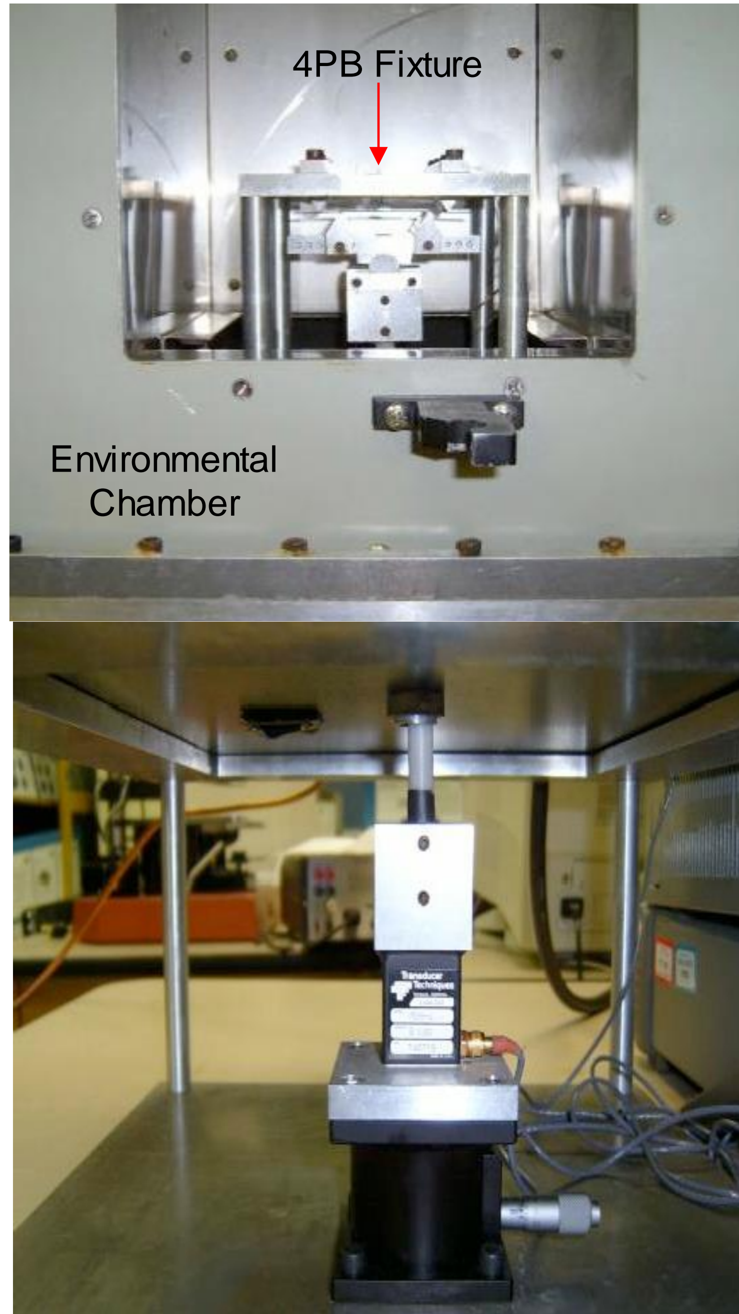

Figure 3.11: Four-point Bending System in an Environmental Chamber

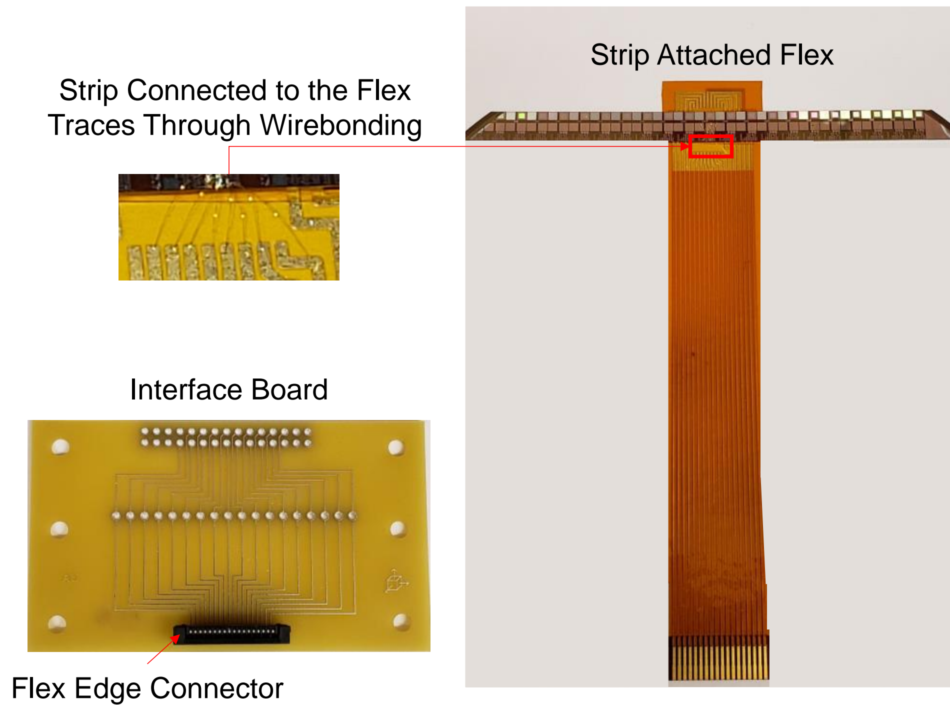

Figure 3.12: Flexible Circuit Approach

Compare to manual probing approach, the flex circuit approach can provide higher accuracy because it eliminates undesirable stresses induced by probes but it also requires wire-bonding for each device.

3.2.3 Hydrostatic Pressure Calibration

As mentioned earlier, the four-point bending method is able to calibrate two in-plane piezoresistive coefficients (π_{11} and π_{12}) by applying the in-plane normal stress. The hydrostatic pressure calibration method can evaluate the out-of-plane piezoresistive coefficient π_{13} by using triaxial normal stresses. In this work, the VDP device is used to evaluate the out-of-plane piezoresistive coefficients.

Fig. 3.13 shows the hydrostatic calibration system which includes following parts: pressure vessel, pumping unit, pressure transducer, electrical connector, and a thermistor. The high-capacity pressure vessel was used to subject a single die to triaxial compression, and the temperature and pressure changes were monitored during the test. The maximum operating pressure was designed to be 14 MPa (2000 psi). The limits were mainly determined by the pressure limit of the commercially available connector used to provide electrical access to the inside of the vessel.

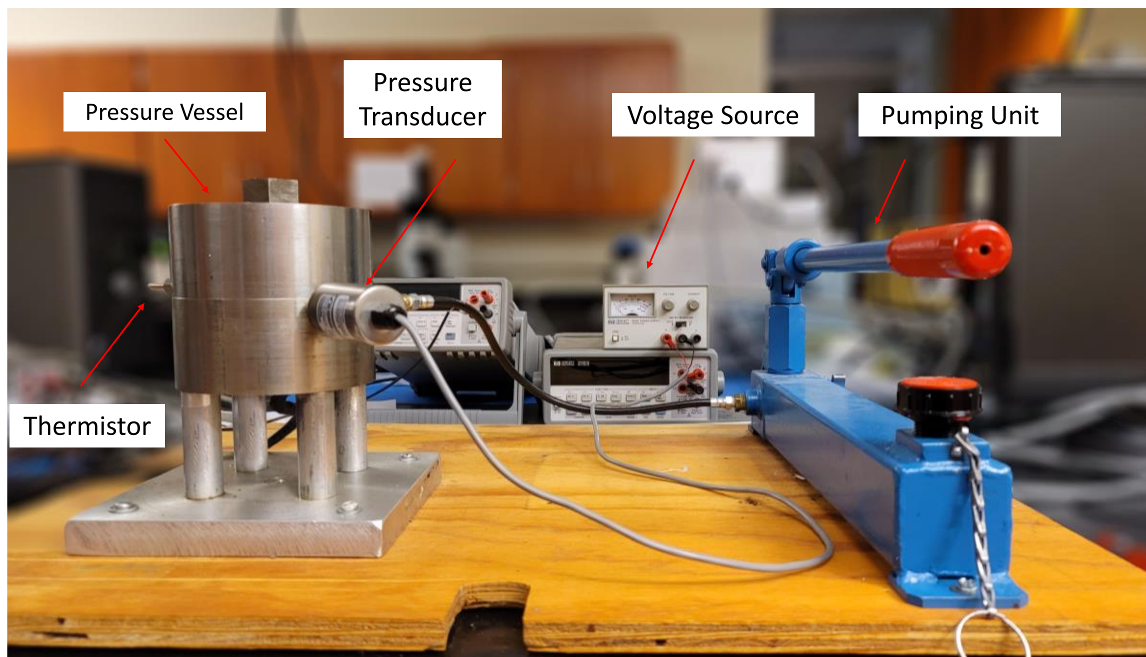

Figure 3.13: Hydrostatic Calibration System

The test sample (Chip on Board) was inserted into the connector inside the vessel. The test sample is shown in Fig. 3.14. The upper-left corner of the 4H-SiC test chip was attached to a specially designed printed circuit board using a small drop of die attachment adhesive (ME 525) in order to satisfy the isotropic compressive stress for the hydrostatic tests. The

square VDP sensor on the chip is wire-bonded to the pads on the PCB to get an electrical access. The PCB was connected to the HP-4156B semiconductor analyzer for resistance measurement. It has been observed experimentally in this study that the hydraulic fluid temperature changes due to a 14 MPa pressure change is around 0.7 °C. The pressure coefficients are small compared to the temperature coefficient of resistance. Thus, accurate determination of the TCR of the sensor elements must be done prior to pressure application and the temperature effects can be removed from the hydrostatic results.

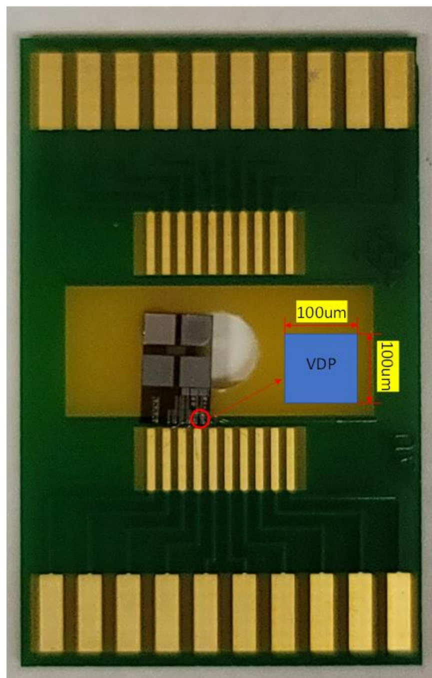

Figure 3.14: A Wire-bonded Chip on Board for TCR and Hydrostatic Test

3.3 Calibration Results

3.3.1 In-plane Piezoresistive Coefficients of Resistor

When there is only one uniaxial stress applied ($\sigma'_{11} = \sigma$), based upon Eq. 3.6, the resistance for R_1 and R_2 becomes

$$\begin{aligned} \frac{\Delta R_1}{R_1} &= \pi_{11}\sigma + \alpha\Delta T \\ \frac{\Delta R_2}{R_2} &= \pi_{12}\sigma + \alpha\Delta T \end{aligned} \tag{3.19}$$

If the temperature is well-controlled, the piezoresistive coefficients can be measured by using a resistor pair. In this work, two resistors along the longitudinal and transverse orientations (Fig. 3.15) are used to extract π_{11} and π_{12}, respectively. The probing approach was used to extract the coefficients in room temperature.

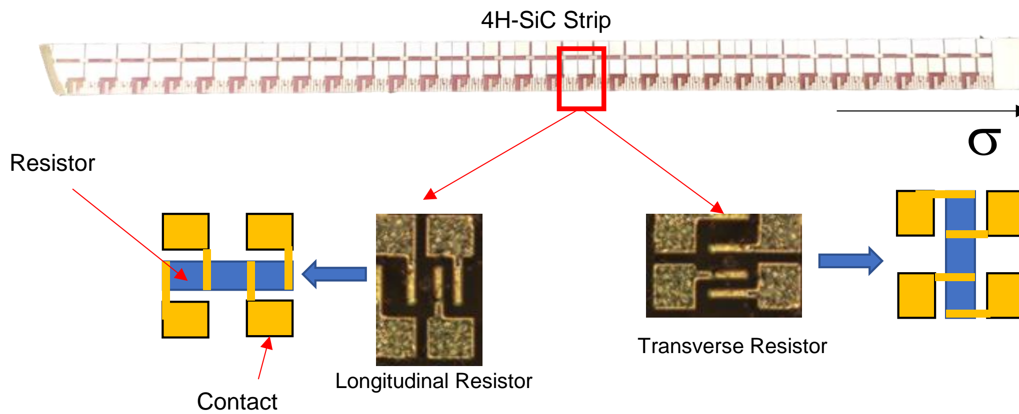

Figure 3.15: 4H-SiC Strip with Resistors

Examples of the stress-induced changes in a n^+- and p^+-type resistor along the transverse direction appear in Fig. 3.16 and Fig. 3.17, corresponding to changes in electron mobility in the material.

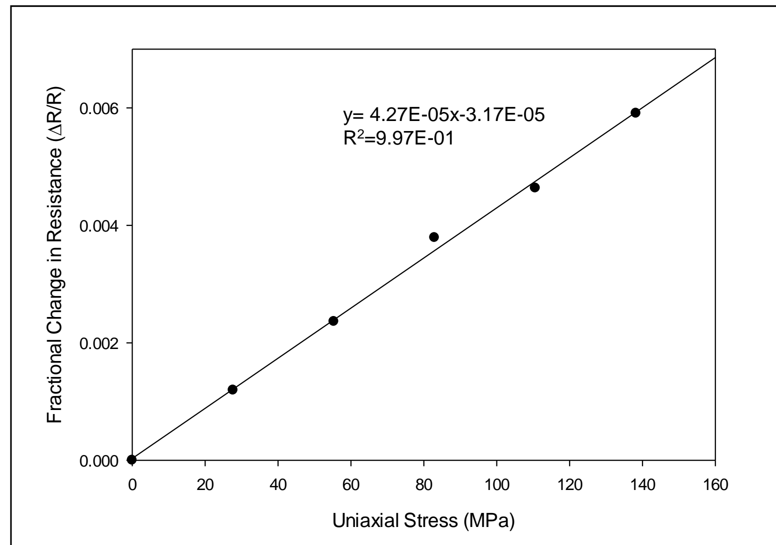

Figure 3.16: Normalized Resistance Change vs. Transverse Stress for a n^+ Resistor

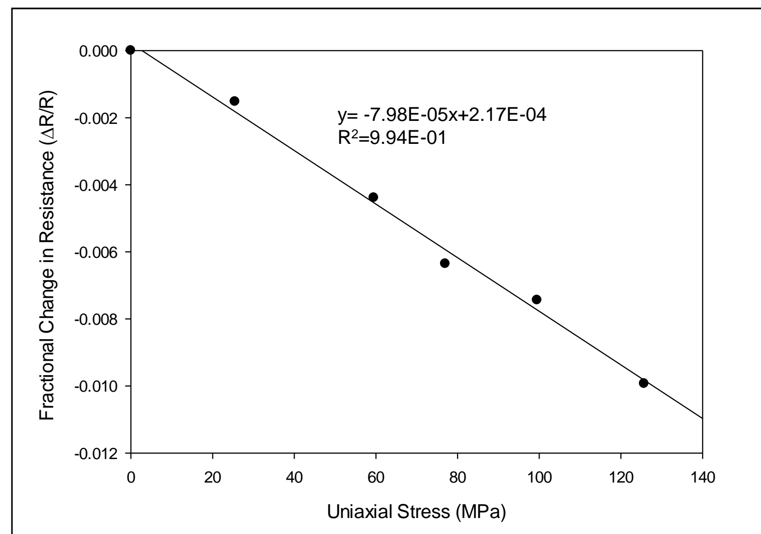

Figure 3.17: Normalized Resistance Change vs. Transverse Stress for a p^+ Resistor

Specimen#	π_{11}^{p+} (/TPa)	π_{12}^{p+} (/TPa)	π_{11}^{n+} (/TPa)	π_{12}^{n+} (/TPa)
1	99	-80	-49	42
2	84	-86	-30	40
3	70	-87	-35	41
4	68	-70	-58	50
5	85	-53	-42	52
Average	81	-75	-43	45
Std. Dev.	12.7	14.3	10.9	5.5

Table 3.1: Measured Values of Piezoresistive Coefficients at Room Temperature

The mean and standard deviation of the extracted coefficients for 5 sets of measurements on two types of resistors appear in Table 3.1. Gauge factors measured by Nguyen et al. [60] for p type material, together with SiC stiffness coefficients, give π_{11}= 66/TPa and $\pi_{12} = -57$/TPa. The mismatch of results could be caused by different measurement temperature, doping level, and loading method, etc. In their work, uniaxial stress was applied to an epitaxial piezoresistor by utilizing cantilever bending method. However, in this work, diffused resistor and four-point bending method are used. The simulation results of Nakamuara et al. [57] predict that, for n type material, the longitudinal and transverse piezoresistive coefficients have similar magnitude and opposite sign, which matches well with our results.

3.3.2 In-plane Piezoresistive Coefficients of VDP device

According to Eq. 3.14, it can be seen that only one combined piezoresistive coefficient π_D is required for temperature compensated stress measurements. In this work, the values of

piezoresistive coefficients under different temperatures were determined and data were collected every 30 ℃ from 23 – 180 ℃. Since samples need to be placed into an environmental chamber, the flex circuit approach was utilized. As mentioned earlier, the VDP device connects to the flex traces through wire-bonding. To check the bonding quality, sheet resistance is measured and compared with standard values on a specification sheet. Four-wire VDP measurements help eliminate the inherent resistance of the wires connecting the measurement instrument to the VDP device being measured. Input and output currents are monitored to ensure the leakage current is not significant.

Three measurements are utilized. Zero-degree, ninety-degree and diagonal measurements yield the value of R_0 , R_{90} and $R_{Diag}^{0/90}$. During calibration, only $\sigma_{11} = \sigma$ is applied and other stress components are zero, so the equations for VDP become:

$$\begin{aligned} \frac{\Delta R_0}{R_0} - \frac{\Delta R_{90}}{R_{90}} &= \frac{\Delta R_{Diag}^{0/90}}{R_S} = 3.157\pi_D\sigma \\ \frac{\Delta R_0}{R_0} + \frac{\Delta R_{90}}{R_{90}} &= \pi_S\sigma + 2\alpha\Delta T \end{aligned} \tag{3.20}$$

Piezoresistive coefficients π_D and π_S can be calculated from the difference and sum of the R_0 and R_{90} without changing the directions of applied stress. A diagonal measurement is used to validate the results of the extracted value of π_D. The VDP device and test strip appear in Fig. 3.18.

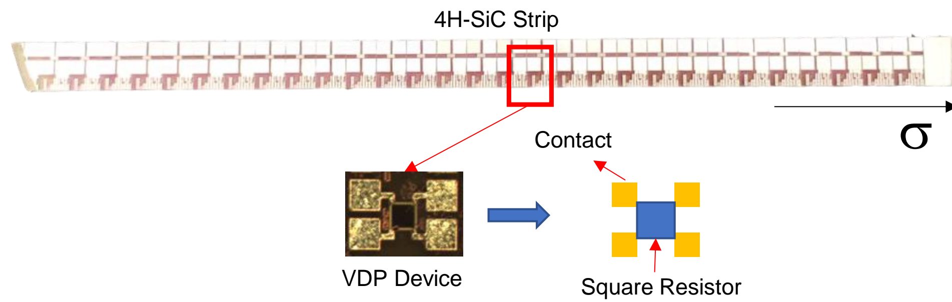

Figure 3.18: 4H-SiC Strip with VDP Device

Fig. 3.19 and Fig. 3.20 show examples of the stress-induced resistance change in a n^+- type VDP stress sensor at 60 °C. A typical set of results for the variations of R_0 and R_{90} under uniaxial stress appear in Fig. 3.19 as well as the sum and difference of the two measurements. The slope of normalized resistance change of R_0 and R_{90} are defined as π_0 and π_{90}, respectively. In this case, the measurement results for R_0 yields $\pi_0 = -121$ /TPa and R_{90} yields $\pi_{90} = 114$ /TPa . Fig. 3.20 depicts the results from the diagonal measurements and the slope is defined as π_{Diag} which is -229 /TPa and very close to the difference measurements (-235/ TPa) in Fig. 3.19. The good linearity is achieved thanks to the high accuracy of flex circuit approach.

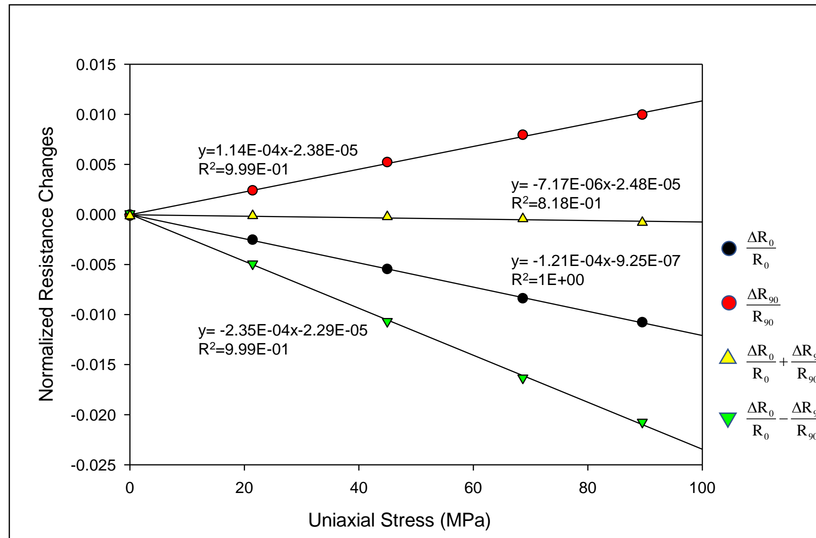

Figure 3.19: Normalized Resistance Changes vs. Stress at 60 ℃

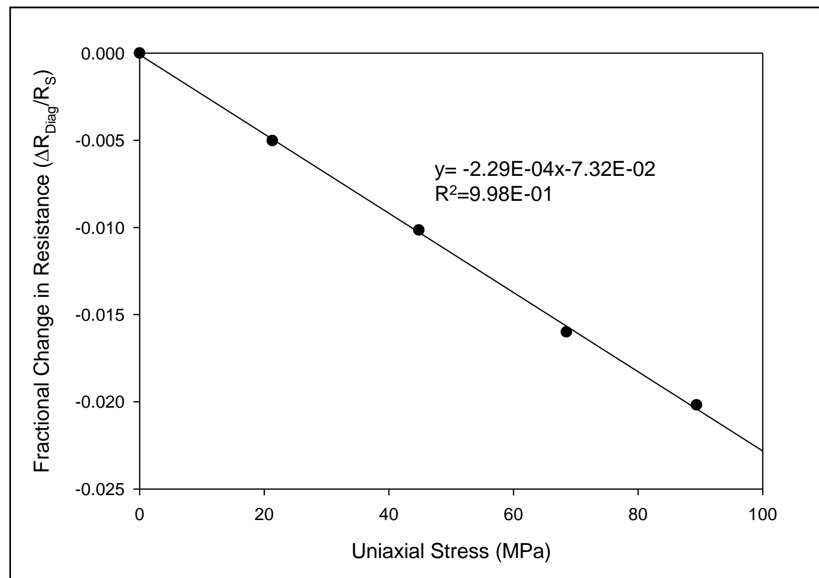

Figure 3.20: Diagonal Measurement Results at 60 ℃

Tables 3.2 and 3.3 present mean and standard deviations of extracted coefficients for 5 sets of measurements on two types of VDP devices. The results show that the sheet

resistance and magnitudes of the coefficient π_D decrease monotonically with increasing temperature for both p- and n-type devices, which agree well with other reports [57][61]. Relative to π_D, π_S values are small but found in non-temperature compensated mode, so that the standard deviations are relatively large. Theoretically, the diagonal measurement is equivalent to difference measurement and yields the same results. To validate the difference measurement, π_{Diag} are reported and compared with $\pi_0 - \pi_{90}$. The results for coefficient π_D at different temperature are presented in Fig. 3.21 and Fig. 3.22. Evidently, the temperature compensated piezoresistive coefficient π_D exhibited good linearity at temperature ranging from 23 to 180 ℃.

Piezoresistive Values for p^+-type VDP -- Averages and Standard Deviations [1/TPa]							
Temperature(℃)	Sheet Resistance R_S [kΩ]	$\pi_0 - \pi_{90}$	π_{Diag}	π_D	π_S	π_{11}	π_{12}
23	20.8	510.6(2.4)	512.4(1.8)	161.7(0.8)	19.4(4.9)	90.5(2.8)	-71.2(2.1)
60	14.3	484.1(10.0)	484.1(6.3)	153.3(3.2)	11.2(11.9)	82.2(6.9)	-71.1(5.4)
90	10.9	460.3(9.7)	459(3.5)	145.8(3.1)	9.1(8.4)	77.5(4.8)	-68.3(4.1)
120	8.7	437.4(12.3)	434.7(4)	138.5(3.9)	19(6.5)	78.8(3.6)	-59.8(4)
150	7.1	414.8(5.3)	409.9(4.8)	131.4(1.7)	13.5(5.9)	72.4(2.4)	-58.9(3.7)
180	6	377.4(18.4)	377.5(17)	119.5(5.8)	-1(3.8)	59.3(1.2)	-60.3(4.8)

Table 3.2: Measured Values of Piezoresistive Coefficients for p^+- type VDP

Piezoresistive Values for n^+-type VDP -- Averages and Standard Deviations [1/TPa]							
Temperature(°C)	Sheet Resistance R_S [Ω]	$\pi_0 - \pi_{90}$	π_{Diag}	π_D	π_S	π_{11}	π_{12}
23	1177	-239.8(4.1)	-238.2(7.5)	-75.9(1.3)	-8.8(9.6)	-42.4(4.3)	33.5(5.3)
60	1093	-231.1(5.1)	-227.5(5.5)	-73.2(1.6)	5.9(22.6)	-33.6(12.1)	39.5(10.5)
90	1033	-224.6(9.4)	-218.8(10.6)	-71.2(2.9)	-0.6(9.4)	-35.9(5.4)	35.3(4.4)
120	990	-215.8(4.7)	-213.7(4.2)	-68.4(1.5)	15.6(15.2)	-26.4(7.9)	41.9(7.4)
150	959	-203.8(7.5)	-202.3(5.9)	-64.6(2.4)	-3.4(33.9)	-34.0(17.9)	30.6(16.0)
180	948	-194.6(2.6)	-196.3(3.2)	-61.6(0.8)	22.2(14.2)	-19.7(6.8)	41.9(7.5)

Table 3.3: Measured Values of Piezoresistive Coefficients for n^+- type VDP

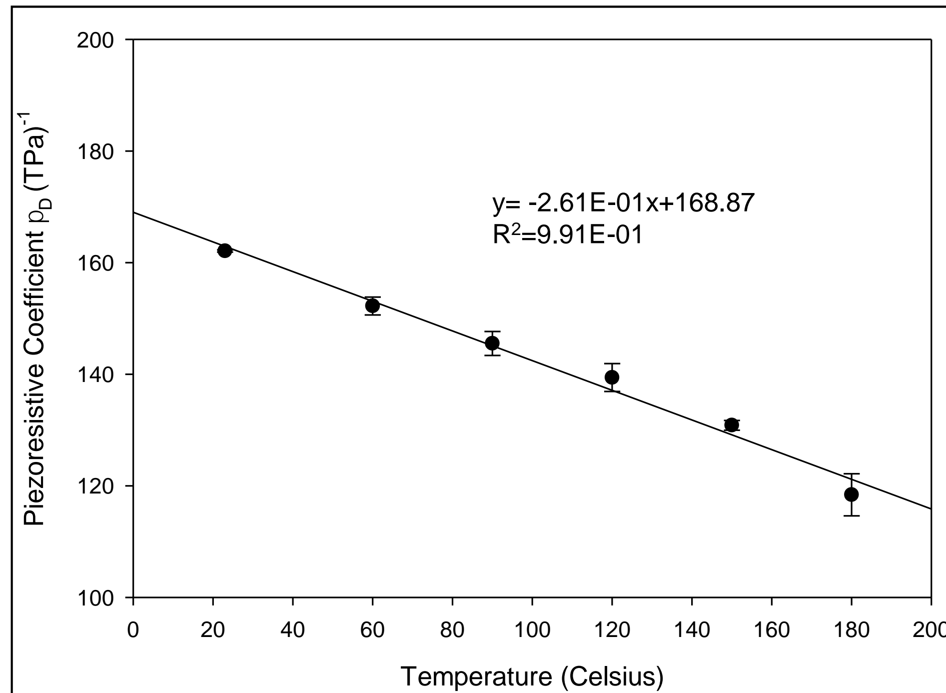

Figure 3.21: Coefficient π_D for p^+-type VDP vs. Temperature

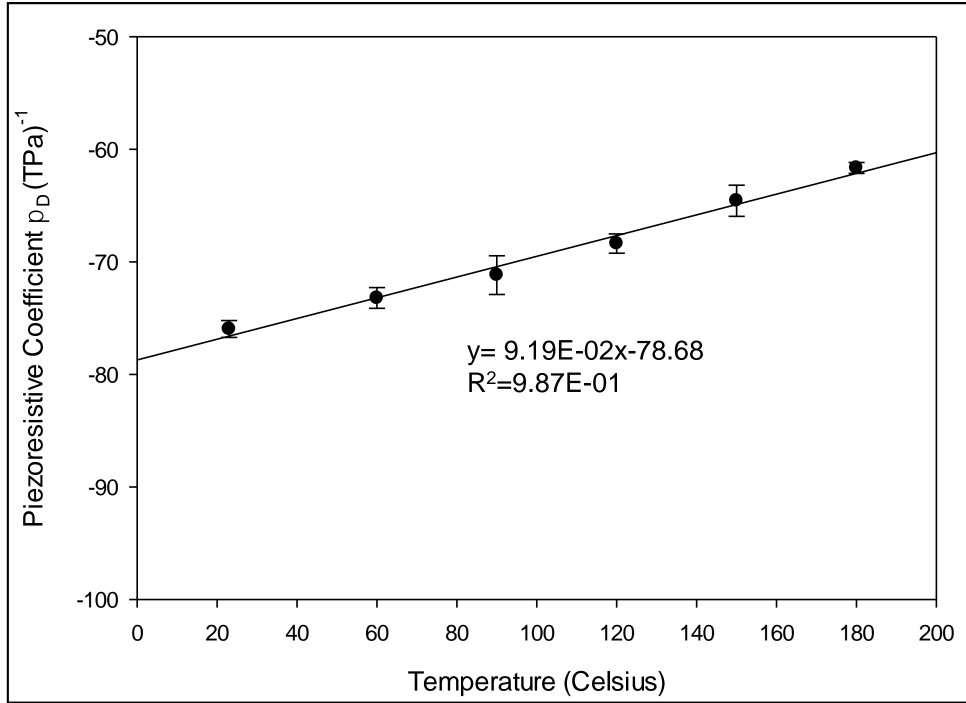

Figure 3.22: Coefficient π_D for n^+-type VDP vs. Temperature

3.3.3 Out-of-plane Piezoresistive Coefficients of VDP device

As shown in Eq. 3.17, the out-of-plane stress measurements require an additional piezoresistive coefficients π_{13}, which can be determined by the hydrostatic pressure method. If a VDP sensor is subjected to hydrostatic pressure ($\sigma'_{11} = \sigma'_{22} = \sigma'_{33} = -p$), the relations in Eq. 3.17 yields the change in resistivity:

$$\begin{aligned}\frac{\Delta R_{0/90}}{R_{0/90}} &= -(\pi_S + \pi_{13})p + \sum \alpha_{(N)} T^N \\ &= \pi_p p + \sum \alpha_{(N)} T^N\end{aligned} \tag{3.21}$$

$$\pi_p = -(\pi_{11} + \pi_{12} + \pi_{13}) \tag{3.22}$$

where the combined piezoresistive coefficient $-(\pi_S + \pi_{13})$ is defined as the piezoresistive "pressure coefficient" π_P. Once π_P is obtained through the hydrostatic test, π_{13} can be calculated by combining the results from four-point bending test. As discussed earlier, the TCR of the sensor elements must be determined prior to pressure application. The resistance R(σ,T) of the VDP is a function of applied stress σ and temperature T. If no stress is applied and the reference temperature is 25 ℃, the normalized resistance change becomes:

$$\begin{aligned} \frac{\Delta R_{0/90}}{R_{0/90}} &= \frac{R(0,T) - R(0,25)}{R(0,25)} \\ &= \sum \alpha_{(N)} \Delta T^N \\ &= \alpha_1 \Delta T + \alpha_2 \Delta T^2 + \alpha_3 \Delta T^3 + \ldots \end{aligned} \tag{3.23}$$

The TCR(α) can be extracted by measuring the resistance change versus temperature change of a sensor in a temperature chamber. During the TCR measurements, the oven temperature was varied from 10 ℃ to 100 ℃ with a step size 5 ℃. Fig. 3.23 and 3.24 show typical plot of the resistance change versus temperature change for unstressed p^+ and n^+ VDP. Since the shape of the curve is slightly parabolic, the resistance change cannot be modeled by a linear term but first and second order terms are required. Table 3.4 represents the TCR results for both p^+ and n^+ type resistors.

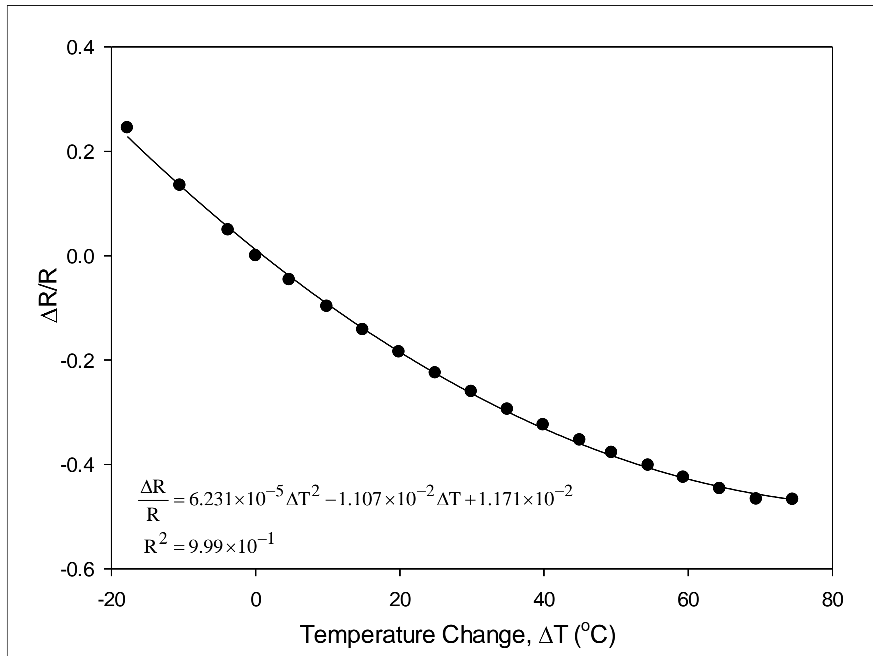

Figure 3.23: Normalized Resistance Change of p+-type VDP vs. Temperature

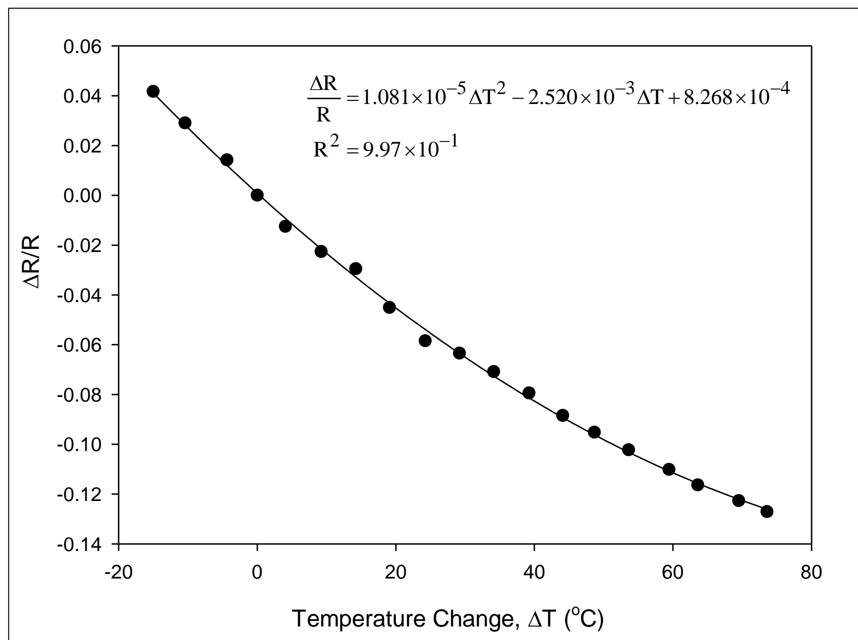

Figure 3.24: Normalized Resistance Change of n+-type VDP vs. Temperature

		α_1 (1/℃)	α_2 $(1/℃)^2$
p^+-type	Average	-1.11E-02	6.32E-5
	Std. Dev	0.04E-02	0.64E-5
n^+-type	Average	-2.54E-03	9.62E-6
	Std. Dev	0.03E-03	1.68E-6

Table 3.4: Measured Values of Piezoresistive Coefficients for n^+ VDP

As shown in Fig. 3.23 and Fig. 3.24, the resistance decreases with increasing temperature for heavily doped p- and n-type 4H-SiC in this temperature range. Elevating the temperature decreases mobility because of enhanced phonon scattering. However, it is compensated by increase of carrier concentration, leading to a decrease of resistivity [65]. For p^+ 4H-SiC, the resistance reduced more than 40% from 25 ℃ to 100 ℃, which agrees with the results in the literature [66].

Before the hydrostatic tests, the TCR for each sample is carefully measured as there is always sample to sample variation. Once TCR measurements are finished, the chips are subjected to hydrostatic pressure using the hydrostatic pressure test setup. The resistance and the fluid temperature are recorded at every load step. During the hydrostatic test, the temperature rises with increasing pressure, so that the measured resistance change is caused by both pressure and temperature change. To determine the pressure coefficient, the effect of temperature must be removed by subtracting the temperature induced resistance change from the total change. In Fig.3.25, the upper curve shows the total resistance change due to pressure and temperature. Since the temperature was recorded at each load step, the

temperature induced resistance change can be plotted (lower curve). The subtraction of two curves is presented in Fig. 3.26, which is the normalized resistance change due to pressure, and the slope of the linear fitted line corresponds to the piezoresistive coefficient π_p. By using the in-plane piezoresistive coefficients (π_S) from the four-point bending test and Eq. 3.22, the π_{13} at the room temperature can be calculated. Table 3.5 shows the values of three fundamental piezoresistive coefficients of p-type resistor obtained by combining four-point bending and hydrostatic test.

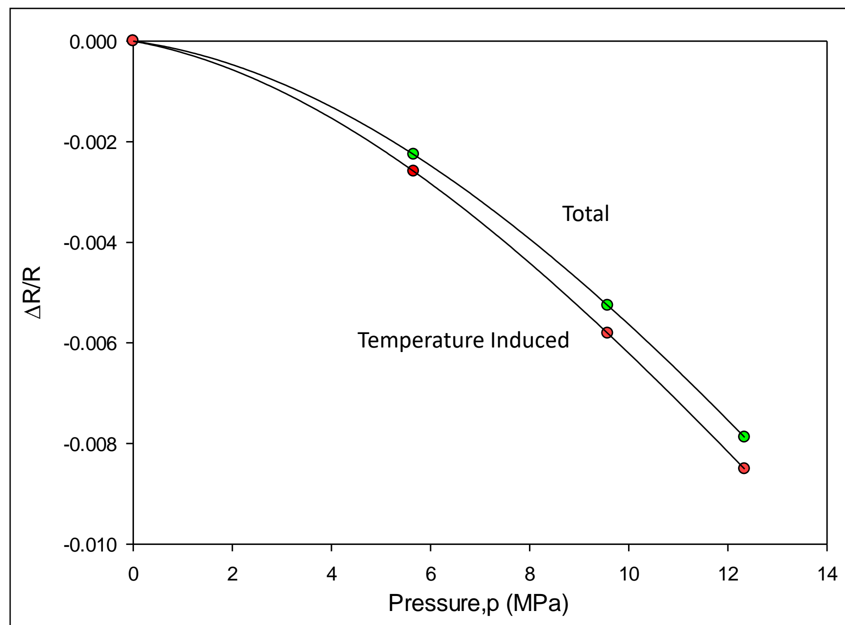

Figure 3.25: An Example of Total and Temperature Induced ΔR/R for p-type VDP

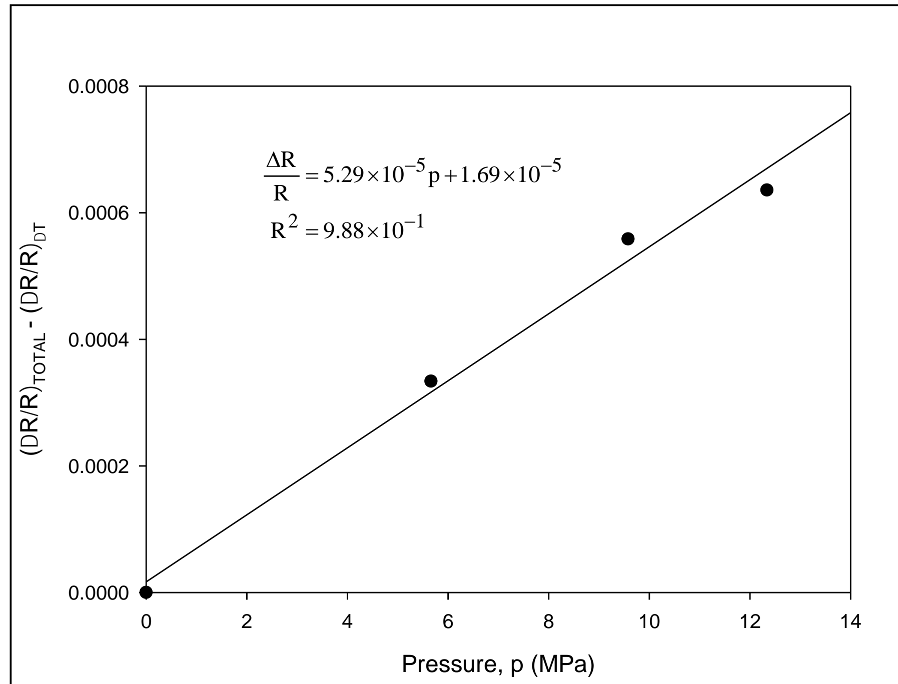

Figure 3.26: An Example of Pressure Induced ΔR/R vs. Pressure For p^+-type VDP

	π_{11}	π_{12}	π_P	π_{13}
Average (1/TPa)	90.5	-71.2	60.9	-80.3
Std.Dev	2.8	2.1	14.7	

Table 3.5: Fundamental Piezoresistive Coefficients of p- type 4H-SiC

It has been found that the resistance for the n^+ VDP is quite small which makes the pressure induced resistance change difficult to measure. Therefore, the more lightly doped n-type resistor is required for out-of-plane stress sensor. The results for n^+ VDP are not reported because of large variation.

3.4 Summary

Silicon carbide offers the advantage of much higher temperature sensor operation than silicon with potential use in a wide range of applications. The present work has established general expressions for the stress dependence of resistors and van der Pauw devices on standard 4H-SiC wafers.

The resistive stress sensors fabricated on the (0001) plane of 4H-SiC, exhibit similarities to those on silicon, and can respond to only four of the six components of the stress state. The difference between two in-plane normal stresses ($\sigma'_{11} - \sigma'_{22}$) and shear stress ($\sigma'_{12}$) can be measured in temperature compensated mode and only one piezoresistive coefficient π_D is required for such measurement. If the temperature is well controlled and the top surface is stress-free, the individual values of σ'_{11} and σ'_{22} can be obtained. Four-terminal VDP devices can provide more than three times sensitivity than that of multi-element resistor rosettes. The experimental results confirmed the theory: the diagonal measurement is equivalent to the differential measurement for VDP devices.

To measure the out-of-plane normal stress component σ'_{33}, dual-polarity (both n-type and p-type) rosettes are needed but the extraction is not temperature compensated. Also, such measurement devices require knowledge of an additional piezoresistive coefficient π_{13}.

The isotropic piezoresistance in the (0001) plane of 4H-SiC was found by the coordinate transformation. The in-plane piezoresistive coefficients (π_{11} and π_{12}, or also referred to as π_L and π_T) of both p- and n-type resistors are calibrated by using the four-

point bending method at the room temperature. The measured piezoresistive coefficients are relatively small (< 100 /TPa) comparing to silicon.

The VDP devices are utilized to find the in-plane piezoresistive coefficients at various temperatures and out-of-plane piezoresistive coefficient at room temperature. The results show that piezoresistivity decreases as the temperature rises. The coefficient π_D is measured with good linearity and stability at different temperatures from 23 to 180 °C. The out-of-plane piezoresistive coefficient π_{13} can be evaluated by combining the four-point bending and hydrostatic test, and TCR measurements must be performed before hydrostatic test since the temperature changes with the applied stress. The hydrostatic pressure piezoresistive coefficient π_p was found to be 60.9/TPa for p^+ VDP. The piezoresistive coefficient π_{13} were further calculated with a known π_S ,which is evaluated with four-point bending method. The extracted π_{13} is -80.3 /TPa, which is around 15% higher than π_{12}. Due to the relatively low reference resistance for n+ VDP, the pressure induced resistance change is not observable. Therefore, the more lightly doped n-type resistor is required for out-of-plane stress sensor.

Chapter 4

MECHANICAL STRESS EFFECTS ON NMOS FETs

4.1 Introduction

Metal-oxide-semiconductor field-effect transistors (MOS FETs) are excellent stress sensors because of their advantages of smaller size, high sensitivity due to lighter doping, and operable in wide temperature range over the traditional resistor sensors [67]. The piezoresistive behavior of MOS transistors on silicon has been studied by numerous researchers [68]-[77], whereas few have investigated the stress effect on 4H-SiC MOS transistors. Stress sensors on silicon carbide offer the potential for much higher temperature operation than with silicon. Moreover, fabrication-induced stress has been utilized in silicon to enhance the mobility of CMOS devices [78],[79] and might have potential application to silicon carbide devices.

Previous characterization of stress response of CMOS devices on silicon have assumed that the transistors are operating in strong inversion where the normalized current change ($\Delta I_D/I_D$) is dominated by mobility variations. Recently, Jaeger et al. has presented large changes in $\Delta I_D/I_D$ as transistor approaches moderate inversion and below and concluded that the change of threshold voltage due to stress must be considered in the subthreshold case [45].

In this work, stress dependent properties and modeling of lateral enhancement-mode NMOS FETs on 4H-SiC are described for a wide range of bias conditions. In addition to the expected mobility components, the piezoresistive response of the FETs is shown to

have a strong threshold voltage component. The design of a four-element NMOS stress sensor rosette is also discussed.

4.2 Review of MOSFET Characteristics

Fig. 4.1 depicts a schematic of a n-channel enhancement-type MOSFET where S is the source, D is the drain, G is the gate, and B is the substrate of the transistor. A gate terminal is separated by a thin insulator (Gate Oxide) from the substrate, and the potential on the gate terminal controls the surface potential (ψ_S) of the substrate and the conducting status of the device channel. For this NMOS FET, the source is the relative low potential terminal where carriers, or electrons, come from, and the carriers then go to the other terminal (drain) which has higher potential. When the potential applied to the gate is lower than the threshold voltage (V_{TN}), the MOSFET is commonly assumed to be "turned off". However, this is not the case in reality. In Fig. 4.1, it can be seen that, near the surface of the NMOS transistor structure, the n^+ source, p substrate and n+ drain form an npn bipolar transistor. Below threshold, electrons still enter the p-region from the source and then diffuse to the drain, just as in a BJT.

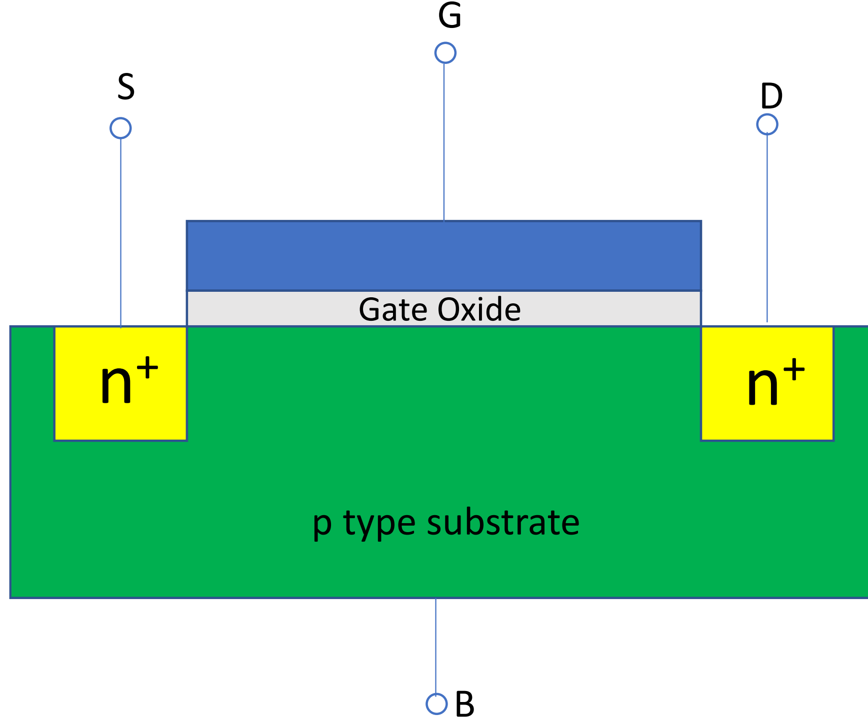

Figure 4.1: MOS FET Structure

Assuming source and substrate are grounded, Eq. 4.1 depicts the relationship between the electron concentration at the surface and the surface potential [80].

$$n_{surface} \approx N_A e^{(\psi_s - 2\phi_F)/V_T}$$
$$\phi_F = \frac{E_i - E_F}{q} \qquad V_T = \frac{kT}{q} \tag{4.1}$$

Here $n_{surface}$ is the electron concentration at the surface (under the insulator), N_A is the acceptor concentration of the p type substrate, ψ_S is the surface potential, ϕ_F is the fermi potential of the substrate, and V_T is the thermal voltage. Eq. 4.1 is plotted in Fig. 4.2 where we can observe that the inversion layer forms at $\psi_S = \phi_F$, so the $n_{surface}$ becomes equal to

the intrinsic concentration. With the increment of ψ_s above ϕ_F, $n_{surface}$ increases significantly. At $\psi_s = 2\phi_F$, the electron concentration near the surface equals the doping concentration in p substrate.

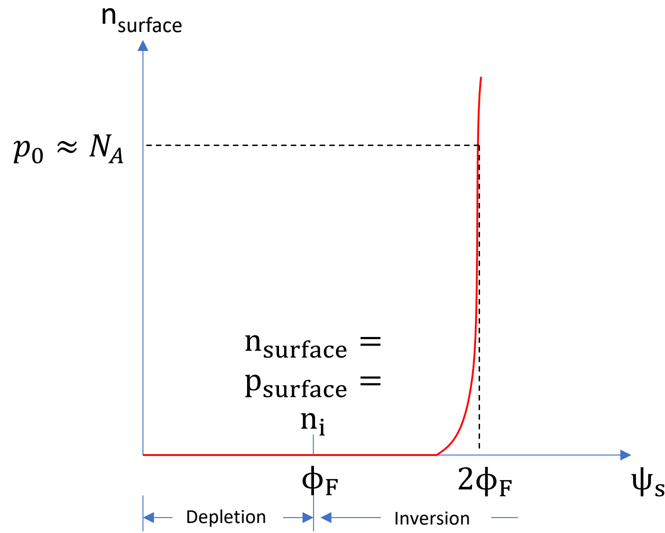

Figure 4.2: Electron Concentration at the Surface vs. Surface Potential. Axes are Linear.

The working region of the device can be defined in terms of surface potential ψ_s:

$$\begin{aligned} &\text{Depletion :} && \psi_s < \phi_F \\ &\text{Weak inversion:} && \phi_F < \psi_s < 2\phi_F \\ &\text{Moderate inversion:} && 2\phi_F < \psi_s < 2\phi_F + 6V_T \\ &\text{Strong inversion:} && 2\phi_F + 6V_T < \psi_s \end{aligned} \tag{4.2}$$

The gate-source voltage can be expressed as a function of surface potential:

$$V_{GS} = V_{FB} + \psi_s + \gamma\sqrt{\psi_s + V_T e^{(\psi_s - 2\phi_F)/V_T}} \tag{4.3}$$

where V_{FB} is the flat band voltage, γ is the body effect coefficient. Since V_{FB}, γ, ϕ_F, and ϕ_t do not change with applied voltage, the surface potential increases with gate-source

voltage. The gate voltage V_{GS} for each working region can be readily obtained by substituting the surface potentials in Eq. 4.2 to Eq. 4.3.

The drain current versus gate-source voltage is plotted in Fig. 4.3 and the "region of constant slope" can be modeled according to bipolar transistor:

$$I_D = I_{D0}\, e^{\left(\frac{V_{GS}-V_{TN}}{nV_T}\right)} \qquad I_{D0} = 2nV_T^2 Kn \tag{4.4}$$

where V_T is the thermal voltage ($kT/q \approx 26mV$ at room temperature), and Kn is the transconductance parameter. The value of n depends on the relative magnitude of fixed oxide capacitance and the voltage dependent depletion-layer capacitance, and its value typically ranges between 1 and 2.

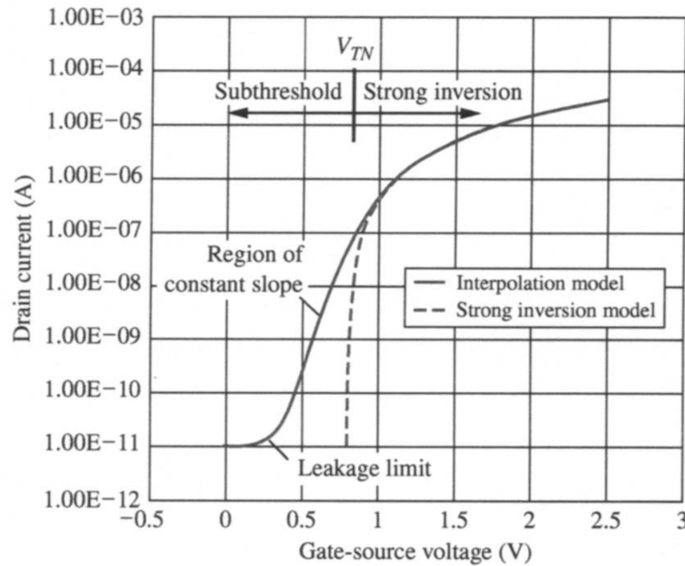

Figure 4.3: Subthreshold Conduction in an NMOS Transistor with V_{TN} = 0.8V. Reprinted from [81].

At very low gate-source voltages, the drain current is very small due to drain-bulk diode leakage. And as the V_{GS} increases, the device gets to weak and moderate inversion region, and the drain current increases exponentially for values of V_{GS} less than V_{TN}. Once the strong inversion is achieved, the MOSFET is "turned on" ($V_{GS}>V_{TN}$).

For an FET operating in the strong inversion, two distinct regions of operation can be identified on its output characteristics, namely, the linear and the saturation regions. The behavior in the linear and the saturation regions are described by the follow relationships:

Linear region (when $V_{GS}> V_{TN}$, and $V_{DS}< V_{GS}-V_{TN}$):

$$\begin{aligned} I_D &= \mu_n \frac{C''_{ox} W}{L}\left[V_{GS} - V_{TN} - \frac{V_{DS}}{2}\right] V_{DS} \\ &= K'_n \frac{W}{L}\left[V_{GS} - V_{TN} - \frac{V_{DS}}{2}\right] V_{DS} \\ &= K_n \left[V_{GS} - V_{TN} - \frac{V_{DS}}{2}\right] V_{DS} \\ K'_n &= \mu_n C''_{ox} \qquad K_n = \mu_n \frac{C''_{ox} W}{L} \end{aligned} \tag{4.5}$$

Saturation region (when $V_{GS}> V_{TN}$, and $V_{DS}\geq V_{GS}-V_{TN}$):

$$I_D = \mu_n \frac{C''_{ox} W}{2L}\left(V_{GS} - V_{TN}\right)^2 \left(1 + \lambda_n V_{DS}\right) \tag{4.6}$$

where μ_n is the mobility of the carriers in the channel, C''_{ox} is the capacitance per unit area of the gate oxide, W and L are the width and length of the channel respectively. k'_n and k_n are called transconductance parameters. λ_n is the channel-length modulation parameter. An example of two regions is plotted below.

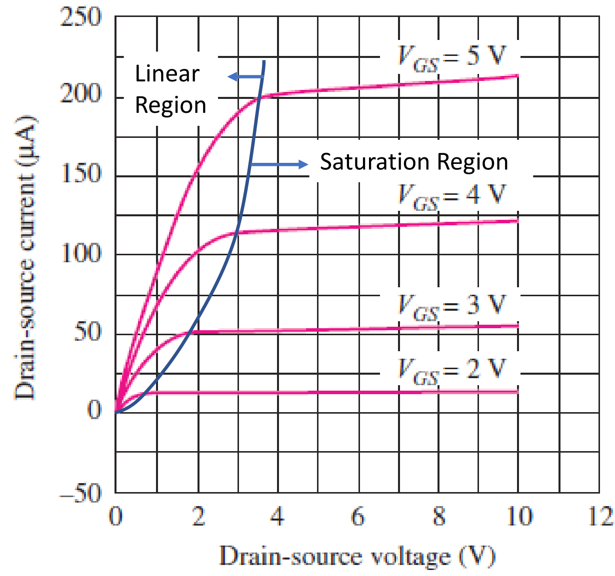

Figure 4.4: Typical Set of Output Characteristics for an n-channel Enhancement Type FET.

4.3 Piezoresistive Theory of FETs

The piezoresistive theory of MOSFET was developed by Mikoshiba [82]. The relationship governing the behavior of FETs in the linear region is

$$
\begin{aligned}
I_D &\approx \mu \frac{W}{L} Q_C V_{DS} \\
Q_C &= C_{ox}\left(V_{GS} - V_{TN} - \frac{V_{DS}}{2}\right)
\end{aligned}
\tag{4.7}
$$

Where Q_C is the carrier charge density in the channel region. When a uniaxial stress is applied, the relative drain current change due to the stress can be expressed

$$
\frac{\Delta I_D}{I_D} = \frac{\Delta W}{W} - \frac{\Delta L}{L} + \frac{\Delta \mu}{\mu} + \frac{\Delta Q_C}{Q_C} \tag{4.8}
$$

Where the unstressed value of the respective quantities appears in the denominator. As mentioned in previous chapter, for semiconductor materials, the piezoresistive coefficients that characterize the stress induced changes in carrier mobility are typically an order or two larger in magnitude than the coefficients that quantify the stress induced by dimensional changes. Thus, the dimensional changes are neglected in Eq. 4.8 and yielding

$$\frac{\Delta I_D}{I_D} = \frac{\Delta \mu}{\mu} + \frac{\Delta Q_C}{Q_C} \tag{4.9}$$

For silicon, the second term $\Delta Q_C/Q_{C0}$ changes with surface potential and becomes small and negligible for strong inversion. For weak and moderate inversion, it can't be neglected because its value is similar to the mobility term [41].

Similar results can be obtained by using the drain current equations (Eq. 4.5), and Eq. 4.10 shows the normalized drain current change due to mechanical stress. The applied stresses not only change the mobility but also alter semiconductor band gap, due to the different shift of conduction and valence band by stress, which leads to a shift of the intrinsic Fermi level or intrinsic carrier concentration, and to a threshold voltage shift [83]. Therefore, the current change is considered as a function of mobility and threshold variations ($I_D = f(\mu, V_{TN})$).

$$\Delta I_D = \frac{\partial I_D}{\partial \mu}\Delta\mu + \frac{\partial I_D}{\partial V_{TN}}\Delta V_{TN}$$

$$\frac{\Delta I_D}{I_D} = \frac{\Delta\mu}{\mu} + \frac{1}{I_D}\frac{\partial I_D}{\partial V_{TN}}\Delta V_{TN} = \frac{\Delta\mu}{\mu} - \frac{g_m}{I_D}\Delta V_{TN} \tag{4.10}$$

$$\left.\frac{g_m}{I_D}\right|_{\text{Strong Inversion}} = \frac{1}{V_{GS} - V_{TN} - \frac{V_{DS}}{2}}$$

In Eq. 4.10, the threshold variations are multiplied by the normalized transconductance of the transistor that is relatively small at large gate drive but grows rapidly as exits strong inversion. Note that in a group of transistors as in a sensor rosette for example, the ΔV_{TN} is common to all devices for a given stress, whereas the mobility terms are dependent upon the orientations of the channel. The normalized transconductance g_m/I_D plays an important role in amplifying the overall contribution of the threshold term, particularly at low gate drive. The value of g_m/I_D for subthreshold region can be obtained by using Eq. 4.4:

$$\left.\frac{g_m}{I_D}\right|_{\text{Weak Inversion}} = \frac{1}{I_D}\frac{\partial I_D}{\partial V_{GS}} = \frac{1}{nV_T} = \frac{q}{nkT} \tag{4.11}$$

Now, expressions for the stress dependence of mobility and threshold voltage can be developed as follows.

A. NMOS mobility model

Mobility variations due to stress in the wafer coordinate system for 4H-SiC are expressed in terms of piezoresistive coefficients of FETs in Eq. 3.5. For MOSFETs, the piezoresistive coefficients are represented by Π's instead of π's [41].

$$\frac{\Delta\mu}{\mu} \cong -\frac{\Delta R}{R} = -\left\{ \begin{array}{l} \left(\Pi_{11}\sigma'_{11} + \Pi_{12}\sigma'_{22}\right)\cos^2\phi + \left(\Pi_{12}\sigma'_{11} + \Pi_{11}\sigma'_{22}\right)\sin^2\phi \\ \quad + \Pi_D\sigma'_{12}\sin 2\phi + \Pi_{13}\sigma'_{33} + \left[\alpha_1\Delta T + \alpha_2\Delta T^2 + \cdots\right] \end{array} \right\} \tag{4.12}$$

where ϕ represents the direction of current relative to the x'_1 direction as shown in Fig. 3.3.

B. Threshold Voltage Model

As mentioned above, the threshold voltage changes due to the intrinsic carrier concentration variations (Δn_i). Prior research [84]-[87] demonstrated that ΔV_{TN} is proportional to $\Delta n_i^2/n_i^2$ which is a quadratic function of stress. Thus, the overall threshold voltage change can be written:

$$\Delta V_{TN} = k_1\sigma + k_2\sigma^2 \tag{4.13}$$

where k_1 and k_2 depend upon the direction of stress and the semiconductor materials. Substitution of Eq. 4.13 in Eq. 4.10 predicts the presence of both first- and second-order piezoresistive coefficients.

4.4 Four-Element Sensor Rosette

The resistive rosette is relatively large and not optimal for use in measuring stresses in critical areas, whereas FETs can be made very small and offer higher stress sensitivity than the heavily-doped resistors. In order to make quality stress measurements, it is best to use differential measurements to eliminate the ΔT and ΔV_{TN}. Similar to resistive rosettes, typical FET sensor rosettes consist of two or more FETs aligned at various angles relative to the primed axes as indicated in Fig. 4.5.

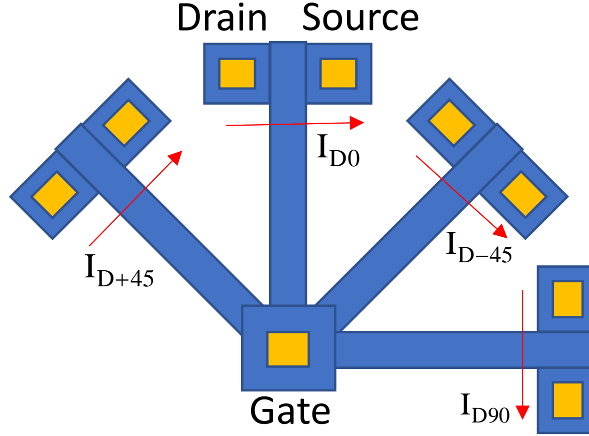

Figure 4.5: NMOS Drain Current Orientations in a Four-Element Rosette

Drain current change equations are found by expanding Eq. 4.12 for angles of 0, 90, +45 -45 degrees (The higher order temperature terms are ignored).

$$
\begin{aligned}
\frac{\Delta I_{D0}}{I_{D0}} &= -\left(\Pi_{11}\sigma'_{11} + \Pi_{12}\sigma'_{22} + \Pi_{13}\sigma'_{33}\right) - \frac{g_m}{I_D}\Delta V_{TN} + \alpha_1 \Delta T \\
\frac{\Delta I_{D90}}{I_{D90}} &= -\left(\Pi_{12}\sigma'_{11} + \Pi_{11}\sigma'_{22} + \Pi_{13}\sigma'_{33}\right) - \frac{g_m}{I_D}\Delta V_{TN} + \alpha_1 \Delta T \\
\frac{\Delta I_{D45}}{I_{D45}} &= -\begin{bmatrix} (\frac{1}{2}\Pi_{11} + \frac{1}{2}\Pi_{12})\sigma'_{11} + (\frac{1}{2}\Pi_{12} + \frac{1}{2}\Pi_{11})\sigma'_{22} + \Pi_{13}\sigma'_{33} \\ +\Pi_D\sigma'_{12} \end{bmatrix} - \frac{g_m}{I_D}\Delta V_{TN} + \alpha_1 \Delta T \\
\frac{\Delta I_{D-45}}{I_{D-45}} &= -\begin{bmatrix} (\frac{1}{2}\Pi_{11} + \frac{1}{2}\Pi_{12})\sigma'_{11} + (\frac{1}{2}\Pi_{12} + \frac{1}{2}\Pi_{11})\sigma'_{22} + \Pi_{13}\sigma'_{33} \\ -\Pi_D\sigma'_{12} \end{bmatrix} - \frac{g_m}{I_D}\Delta V_{TN} + \alpha_1 \Delta T
\end{aligned} \tag{4.14}
$$

The temperature compensated measurements are made by subtracting the normalized drain current terms of pairs of orthogonal transistors as demonstrated in Eq. 4.15.

$$\frac{\Delta I_{D0}}{I_{D0}} - \frac{\Delta I_{D90}}{I_{D90}} = -\Pi_D(\sigma'_{11} - \sigma'_{22})$$
$$\frac{\Delta I_{D45}}{I_{D45}} - \frac{\Delta I_{D-45}}{I_{D-45}} = -2\Pi_D\sigma'_{12} \tag{4.15}$$

Like the resistive rosettes, two compensated quantities, the normal stress difference and shear stress can be extracted, and a free surface is not required because the out-of-place normal stress terms cancel out. For the specific case of a free top surface, careful control of temperature, and ΔV_{TN} correction, the two individual normal stresses can be measured by combining the sum terms in Eq. 4.16 with Eq. 4.15.

$$\frac{\Delta I_{D0}}{I_{D0}} + \frac{\Delta I_{D90}}{I_{D90}} = -\Pi_S(\sigma'_{11} + \sigma'_{22}) - 2\frac{g_m}{I_D}\Delta V_{TN} + 2\alpha_1\Delta T$$
$$\frac{\Delta I_{D45}}{I_{D45}} + \frac{\Delta I_{D-45}}{I_{D-45}} = -\Pi_S(\sigma'_{11} + \sigma'_{22}) - 2\frac{g_m}{I_D}\Delta V_{TN} + 2\alpha_1\Delta T \tag{4.16}$$

For strong inversion case, the stress induced threshold voltage variations are negligible and the drain current change is mainly due to the mobility change, thus, Eq. 3.30 to 3.32 are also valid if the $(g_m/I_D)\Delta V_{TN}$ terms are removed and the same stress components can be measured.

4.5 Experimental Method

Fig. 4.6 displays the layout of 10/1 lateral NMOS test devices utilized in this work where the x'_1 and x'_2 directions correspond to applied longitudinal and transverse stresses relative to the drain current directed in x'_1 direction. The four-point bending method (Fig. 3.8) was used to apply stress and the NMOS devices are probed through a hole in top of

the fixture. Since the four-point bending method generates uniaxial stress along the beam, SiC strips cut along x'_1 and x'_2 directions are utilized. Measurements to be presented in this work are made in the linear operation of the transistor with a drain-source voltage of 50 - 100mV. All measurements utilized an Agilent Semiconductor Parameter Analyzer

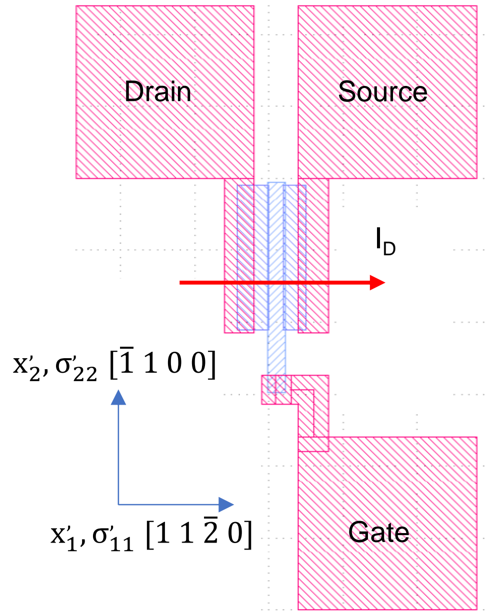

Figure 4.6: Layout of the 10/1 Lateral NMOS Transistor

4.6 Experimental Results

4.6.1 NMOS Device Characteristics

SiC MOSFETs are well known to have large trap densities at the SiC/SiO_2 interface [88],[89]. Changes in the charge state of these interface traps affect the threshold voltage of the transistor, and the additional capacitance alters the relationship between gate voltage and surface potential. Fig. 4.7 and 4.8 presents examples of the impact of these effects.

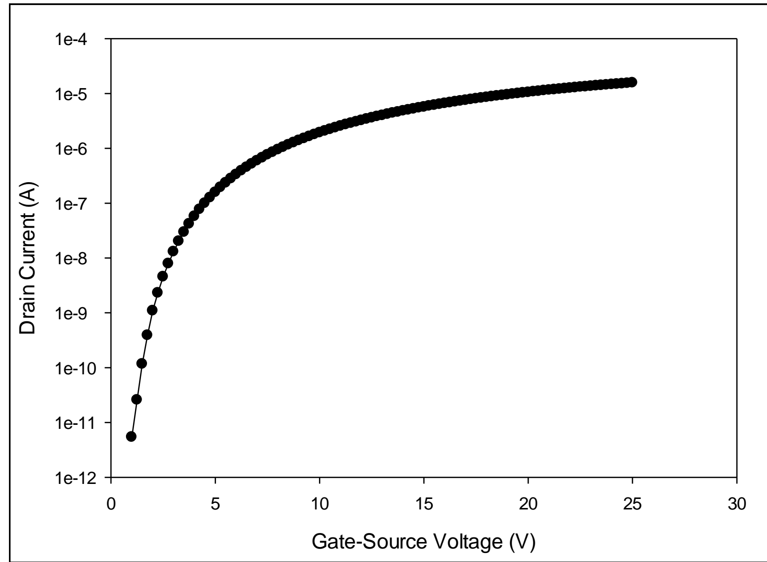

Figure 4.7: Semi-logarithmic Graph of the Turn-on Characteristic

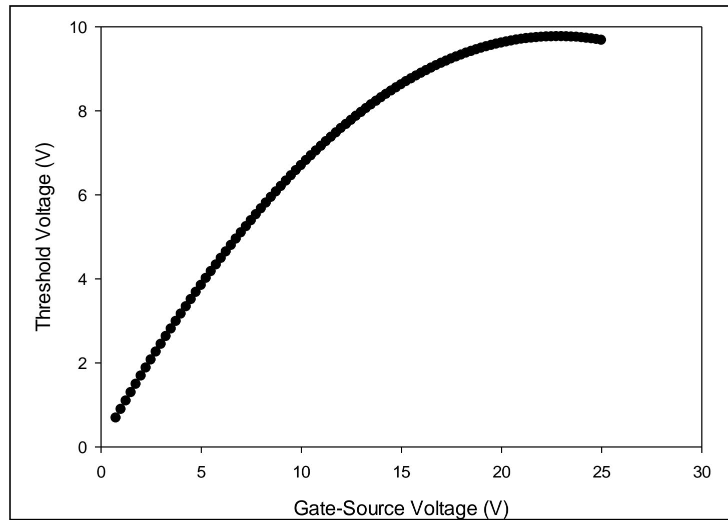

Figure 4.8: Threshold Voltage versus Gate-source Voltage Extracted from Linear Region Measurements with V_{DS} = 100 mV

Fig. 4.7 depicts the turn-on characteristic in which the subthreshold slope never reaches a limit as the gate voltage sweeps the surface potential down through the bandgap

changing the state of the interface traps. The threshold voltage extracted from linear region extrapolation appears in Fig. 4.8 and increases rapidly from less than 1 V to a plateau of approximately 9.6 V as the trap levels become saturated for high gate voltage.

According to the turn-on characteristic, the normalized transconductance from direct measurements can be found using Eq .4.17.

$$\frac{g_m}{I_D} = \frac{1}{I_D}\frac{\partial I_D}{\partial V_{GS}} \tag{4.17}$$

And the theory in Eq. 4.10 gives the following relation

$$\left.\frac{g_m}{I_D}\right|_{\text{Strong Inversion}} = \frac{1}{V_{GS} - V_{TN} - \frac{V_{DS}}{2}} \tag{4.18}$$

where the V_{TH} changes with V_{GS} as shown in Fig. 4.8.

Fig. 4.9 shows the comparison of measured results with theory for normalized transconductance g_m/I_D versus gate-source voltage in the linear region of the NMOS transistor.

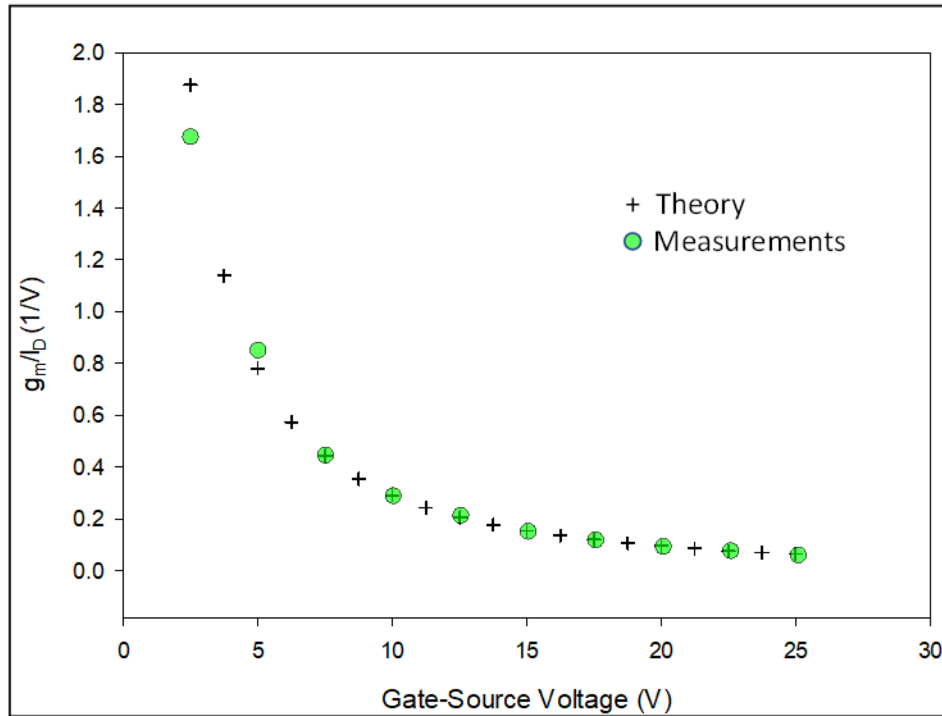

Figure 4.9: Comparison of Measurements with Theory for Normalized Transconductance

4.6.2 NMOS Stress Characterization

The current changes with applied uniaxial stress and examples of the overall stress-induced changes in the NMOS transfer characteristic appear in Fig. 4.10 and Fig. 4.11. The results exhibit approximately a 1.3% decrease in drain current per 100 MPa increase in uniaxial stress corresponding to an overall piezoresistive coefficient of 130 /TPa.

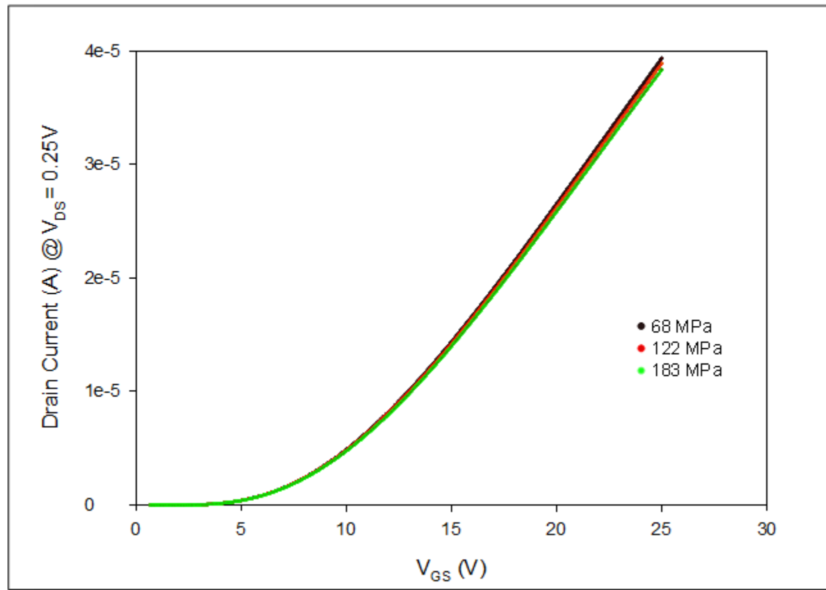

Figure 4.10: A Linear Region Turn-on Characteristics for Three Levels of Uniaxial Stress (V_{DS}=0.25V)

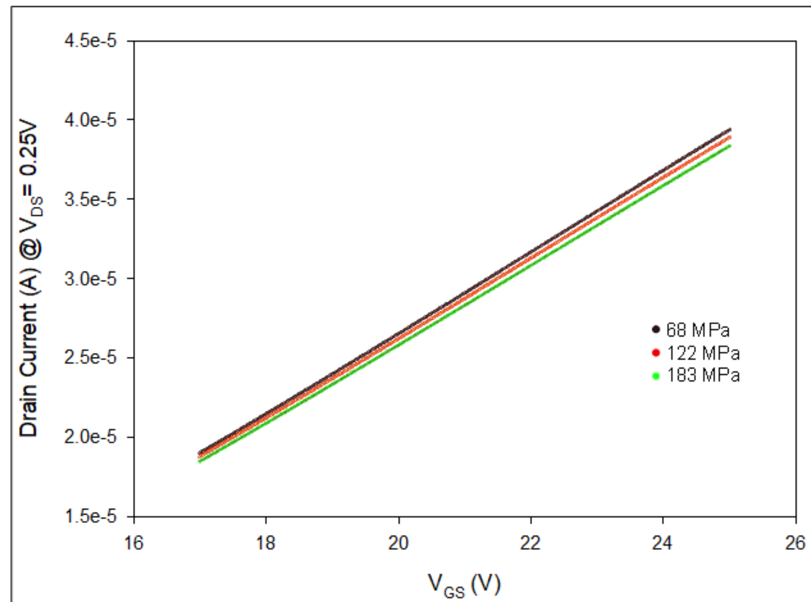

Figure 4.11: Expansion of the Region Between 15 and 20 Volts.

Applying the results from Eq. 4.14, the overall stress response of the individual NMOS transistor to uniaxial stress is described by 4.19 in which temperature is assumed to be well-controlled.

$$\begin{aligned}\left.\frac{\Delta I_{D0}}{I_{D0}}\right|_{\sigma=\sigma'_{11}} &= \Xi_{11}\sigma'_{11} = -\Pi_{11}\sigma'_{11} - \frac{g_m^0}{I_{D0}^0}\Delta V_{TN} \\ \left.\frac{\Delta I_{D0}}{I_{D0}}\right|_{\sigma=\sigma'_{22}} &= \Xi_{12}\sigma'_{22} = -\Pi_{12}\sigma'_{22} - \frac{g_m^0}{I_{D0}^0}\Delta V_{TN}\end{aligned} \tag{4.19}$$

where Ξ_{ij} represent the overall piezoresistive coefficients which include both the mobility and threshold voltage terms. g_m^0/I_{D0}^0 is the initial unstressed values but remain functions of V_{GS}. Based upon Eq. 4.13, the overall piezoresistive coefficients can be written as

$$\begin{aligned}\Xi_{11} &= -\Pi_{11} - \frac{g_m^0}{I_{D0}^0}K_1 \\ \Xi_{12} &= -\Pi_{12} - \frac{g_m^0}{I_{D0}^0}K_1 \\ \Xi_D &= \Xi_{11} - \Xi_{12}\end{aligned} \tag{4.20}$$

where k_1 is treated as fitting parameter ($\Delta V_{TN} = K_1\sigma$). In this work, the second-order term ($K_2\sigma^2$) is not considered since substantial curvature has not been observed in our stress characteristics measured at relatively low levels of stress.

The following figures show the examples of stress dependent results for NMOS devices operating in the linear region. Linear region conductance was measured by sweeping V_{DS} from 0 to 100 mV. The slope of each curve represents a single value of Ξ_{12}.

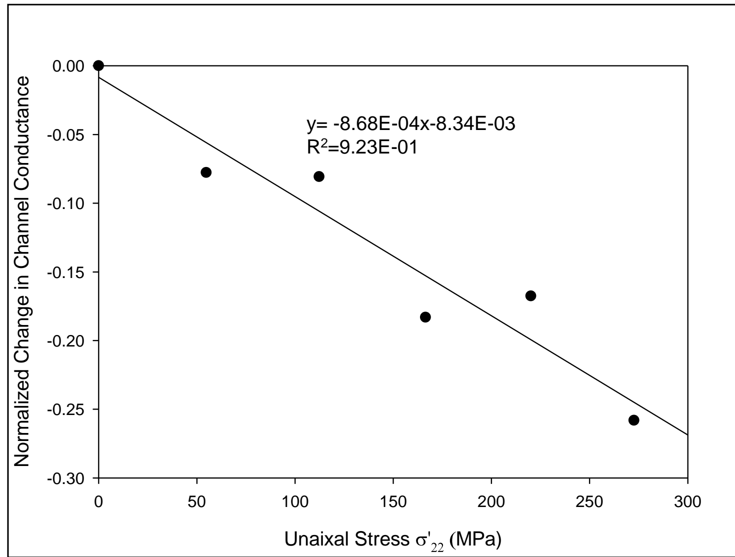

Figure 4.12: Example of Normalized Change in NMOS Channel Conductance vs. Applied Stress at V_{GS}= 2.5 V Yielding $\Xi_{12} = -868$ /TPa

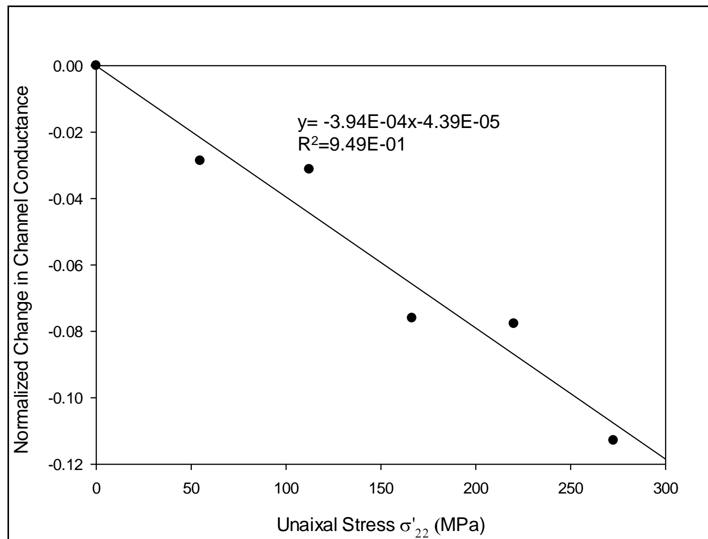

Figure 4.13: Example of Normalized Change in NMOS Channel Conductance vs. Applied Stress at V_{GS}= 5 V Yielding $\Xi_{12} = -394$ /TPa

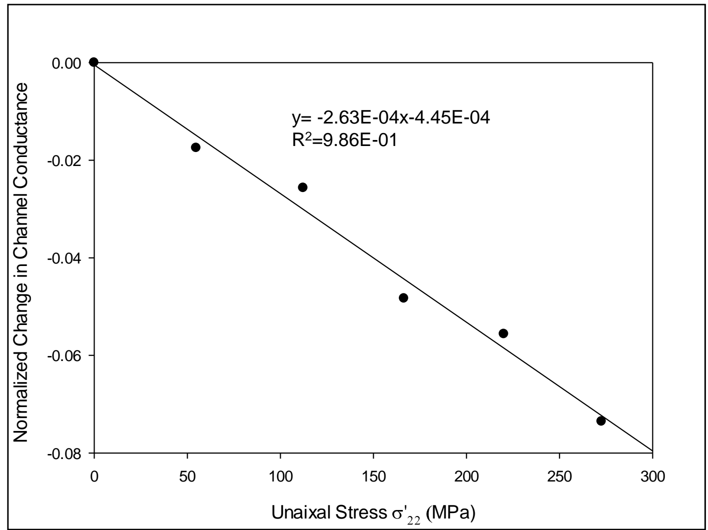

Figure 4.14: Example of Normalized Change in NMOS Channel Conductance vs. Applied Stress at V_{GS}= 7.5 V Yielding $\Xi_{12} = -263$ /TPa

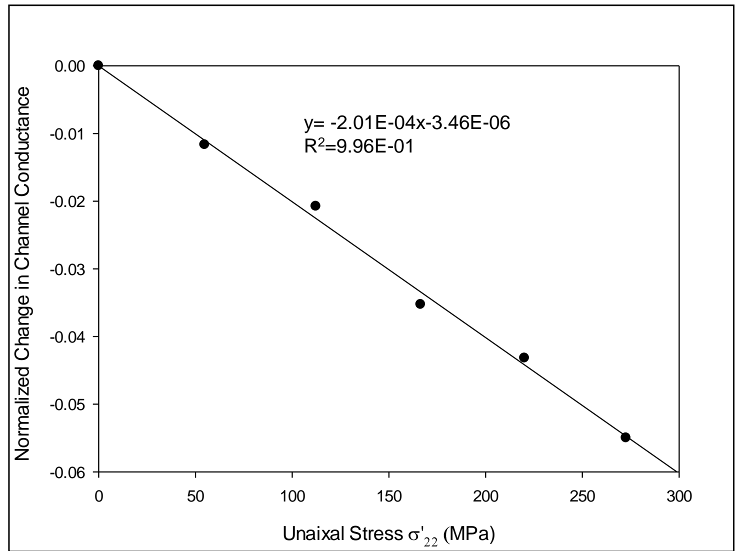

Figure 4.15: Example of Normalized Change in NMOS Channel Conductance vs. Applied Stress at V_{GS}= 10 V Yielding $\Xi_{12} = -201$ /TPa

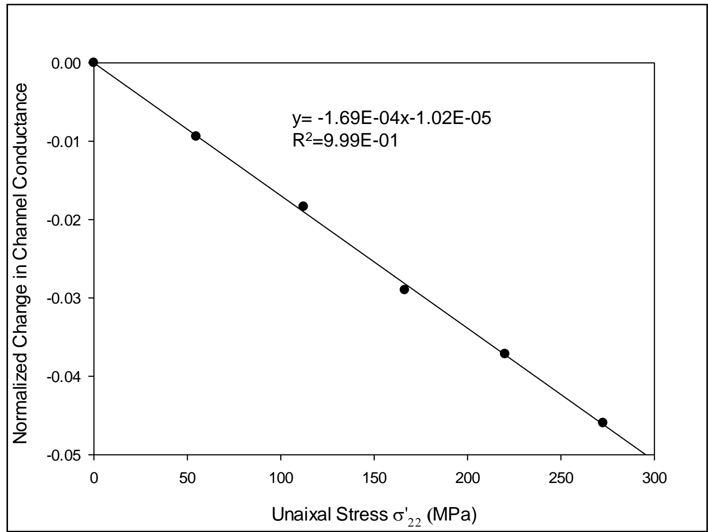

Figure 4.16: Example of Normalized Change in NMOS Channel Conductance vs. Applied Stress at V_{GS}= 12.5 V Yielding $\Xi_{12} = -169$ /TPa

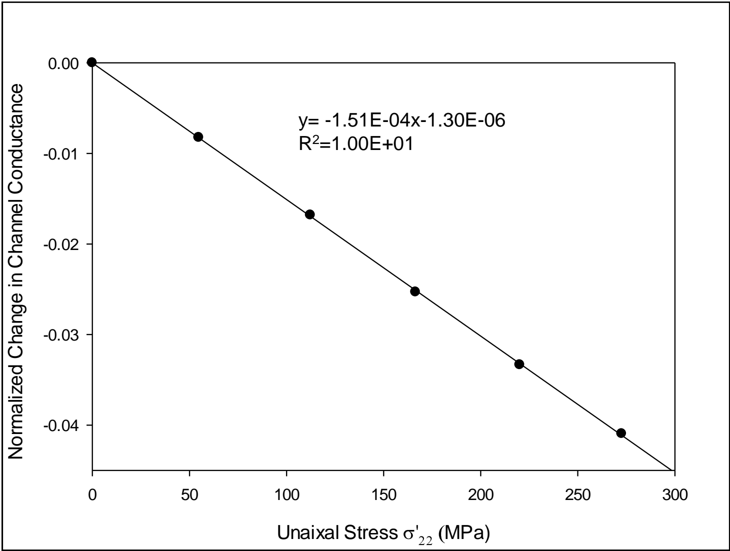

Figure 4.17: Example of Normalized Change in NMOS Channel Conductance vs. Applied Stress at V_{GS}= 15 V Yielding $\Xi_{12} = -151$ /TPa

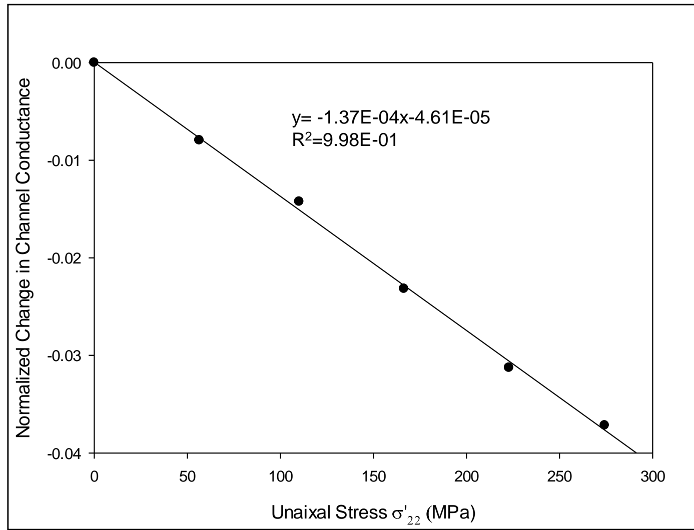

Figure 4.18: Example of Normalized Change in NMOS Channel Conductance vs. Applied Stress at V_{GS}= 17.5 V Yielding $\Xi_{12} = -137$ /TPa

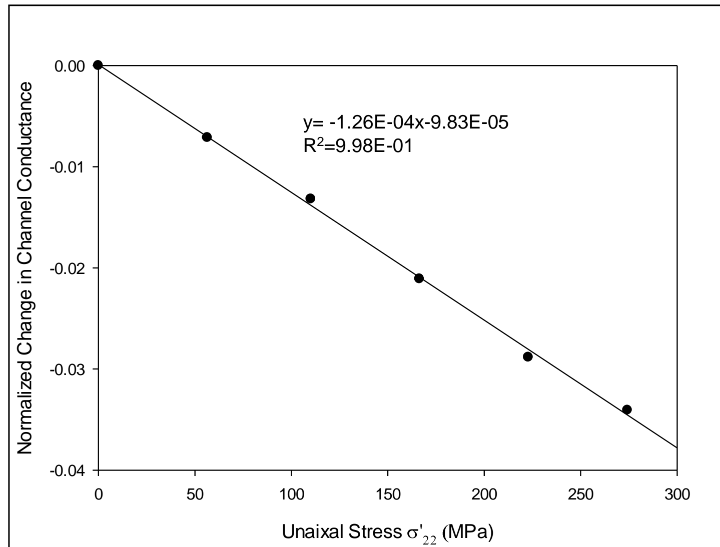

Figure 4.19: Example of Normalized Change in NMOS Channel Conductance vs. Applied Stress at V_{GS}= 20 V Yielding $\Xi_{12} = -126$ /TPa

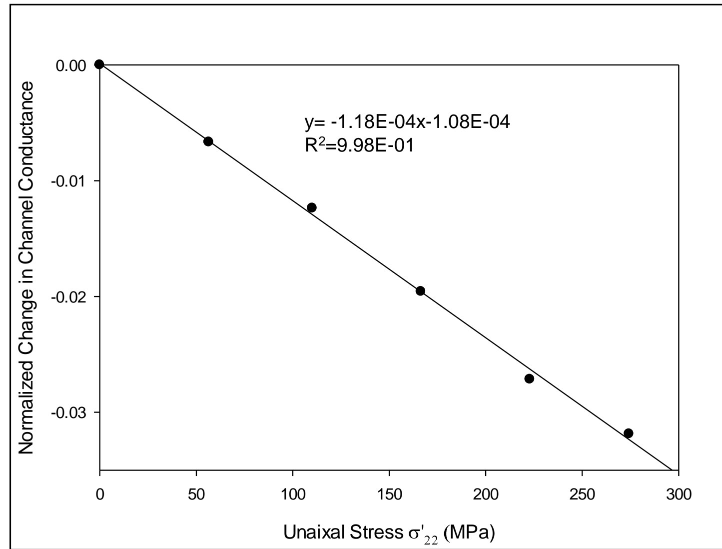

Figure 4.20: Example of Normalized Change in NMOS Channel Conductance vs. Applied Stress at V_{GS}= 22.5 V Yielding $\Xi_{12} = -118$ /TPa

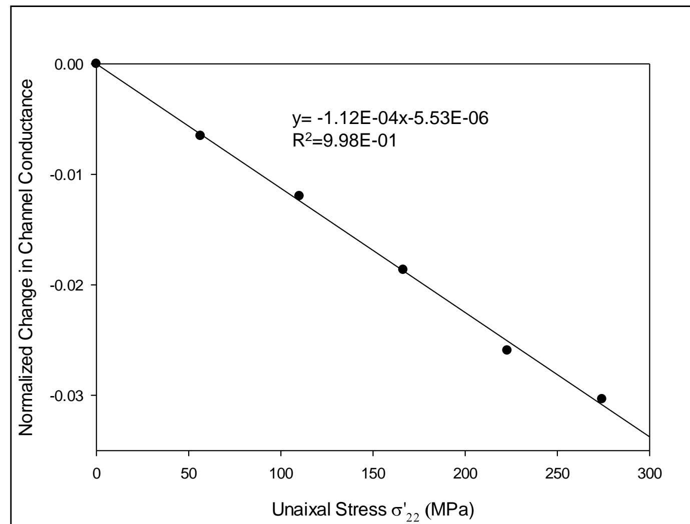

Figure 4.21: Example of Normalized Change in NMOS Channel Conductance vs. Applied Stress at V_{GS}= 25 V Yielding $\Xi_{12} = -112$ /TPa

Complete measurement results appear in Table 4.1 in which each table element represents the average of data sets for 10 individual transistors.

Piezoresistive Coefficients Results			
V_{GS} (V)	Ξ_{11} (1/Tpa)	Ξ_{12} (1/Tpa)	Ξ_D (1/Tpa)
2.5	-488	-823	335
5	-185	-374	189
7.5	-107	-261	154
10	-66.3	-200	134
12.5	-45.6	-167	121
15	-38.6	-145	106
17.5	-24.8	-132	107
20	-17.4	-123	106
22.5	-11.6	-115	103
25	-11.4	-110	98.6

Table 4.1: Piezoresistive Coefficient Results

Fig. 4.22 presents comparisons between graphs of Eq. 4.20 and the result of the measurements of the individual NMOS devices. The two lower pairs of curves represent Ξ_{11} and Ξ_{12}, whereas the upper pair of curves are for the difference Ξ_D. The plot of the theory in Fig. 4.22 represents a simultaneous least square fit to the data using measured values of g_m^0/I_{D0}^0 for the individual transistor and a single value of K_1 for both Ξ_{11} and Ξ_{12}.

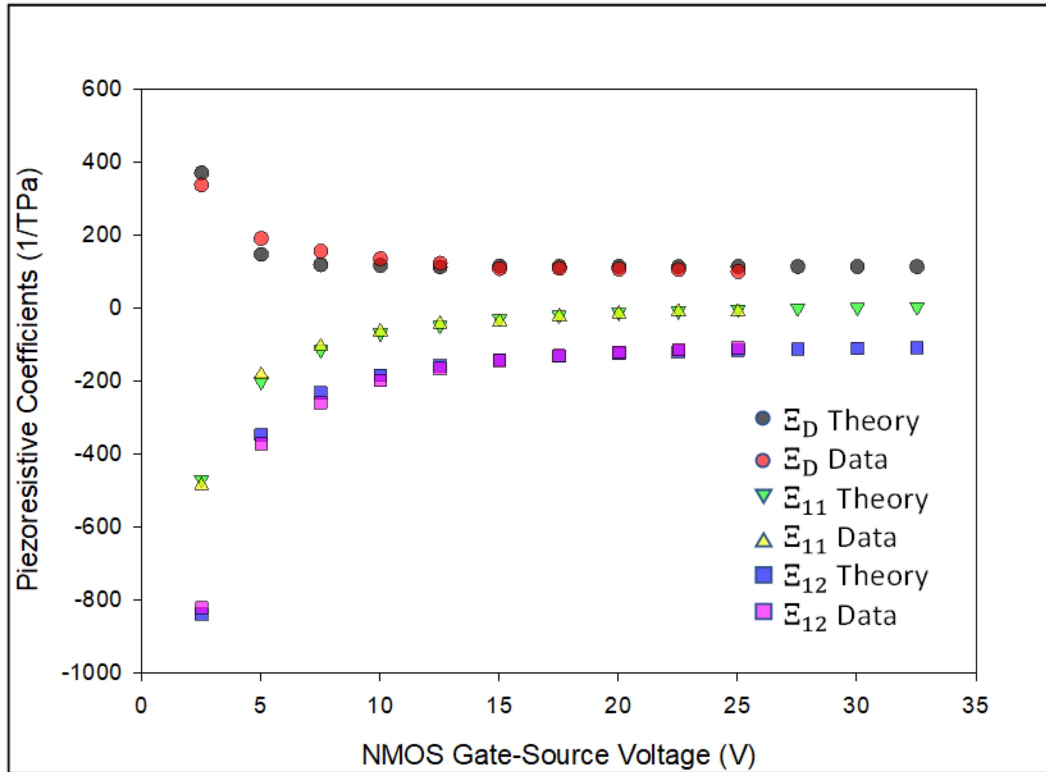

Figure 4.22: Comparison Between the Measured Values of First-Order Coefficients and the Theory in Eq. 4.20.

Note the unexpected upturns in Fig. 4.22 for the extracted data for Ξ_D at low bias voltage, whereas the ideal theory is constant. It is caused by the non-zero initial offset current of the device pairs. At high gate drive the initial current mismatch is small but grows rapidly as (V_{GS}-V_{TN}) decreases, and this effect causes the turn up in the effective value of Ξ_D.

Π_{11} (/TPa)	Π_{12} (/TPa)	Π_D (/TPa)	K_1
-14	98	-112	290

Table 4.2: Results of a Simultaneous Least Square Fit to Table 4.1 Data

Overall, the magnitude of the piezoresistive coefficients is not large compared to silicon. There is clearly a sensitivity advantage by operating the devices at low gate voltages approaching threshold in stress sensor applications, but the increased sensitivity comes with a greater sensitivity to operating point variations at low gate drive. Substantial improvement can be achieved by implementing NMOS rosettes as a multi-terminal inversion layer device [90]-[91], and an eight-terminal inversion layer van der Pauw structure should provide a 3.16X improvement in stress sensitivity to both $(\sigma'_{11} - \sigma'_{22})$ and σ'_{12}.

4.7 Summary

This chapter review the piezoresistive effects on NMOS FET devices and developed theory for the stress dependence of NMOS transistors on 4H-SiC. The stress model for NMOS FETs contains the classic mobility terms plus a new term describing changes in threshold voltage. The threshold voltage term is strongly dependent on operating point, particularly at low values of gate drive.

Measurement results were presented for the longitudinal and transverse piezoresistive coefficients for 4H-SiC transistors. The developed model agrees closely with both sets of measurements.

In general, the measured piezoresistive coefficients of the various devices are relatively small at high gate drives, but can become significant at low gate drives approaching moderate inversion and below since the g_m/I_D term cannot be neglected.

The coefficients reported are relatively small for large gate drive, so little improvement in mobility would be expected with low values of built-in stress. Much higher

levels of stress similar to those as used in silicon (i.e. GPa), would probably produce more significant changes and would be required to enhance the overall mobilities of silicon carbide in a manner similar to that done in silicon [78][79].

Similar to resistive sensors, a four-element NMOS stress sensor rosette was proposed that can measure two important temperature compensated stress quantities and requires only a single value of piezoresistive coefficient Π_D. The transistor sensors can be directly implemented with a multi-terminal inversion-layer van der Paus test structure with its 3.16 times higher sensitivity.

Chapter 5

EVALUATION OF IMPACT OF FOUR-DEGREE OFF-AXIS WAFERS ON 4H-SiC STRESS SENSORS

5.1 Introduction

As discussed earlier, the piezoresistive stress sensors have been shown to represent a powerful tool for experimental evaluation of the die stress distributions. Successful application of these piezoresistive sensors for stress measurement requires both properly designed sensors and accurately calibrated values of the piezoresistive coefficients. In the past, the analysis and design of stress sensors on silicon carbide have assumed that the wafer surface is aligned with the crystallographic axes. However, 4H silicon carbide wafers are produced with an off-axis cut to ensure high-quality homoepitaxial growth. Thus, the existing "on-axis" theory based on perfect alignment of the device surface with the crystallographic axes is an approximation, and modifications are necessary to improve the accuracy of the formulation.

In this work, fundamental aspects for the hexagonal silicon carbide homoepitaxial growth are described and the off-axis angle for our sample is determined by electron backscattering diffraction analysis (EBSD). The theory and extraction of piezoresistive coefficients for 4H-SiC silicon carbide materials in the presence of off-axis starting wafers are discussed. It has been found that many of the elements of the ideal on-axis π-matrix are zero, while the off-axis π-matrix is filled with non-zero values indicating additional

coupling between the sensor resistances and the six stress components. Examples of the overall impact of these new terms on calibration are discussed.

The impact of off-axis wafers on stress measurements depends on the value of piezoresistive coefficients and the stress distribution. Accurate calculation of errors requires the values for all fundamental piezoresistive coefficients, which are still not available in the literatures to date.

5.2 Epitaxial Growth of SiC

Epitaxy is a process of growing a crystal on top of another crystal, which is essential to produce active layers with designed doping density and thickness. There are several epitaxy techniques to deposit films, such as molecular beam epitaxy (MBE), epitaxial chemical vapor deposition (CVD), or liquid phase epitaxy (LPE), etc. Early epitaxial growth of α-SiC was performed by LPE which produces uniform epilayer thickness and impurity doping, but also suffers from polytype mixing. [92],[93]. Nowadays, homoepitaxial growth technology by CVD has shown remarkable progress and has become standard technology for SiC device development [94]-[96]. Homoepitaxial growth of 6H-SiC with smooth surface was achieved by using step-flow growth on 2-6° off-axis 6H-SiC. In the same manner, high quality homoepitaxial CVD growth of 4H-SiC requires off-axis substrates. When the off-axis is introduced, the [0001] axis is tilted several degrees (typically 4°) toward $[\bar{1}\bar{1}20]$, as shown in Fig .5.1 [51][97]-[102].

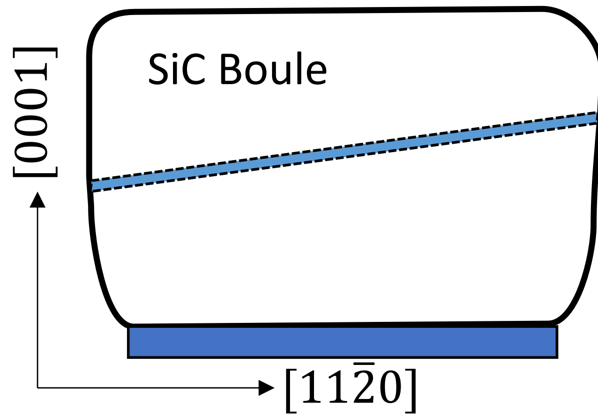

Figure 5.1: Off-axis SiC Wafer Cutting Orientation.

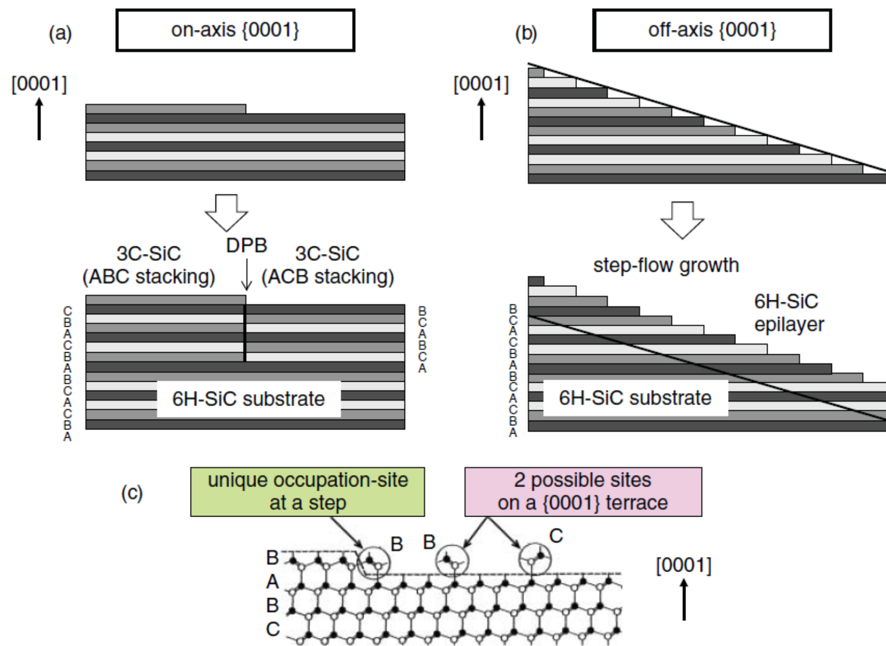

Figure 5.2: Schematic Illustration of Growth Modes and Stacking Sequences of SiC Layers Grown on (a) on-axis 6H-SiC (0001) and (b) off-axis 6H-SiC (0001). (c) Bond Configuration Near an Atomic Step and on the (0001) Terrace. Borrowed from [51].

In Fig. 5.2 (a), the step density is very low, and the crystal growth may initially occur on terraces. This leads to the growth of 3C-SiC, which is stable at low temperature. The growing 3C-SiC can take two possible stacking orders of ABCABC and ACBACB. On the other hand, on off-axis (0001) surface in Fig. 5.2 (b), the step density is high, and the incorporate site (A, B, C) is uniquely determined by bonds form the step, as shown in Fig. 5.2 (c).

Therefore, the CVD growth process usually consists of in-situ etching and main epitaxial growth. The purpose of in situ etching is to remove the subsurface damage and to obtain regular step structure (Fig.5.2(b)). Immediately after the etching, the main growth of SiC is performed.

5.3 Off-axis Angle Measurement

In this work, the off-axis angle of our specimen is determined by EBSD analysis, which is a common tool to measure crystal orientations. The experimental procedure is presented in Fig. 5.3.

The 4H-SiC sensor chip was carefully cleaned with deionized water and mounted on the holder with conductive adhesives. To ensure the measurement accuracy, an “on-axis” (100) chip is used as a reference sample and placed with an SiC chip side by side. The specimen is usually tilted around 70° from the horizontal plane for better EBSD results. A scanning electron microscope (ZEISS Crossbeam 550) was utilized in this work, and the specimen was placed into the instrument chamber for EBSD analysis. When a focused electron beam impinges on the sample, a Kikuchi pattern is formed by diffraction of backscattered electrons. The geometry of a Kikuchi is unique for the crystal structure and

the crystal lattice orientation under the beam [103]. Once the pattern is extracted, the Eurler angles can be determined by commercial EBSD software (Aztec Crystal).

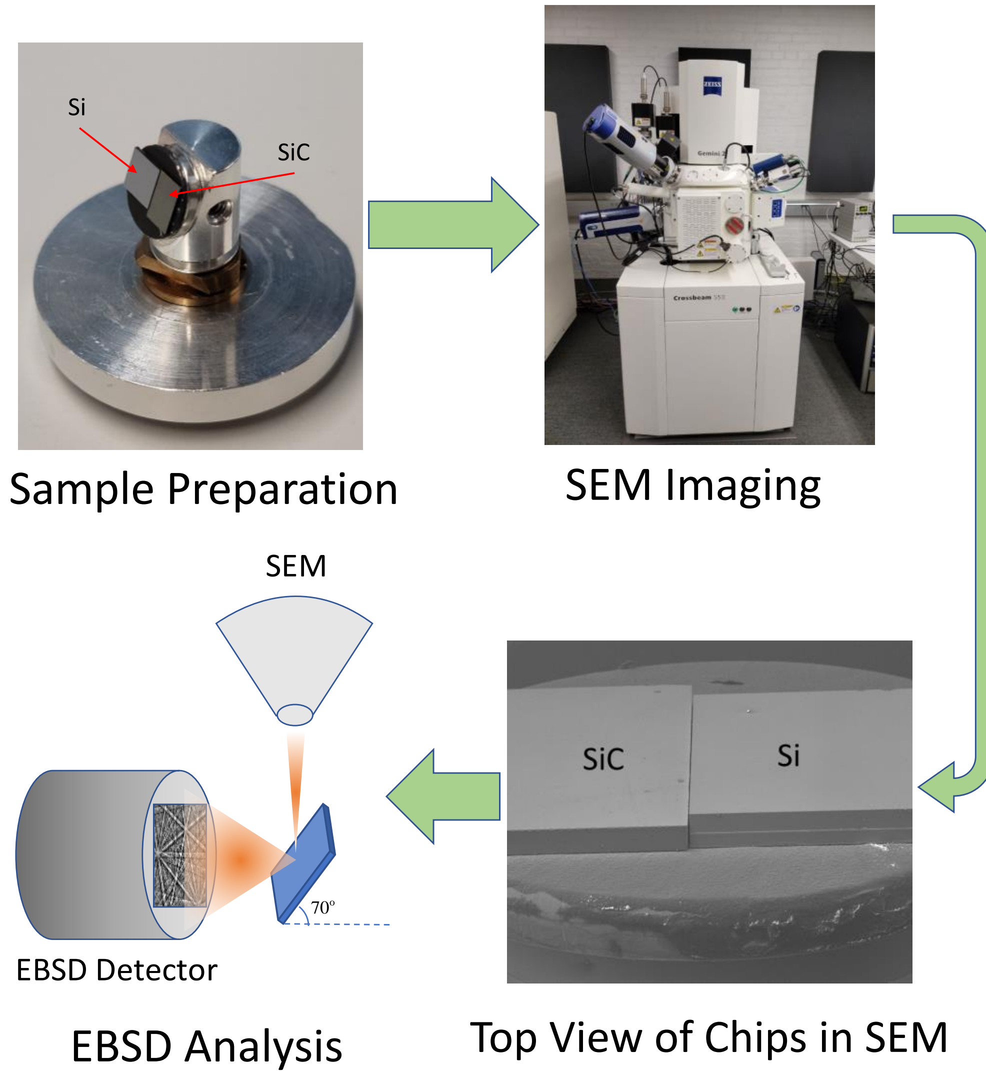

Figure 5.3: – Flow Chart of Experimental Procedure (Including ZEISS Crossbeam 550)

Fig. 5.4 shows a typical result for the reference sample ((100) silicon chip). For each crystallographic axis, the off-axis angles caused by inevitable experimental errors are

presented below the miller indices. The average off-axis angle for [001] axis is 0.22°. Thus, the experimental errors for EBSD measurement are expected to be around 0.22°.

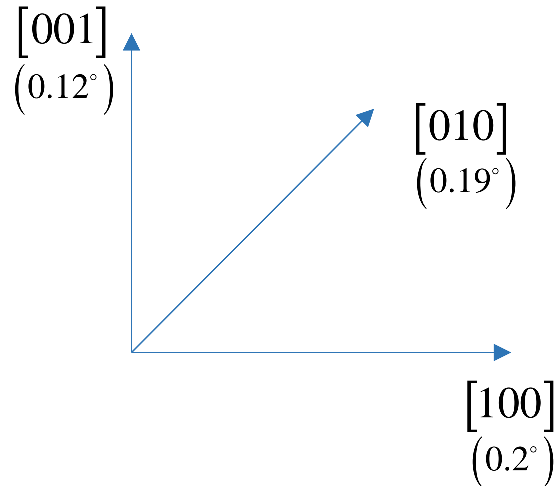

Figure 5.4: Typical EBSD Result for (100) Silicon

For 4H-SiC, 10 different areas (more than 50 thousand data points) on the die surface were probed and the average and standard deviation of the off-axis angle are 4.11° and 0.09°, respectively. Thus, this work will discuss the 4 degrees off-axis case.

5.4 Impact of Off-axis Wafers on Calibration

Fig. 5.5 shows the coordinate systems for the "on-axis" theory. As discussed in Chapter 3, the unprimed coordinate system x_1-x_2-x_3 represents the conventional coordinate system which corresponds to the fundamental piezoresistive matrix. The primed coordinate system is the wafer coordinate system which is formed by rotating the unprimed crystallographic axes 30 degrees about the x_3 axis, so that the x_1' and x_2' axes are oriented

in the directions parallel and perpendicular to the primary wafer flat, while the x_3 and x'_3 axes are coincident and normal to the wafer surface.

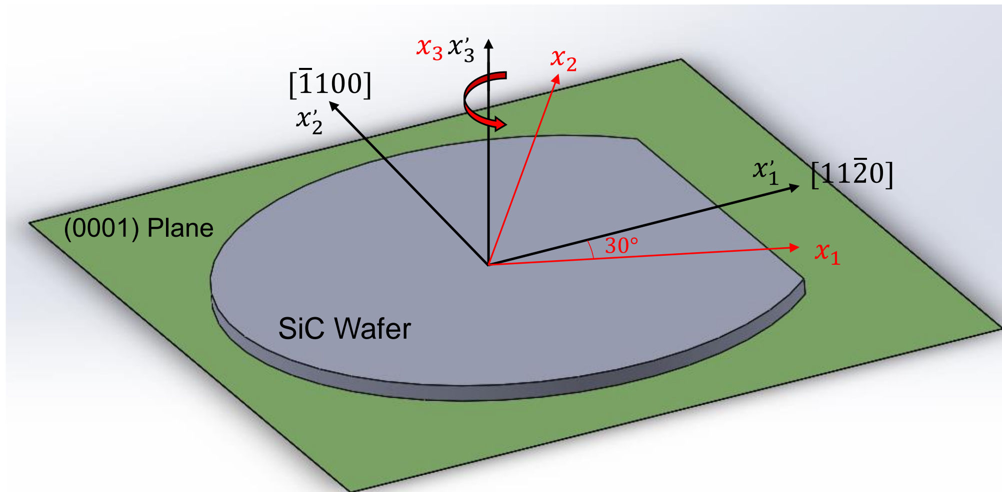

Figure 5.5: Untilted wafer plane

For the 4 degrees off-axis wafer, we introduce a new wafer coordinate system x_1^*-x_2^*-x_3^* and the wafer surface is no longer aligned with (0001) plane. In Fig. 5.6, the x_1^* and x_2^* axes are oriented along the directions parallel and perpendicular to the wafer flat of a tilted wafer, whereas the x_3^* direction is normal to the tilted wafer plane.

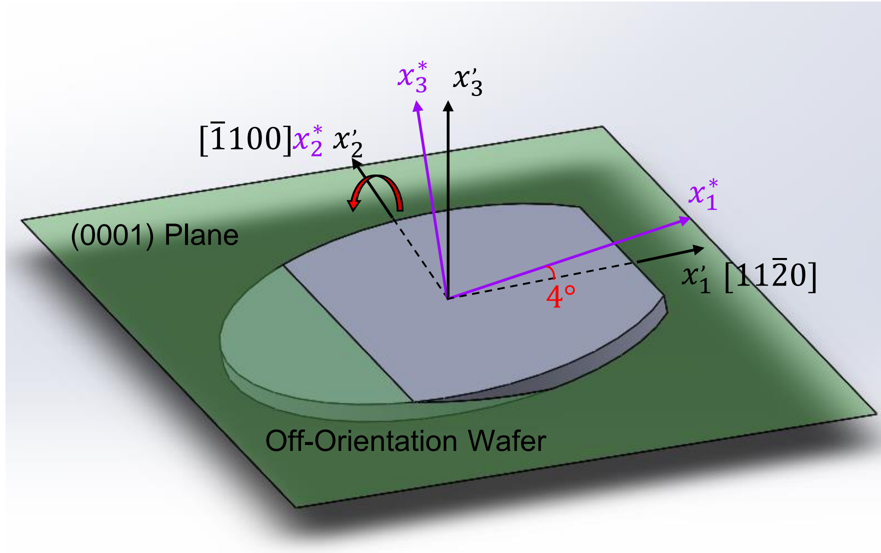

Figure 5.6: Tilted wafer plane

The $x_1^* - x_2^* - x_3^*$ axes are obtained from the unprimed axes by first rotating about the x_3 axis through an angle of 30 degrees and then rotating about the x_2' through an angle of 4 degrees. Therefore, piezoresistive matrix of the tilted wafer coordinate system can be calculated by performing the coordinate transformation two times:

$$\begin{aligned} \left[\pi'\right] &= \left[T_1\right]\left[\pi\right]\left[T_1\right]^{-1} \\ \left[\pi^*\right] &= \left[T_2\right]\left[\pi'\right]\left[T_2\right]^{-1} \end{aligned} \tag{5.1}$$

Where T_1 and T_2 are the transformation matrix of 30 degrees and 4 degrees rotation, respectively. From Chapter 3, we know that $[\pi] = [\pi']$ because (0001) plane is isotropic. The direction cosines for 4 degrees rotation are shown in Eq. 5.2.

$$\left[a_{ij}\right] = \begin{bmatrix} l_1 & m_1 & n_1 \\ l_2 & m_2 & n_2 \\ l_3 & m_3 & n_3 \end{bmatrix} = \begin{bmatrix} \cos(4^\circ) & 0 & \cos(86^\circ) \\ 0 & 1 & 0 \\ \cos(94^\circ) & 0 & \cos(4^\circ) \end{bmatrix} \tag{5.2}$$

Substitution of Eq. 5.2 into Eq. 3.3 leads to transformation matrix $[T_2]$ and the calculated piezoresistive coefficients $[\pi^*]$ in tilted wafer plane are listed in Eq. 5.3.

$$
\begin{bmatrix} \pi^*_{11} \\ \pi^*_{12} \\ \pi^*_{13} \\ \pi^*_{14} \\ \pi^*_{15} \\ \pi^*_{16} \\ \pi^*_{21} \\ \pi^*_{22} \\ \pi^*_{23} \\ \pi^*_{24} \\ \pi^*_{25} \\ \pi^*_{26} \\ \pi^*_{31} \\ \pi^*_{32} \\ \pi^*_{33} \\ \pi^*_{34} \\ \pi^*_{35} \\ \pi^*_{36} \\ \pi^*_{41} \\ \pi^*_{42} \\ \pi^*_{43} \\ \pi^*_{44} \\ \pi^*_{45} \\ \pi^*_{46} \\ \pi^*_{51} \\ \pi^*_{52} \\ \pi^*_{53} \\ \pi^*_{54} \\ \pi^*_{55} \\ \pi^*_{56} \\ \pi^*_{61} \\ \pi^*_{62} \\ \pi^*_{63} \\ \pi^*_{64} \\ \pi^*_{65} \\ \pi^*_{66} \end{bmatrix}
=
\begin{bmatrix}
0.99 & 0 & 4.8\times10^{-3} & 4.8\times10^{-3} & 2.4\times10^{-5} & 9.7\times10^{-3} \\
0 & 0.99 & 0 & 4.9\times10^{-3} & 0 & 0 \\
4.8\times10^{-3} & 0 & 0.99 & 2.4\times10^{-5} & 4.8\times10^{-3} & -9.7\times10^{-3} \\
-0.14 & 0 & 0.14 & -6.8\times10^{-4} & 6.8\times10^{-4} & 0.14 \\
0 & 0 & 0 & 0 & 0 & 0 \\
0 & 0 & 0 & 0 & 0 & 0 \\
0 & 0.99 & 4.9\times10^{-3} & 0 & 0 & 0 \\
1 & 0 & 0 & 0 & 0 & 0 \\
0 & 4.9\times10^{-3} & 0.99 & 0 & 0 & 0 \\
0 & -0.14 & 0.14 & 0 & 0 & 0 \\
0 & 0 & 0 & 0 & 0 & 0 \\
0 & 0 & 0 & 0 & 0 & 0 \\
4.8\times10^{-3} & 0 & 2.4\times10^{-5} & 0.99 & 4.8\times10^{-3} & -9.6\times10^{-3} \\
0 & 4.9\times10^{-3} & 0 & 0.99 & 0 & 0 \\
2.4\times10^{-5} & 0 & 4.8\times10^{-3} & 4.8\times10^{-3} & 0.99 & 9.7\times10^{-3} \\
-6.8\times10^{-4} & 0 & 6.8\times10^{-4} & -0.14 & 0.14 & -0.14 \\
0 & 0 & 0 & 0 & 0 & 0 \\
0 & 0 & 0 & 0 & 0 & 0 \\
-6.9\times10^{-2} & 0 & -3.3\times10^{-4} & 6.9\times10^{-2} & 3.3\times10^{-4} & 6.9\times10^{-2} \\
0 & -6.9\times10^{-2} & 0 & 6.9\times10^{-2} & 0 & 0 \\
-3.4\times10^{-4} & 0 & -6.9\times10^{-2} & 3.4\times10^{-4} & 6.9\times10^{-2} & -6.9\times10^{-2} \\
9.7\times10^{-3} & 0 & -9.6\times10^{-3} & -9.6\times10^{-3} & 9.6\times10^{-3} & 0.98 \\
0 & 0 & 0 & 0 & 0 & 0 \\
0 & 0 & 0 & 0 & 0 & 0 \\
0 & 0 & 0 & 0 & 0 & 0 \\
0 & 0 & 0 & 0 & 0 & 0 \\
0 & 0 & 0 & 0 & 0 & 0 \\
0 & 0 & 0 & 0 & 0 & 0 \\
4.9\times10^{-3} & -4.9\times10^{-3} & 0 & 0 & 0 & 0.99 \\
-7.0\times10^{-2} & 7.0\times10^{-2} & 0 & 0 & 0 & 7.0\times10^{-2} \\
0 & 0 & 0 & 0 & 0 & 0 \\
0 & 0 & 0 & 0 & 0 & 0 \\
0 & 0 & 0 & 0 & 0 & 0 \\
0 & 0 & 0 & 0 & 0 & 0 \\
-7.0\times10^{-2} & 7.0\times10^{-2} & 0 & 0 & 0 & 7.0\times10^{-2} \\
0.99 & -0.99 & 0 & 0 & 0 & 4.9\times10^{-3}
\end{bmatrix}
\begin{bmatrix} \pi_{11} \\ \pi_{12} \\ \pi_{13} \\ \pi_{31} \\ \pi_{33} \\ \pi_{44} \end{bmatrix}
\tag{5.3}
$$

Comparing the π-matrix in the untilted (Eq. 3.1) and tilted cases (Eq. 5.3), it can be observed that many of the elements of the ideal on-axis π-matrix are zero, whereas in the

off-axis version all the original matrix elements are modified and a number of additional elements are no longer zero.

In Chapter 3, we calibrated the fundamental piezoresistive coefficients π_{11} and π_{12} with both resistor and VDP sensors, and π_{13} with only VDP sensors. Here, we discuss the impact of 4 degrees off-axis wafer on our calibration.

For resistor sensors, the fundamental piezoresistive coefficients are extracted readily using uniaxial stress according to the "on-axis" theory (Eq. 3.19):

$$\begin{aligned} \frac{\Delta R_1}{R_1} &= \pi_{11}\sigma'_{11} \\ \frac{\Delta R_2}{R_2} &= \pi_{12}\sigma'_{11} \end{aligned} \tag{5.4}$$

Since the devices are fabricated on the off-axis wafer plane, the π_{ij} we calibrated are the apparent values. Substitution of π^*_{11} and π^*_{12} into Eq. 5.4 yields:

$$\begin{aligned} \frac{\Delta R_1}{R_1} &= \left(\pi_{11}\right)_{\text{apparent}} \sigma'_{11} = \pi^*_{11}\sigma'_{11} \\ &= \sigma'_{11}\begin{pmatrix} 0.99\pi_{11} + 4.8\times10^{-3}(\pi_{13}+\pi_{31}) \\ +2.4\times10^{-5}\pi_{33} + 9.7\times10^{-3}\pi_{44} \end{pmatrix}_{\text{Actual}} \\ \frac{\Delta R_2}{R_2} &= \left(\pi_{12}\right)_{\text{apparent}} \sigma'_{11} = \pi^*_{12}\sigma'_{11} \\ &= \sigma'_{11}\left(\pi_{12} - 0.005\pi_{12} + 4.9\times10^{-3}\pi_{13}\right)_{\text{Actual}} \end{aligned} \tag{5.5}$$

Therefore,

$$\begin{aligned}\left(\pi_{11}\right)_{\text{Apparent}} &= \begin{pmatrix}0.99\pi_{11} + 4.8\times10^{-3}(\pi_{13}+\pi_{31}) \\ +2.4\times10^{-5}\pi_{33} + 9.7\times10^{-3}\pi_{44}\end{pmatrix}_{\text{Actual}} \\ \left(\pi_{12}\right)_{\text{Apparent}} &= \left(\pi_{12} - 0.005\pi_{12} + 4.9\times10^{-3}\pi_{13}\right)_{\text{Actual}}\end{aligned} \tag{5.6}$$

In the above equation, the piezoresistive coefficient that we intend to extract from the calibration are defined as apparent coefficient which is expressed as a function of actual piezoresistive coefficients. The difference between the apparent and actual values are the errors induced by the off-axis wafer.

$$\begin{aligned}\left(\pi_{11}\right)_{\text{Error}} &= \left(\pi_{11}\right)_{\text{Apparent}} - \left(\pi_{11}\right)_{\text{Actual}} \\ &= \begin{pmatrix}-0.01\pi_{11} + 4.8\times10^{-3}(\pi_{13}+\pi_{31}) \\ +2.4\times10^{-5}\pi_{33} + 9.7\times10^{-3}\pi_{44}\end{pmatrix}_{\text{Actual}} \\ \left(\pi_{12}\right)_{\text{Error}} &= \left(\pi_{12}\right)_{\text{Apparent}} - \left(\pi_{12}\right)_{\text{Actual}} \\ &+ \left(-0.005\pi_{12} + 4.9\times10^{-3}\pi_{13}\right)_{\text{Actual}}\end{aligned} \tag{5.7}$$

For VDP sensors, the fundamental piezoresistive coefficients are calculated based on sum and difference between R_0 and R_{90}. Based on the “on-axis” theory, we have

$$\begin{aligned}\frac{\Delta R_0}{R_0} - \frac{\Delta R_{90}}{R_{90}} &= 3.157\left(\pi_{11} - \pi_{12}\right)\sigma'_{11} \\ \frac{\Delta R_0}{R_0} + \frac{\Delta R_{90}}{R_{90}} &= \left(\pi_{11} + \pi_{12}\right)\sigma'_{11}\end{aligned} \tag{5.8}$$

Similarly, the piezoresistive coefficients we extracted from the experiment are the apparent values.

$$
\begin{aligned}
&\frac{(\frac{\Delta R_0}{R_0}-\frac{\Delta R_{90}}{R_{90}})+3.157(\frac{\Delta R_0}{R_0}+\frac{\Delta R_{90}}{R_{90}})}{6.314}=(\pi_{11})_{\text{Apparent}}\,\sigma'_{11}=\pi^*_{11}\sigma'_{11} \\
&\frac{3.157(\frac{\Delta R_0}{R_0}+\frac{\Delta R_{90}}{R_{90}})-(\frac{\Delta R_0}{R_0}-\frac{\Delta R_{90}}{R_{90}})}{6.314\sigma}=(\pi_{12})_{\text{Apparent}}\,\sigma'_{11}=\pi^*_{12}\sigma'_{11}
\end{aligned}
\tag{5.9}
$$

Substitution of π^*_{11} and π^*_{12} into Eq. 5.9 leads to

$$
\begin{aligned}
(\pi_{11})_{\text{Error}} &= (\pi_{11})_{\text{Apparent}}-(\pi_{11})_{\text{Actual}} \\
&= \begin{pmatrix} -0.01\pi_{11}+4.8\times10^{-3}(\pi_{13}+\pi_{31}) \\ +2.4\times10^{-5}\pi_{33}+9.7\times10^{-3}\pi_{44} \end{pmatrix}_{\text{Actual}} \\
(\pi_{12})_{\text{Error}} &= (\pi_{12})_{\text{Apparent}}-(\pi_{12})_{\text{Actual}} \\
&\quad +\left(-0.005\pi_{12}+4.9\times10^{-3}\pi_{13}\right)_{\text{Actual}}
\end{aligned}
\tag{5.10}
$$

Likewise, the impact of the tilted wafer plane on hydrostatic calibration can be evaluated. When the triaxial stress (-p) is applied to the VDP, the normalized resistance change is

$$
\frac{\Delta R_0}{R_0}=-p(\pi_{11}+\pi_{12}+\pi_{13}) \tag{5.11}
$$

For the tilted wafer plane,

$$
(\pi_{13})_{\text{Apparent}}=-\frac{1}{p}\left(\frac{\Delta R_0}{R_0}\right)_{\text{off-axis}}-(\pi_{11}+\pi_{12})_{\text{Apparent}} \tag{5.12}
$$

Thus,

$$
\begin{aligned}
(\pi_{13})_{\text{Error}} &= (\pi_{13})_{\text{Apparent}}-(\pi_{13})_{\text{Actual}} \\
&= \begin{pmatrix} 4.8\times10^{-3}\pi_{11}-0.005\pi_{13}+2.4\times10^{-5}\pi_{31} \\ +4.8\times10^{-3}\pi_{33}-9.7\times10^{-3}\pi_{44} \end{pmatrix}_{\text{Actual}}
\end{aligned}
\tag{5.13}
$$

It can be seen that the errors induced by off-axis wafer are highly dependent on the piezoresistive coefficient values. If all the piezoresistive coefficients are in the same size, the difference between apparent and actual values should be negligible as the coefficients of all additional terms are pretty small. Comparing Eq. 5.7 and Eq. 5.10, the off-axis wafers have the exactly same impact on resistor rosettes and VDP device during the calibration, even though the VDP sensors provides a more than three times higher sensitivity than resistor rosettes.

5.5 Impact of Off-axis Wafers on Measurements

The tilted wafer plane can also affect the accuracy of the stress measurement. Based upon Eq. 5.3, the tilted case indicates additional coupling, particularly from the shear stresses and more fundamental piezoresistive coefficients will be involved in resistance change equations. Take four-element resistor rosettes (Fig. 3.4) as an example, the normalized resistance change of the "off-axis" resistive sensors can be calculated by expanding Eq. 3.5:

$$
\begin{aligned}
\frac{\Delta R_1}{R_1} &= \pi^*_{11}\sigma'_{11} + \pi^*_{12}\sigma'_{22} + \pi^*_{13}\sigma'_{33} + \pi^*_{14}\sigma'_{13} + \pi^*_{15}\sigma'_{23} + \pi^*_{16}\sigma'_{12} + \alpha\Delta T \\
\frac{\Delta R_2}{R_2} &= \pi^*_{21}\sigma'_{11} + \pi^*_{22}\sigma'_{22} + \pi^*_{23}\sigma'_{33} + \pi^*_{24}\sigma'_{13} + \pi^*_{25}\sigma'_{23} + \pi^*_{26}\sigma'_{12} + \alpha\Delta T \\
\frac{\Delta R_3}{R_3} &= (\frac{1}{2}\pi^*_{11} + \frac{1}{2}\pi^*_{21} + \pi^*_{61})\sigma'_{11} + (\frac{1}{2}\pi^*_{12} + \frac{1}{2}\pi^*_{22} + \pi^*_{62})\sigma'_{22} + (\frac{1}{2}\pi^*_{13} + \frac{1}{2}\pi^*_{23} + \pi^*_{63})\sigma'_{33} \\
&\quad + (\frac{1}{2}\pi^*_{14} + \frac{1}{2}\pi^*_{24} + \pi^*_{64})\sigma'_{13} + (\frac{1}{2}\pi^*_{15} + \frac{1}{2}\pi^*_{25} + \pi^*_{65})\sigma'_{23} + (\frac{1}{2}\pi^*_{16} + \frac{1}{2}\pi^*_{26} + \pi^*_{66})\sigma'_{12} + \alpha\Delta T \\
\frac{\Delta R_4}{R_4} &= (\frac{1}{2}\pi^*_{11} + \frac{1}{2}\pi^*_{21} - \pi^*_{61})\sigma'_{11} + (\frac{1}{2}\pi^*_{12} + \frac{1}{2}\pi^*_{22} - \pi^*_{62})\sigma'_{22} + (\frac{1}{2}\pi^*_{13} + \frac{1}{2}\pi^*_{23} - \pi^*_{63})\sigma'_{33} \\
&\quad + (\frac{1}{2}\pi^*_{14} + \frac{1}{2}\pi^*_{24} - \pi^*_{64})\sigma'_{13} + (\frac{1}{2}\pi^*_{15} + \frac{1}{2}\pi^*_{25} - \pi^*_{65})\sigma'_{23} + (\frac{1}{2}\pi^*_{16} + \frac{1}{2}\pi^*_{26} - \pi^*_{66})\sigma'_{12} + \alpha\Delta T
\end{aligned}
\tag{5.14}
$$

Eq. 5.15 compares the normalized resistance change of "on-axis" and "off-axis" resistive sensors. It can be seen that the stress sensors fabricated on the tilted wafer plane are sensitive to more stress components, especially the shear stresses. The resistors R_1 and R_2 are sensitive to out-of-plane shear stress σ'_{13} and R_3 and R_4 are sensitive to all shear stress components. As shown in Eq. 5.16, the normalized resistance change equations for off-axis case can be rewritten as the sum of the on-axis terms and additional correction terms which are generated by the tilted wafer plane. For the untilted case, only π_{11} and π_{12} are required to measure the normal stress difference $(\sigma'_{11} - \sigma'_{22})$ and shear stress σ'_{12} as other terms can be cancelled by combining the resistor changes. In contrast for the tilted case, all six fundamental piezoresistive coefficients are present and can't be cancelled. Additionally, the magnitudes of errors are not only dependent on the values of piezoresistive coefficients but also on the stress distributions. It is possible to evaluate the measurement errors induced by the tilted wafer plane with finite element method if all fundamental piezoresistive coefficients are known. For 4H-SiC, not all fundamental piezoresistive coefficients are measured and available in literatures. But even so, we can still roughly estimate the errors from the resistance change equations.

$$
\begin{aligned}
\left(\frac{\Delta R_1}{R_1}\right)_{on-axis} &= \pi_{11}\sigma'_{11} + \pi_{12}\sigma'_{22} + \pi_{13}\sigma'_{33} + \alpha\Delta T \\
\left(\frac{\Delta R_1}{R_1}\right)_{off-axis} &= \left(0.99\pi_{11} + 4.8\times10^{-3}(\pi_{13}+\pi_{31}) + 2.4\times10^{-5}\pi_{33} + 9.7\times10^{-3}\pi_{44}\right)\sigma'_{11} \\
&\quad +\left(0.99\pi_{12} + 4.9\times10^{-3}\pi_{31}\right)\sigma'_{22} \\
&\quad +\left(0.99\pi_{13} + 4.8\times10^{-3}(\pi_{11}+\pi_{33}) + 2.4\times10^{-5}\pi_{31} - 9.7\times10^{-3}\pi_{44}\right)\sigma'_{33} \\
&\quad +\left(0.14\left(\pi_{13}+\pi_{44}-\pi_{11}\right) + 6.8\times10^{-4}\left(\pi_{33}-\pi_{13}\right)\right)\sigma'_{13} + \alpha\Delta T \\
\left(\frac{\Delta R_2}{R_2}\right)_{on-axis} &= \pi_{12}\sigma'_{11} + \pi_{11}\sigma'_{22} + \pi_{13}\sigma'_{33} + \alpha\Delta T \\
\left(\frac{\Delta R_2}{R_2}\right)_{off-axis} &= \left(0.99\pi_{12} + 4.9\times10^{-3}\pi_{13}\right)\sigma'_{11} \\
&\quad +\pi_{11}\sigma'_{22} + \left(0.99\pi_{13} + 4.9\times10^{-3}\pi_{12}\right)\sigma'_{33} \\
&\quad +\left(0.14\left(\pi_{13}-\pi_{12}\right)\right)\sigma'_{13} + \alpha\Delta T \\
\left(\frac{\Delta R_3}{R_3}\right)_{on-axis} &= \frac{1}{2}(\pi_{11}+\pi_{12})(\sigma'_{11}+\sigma'_{22}) + \pi_{13}\sigma'_{33} + \pi_D\sigma'_{12} + \alpha\Delta T \\
\left(\frac{\Delta R_3}{R_3}\right)_{off-axis} &= (0.49(\pi_{11}+\pi_{12}) + 4.8\times10^{-3}(\pi_{13}+\pi_{44}) + 2.4\times10^{-3}\pi_{13} + 1.2\times10^{-5}\pi_{33})\sigma'_{11} \\
&\quad +(0.5(\pi_{11}+\pi_{12}) + 2.4\times10^{-3}\pi_{31})\sigma'_{22} \\
&\quad +(2.4\times10^{-3}(\pi_{11}+\pi_{12}+\pi_{33}-2\pi_{44}) + 0.99\pi_{13} + 1.2\times10^{-5}\pi_{31})\sigma'_{33} \\
&\quad +(0.07(-\pi_{11}-\pi_{12}+\pi_{44}) + 0.14\pi_{13} + 3.4\times10^{-4}(\pi_{33}-\pi_{31}))\sigma'_{13} \\
&\quad +(0.07(-\pi_{11}+\pi_{12}+\pi_{44}))\sigma'_{23} + (0.99(\pi_{11}-\pi_{12}) + 4.8\times10^{-3}\pi_{44})\sigma'_{12} + \alpha\Delta T \\
\left(\frac{\Delta R_4}{R_4}\right)_{on-axis} &= \frac{1}{2}(\pi_{11}+\pi_{12})(\sigma'_{11}+\sigma'_{22}) + \pi_{13}\sigma'_{33} - \pi_D\sigma'_{12} + \alpha\Delta T \\
\left(\frac{\Delta R_4}{R_4}\right)_{off-axis} &= (0.49(\pi_{11}+\pi_{12}) + 4.8\times10^{-3}(\pi_{13}+\pi_{44}) + 2.4\times10^{-3}\pi_{13} + 1.2\times10^{-5}\pi_{33})\sigma'_{11} \\
&\quad +(0.5(\pi_{11}+\pi_{12}) + 2.4\times10^{-3}\pi_{31})\sigma'_{22} \\
&\quad +(2.4\times10^{-3}(\pi_{11}+\pi_{12}+\pi_{33}-2\pi_{44}) + 0.99\pi_{13} + 1.2\times10^{-5}\pi_{31})\sigma'_{33} \\
&\quad +(0.07(-\pi_{11}-\pi_{12}+\pi_{44}) + 0.14\pi_{13} + 3.4\times10^{-4}(\pi_{33}-\pi_{31}))\sigma'_{13} \\
&\quad +(0.07(\pi_{11}-\pi_{12}-\pi_{44}))\sigma'_{23} + (0.99(-\pi_{11}+\pi_{12}) - 4.8\times10^{-3}\pi_{44})\sigma'_{12} + \alpha\Delta T
\end{aligned}
\tag{5.15}
$$

$$
\begin{aligned}
\left(\frac{\Delta R_1}{R_1}-\frac{\Delta R_2}{R_2}\right)_{On-axis} &= (\pi_{11}-\pi_{12})(\sigma'_{11}-\sigma'_{22}) \\
\left(\frac{\Delta R_1}{R_1}-\frac{\Delta R_2}{R_2}\right)_{Off-axis} &= \left(\frac{\Delta R_1}{R_1}-\frac{\Delta R_2}{R_2}\right)_{On-axis} \\
&+[\left(-0.01\pi_{11}+0.005\pi_{12}-2.4\times10^{-5}(-\pi_{13}+\pi_{33})+4.8\times10^{-3}\pi_{31}+9.7\times10^{-3}\pi_{44}\right)\sigma'_{11} \\
&+\left(0.005\pi_{12}+4.9\times10^{-3}\pi_{31}\right)\sigma'_{22} \\
&+\left(4.8\times10^{-3}(\pi_{11}-\pi_{12}-\pi_{13}+\pi_{33})+2.4\times10^{-5}\pi_{31}-9.7\times10^{-3}\pi_{44}\right)\sigma'_{33} \\
&+\left(0.14(-\pi_{11}+\pi_{12}+\pi_{44})+6.8\times10^{-4}(-\pi_{13}-\pi_{31}+\pi_{33})\right)\sigma'_{13}]_{Correction} \\
\left(\frac{\Delta R_3}{R_3}-\frac{\Delta R_4}{R_4}\right)_{On-axis} &= 2(\pi_{11}-\pi_{12})\sigma'_{12} \\
\left(\frac{\Delta R_3}{R_3}-\frac{\Delta R_4}{R_4}\right)_{Off-axis} &= \left(\frac{\Delta R_3}{R_3}-\frac{\Delta R_4}{R_4}\right)_{On-axis} \\
&+[0.14(-\pi_{11}+\pi_{12}+\pi_{44})\sigma'_{23} \\
&+\left(-0.01(\pi_{11}-\pi_{12})+9.7\times10^{-3}\pi_{44}\right)\sigma'_{12}]_{Correction}
\end{aligned}
\quad (5.16)
$$

In Eq. 5.16, The coefficients of correction terms are very small except the red ones for the shear stress components σ'_{13} and σ'_{23}. Considering the in-plane piezoresistive coefficients π_{11} and π_{12} have similar magnitude and opposite sign, the red correction terms are mainly determined by the value of π_{44} and the shear stress level. In most high-temperature electronic packages (hermetically sealed ceramic packages for example), the top surface of the chip is the free surface which means all out-of-plane stress components are zero and the overall magnitude of the error terms are expected to be relatively small. However, the overall accuracy of measurements is dependent on the piezoresistive coefficient values (doping dependent) and stress distributions which depends on packing technique and operation environment. Even though piezoresistive coefficients π_{31}, π_{33} and π_{44} are not required for stress measurements, it is still worth to explore their values in order to more accurately evaluate the off-axis wafer induced errors.

5.5 Summary

In this chapter, errors in piezoresistive coefficients caused by a 4° off-axis wafer plane has been discussed. We developed expressions and compared the piezoresistive coefficients changes introduced by tilted wafer plane. Calibration errors for resistive rosette and VDP device were discussed. Calibration errors for resistor rosette and van der Pauw device were discussed. It has been found that even if the VDP sensors can provide more than three times sensitivity to the $(\sigma'_{11} - \sigma'_{12})$ and σ'_{12} stress terms than resistive rosette, the error values are exactly same for both sensors during the calibration. piezoresistive coefficient changes introduced by tilted wafer plane. The resistance change equations for a four-element rosette on the tilted wafer plane are developed. It has been demonstrated that the accuracy of the measurement is strongly dependent on the piezoresistive coefficient values (doping dependent) and stress distributions in the SiC die. The coefficients of additional correction terms are relatively small which makes the measurement errors tend to be small as well. If the five fundamental piezoresistive coefficients are in the same size, the errors induced by tilted wafer plane would not be significant to stress measurement and calibration. More accurate error evaluation requires values for all fundamental piezoresistive coefficients.

Chapter 6

EVALUATION OF IMPACT OF FOUR-DEGREE OFF-AXIS WAFERS ON SILICON STRESS SENSORS

6.1 Introduction

Not only 4H-SiC but also silicon wafers are produced by cutting an on-axis crystal at an appropriate angle [104]-[106]. Since silicon wafers do not have the polytype mixing issue, the major reason is that high quality III-V semiconductor materials can be directly grown on the off-axis wafers. Therefore, the III-V devices can be integrated on silicon substrate and it would tremendously increase the functionality of the chip [107]-[110]. Silicon wafers with misorientation angle of 4 to 6 degrees are mostly used to reduce the mismatch between silicon and III-V lattices.

This section will discuss the theory and review the coordinate transformation for the piezoresistive coefficients of silicon. The piezoresistive coefficients for the 4 degrees off-axis wafer plane are evaluated and compared with the on-axis case. Since all piezoresistive coefficients of silicon are known, a case study is conducted to evaluate the error values by using the finite element simulation.

6.2 Review of Basic Equations

(a) (100) Silicon

As depicted in Fig. 6.1, the surface of the wafer is a (100) plane, and the unprimed axes are the crystallographic axes of the silicon. It is more convenient to work in a chip

coordinate system, thus, an off-axis primed wafer coordinate system was defined where the x'_2 and x'_1 axes are parallel and perpendicular to the primary wafer flat [29].

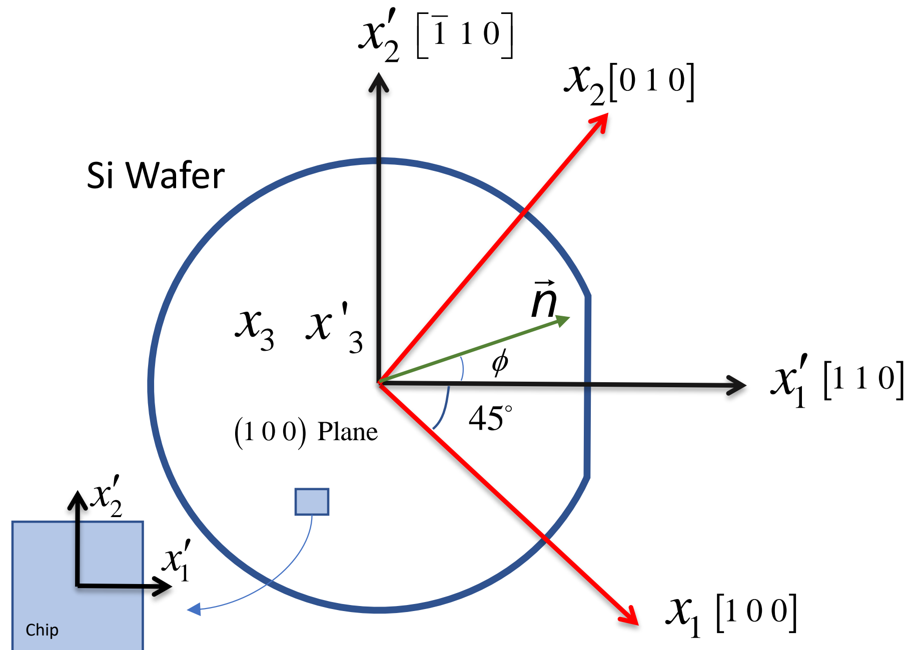

Figure 6.1: Wafer Coordinate System on the (001) Silicon

Eq. 6.1 is the piezoresistive coefficient matrix in an unprimed crystallographic coordinate system. To work in a wafer coordinate system, the 36 off-axis piezoresistive coefficients must be evaluated using coordinate transformation. For (100) silicon, the primed wafer coordinate system is 45° from the principal crystallographic axes as shown in Fig. 6.1, and the corresponding direction cosines are shown in Eq. 6.2. Since silicon has cubic crystal structure, based upon crystal symmetry, it only has 3 independent piezoresistive coefficients as shown in Eq. 6.1. From Eq. 6.1 and Eq. 6.2, the piezoresistive coefficients in the wafer coordinate system can be obtained, and substitution of these off-

axis coefficients into Eq. 3.5 yields Eq. 6.3 which can be used to evaluate normalized resistance change in any in-plane directions.

$$\left[\pi_{\alpha\beta}\right]=\begin{bmatrix}\pi_{11} & \pi_{12} & \pi_{12} & 0 & 0 & 0\\ \pi_{12} & \pi_{11} & \pi_{12} & 0 & 0 & 0\\ \pi_{12} & \pi_{12} & \pi_{11} & 0 & 0 & 0\\ 0 & 0 & 0 & \pi_{44} & 0 & 0\\ 0 & 0 & 0 & 0 & \pi_{44} & 0\\ 0 & 0 & 0 & 0 & 0 & \pi_{44}\end{bmatrix} \tag{6.1}$$

$$\left[a_{ij}\right]=\begin{bmatrix}l_1 & m_1 & n_1\\ l_2 & m_2 & n_2\\ l_3 & m_3 & n_3\end{bmatrix}=\begin{bmatrix}\frac{1}{\sqrt{2}} & \frac{1}{\sqrt{2}} & 0\\ -\frac{1}{\sqrt{2}} & \frac{1}{\sqrt{2}} & 0\\ 0 & 0 & 1\end{bmatrix} \tag{6.2}$$

$$\begin{aligned}\frac{\Delta R}{R}=&\left[\left(\frac{\pi_{11}+\pi_{12}+\pi_{44}}{2}\right)\sigma'_{11}+\left(\frac{\pi_{11}+\pi_{12}-\pi_{44}}{2}\right)\sigma'_{22}\right]\cos^2\phi\\ &+\left[\left(\frac{\pi_{11}+\pi_{12}-\pi_{44}}{2}\right)\sigma'_{11}+\left(\frac{\pi_{11}+\pi_{12}+\pi_{44}}{2}\right)\sigma'_{22}\right]\sin^2\phi\\ &+\pi_{12}\sigma'_{33}+\left(\pi_{11}-\pi_{12}\right)\sigma'_{12}\sin 2\phi+\alpha\Delta T\end{aligned} \tag{6.3}$$

where ϕ is the angle between the x'_1 axis and the resistor orientation.

(b) (111) Silicon

Fig. 6.2 shows a general (111) silicon wafer. The surface of the wafer is a (111) plane, and the [111] direction is normal to the wafer plane. The principal crystallographic axes are not indicated as they no longer lie in the wafer plane. The off-axis primed wafer

coordinate system is defined in a manner similar to (100) silicon. The underlying piezoresistive coefficients in Eq. 6.1 are still valid for (111) silicon and the piezoresistive coefficients in the primed wafer coordinate system can be evaluated by using the same coordinate transformation method but with different direction cosines. In this case, the appropriate direction cosines for the primed coordinate directions with respect to unprimed coordinate directions are shown in Eq. 6.4. Substitution of the piezoresistive coefficients into Eq. 3.5 yields Eq. 6.5 [29].

$$\left[a_{ij}\right] = \begin{bmatrix} l_1 & m_1 & n_1 \\ l_2 & m_2 & n_2 \\ l_3 & m_3 & n_3 \end{bmatrix} = \begin{bmatrix} -\frac{1}{\sqrt{2}} & \frac{1}{\sqrt{2}} & 0 \\ -\frac{1}{\sqrt{6}} & -\frac{1}{\sqrt{6}} & \frac{2}{\sqrt{6}} \\ \frac{1}{\sqrt{3}} & \frac{1}{\sqrt{3}} & \frac{1}{\sqrt{3}} \end{bmatrix} \tag{6.4}$$

$$\begin{aligned} \frac{\Delta R}{R} = & \left[B_1\sigma'_{11} + B_2\sigma'_{22} + B_3\sigma'_{33} + 2\sqrt{2}(B_2 - B_3)\sigma'_{23}\right]\cos^2\phi \\ & + \left[B_2\sigma'_{11} + B_1\sigma'_{22} + B_3\sigma'_{33} - 2\sqrt{2}(B_2 - B_3)\sigma'_{23}\right]\sin^2\phi \\ & + \left[2\sqrt{2}\left(B_2 - B_3\right)\sigma'_{13} + \left(B_1 - B_2\right)\sigma'_{12}\right]\sin 2\phi + \alpha\Delta T \end{aligned} \tag{6.5}$$

where ϕ is the angle between the x'_1 axis and the resistor orientation. B_1, B_2 and B_3 are combined piezoresistive parameters as shown in Eq. 6.6.

$$
\begin{aligned}
B_1 &= \frac{\pi_{11} + \pi_{12} + \pi_{44}}{2} \\
B_2 &= \frac{\pi_{11} + 5\pi_{12} - \pi_{44}}{6} \\
B_3 &= \frac{\pi_{11} + 2\pi_{12} - \pi_{44}}{3}
\end{aligned}
\tag{6.6}
$$

For both (001) and (111) silicon, the piezoresistive coefficients in wafer coordinate system (Untilted wafer plane) appear in Fig. 6.7.

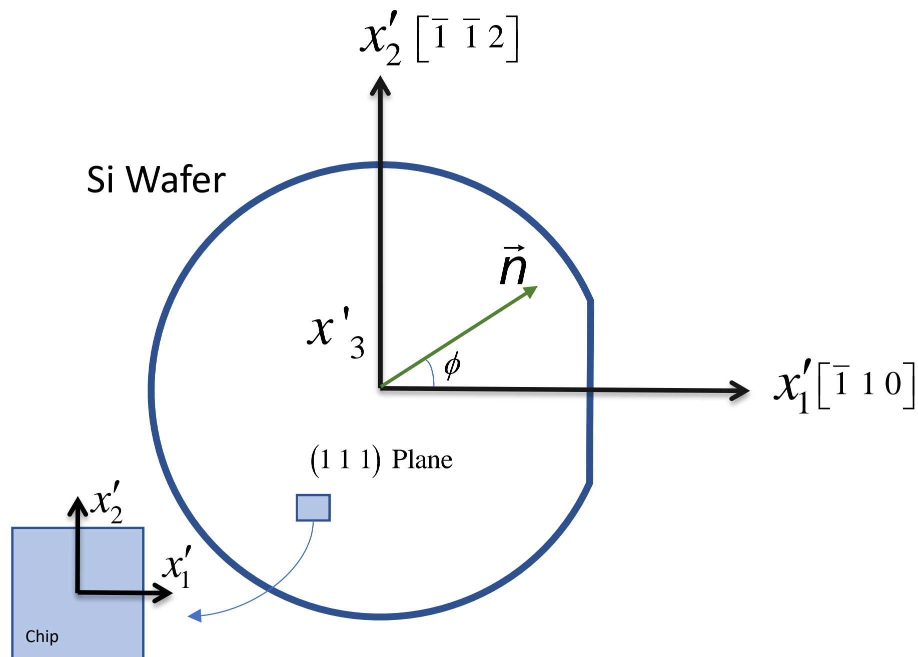

Figure 6.2: Wafer Coordinate System on the (111) Silicon

6.3 Off-axis Wafer Plane Errors

In the above analyses, the wafer surface was assumed to be perfectly aligned with the crystallographic axes, whereas it is often tilted several degrees from its intended

orientation. Thus, errors will be present in the utilized theoretical equations. In this study, the four-degree off-axis wafers are discussed.

(a) (100) Silicon

For (100) silicon, the untilted and tilted wafer planes are shown in Fig. 6.3 and Fig. 6.4. In Fig. 6.3, the primed wafer coordinate system is formed by rotating the unprimed crystallographic axes 45 degrees about the x_3 axis, so that the x'_1 and x'_2 axes are oriented in the directions parallel and perpendicular to the primary wafer flat, while the x'_3 and x_3 axes are coincident and normal to the wafer surface. Fig. 6.2 offers the 2D view of primed and unprimed coordinate systems.

In the tilted wafer plane (Fig. 6.4), the x_1^* and x_2^* axes are oriented along the directions parallel and perpendicular to the wafer flat of a tilted wafer, whereas the x_3^* direction is normal to the tilted wafer plane. The $x_1^* - x_2^* - x_3^*$ axes are obtained from the unprimed axes by first rotating about the x_3 axis through an angle of 45 degrees and then rotating about the x'_2 through an angle of 4 degrees. Therefore, the piezoresistive coefficients in tilted wafer coordinate system ($x_1^* - x_2^* - x_3^*$) can be evaluated using transformation with respect to π'-matrix and the appropriate direction cosines:

$$\left[a_{ij}\right] = \begin{bmatrix} l_1 & m_1 & n_1 \\ l_2 & m_2 & n_2 \\ l_3 & m_3 & n_3 \end{bmatrix} = \begin{bmatrix} \cos(4^\circ) & 0 & \cos(86^\circ) \\ 0 & 1 & 0 \\ \cos(94^\circ) & 0 & \cos(4^\circ) \end{bmatrix} \quad (6.7)$$

Substitution of Eq. 6.4 and Eq. 6.7 into Eq. 3.3 leads to the transformation matrices [T] and [T*]. The piezoresistive coefficients in the tilted wafer plane [π*] can be expressed using:

$$\begin{aligned}\left[\pi^*\right] &= \left[T^*\right]\left[\pi'\right]\left[T^*\right]^{-1} \\ &= \left[T^*\right]\left[T\right]\left[\pi\right]\left[T\right]^{-1}\left[T^*\right]^{-1}\end{aligned} \tag{6.8}$$

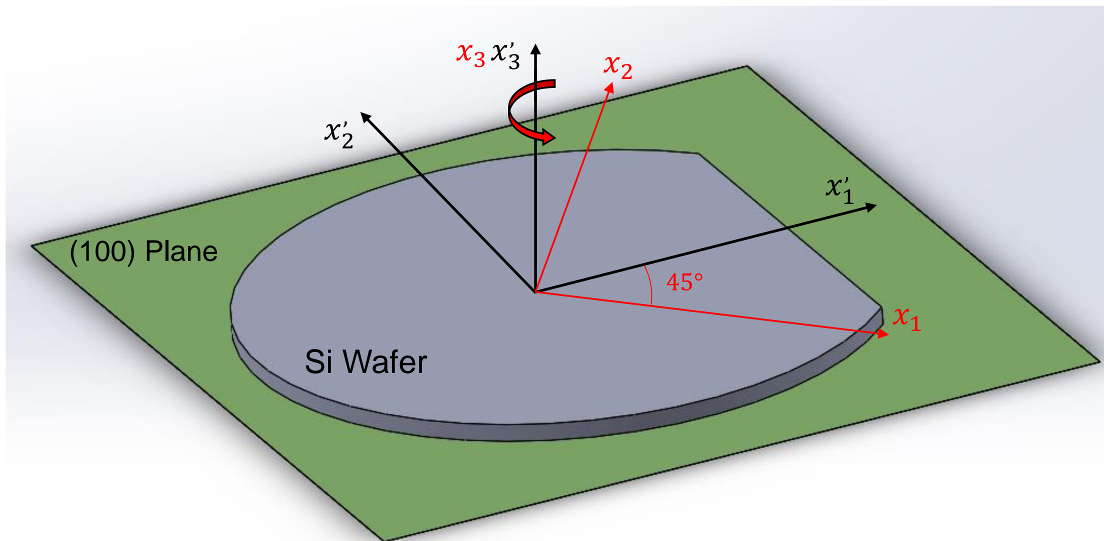

Figure 6.3: Untilted Wafer Plane for (100) Silicon

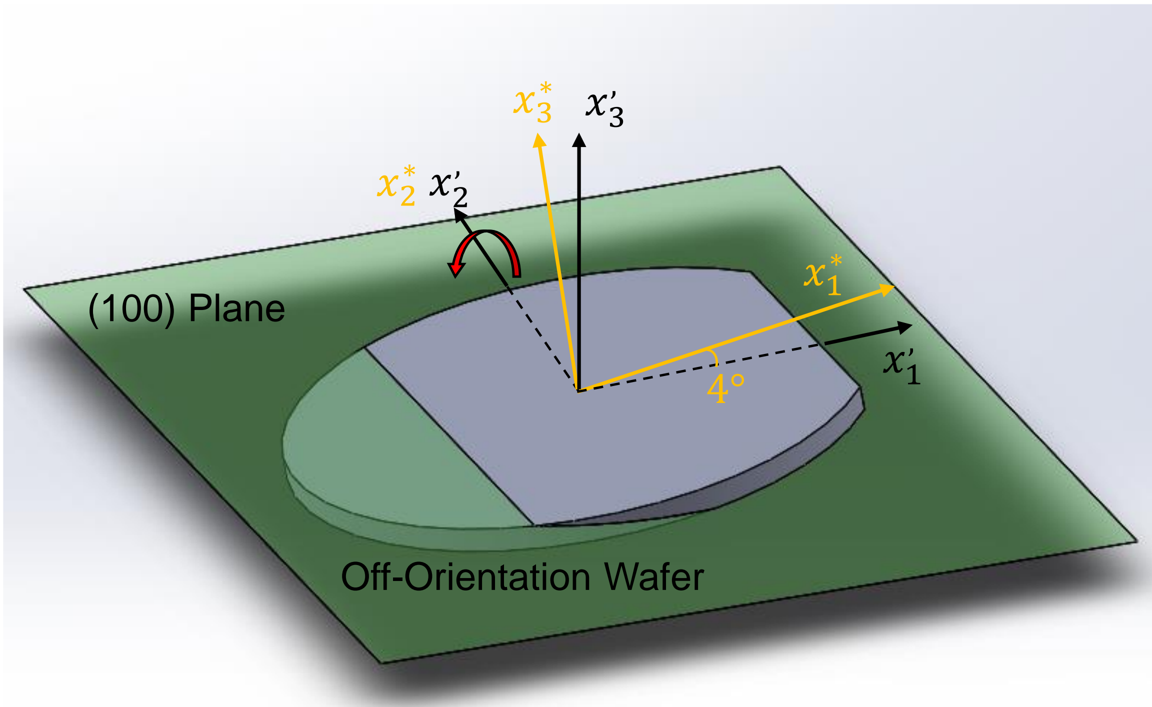

Figure 6.4: Tilted Wafer Plane for (100) Silicon

(b) (111) Silicon

Fig. 6.5 and Fig. 6.6 display the untilted and tilted wafer planes. The unprimed crystallographic axes and primed wafer coordinate system are shown in Fig. 6.5. Again, the tilted wafer coordinate system is obtained from the primed axes by rotating x'_2 axis through an angle of 4 degrees. In this case, the piezoresisitive coefficients in the tilted wafer coordinate system ([π*]-matrix) can be calculated by substituting the [π']-matrix for (111) silicon into Eq. 6.8, and the direction cosines for the untilted and tilted wafer coordinate system are in Eq. 6.7. For both (100) and (111), the calculated piezoresistive coefficients matrices for tilted and untilted wafer planes appear in Fig. 6.7.

Comparing the π matrix in the untilted and tilted cases in Fig. 6.7 for the (100) case, it can be observed that many of the elements of the ideal on-axis -matrices are zero, whereas in the off-axis version all the original matrix elements are modified and a number of additional elements are no longer zero. For the (111) case, all of the original coefficients are changed and there are no longer any zero valued elements. The tilted cases both indicate additional coupling, particularly from shear stresses.

For these non-zero on-axis [π'] elements, the corresponding elements in [π*] matrix have more fundamental piezoresistive coefficients π_{ij} involved. It is hard to evaluate the impact of off-axis wafer by comparing the coefficients in [π'] and [π*] directly as the difference of each element would be highly dependent on the individual values of fundamental piezoresistive coefficients π_{ij}. For example, $\pi_D = \pi_{11} - \pi_{12}$ is large for n-type material whereas π_{44} is large for p-type silicon. Thus, a case study on plastic ball grid array (PBGA) package is conducted to better illustrate the impact of the off-axis wafer on stress measurements.

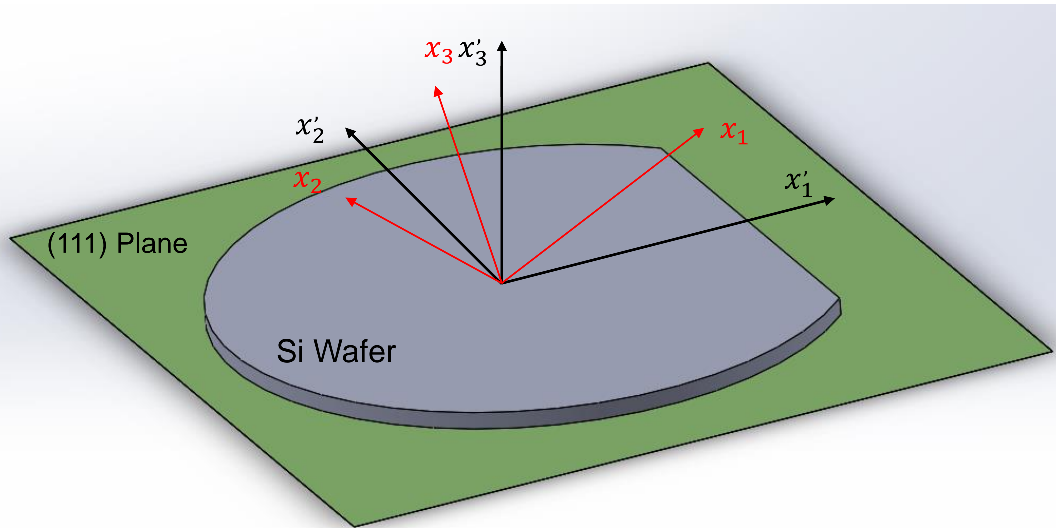

Figure 6.5: Untilted Wafer Plane for (111) Silicon

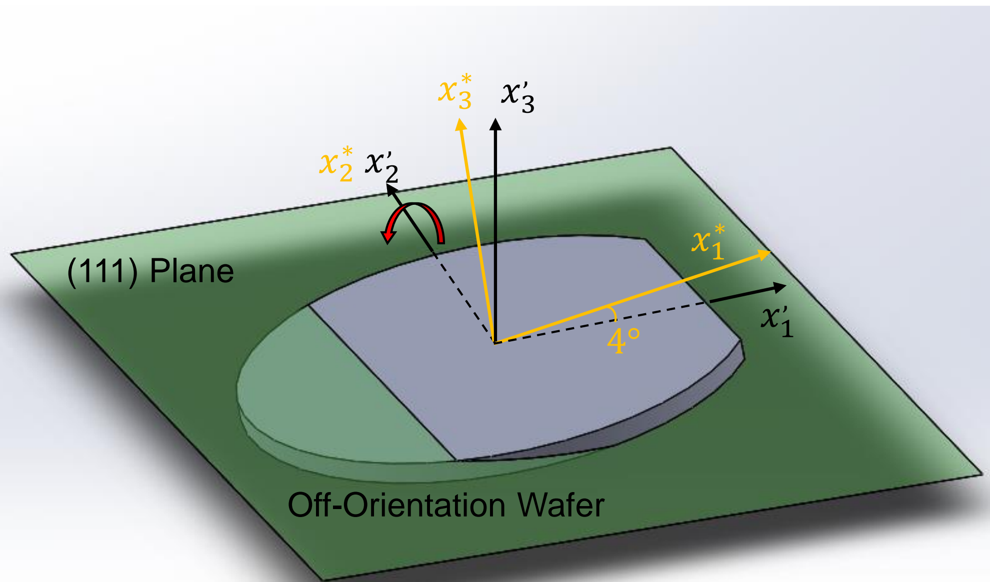

Figure 6.6: Tilted Wafer Plane for (111) Silicon

[π′] – Matrices for (100) Silicon

$$[\pi'] = \begin{bmatrix} 0.5(\pi_{11}+\pi_{12}+\pi_{44}) & 0.5(\pi_{11}+\pi_{12}-\pi_{44}) & \pi_{12} & 0 & 0 & 0 \\ 0.5(\pi_{11}+\pi_{12}-\pi_{44}) & 0.5(\pi_{11}+\pi_{12}+\pi_{44}) & \pi_{12} & 0 & 0 & 0 \\ \pi_{12} & \pi_{12} & \pi_{11} & 0 & 0 & 0 \\ 0 & 0 & 0 & \pi_{44} & 0 & 0 \\ 0 & 0 & 0 & 0 & \pi_{44} & 0 \\ 0 & 0 & 0 & 0 & 0 & \pi_{11}-\pi_{12} \end{bmatrix}$$

[π*] – Matrices for (100) Silicon

$$[\pi^*] = \begin{bmatrix} 0.495\pi_{11}+0.505(\pi_{12}+\pi_{44}) & 0.498(\pi_{11}-\pi_{44})+0.502\pi_{12} & 0.007(\pi_{11}-\pi_{44})+0.993\pi_{12} & 0.069(-\pi_{11}+\pi_{12}+\pi_{44}) & 0 & 0 \\ 0.498(\pi_{11}-\pi_{44})+0.502\pi_{12} & 0.5(\pi_{11}+\pi_{12}+\pi_{44}) & 0.002(\pi_{11}-\pi_{44})+0.998\pi_{12} & 0.070(-\pi_{11}+\pi_{12}+\pi_{44}) & 0 & 0 \\ 0.007(\pi_{11}-\pi_{44})+0.993\pi_{12} & 0.002(\pi_{11}-\pi_{44})+0.998\pi_{12} & 0.993\pi_{11}+0.010(\pi_{12}+\pi_{44}) & 0.138(\pi_{11}-\pi_{12}-\pi_{44}) & 0 & 0 \\ 0.034(-\pi_{11}+\pi_{12}+\pi_{44}) & 0.035(-\pi_{11}+\pi_{12}+\pi_{44}) & 0.691(\pi_{11}-\pi_{12}-\pi_{44}) & 0.015(\pi_{11}-\pi_{12})+0.985\pi_{44} & 0 & 0 \\ 0 & 0 & 0 & 0 & 0.049(\pi_{11}-\pi_{12})+0.995\pi_{44} & 0.070(-\pi_{11}+\pi_{12}+\pi_{44}) \\ 0 & 0 & 0 & 0 & 0.070(-\pi_{11}+\pi_{12}+\pi_{44}) & 0.995(\pi_{11}-\pi_{12})+0.005\pi_{44} \end{bmatrix}$$

[π′] – Matrices for (111) Silicon

$$[\pi^*] = \begin{bmatrix} 0.5(\pi_{11}+\pi_{12}+\pi_{44}) & 0.167(\pi_{11}-\pi_{44})+0.833\pi_{12} & 0.333(\pi_{11}-\pi_{44})+0.667\pi_{12} & 0 & 0.471(-\pi_{11}+\pi_{12}+\pi_{44}) & 0 \\ 0.167(\pi_{11}-\pi_{44})+0.833\pi_{12} & 0.5(\pi_{11}+\pi_{12}+\pi_{44}) & 0.333(\pi_{11}-\pi_{44})+0.667\pi_{12} & 0 & 0.471(\pi_{11}-\pi_{12}-\pi_{44}) & 0 \\ 0.333(\pi_{11}-\pi_{44})+0.667\pi_{12} & 0.333(\pi_{11}-\pi_{44})+0.667\pi_{12} & 0.333\pi_{11}+0.667(\pi_{12}+\pi_{44}) & 0 & 0 & 0 \\ 0 & 0 & 0 & 0.667(\pi_{11}-\pi_{12})+0.333\pi_{44} & 0 & 0.471(-\pi_{11}+\pi_{12}+\pi_{44}) \\ 0.236(-\pi_{11}+\pi_{12}+\pi_{44}) & 0.236(\pi_{11}-\pi_{12}-\pi_{44}) & 0 & 0 & 0.667(\pi_{11}-\pi_{12})+0.333\pi_{44} & 0 \\ 0 & 0 & 0 & 0.471(-\pi_{11}+\pi_{12}+\pi_{44}) & 0 & 0.333(\pi_{11}-\pi_{12})+0.667\pi_{44} \end{bmatrix}$$

[π*] – Matrices for (111) Silicon

$$[\pi^*] = \begin{bmatrix} 0.505\pi_{11}+0.495(\pi_{12}+\pi_{44}) & 0.167(\pi_{11}-\pi_{44})+0.832\pi_{12} & 0.328(\pi_{11}-\pi_{44})+0.672\pi_{12} & 0.069(\pi_{11}-\pi_{12}-\pi_{44}) & 0.463(-\pi_{11}+\pi_{12}+\pi_{44}) & 0.098(-\pi_{11}+\pi_{12}+\pi_{44}) \\ 0.167(\pi_{11}-\pi_{44})+0.832\pi_{12} & 0.5(\pi_{11}+\pi_{12}+\pi_{44}) & 0.333(\pi_{11}-\pi_{44})+0.667\pi_{12} & 0.023(\pi_{11}-\pi_{12}-\pi_{44}) & 0.470(\pi_{11}-\pi_{12}-\pi_{44}) & 0.033(\pi_{11}-\pi_{12}-\pi_{44}) \\ 0.327(\pi_{11}-\pi_{44})+0.672\pi_{12} & 0.333(\pi_{11}-\pi_{44})+0.667\pi_{12} & 0.340\pi_{11}+0.660(\pi_{12}+\pi_{44}) & 0.092(-\pi_{11}+\pi_{12}+\pi_{44}) & 0.007(-\pi_{11}+\pi_{12}+\pi_{44}) & 0.065(\pi_{11}-\pi_{12}-\pi_{44}) \\ 0.034(\pi_{11}-\pi_{12}-\pi_{44}) & 0.012(\pi_{11}-\pi_{12}-\pi_{44}) & 0.046(-\pi_{11}+\pi_{12}+\pi_{44}) & 0.655(\pi_{11}-\pi_{12})+0.345\pi_{44} & 0.065(\pi_{11}-\pi_{12}-\pi_{44}) & 0.463(-\pi_{11}+\pi_{12}+\pi_{44}) \\ 0.232(-\pi_{11}+\pi_{12}+\pi_{44}) & 0.235(\pi_{11}-\pi_{12}-\pi_{44}) & 0.003(-\pi_{11}+\pi_{12}+\pi_{44}) & 0.065(\pi_{11}-\pi_{12}-\pi_{44}) & 0.665(\pi_{11}-\pi_{12})+0.335\pi_{44} & 0.023(\pi_{11}-\pi_{12}-\pi_{44}) \\ 0.049(-\pi_{11}+\pi_{12}+\pi_{44}) & 0.016(\pi_{11}-\pi_{12}-\pi_{44}) & 0.033(\pi_{11}-\pi_{12}-\pi_{44}) & 0.463(-\pi_{11}+\pi_{12}+\pi_{44}) & 0.023(\pi_{11}-\pi_{12}-\pi_{44}) & 0.335(\pi_{11}-\pi_{12})+0.665\pi_{44} \end{bmatrix}$$

Figure 6.7: Piezoresistive Coefficients Matrices for Untilted and Tilted wafer plane.

6.4 A Case Study on Four-element Rosette on (100) Silicon

A four-element dual-polarity sensor rosette on (100) is shown in Fig. 6.8. The rosette contains a 0-90° p-type resistor pair and a ±45° n-type resistor pair. This choice of sensor orientations minimized thermally induced errors as well as those due to resistor misalignment relative to the true compensated measurement of the value of the in-plane normal stress difference ($\sigma'_{11} - \sigma'_{22}$) and the in-plane shear stress σ'_{12} [111].

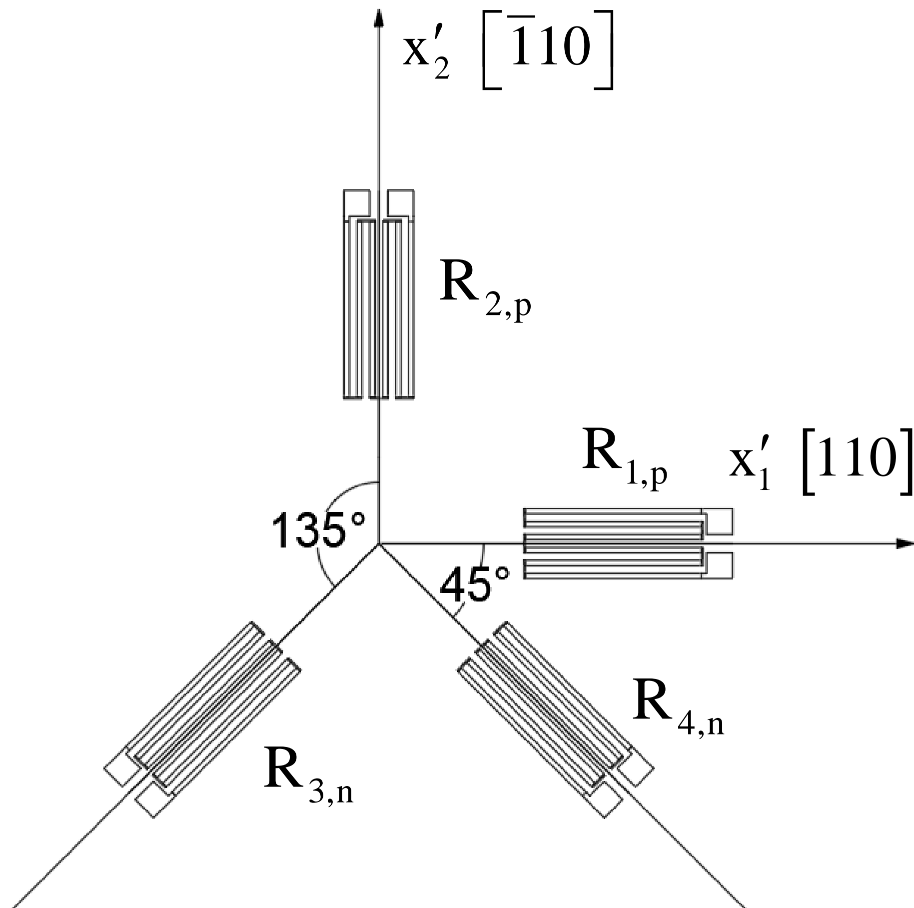

Figure 6.8: Four-Element Rosette on (100) Silicon

For untilted case, the application of Eq. 6.3 gives the following relations between the resistance changes and the stresses at the rosette site:

$$
\begin{aligned}
\frac{\Delta R_1}{R_1} &= \frac{(\pi_{11}^p + \pi_{12}^p + \pi_{44}^p)}{2}\sigma'_{11} + \frac{(\pi_{11}^p + \pi_{12}^p - \pi_{44}^p)}{2}\sigma'_{22} + \pi_{12}^p\sigma'_{33} + \alpha_1^p T \\
\frac{\Delta R_2}{R_2} &= \frac{(\pi_{11}^p + \pi_{12}^p - \pi_{44}^p)}{2}\sigma'_{11} + \frac{(\pi_{11}^p + \pi_{12}^p + \pi_{44}^p)}{2}\sigma'_{22} + \pi_{12}^p\sigma'_{33} + \alpha_1^p T \\
\frac{\Delta R_3}{R_3} &= \frac{(\pi_{11}^n + \pi_{12}^n)}{2}(\sigma'_{11} + \sigma'_{22}) + \pi_D^n\sigma'_{12} + \pi_{12}^n\sigma'_{33} + \alpha_1^n T \\
\frac{\Delta R_4}{R_4} &= \frac{(\pi_{11}^n + \pi_{12}^n)}{2}(\sigma'_{11} + \sigma'_{22}) - \pi_D^n\sigma'_{12} + \pi_{12}^n\sigma'_{33} + \alpha_1^n T
\end{aligned}
\tag{6.9}
$$

Where superscripts n and p are used to denote the piezoresistive coefficients of the n-type and p-type resistors, respectively. Direct combination of the expressions in Eq. 6.9 also leads to the following two temperature compensated resistance stress expressions:

$$
\begin{aligned}
\sigma'_{11} - \sigma'_{22} &= \frac{1}{\pi_{44}^p}\left[\frac{\Delta R_1}{R_1} - \frac{\Delta R_2}{R_2}\right] \\
\sigma'_{12} &= \frac{1}{2\pi_D^n}\left[\frac{\Delta R_3}{R_3} - \frac{\Delta R_4}{R_4}\right]
\end{aligned}
\tag{6.10}
$$

The piezoresistive coefficients needed to solve for the stress components can be measured using a combination of uniaxial and hydrostatic pressure calibration testing. The choice of the n-and p-type material for the four resistors is based upon the values of π_{44}^p and π_D^n in Table 6.1.

Piezoresistive Coefficient	n-type Silicon(TPa)$^{-1}$	p-type silicon(TPa)$^{-1}$
π_{11}	-1022	66
π_{12}	534	-11
π_{44}	-136	1381

Table 6.1: Typical Piezoresistive Coefficient Values for Lightly Doped Silicon (TPa)$^{-1}$

Application of [π*] to the Eq. 3.5 gives the normalized resistance changes in the tilted wafer plane. Eq. 6.11 shows the normalized resistance change equations for both untilted (on-axis) and tilted (off-axis) cases and classic fundamental piezoresistive coefficient values (Table 6.1) at room temperature [24] are used.

$$\left(\frac{\Delta R_1}{R_1}\right)_{on-axis} = 718\sigma'_{11} - 663\sigma'_{22} - 11\sigma'_{33} + \alpha_1^p T$$

$$\left(\frac{\Delta R_1}{R_1}\right)_{off-axis} = 724\sigma'_{11} - 660\sigma'_{22} - 20\sigma'_{33} + 89\sigma'_{13} + \alpha_1^p T$$

$$\left(\frac{\Delta R_2}{R_2}\right)_{on-axis} = -663\sigma'_{11} + 718\sigma'_{22} - 11\sigma'_{33} + \alpha_1^p T$$

$$\left(\frac{\Delta R_2}{R_2}\right)_{off-axis} = -660\sigma'_{11} + 718\sigma'_{22} - 14\sigma'_{33} + 91\sigma'_{13} + \alpha_1^p T$$

$$\left(\frac{\Delta R_3}{R_3}\right)_{on-axis} = -244(\sigma'_{11} - \sigma'_{22}) + 534\sigma'_{33} + 1556\sigma'_{12} + \alpha_2^n T$$

$$\left(\frac{\Delta R_3}{R_3}\right)_{off-axis} = -239\sigma'_{11} - 242\sigma'_{22} + 526\sigma'_{33} + 1549\sigma'_{12} + 98(\sigma'_{13} - \sigma'_{23}) + \alpha_2^n T$$

$$\left(\frac{\Delta R_4}{R_4}\right)_{on-axis} = -244(\sigma'_{11} - \sigma'_{22}) + 534\sigma'_{33} - 1556\sigma'_{12} + \alpha_2^n T$$

$$\left(\frac{\Delta R_4}{R_4}\right)_{off-axis} = -239\sigma'_{11} - 242\sigma'_{22} + 526\sigma'_{33} - 1549\sigma'_{12} + 98(\sigma'_{13} + \sigma'_{23}) + \alpha_2^n T$$

(6.11)

The combination of the expressions in Eq. 6.11 leads to the following resistance-stress expressions.

$$
\begin{aligned}
\left(\frac{\Delta R_1}{R_1}-\frac{\Delta R_2}{R_2}\right)_{on-axis} &= 1381(\sigma'_{11}-\sigma'_{22}) \\
\left(\frac{\Delta R_1}{R_1}-\frac{\Delta R_2}{R_2}\right)_{off-axis} &= 1381\left(\sigma'_{11}-\sigma'_{22}\right)+3\left(\sigma'_{11}+\sigma'_{22}\right)-6\sigma'_{33}-2\sigma'_{13} \\
\left(\frac{\Delta R_3}{R_3}-\frac{\Delta R_4}{R_4}\right)_{on-axis} &= -3112\sigma'_{12} \\
\left(\frac{\Delta R_3}{R_3}-\frac{\Delta R_4}{R_4}\right)_{off-axis} &= -3112\left(\sigma'_{12}\right)+14\left(\sigma'_{12}\right)+196\sigma'_{23}
\end{aligned}
\tag{6.12}
$$

As shown above, for the untilted case, stress components $(\sigma'_{11}-\sigma'_{22})$ and σ'_{12} can be extracted readily in temperature compensated mode if the resistance changes are measured. On the other hand, for the tilted case, these stress components can't be extracted directly in the presence of the shear stresses. In order to evaluate the error induced by tilted wafer plane, the difference between apparent and actual stress are calculated and discussed. Take $(\sigma'_{11}-\sigma'_{22})$ as an example, the measured resistance change was assumed to be $1381(\sigma'_{11}-\sigma'_{22})$ which is defined as the apparent stress. In fact, the measured resistance changes are affected by more stress components as shown in Eq. 6.13 in which apparent (untilted case) and actual stresses (tilted case) are compared.

$$
\begin{aligned}
\left(\frac{\Delta R_1}{R_1}-\frac{\Delta R_2}{R_2}\right)_{measured} &= 1381\left(\sigma'_{11}-\sigma'_{22}\right)_{apparent} \\
&= \left(1381\left(\sigma'_{11}-\sigma'_{22}\right)+3\left(\sigma'_{11}+\sigma'_{22}\right)-6\sigma'_{33}-2\sigma'_{13}\right)_{actual}
\end{aligned}
\tag{6.13}
$$

Based upon Eq. 6.13, the relationship between apparent and actual stresses can be found in Eq. 6.14 and the measurement errors can be expressed using actual stresses as shown in Eq. 6.15.

$$\left(\sigma'_{11}-\sigma'_{22}\right)_{\text{apparent}} = \frac{\left(1381\left(\sigma'_{11}-\sigma'_{22}\right)+3\left(\sigma'_{11}+\sigma'_{22}\right)-6\sigma'_{33}-2\sigma'_{13}\right)_{\text{actual}}}{1381} \tag{6.14}$$

$$\begin{aligned}\left(\sigma'_{11}-\sigma'_{22}\right)_{\text{error}} &= \left(\sigma'_{11}-\sigma'_{22}\right)_{\text{apparent}} - \left(\sigma'_{11}-\sigma'_{22}\right)_{\text{actual}} \\ &= \frac{\left(3\left(\sigma'_{11}+\sigma'_{22}\right)-6\sigma'_{33}-2\sigma'_{13}\right)_{\text{acutal}}}{1381}\end{aligned} \tag{6.15}$$

Similarly, the measurement error for (σ'_{12}) can be defined

$$\begin{aligned}\left(\sigma'_{12}\right)_{\text{error}} &= \left(\sigma'_{12}\right)_{\text{apparent}} - \left(\sigma'_{12}\right)_{\text{actual}} \\ &= \frac{\left(14\left(\sigma'_{12}\right)+196\sigma'_{23}\right)_{\text{actual}}}{-3112}\end{aligned} \tag{6.16}$$

It can be observed that the measurement error values can be defined using actual stresses and highly dependent on the actual stress distributions. Also, it can be predicted that errors should not be significant from equations above. In Eq. 6.15, the coefficients of each stress component is very small so that the value of error tends to be small compared with $(\sigma'_{11} - \sigma'_{22})$. In Eq. 6.16, even though the coefficient of σ'_{23} is relatively big, σ'_{23} is usually lower than σ'_{12} which also generates small errors. To verify our predictions, simulation is performed to further explore the measurement errors induced by tilted wafer.

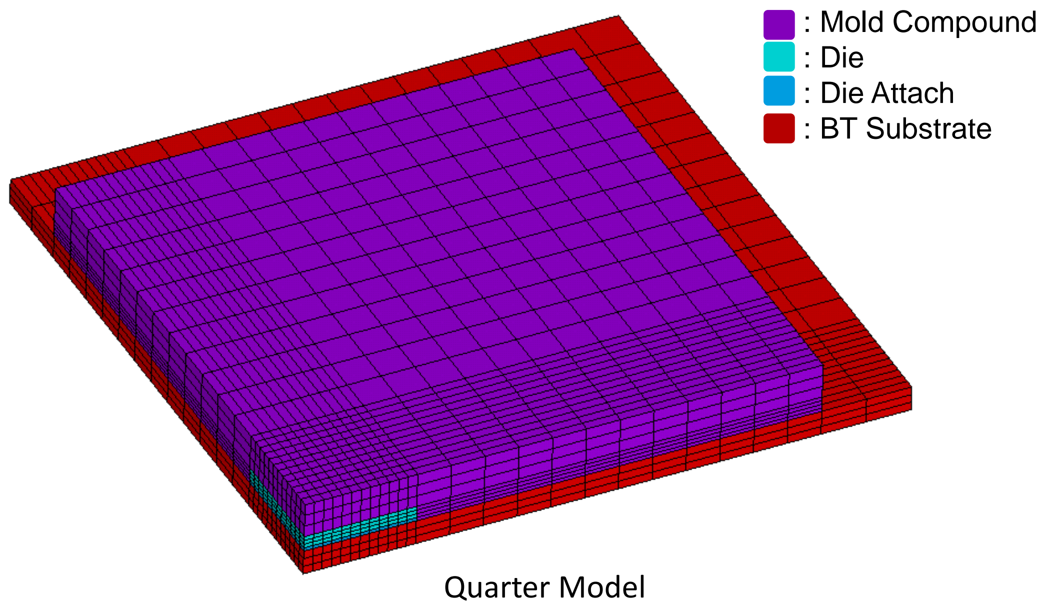

Figure 6.9: Plastic Ball Grid Array Package Model

In Fig. 6.9, a meshed quarter model of plastic ball grid array package is constructed including mold compound, die, die attach, and BT substrate. The material properties are all considered to be linear elastic and isotropic as shown in Table 6.2. Ansys® was used to obtain the stress distribution over the surface of the die resulting from cooling the die from its assumed stress-free state at 155°C to the room temperature of 25°C. The finite element stress predictions can be combined with the error estimation formulas to generate plots of the errors over the die surface.

	E(GPa)	$\boldsymbol{\nu}$	**CTE**($℃^{-1}$)
Chip	169	0.28	2.6×10^{-6}
Mold Compound	33.5	0.25	22×10^{-6}
BT substrate	17.9	0.39	12.4×10^{-6}
Die Attach	6.7	0.35	83×10^{-6}

Table 6.2: Material Properties

The resulting stress distributions of $(\sigma'_{11} - \sigma'_{22})$ and σ'_{12} over the die surface are shown in Fig. 6.10 and Fig. 6.11 and the errors for these stresses are also plotted as shown in Fig. 6.12 and Fig. 6.13.

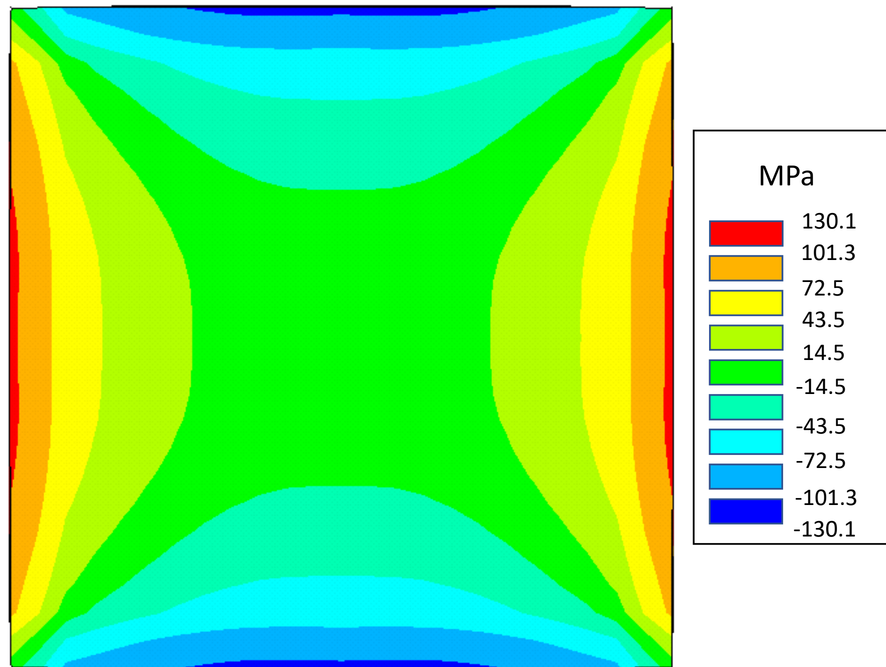

Figure 6.10: Simulated Stress Distribution of $(\sigma'_{11} - \sigma'_{22})$

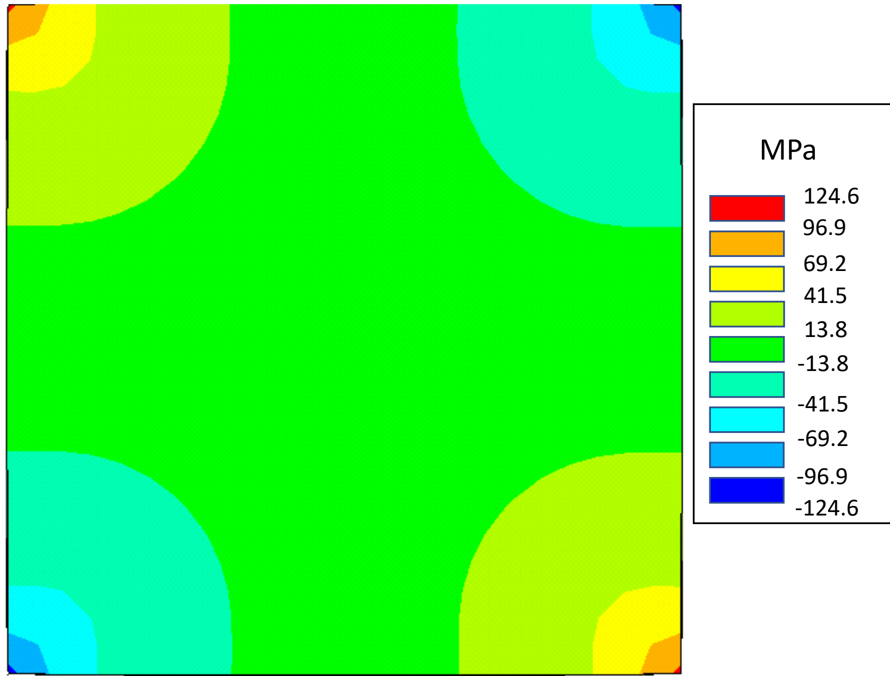

Figure 6.11: Simulated Stress Distribution of σ'_{12}

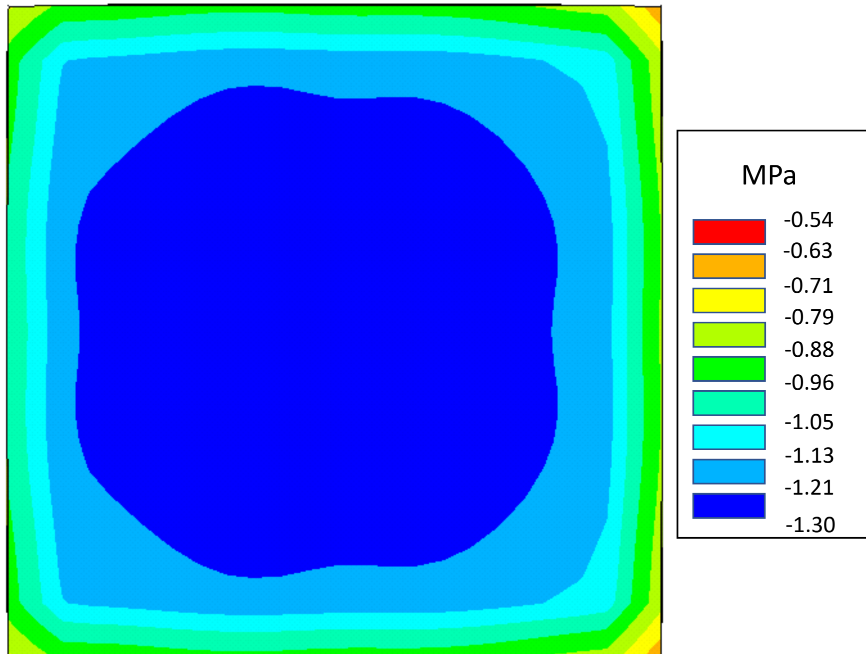

Figure 6.12: Calculated Errors Plot for $(\sigma'_{11} - \sigma'_{22})$ Using Eq. 6.15

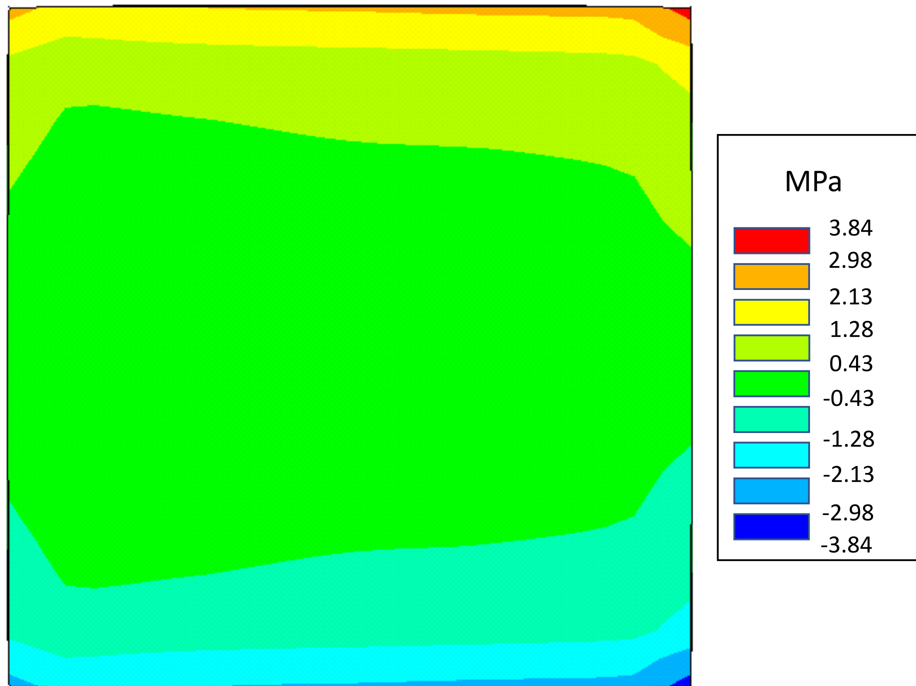

Figure 6.13: Calculated Errors Plot for σ'_{12} Using Eq. 6.16

In Fig. 6.10 and Fig.6 11, we can observe that values of $(\sigma'_{11} - \sigma'_{22})$ and σ'_{12} range from around -130MPa to 130MPa. In contrast, the maximum error values for $(\sigma'_{11} - \sigma'_{22})$ and σ'_{12} are 1.3MPa and 3.8MPa, respectively, so errors induced by tilted wafer plane are not significant. It is worth noting that the simulation in this study is just one example, and the piezoresistive coefficients are dependent upon the doping level which leads to different errors.

6.5 Summary and Conclusion

This chapter discussed methods to evaluate the impact of off-axis wafer planes on stress sensors fabricated on (100) and (111) silicon. The work reviewed coordinate transformations for the piezoresistive coefficients, and then developed expressions and

compared the piezoresistive coefficient changes introduced by a 4° off-axis tilt of the wafer plane. We found that many zero elements in ideal on-axis [π'] become non-zero for the off-axis case indicating additional coupling, particularly from shear stresses. For many non-zero elements in on-axis [π'], the corresponding elements in off-axis [π*] have more fundamental piezoresistive coefficients involved.

To better illustrate the impact of off-axis wafer planes, error equations for a four-element rosette were developed using typical piezoresistive coefficients. Stress simulation results were utilized to estimate stress extraction errors for an example of a die encapsulated in a PBGA for (100) silicon. The magnitude and importance of the error terms will be a strong function of the (doping dependent) piezoresistive coefficient values and the stress distributions in the silicon die. Thus, significant differences should be expected among the wide range of packaging technologies utilized by the semiconductor industry.

Chapter 7

STRESS-STRAIN RELATIONS OF 4H-SIC

7.1 Introduction

The elastic modulus and Poisson's ratio are the key parameters for design and application of semiconductor sensors. For example, once stress distribution of the chip is measured with piezoresistive stress sensors and the strain distribution can be evaluated from the stresses according to elastic constants. In the field of MEMS, the elastic properties are required to predict the deformation/displacement of the moving elements (e.g., cantilever beam). In addition, finite element simulations on sensor design needs accurate value of elastic constants.

4H-SiC is an anisotropic material whose material properties are dependent on the orientation relative to the crystal lattice. Thus, a matrix of elastic constants is needed to describe the mechanical properties of 4H-SiC. Many techniques are available to measure such elastic properties. The direct measurement of strain as a function of stress can be performed using strain gauges. In ultrasonic measurements, the elastic constants are evaluated by measuring the propagation velocity of the acoustic waves (typically MHz) [112]. In Brillouin scattering study, the incident laser light is scattered by the target material and the frequency shift of laser light is detected to determine the phonon energies, from which the full elastic tensor can be calculated [113]. It is also possible to determine the elastic constants using computational studies, such as ab-initio calculation which is based on density functional theory (DFT) [114]. The elastic tensor of 4H-SiC had been studied

by serval groups using different methods, but the difference of the measured calculated elastic constants are relatively large [114][122]-[124]. The variations could come from different fabrication process of the material or experimental methods.

In this study, the elastic properties of 4H-SiC chips are determined by four-point bending and nano-indentation method. Strain gauges were also used for validation of elastic modulus and measurement of the Poisson's ratio. The elastic stiffness coefficients for 4H-SiC available in the literature were compared with our data.

7.2 Stress-Strain Relations of 4H-SiC

4H-SiC exhibits linear elastic material behavior which is described by the Hooke's law [115]:

$$\begin{bmatrix} \sigma_{11} \\ \sigma_{22} \\ \sigma_{33} \\ \sigma_{23} \\ \sigma_{31} \\ \sigma_{12} \\ \sigma_{32} \\ \sigma_{13} \\ \sigma_{21} \end{bmatrix} = \begin{bmatrix} C_{1111} & C_{1122} & C_{1133} & C_{1123} & C_{1131} & C_{1112} & C_{1132} & C_{1113} & C_{1121} \\ C_{2211} & C_{2222} & C_{2233} & C_{2223} & C_{2231} & C_{2212} & C_{2232} & C_{2213} & C_{2221} \\ C_{3311} & C_{3322} & C_{3333} & C_{3323} & C_{3331} & C_{3312} & C_{3332} & C_{3313} & C_{3321} \\ \cdots & \cdots & \cdots & \cdots & \cdots & \cdots & \cdots & \cdots & \cdots \\ \cdots & \cdots & \cdots & \cdots & \cdots & \cdots & \cdots & \cdots & \cdots \\ \cdots & \cdots & \cdots & \cdots & \cdots & \cdots & \cdots & \cdots & \cdots \\ \cdots & \cdots & \cdots & \cdots & \cdots & \cdots & \cdots & \cdots & \cdots \\ \cdots & \cdots & \cdots & \cdots & \cdots & \cdots & \cdots & \cdots & \cdots \\ C_{2111} & C_{2122} & C_{2133} & C_{2123} & C_{2131} & C_{2112} & C_{2132} & C_{2113} & C_{2121} \end{bmatrix} \begin{bmatrix} \varepsilon_{11} \\ \varepsilon_{22} \\ \varepsilon_{33} \\ \varepsilon_{23} \\ \varepsilon_{31} \\ \varepsilon_{12} \\ \varepsilon_{32} \\ \varepsilon_{13} \\ \varepsilon_{21} \end{bmatrix} \tag{7.1}$$

where [C] is a 9×9 matrix of elastic constants having 81 components. The first two subscripts on the elastic constants correspond to those of the stress, whereas the last two subscripts correspond to those of strain. Since both stresses and strains are symmetric, there are only six independent stress components and six independent strain components. Thus, the elastic constants must be symmetric with respect to the first two subscripts and with

respect to the last two subscripts ($C_{ijkl}=C_{jikl}$ and $C_{jikl}=C_{ijlk}$). And the number of non-zero elastic constants is now reduced to 36. These simplifications lead to reduced index notation:

$$\begin{bmatrix} \sigma_{11} \\ \sigma_{22} \\ \sigma_{33} \\ \sigma_{13} \\ \sigma_{23} \\ \sigma_{12} \end{bmatrix} = \begin{bmatrix} \sigma_1 \\ \sigma_2 \\ \sigma_3 \\ \sigma_4 \\ \sigma_5 \\ \sigma_6 \end{bmatrix} \qquad \begin{bmatrix} \varepsilon_{11} \\ \varepsilon_{22} \\ \varepsilon_{33} \\ 2\varepsilon_{13} \\ 2\varepsilon_{23} \\ 2\varepsilon_{12} \end{bmatrix} = \begin{bmatrix} \varepsilon_{11} \\ \varepsilon_{22} \\ \varepsilon_{33} \\ \gamma_{13} \\ \gamma_{23} \\ \gamma_{12} \end{bmatrix} = \begin{bmatrix} \varepsilon_1 \\ \varepsilon_2 \\ \varepsilon_3 \\ \varepsilon_4 \\ \varepsilon_5 \\ \varepsilon_6 \end{bmatrix} \tag{7.2}$$

With this reduced notation, the generalized Hook's law can now be written as

$$\sigma_i = C_{ij}\varepsilon_j \qquad i,j= 1,2,...,6 \tag{7.3}$$

In a matrix form

$$[\sigma] = [C][\varepsilon] \tag{7.4}$$

Where the elastic constant matrix or stiffness [C] is a 6 × 6 with 36 components and the stresses [σ] and strain [ε] are column vectors. Alternatively, the generalized Hook's law relating strains to stresses can be written as

$$\varepsilon_i = S_{ij}\sigma_j \qquad i,j= 1,2,...,6 \tag{7.5}$$

Or in a matrix form

$$[\varepsilon] = [S][\sigma] \tag{7.6}$$

Where [S] is the compliance matrix, which is the inverse of the stiffness matrix ($[S] = [C]^{-1}$).

The generalized anisotropic Hook's law can be simplified using various symmetry conditions. The first symmetric condition is a result of the existence of a strain energy density function, so that it has nothing to do with the material symmetry. The strain energy density function for a linear elastic material is

$$w = \frac{1}{2}\sigma_i \varepsilon_j = \frac{1}{2} C_{ij} \varepsilon_i \varepsilon_j \tag{7.7}$$

The stress can be derived according to the equation:

$$\sigma_i = \frac{\partial w}{\partial \varepsilon_i} = C_{ij} \varepsilon_j \tag{7.8}$$

By taking a second derivative of W, we have

$$\sigma_i = \frac{\partial^2 w}{\partial \varepsilon_i \partial \varepsilon_j} = C_{ij} \tag{7.9}$$

By reversing the order of differentiation, we have

$$\sigma_i = \frac{\partial^2 w}{\partial \varepsilon_j \partial \varepsilon_i} = C_{ji} \tag{7.10}$$

Since the result must be the same regardless of the order of the differentiation, the stiffness matrix is symmetric ($C_{ij} = C_{ji}$). Similarly, W can be expressed in terms of compliance

matrix, and by taking two derivatives with respect to stresses, it can be shown that $S_{ij}= S_{ji}$. Thus, the compliance matrix is also symmetric. The point group of 4H-SiC is 6mm, which has one six-fold rotation and six mirror planes with no inversion. The elastic properties of 6mm group material is [116]

$$[C]=\begin{bmatrix} C_{11} & C_{12} & C_{13} & 0 & 0 & 0 \\ C_{12} & C_{11} & C_{13} & 0 & 0 & 0 \\ C_{13} & C_{13} & C_{33} & 0 & 0 & 0 \\ 0 & 0 & 0 & C_{44} & 0 & 0 \\ 0 & 0 & 0 & 0 & C_{44} & 0 \\ 0 & 0 & 0 & 0 & 0 & \frac{C_{11}-C_{12}}{2} \end{bmatrix} \tag{7.11}$$

Therefore, there are five unique elastic constants (C_{11}, C_{12}, C_{13}, C_{33}, C_{44}) for 4H-SiC.

7.3 General Coordinate Transformations

As mentioned earlier, it is more convenient to work in the wafer coordinate system. Before the experiment, we must understand how the elastic matrix changes in different coordinate systems. As shown in Fig. 7.1, two coordinate systems $x_1 - x_2 - x_3$ and $x'_1 - x'_2 - x'_3$ rotated arbitrarily with each other.

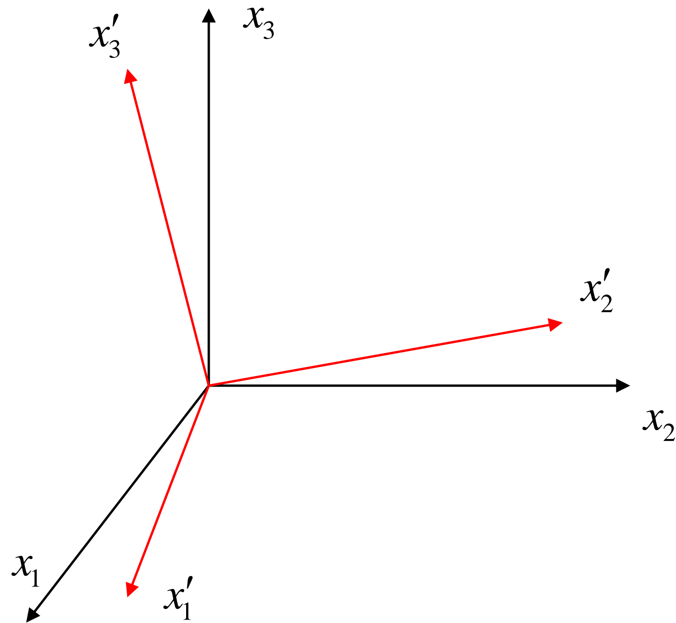

Figure 7.1: Rotated Cartesian Coordinate System

The components of the tensorial strain and stress are transformed from one coordinate system to another using the standard tensor transformation rules:

$$
\begin{aligned}
[\varepsilon'] &= [a][\varepsilon][a]^T \\
[\sigma'] &= [a][\sigma][a]^T
\end{aligned}
\tag{7.12}
$$

where $[\varepsilon]$ and $[\sigma]$ are 3×3 strain and stress matrix and $[a]$ is a 3×3 transformation matrix. Expanding the above equation gives:

$$
\begin{aligned}
\varepsilon'_{11} &= a_{11}^2\varepsilon_{11} + a_{12}^2\varepsilon_{22} + a_{13}^2\varepsilon_{33} + 2a_{11}a_{13}\varepsilon_{13} + 2a_{12}a_{13}\varepsilon_{23} + 2a_{11}a_{12}\varepsilon_{12} \\
\varepsilon'_{22} &= a_{21}^2\varepsilon_{11} + a_{22}^2\varepsilon_{22} + a_{23}^2\varepsilon_{33} + 2a_{21}a_{23}\varepsilon_{13} + 2a_{22}a_{23}\varepsilon_{23} + 2a_{21}a_{22}\varepsilon_{12} \\
\varepsilon'_{33} &= a_{31}^2\varepsilon_{11} + a_{32}^2\varepsilon_{22} + a_{33}^2\varepsilon_{33} + 2a_{31}a_{33}\varepsilon_{13} + 2a_{32}a_{33}\varepsilon_{23} + 2a_{31}a_{32}\varepsilon_{12} \\
\varepsilon'_{13} &= a_{11}a_{31}\varepsilon_{11} + a_{12}a_{32}\varepsilon_{22} + a_{13}a_{33}\varepsilon_{33} \\
&\quad + (a_{13}a_{31} + a_{11}a_{33})\varepsilon_{13} + (a_{12}a_{33} + a_{13}a_{32})\varepsilon_{23} + (a_{12}a_{31} + a_{11}a_{32})\varepsilon_{12} \\
\varepsilon'_{23} &= a_{21}a_{31}\varepsilon_{11} + a_{22}a_{32}\varepsilon_{22} + a_{23}a_{33}\varepsilon_{33} \\
&\quad + (a_{31}a_{23} + a_{21}a_{33})\varepsilon_{13} + (a_{23}a_{32} + a_{22}a_{33})\varepsilon_{23} + (a_{22}a_{31} + a_{21}a_{32})\varepsilon_{12} \\
\varepsilon'_{12} &= a_{11}a_{21}\varepsilon_{11} + a_{12}a_{22}\varepsilon_{22} + a_{13}a_{23}\varepsilon_{33} \\
&\quad + (a_{13}a_{21} + a_{11}a_{23})\varepsilon_{13} + (a_{13}a_{22} + a_{12}a_{23})\varepsilon_{23} + (a_{12}a_{21} + a_{11}a_{22})\varepsilon_{12}
\end{aligned}
\tag{7.13}
$$

where

$$
[a] = \begin{bmatrix} l_1 & m_1 & n_1 \\ l_2 & m_2 & n_2 \\ l_3 & m_3 & n_3 \end{bmatrix}
\tag{7.14}
$$

The l_i, m_i, and n_i are direction cosines between two coordinate systems. Substitution of Eq. 7.14 into Eq. 7.13 gives the strain matrix in primed coordinate system:

$$
\begin{bmatrix} \varepsilon'_{11} \\ \varepsilon'_{22} \\ \varepsilon'_{33} \\ \varepsilon'_{13} \\ \varepsilon'_{23} \\ \varepsilon'_{12} \end{bmatrix}
=
\begin{bmatrix}
l_1^2 & m_1^2 & n_1^2 & 2l_1n_1 & 2m_1n_1 & 2l_1m_1 \\
l_2^2 & m_2^2 & n_2^2 & 2l_2n_2 & 2m_2n_2 & 2l_2m_2 \\
l_3^2 & m_3^2 & n_3^2 & 2l_3n_3 & 2m_3n_3 & 2l_3m_3 \\
l_1l_3 & m_1m_3 & n_1n_3 & l_1n_3 + l_3n_1 & m_1n_3 + m_3n_1 & l_3m_1 + l_1m_3 \\
l_2l_3 & m_2m_3 & n_2n_3 & l_2n_3 + l_3n_2 & m_2n_3 + m_3n_2 & l_2m_3 + l_3m_2 \\
l_1l_2 & m_1m_2 & n_1n_2 & l_1n_2 + l_2n_1 & m_1n_2 + m_2n_1 & l_1m_2 + l_2m_1
\end{bmatrix}
\begin{bmatrix} \varepsilon_{11} \\ \varepsilon_{22} \\ \varepsilon_{33} \\ \varepsilon_{13} \\ \varepsilon_{23} \\ \varepsilon_{12} \end{bmatrix}
$$

$$
[\varepsilon'] = [T][\varepsilon]
\tag{7.15}
$$

Similarly, the stress matrix in the primed coordinate system can be expressed as

$$\begin{bmatrix} \sigma'_{11} \\ \sigma'_{22} \\ \sigma'_{33} \\ \sigma'_{13} \\ \sigma'_{23} \\ \sigma'_{12} \end{bmatrix} = \begin{bmatrix} l_1^2 & m_1^2 & n_1^2 & 2l_1n_1 & 2m_1n_1 & 2l_1m_1 \\ l_2^2 & m_2^2 & n_2^2 & 2l_2n_2 & 2m_2n_2 & 2l_2m_2 \\ l_3^2 & m_3^2 & n_3^2 & 2l_3n_3 & 2m_3n_3 & 2l_3m_3 \\ l_1l_3 & m_1m_3 & n_1n_3 & l_1n_3 + l_3n_1 & m_1n_3 + m_3n_1 & l_3m_1 + l_1m_3 \\ l_2l_3 & m_2m_3 & n_2n_3 & l_2n_3 + l_3n_2 & m_2n_3 + m_3n_2 & l_2m_3 + l_3m_2 \\ l_1l_2 & m_1m_2 & n_1n_2 & l_1n_2 + l_2n_1 & m_1n_2 + m_2n_1 & l_1m_2 + l_2m_1 \end{bmatrix} \begin{bmatrix} \sigma_{11} \\ \sigma_{22} \\ \sigma_{33} \\ \sigma_{13} \\ \sigma_{23} \\ \sigma_{12} \end{bmatrix}$$

$$[\sigma'] = [T][\sigma] \tag{7.16}$$

Note that the transformation matrix [T] for stress and strain in the above equation is also valid for resistivity [ρ] (Eq. 2.9).

The generalized Hooke's law is usually written in Voigt notation, in which engineering strains are applied. The stress-strain relationship for the unprimed coordinate system is shown in Eq. 7.17 and is also valid for the rotated orthogonal ($x'_1 - x'_2 - x'_3$) coordinate system.

$$\begin{aligned} [\sigma] &= [C][e] \\ [\sigma'] &= [C'][e'] \end{aligned} \tag{7.17}$$

where [C] and [C'] are the elastic matrix in unprimed and primed coordinate systems, respectively, and [e] is the engineering strain matrix. To use Eq. 7.17, the transformation matrix for engineering strain must be determined. From Eq. 7.15, the transformation equation can be expressed as:

$$\begin{bmatrix} \varepsilon'_{11} \\ \varepsilon'_{22} \\ \varepsilon'_{33} \\ \gamma'_{13} \\ \gamma'_{23} \\ \gamma'_{12} \end{bmatrix} = \begin{bmatrix} l_1^2 & m_1^2 & n_1^2 & l_1n_1 & m_1n_1 & l_1m_1 \\ l_2^2 & m_2^2 & n_2^2 & l_2n_2 & m_2n_2 & l_2m_2 \\ l_3^2 & m_3^2 & n_3^2 & l_3n_3 & m_3n_3 & l_3m_3 \\ 2l_1l_3 & 2m_1m_3 & 2n_1n_3 & l_1n_3+l_3n_1 & m_1n_3+m_3n_1 & l_3m_1+l_1m_3 \\ 2l_2l_3 & 2m_2m_3 & 2n_2n_3 & l_2n_3+l_3n_2 & m_2n_3+m_3n_2 & l_2m_3+l_3m_2 \\ 2l_1l_2 & 2m_1m_2 & 2n_1n_2 & l_1n_2+l_2n_1 & m_1n_2+m_2n_1 & l_1m_2+l_2m_1 \end{bmatrix} \begin{bmatrix} \varepsilon_{11} \\ \varepsilon_{22} \\ \varepsilon_{33} \\ \gamma_{13} \\ \gamma_{23} \\ \gamma_{12} \end{bmatrix}$$

$$[e'] = [T_e][e] \tag{7.18}$$

where $[T_e]$ is the transformation matrix for engineering strain. Substitution of Eq. 7.16 and Eq. 7.18 into Eq. 7.17 leads to

$$\begin{aligned} [\sigma'] &= [T][\sigma] = [C'][e'] = [C'][T_e][e] \\ [\sigma] &= [T]^{-1}[C'][T_e][e] \\ [\sigma] &= [C][e] \end{aligned} \tag{7.19}$$

The relationship between [C] and [C’] can be obtained

$$\begin{aligned} [C] &= [T]^{-1}[C'][Te] \\ [C'] &= [T][C][T_e]^{-1} \end{aligned} \tag{7.20}$$

Since the energy density of the system is the same, we can have

$$\begin{aligned} [e]^T[\sigma] &= [e']^T[\sigma'] \\ &= ([T_e][e])^T[\sigma'] \\ &= [e]^T[T_e]^T[\sigma'] \end{aligned} \tag{7.21}$$

And the relationship between [T] and $[T_e]$ is

$$\begin{aligned} [\sigma] &= [T_e]^T [\sigma'] \\ [\sigma] &= [T]^{-1} [\sigma'] \\ [T_e]^T &= [T]^{-1} \end{aligned} \tag{7.22}$$

According to Eq. 7.20, the coordination transformation equation can be expressed in terms of [T].

$$[C'] = [T][C][T]^T \tag{7.23}$$

Note that the coordination transformation equation for the piezoresistive matrix is expressed in a different form ($[\pi'] = [T][\pi'][T]^{-1}$), the reason is that the engineering shear strains (γ_{ij}) are used in the stress-strain relationship.

7.4 Elastic Properties on (0001) Plane

Figure 7.2 shows the hexagonal crystal structure of 4H-SiC and the coordinate system definitions for the (0001) surface. a_1-a_2-a_3-c represent the crystallographic axes of the 4H-SiC material, whereas x_1-x_2-x_3 axes are the orthogonal axes corresponding to the underlying elastic constants as shown in Eq. 7.11. The c and x_3 axes are coincident and perpendicular to the page. Considering a primed coordinate system x_1'-x_2'-x_3' rotated θ degrees about the x_3 axis (rotation within the basal plane), the elastic constants in the primed coordinate system can be found using Eq. 7.23 with appropriate direction cosines. Eq. 7.24 shows the direction cosines of the x_i' axis with respect to the x_1, x_2, x_3 axes, respectively. It has been found that the elements of elastic matrix are identical ([C]= [C'])

for rotations within the basal plane. Therefore, 4H-SiC is a transversely isotropic material. All the calculations have been performed symbolically using the mathematical software MATLAB®.

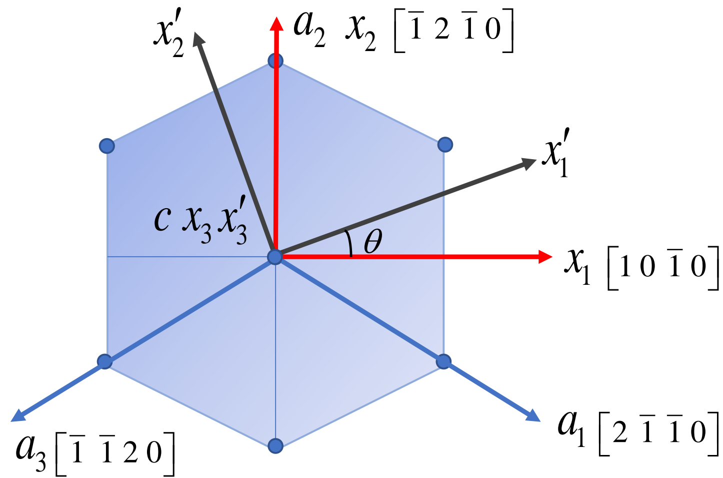

Figure 7.2: Coordinate Systems for (0001) 4H-SiC Wafers

$$[\mathrm{a}] = \begin{bmatrix} \cos(\theta) & \sin(\theta) & 0 \\ -\sin(\theta) & \cos(\theta) & 0 \\ 0 & 0 & 1 \end{bmatrix} \tag{7.24}$$

Eq. 7.11 can be inverted to get the compliance matrix by introducing the elastic constants E, ν and G in place of the S_{ij}.

$$[S]=\begin{bmatrix} \frac{1}{E_1} & -\frac{\nu_{12}}{E_1} & -\frac{\nu_{31}}{E_3} & 0 & 0 & 0 \\ -\frac{\nu_{12}}{E_1} & \frac{1}{E_1} & -\frac{\nu_{31}}{E_3} & 0 & 0 & 0 \\ -\frac{\nu_{13}}{E_1} & -\frac{\nu_{13}}{E_1} & \frac{1}{E_3} & 0 & 0 & 0 \\ 0 & 0 & 0 & \frac{1}{G_{13}} & 0 & 0 \\ 0 & 0 & 0 & 0 & \frac{1}{G_{13}} & 0 \\ 0 & 0 & 0 & 0 & 0 & \frac{2(1+\nu_{12})}{E_1} \end{bmatrix} \tag{7.25}$$

where E_i is the elastic modulus of the material in direction i = 1, 2, 3, ν_{ij} are the Poisson's ratio, and G_{ij} are the shear moduli. There are six parameters in the [S] matrix, but only five of them are independent. The reason is that [S] matrix must be symmetric, thereby, $\nu_{13}/E_1 = \nu_{31}/E_3$. The stiffness matrix can be also expressed in terms of E, ν_{ij} and G_{ij}.

$$[C]=\begin{bmatrix} \frac{1-\nu_{13}\nu_{31}}{E_1E_3\Delta} & \frac{\nu_{12}+\nu_{13}\nu_{31}}{E_1E_3\Delta} & \frac{\nu_{31}+\nu_{12}\nu_{31}}{E_1E_3\Delta} & 0 & 0 & 0 \\ \frac{\nu_{12}+\nu_{13}\nu_{31}}{E_1E_3\Delta} & \frac{1-\nu_{13}\nu_{31}}{E_1E_3\Delta} & \frac{\nu_{31}+\nu_{12}\nu_{31}}{E_1E_3\Delta} & 0 & 0 & 0 \\ \frac{\nu_{13}+\nu_{12}\nu_{13}}{E_1^2\Delta} & \frac{\nu_{13}(1+\nu_{12})}{E_1^2\Delta} & \frac{1-\nu_{12}^2}{E_1^2\Delta} & 0 & 0 & 0 \\ 0 & 0 & 0 & G_{13} & 0 & 0 \\ 0 & 0 & 0 & 0 & G_{13} & 0 \\ 0 & 0 & 0 & 0 & 0 & \frac{E_1}{2(1+\nu_{12})} \end{bmatrix} \tag{7.26}$$

$$\Delta = \frac{(1+\nu_{12})(1-\nu_{12}-2\nu_{13}\nu_{31})}{E_1^2E_3}$$

7.5 Four Point Bending Method

The four-point bending system illustrated in Fig. 3.9 is used to determine the elastic modulus E_1. In Fig. 7.3, the test strips cut from SiC wafer are in $[11\bar{2}0]$ direction and the top surface of the wafer is an (0001) plane. The elastic constants are identical within the basal plane ([C] = [C']) which means elastic properties are the same in both primed wafer coordinate system and unprimed coordinate system, thus, coordinate transformation is not necessary. During experiments, the test strip is placed on the bottom supports of the four-point-bending fixture. Force generated by a vertical translation stage is applied in the four-point bending fixture and measured by a load cell. Deflection δ is measured by a micrometer.

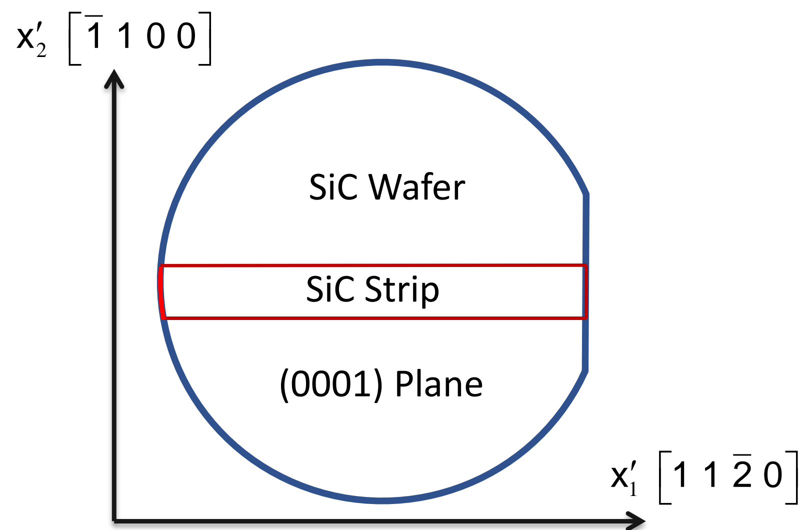

Figure 7.3: Test Strip Cut from SiC Wafer

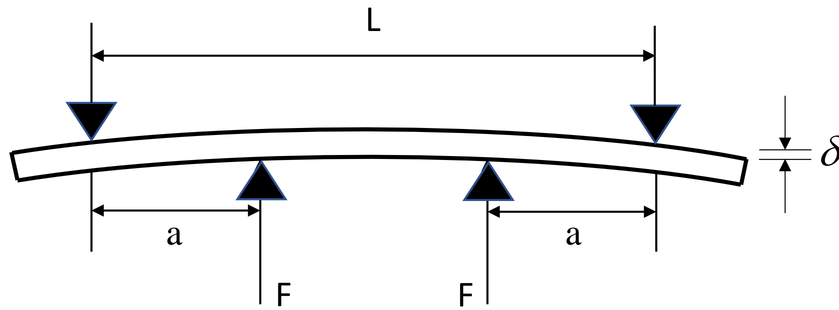

Figure 7.4: Deflection of a Beam in a Four-Point Bending Fixture

In Fig. 7.4, "L" is the distance between the two top supports, "a" is the distance between the top support to the adjacent bottom support, and "δ" is the displacement of bottom supports. "F" is the applied force. Note that the measured force from the transducer is the total force from the bottom support, which is 2F. in Fig. According to the Euler-Bernoulli beam theory, the elastic modulus can be evaluated using Eq. 7.27.

$$\delta = \frac{Fa^2(3L-4a)}{6EI} \qquad E = \frac{Fa^2(3L-4a)}{6\delta I} \tag{7.27}$$

In Eq. 7.27, the elastic modulus can be written as

$$E = \frac{F'}{\delta} \qquad F' = \frac{Fa^2(3L-4a)}{6I} \tag{7.28}$$

The moment of inertia I is defined as $bh^3/12$ in which b is the width and h is the thickness of the strip. The beam theory expressions in Eqs. 7.27-7.28 are valid for

anisotropic materials such as SiC, as long as the length of the beam is directed along one of the material symmetry directions and the value of E is the directional modulus along the length of the beam [117].

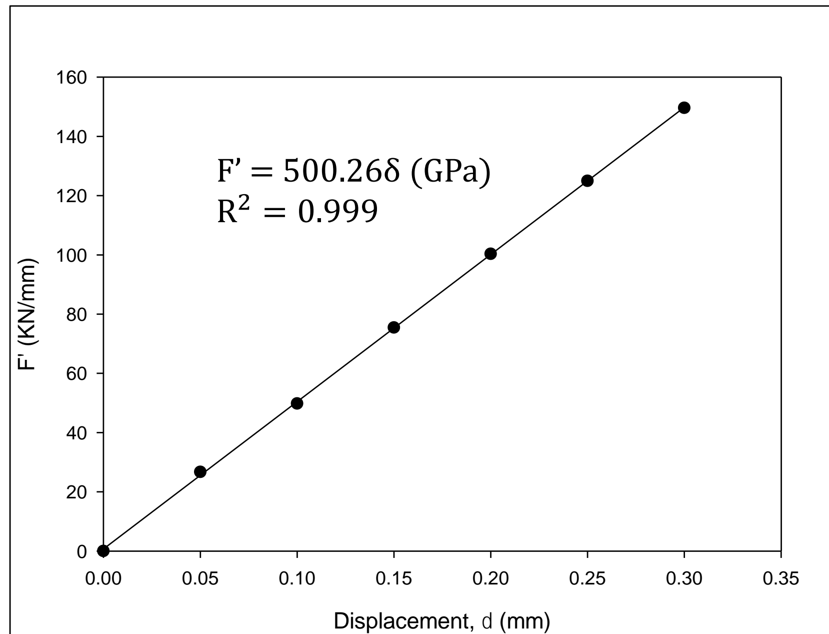

Figure 7.5: F' vs. Displacement

A typical measurement results appears in Fig. 7.5 where E_1 is the slope of F' with respect to δ. The mean and standard deviation of the extracted elastic modulus E_1 are listed in Table 7.1.

Sample Number	Elastic Modulus (GPa)
1	496.6
2	497.2
3	495.3
4	503.9
5	506.6
6	506.2
7	494.7
8	497.2
9	494.9
10	502.5
11	499.2
12	500.2
13	497.6
14	496.8
15	497.1
Average	499.1
Standard Deviation	3.9

Table 7.1: Extracted Elastic Modulus E_1 From 4PB method

7.6 Strain Gauge Method

In this work, a strain gauge technique was used to measure Poisson's ratio and validate the results from the four-point bending method. Specimen strips are cut from the SiC wafer along the $[11\bar{2}0]$ direction.

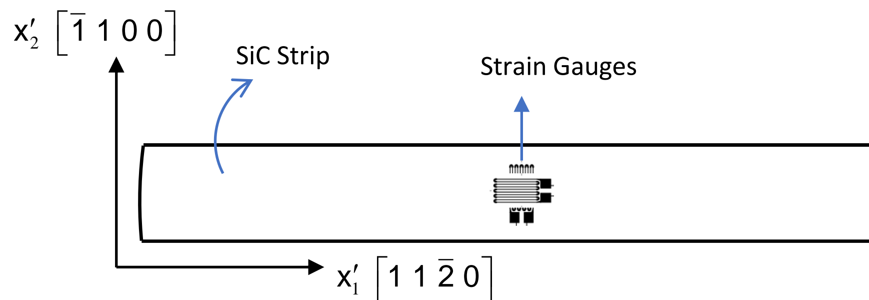

Figure 7.6: Strain Gauges on SiC Strip

Poisson's ratio can be evaluated readily with two strain gauges using Eq. 7.29. To measure strains in longitudinal and transverse directions, we mounted strain gauges on each specimen in two directions, one on the top surface and one on the bottom surface as shown in Fig. 7.6. Again, the four-point-bending fixture is used to apply an uniaxial stress σ to the strips. Hence, only $\sigma'_{11} = \sigma$ is applied, and other stress components are zero. Based upon the beam theory and Hooke's law, the elastic modulus can be found as in Eq. 7.30.

$$\nu_{12} = -\frac{\varepsilon_2'}{\varepsilon_1'} \tag{7.29}$$

$$E_1 = \frac{\sigma}{\varepsilon_1'} = \frac{6Fa}{bh^2\varepsilon_1'} \tag{7.30}$$

Where ν_{12} is Poisson's ratio, ε'_i is the strain in the i direction and all other parameters in Eq. 7.30 have been defined earlier in Eq. 7.28.

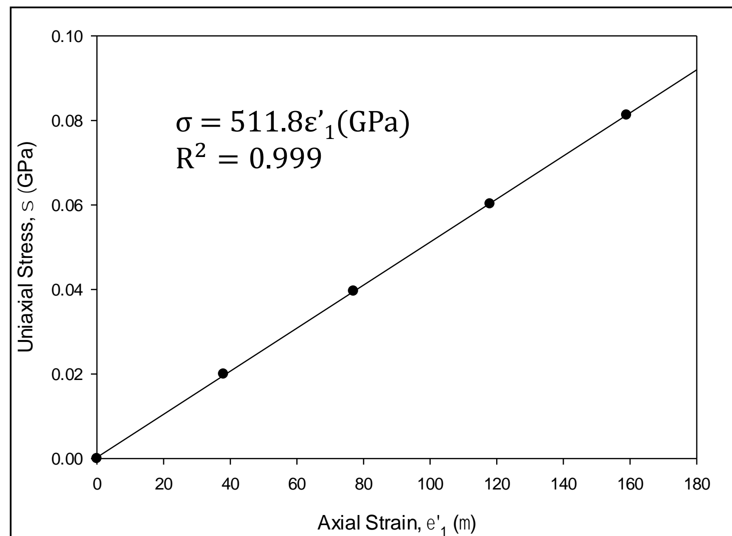

Figure 7.7: Uniaxial Stress vs. Axial Strain

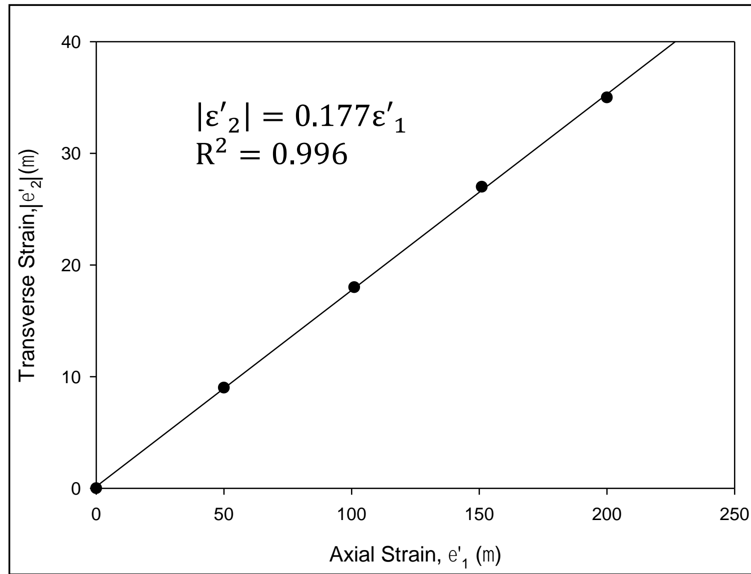

Figure 7.8: Transverse Strain vs. Axial Strain

Typical strain gauge data for elastic modulus E_1 and Poisson's ratio ν_{12} are shown in Fig. 7.7 and Fig. 7.8. The extracted material properties for 10 sets of measurements are listed in Table 7.2.

Sample Number	Elastic Modulus (GPa)	Poisson's Ratio
1	513.2	0.174
2	511.8	0.176
3	511.1	0.177
4	506.9	0.182
5	505.7	0.179
6	507.0	0.181
7	513.9	0.183
8	515.7	0.181
9	508.5	0.178
10	508.4	0.179
Average	510.2	0.179
Standard Deviation	3.4	0.003

Table 7.2: Material Properties Extracted by Strain Gauge Method

The elastic modulus E_1 evaluated by four-point bending and strain gauge method are quite close to each other, with the difference by 2%. Such difference may result from the wide-beam effect [118] and the results from strain gauge method are believed to be more accurate.

7.6 Nanoindentation Method

Depth-sensing indentation has been widely used for determining mechanical properties of small specimens. The Oliver and Pharr method [119] has been the most common method to determine the elastic modulus from its unloading curves. The analysis method provides the elastic modulus using Eq. 7.31 with the assumption that the elastic modulus is the value in the indentation direction.

$$\frac{1}{E_r} = \frac{\left(1-\nu_s^2\right)}{E_s} + \frac{\left(1-\nu_i^2\right)}{E_i} \tag{7.31}$$

In the above equation, E and ν represent the elastic modulus and the Poisson's ratio, respectively. Subscripts i and s denote indenter tip and specimen. For a diamond tip, E_i and ν_i are 1140 GPa and 0.07. The reduced modulus E_r is calculated by:

$$E_r = \frac{S\sqrt{\pi}}{2\beta\sqrt{A_C}} \tag{7.32}$$

S is the unloading contact stiffness, A_C is the projected contact area, and β is the indenter tip shape factor. Fig. 7.9 shows the typical load-displacement curve and the unloading contact stiffness (S) is the slope of the unloading curve.

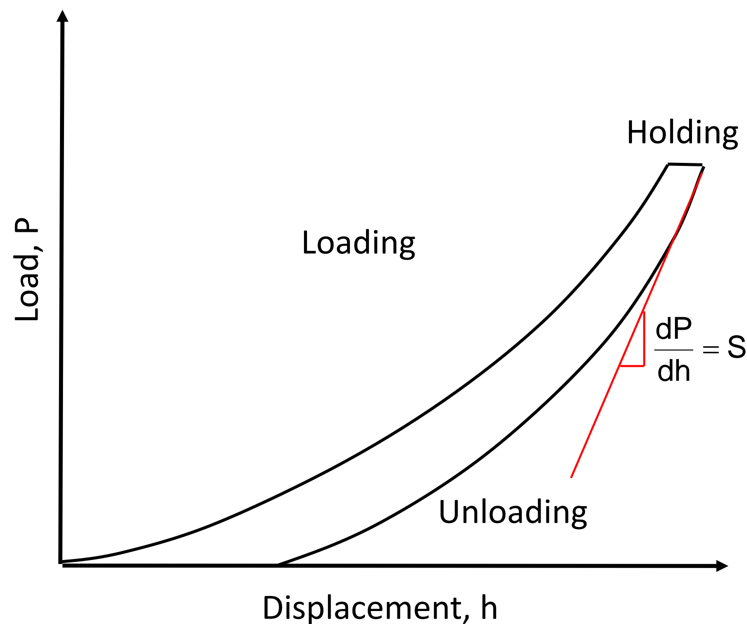

Figure 7.9: Typical Load-displacement Curve of Nanoindentation

Note that Eqs. 7.31-7.32 are applicable for isotropic materials and 4H-SiC is a transversely isotropic material. Even though some effect from other directions exist in transversely isotropic case, it is possible to estimate the elastic constants in the indentation direction with these equations [120]-[121].

In this study, square specimens are cut from SiC strip and the primed wafer coordinate system is shown in Fig. 7.10. Specimen faces are carefully polished to remove damages and residual stress induced by cutting. For 4H-SiC, the (0001) plane is the isotropic plane, so that indentation experiments are carried out only on this plane using a Berkovich pyramidal diamond indenter.

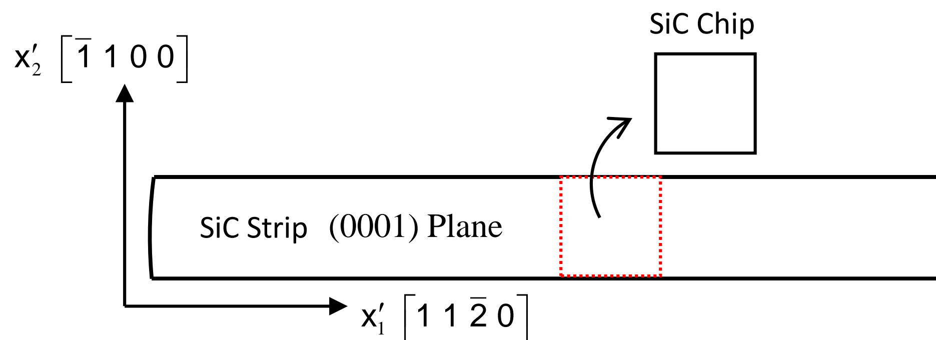

Figure 7.10: SiC Chip Cut from the Strip

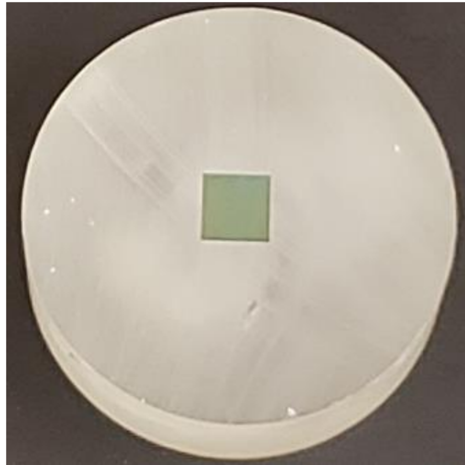

Figure 7.11: SiC Chip Embedded in Resins

Fig. 7.11 shows the nanoindentation load displacement curve for SiC chips. A maximum load of 20000 μN was applied with a loading rate of 3 mN/s. Then a holding time of 2 seconds was applied followed by the unloading at the same rate of 3 mN/s. From the unloading curve, the reduced modulus and corresponding elastic modulus was calculated using the Oliver and Pharr method. Table 7.3 shows the value of reduced modulus and elastic modulus value for SiC chip.

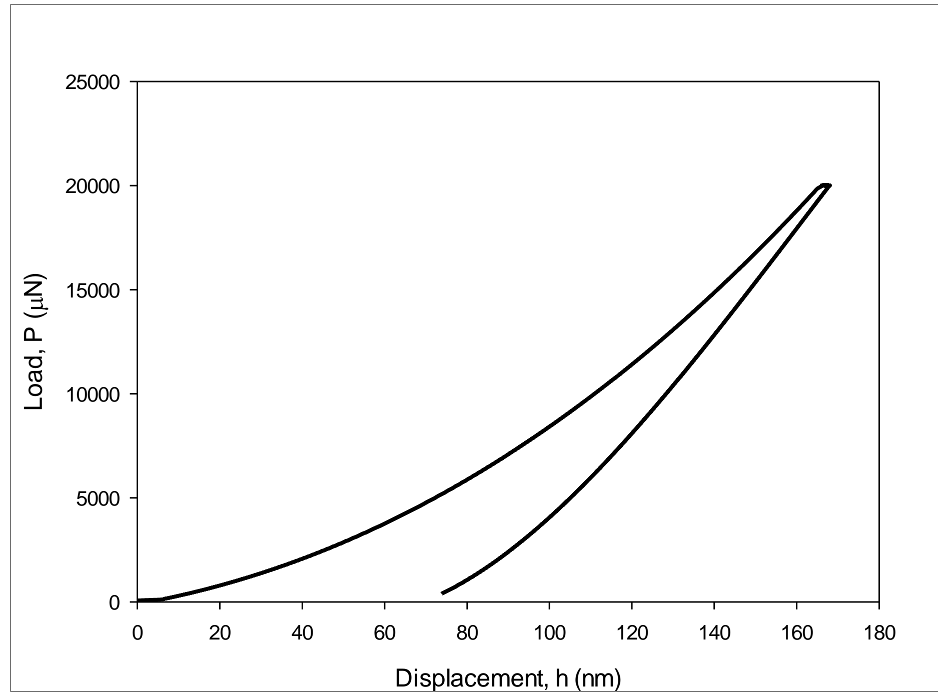

Figure 7.12: Nanoindentation Load-Displacement Curve for 4H-SiC

Sample Number	Reduced Modulus E_r (GPa)	Elastic Modulus E_3 (GPa)
1	379.9	551.9
2	380.8	553.8
3	381.3	555.0
4	379.9	551.9
5	381.8	556.1
6	384.7	562.5
7	381.4	555.2
Average	382	555
Standard Deviation	1.55	3.5

Table 7.3: Modulus of 4H-SiC Extracted from Nanoindentation

7.7 Elastic Properties Comparison

The elastic constants of 4H-SiC available in the literature are listed in Table 7.4. These constants are converted into elastic modulus and Poisson's ratio values by comparing Eq. 7.10 and Eq. 7.24, and then compared with our experimental data as shown in Table 7.5.

Reference	C_{11}	C_{12}	C_{13}	C_{33}	C_{44}
Pizzagalli [122]	498	91	52	535	159
Kamitani [123]	501	111	52	553	163
Nuruzzaman [124]	503	92	48	533	161
Iuga [114]	534	96	50	574	171

Table 7.4: Elastic Constants (C_{ij} in GPa)

Reference	E_1	E_3	ν_{12}	ν_{13}	G_{13}
Pizzagalli [122]	478	526	0.174	0.080	159
Kamitani [123]	473	544	0.214	0.074	163
Nuruzzaman [124]	483	525	0.180	0.074	161
Iuga [114]	514	566	0.173	0.072	171
This Work	510	555	0.179		

Table 7.5: Elastic Modulus (E_{ij} in GPa) and Poisson's Ratio [114] [122]-[124]

4H-SiC is described by 5 independent elastic constants which differ significantly between different methods. In Table 7.5, the comparison shows that the elastic properties extracted by our study are in well agreement with results in [114]. Especially for elastic modulus E_1 , the value is underestimated by 0.5%. Even though the value of Poisson's ratio ν_{12} is slightly higher than results in [114] and closer to [124], the elastic modulus E_1 and E_3 in

[124] are much lower than our results. Overall, results reported in [114] best match our results. It is hard to measure ν_{13} and G_{13} with thin 4H-SiC specimens, so that they are not discussed in this study.

7.8 Summary and Conclusion

In this study, we reviewed the coordinate transformations of engineering strain, tensorial strain, stress, and stiffness matrices. For 4H-SiC, the (0001) plane was found to be an isotropic plane so that coordinate transformation is not necessary before the experiment. Unlike many acoustic experiments or simulation studies, the elastic properties were extracted by traditional methods. The four-point bending and strain gauge methods were used to extract the elastic modulus E_1 which is 510 GPa from our measurement. The Poisson's ratio ν_{12} was measured with two strain gauges and getting the value of 0.179. The elastic modulus in [0001] direction E_3 was found to be 555 GPa using the nanoindentation method.

The elastic stiffness coefficients available in the literature were converted into elastic modulus and Poisson's ratios values, and then compared with our data. The elastic properties evaluated by Iuga et al. [114] agree best with our results.

Chapter 8

DIE STRESS MEASUREMENT IN CERAMIC DIP PACKAGE USING VDP SENSORS

8.1 Experimental Procedure

Due to the mismatch of coefficient of thermal expansion (CTE) of the various materials in electronic packaging, high temperature stresses can be induced during and after packaging process. In this section, the VDP device has been used to characterize the variation of die stress after the encapsulant process.

As shown in Fig. 8.1, an $7.22 \text{ mm} \times 4.54 \text{ mm}$ test chip was first attached to a ceramic dual in-line package (DIP) using an epoxy underfill material (ME525). Gold wires were then used to provide the interconnections from the die bond pads to the metal traces on the DIP. Before encapsulation, the initial resistance of the sensor was recorded every 25℃ from 25 - 125 ℃. To achieve a stable uniform temperature of the sample, the oven remained at each temperature for an hour before measurement. And then, the liquid encapsulant (ME525) were applied and the samples were cured in an oven for 30 minutes at 150℃ per vendor instructions (Figs. 8.2, 8.3). After removal from the cure oven, the samples were cooled to a room temperature environment of 25 ℃, after which the samples were placed in the oven again and the resistance of the sensor was monitored from 25 to 125℃. According to measured resistance changes, the stresses at the VDP device on the die surface were calculated. In this work, results for temperature compensated stress

component $(\sigma'_{11} - \sigma'_{22})$ is presented. Fig. 8.4 indicates the locations of VDP sensors and the chip coordinate system (primed coordinate system).

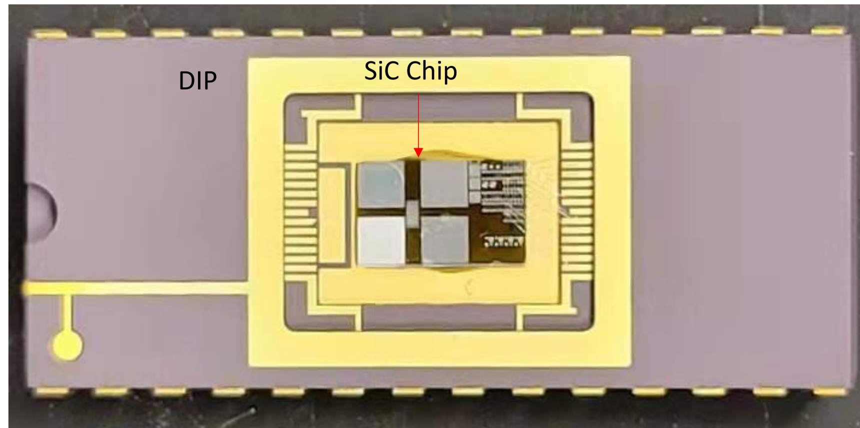

Figure 8.1: Ceramic DIP Before Encapsulation

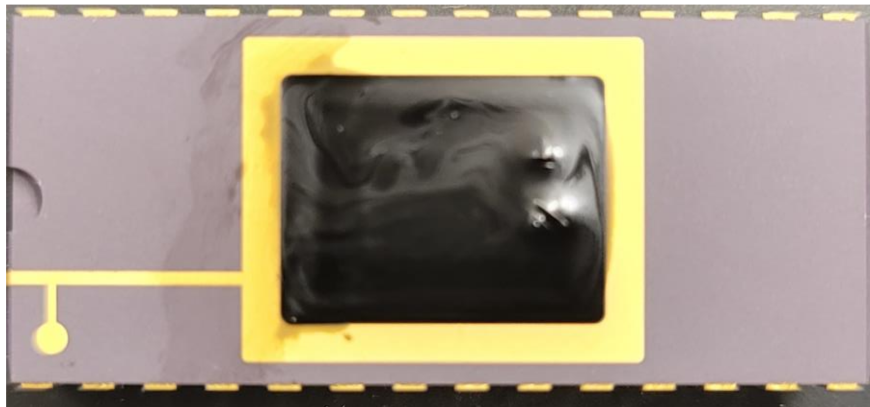

Figure 8.2: Ceramic DIP After Encapsulation

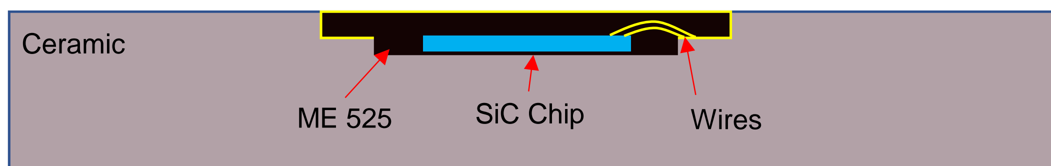

Figure 8.3: Schematic of the Encapsulated DIP (Cross Section)

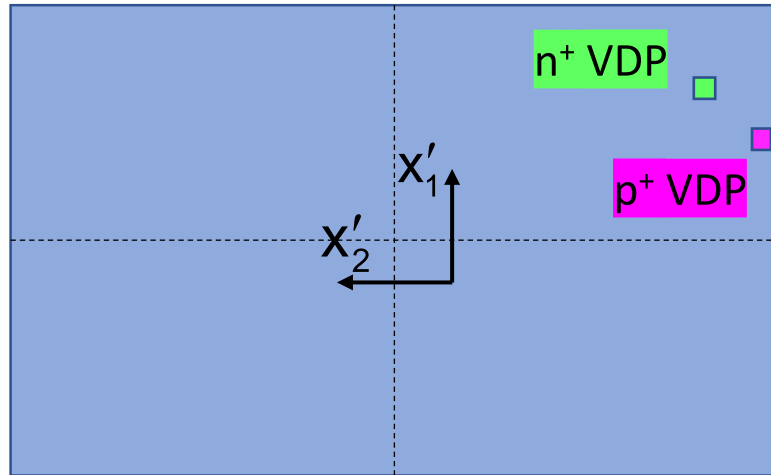

Figure 8.4: VDP Sensor Locations

8.2 Experimental Results

The resistance changes before and after encapsulation from 25-125 ℃ are collected and the in-plane normal stress difference $(\sigma'_{11} - \sigma'_{22})$ is calculated using Eq. 3.14. Since the piezoresistive coefficient π_D is a function of temperature, the π_D value used for this study is calculated from the fitted function in Fig. 3.12 and Fig. 3.22. The measured values of the in-plane normal stress difference $(\sigma'_{11} - \sigma'_{22})$ for p^+ VDP at various temperatures are shown in Table 8.1 and Fig. 8.5.

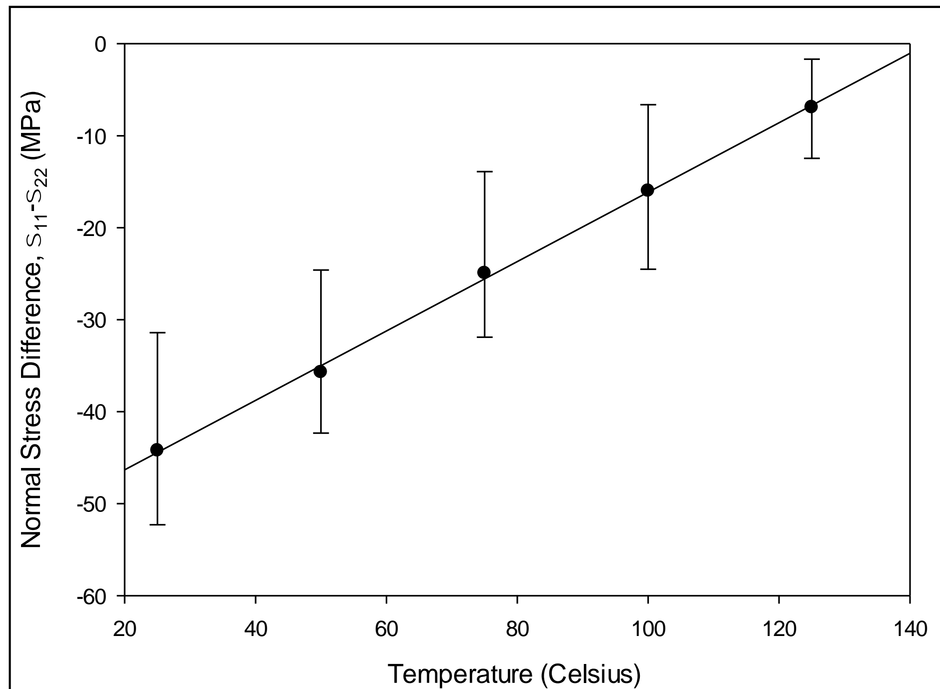

Figure 8.5: Normal Stress Difference vs. Temperature for p^+ VDP

P^+	Normal Stress Difference (MPa) at				
Sample Number	**25**℃	**50**℃	**75**℃	**100**℃	**125**℃
1	-52.3	-42	-31.9	-24.5	-8.5
2	-49.8	-42.3	-29.4	-18.9	-12.4
3	-31.4	-24.6	-13.9	-6.62	-1.68
4	-52.2	-40.7	-28.9	-18.4	-7.3
5	-35.5	-29	-20.7	-11.6	-4.59
Average	-44.2	-35.7	-24.9	-16	-6.9
Standard Deviation	10.3	8.7	7.3	5.8	4.5

Table 8.1: Normal Stress Difference vs. Temperature Data

The assembly is considered to be stress free above 135 ℃, which is the glass transition temperature of the encapsulant material. During the cooling, the encapsulant

becomes stiffer and would like to contract more than other components (SiC and ceramic). Therefore, individual stress components (σ_{11} and σ_{22}) are expected to be increasing as temperature decreases. However, the change of the combined stress component $(\sigma'_{11} - \sigma'_{22})$ is hard to predict directly due to the complexity of material properties and encapsulant shape.

Fig. 8.5 presents the results of measured stress difference $(\sigma'_{11} - \sigma'_{22})$ at different temperatures for p^+ VDP and the error bar shows the upper and lower limit of the measured data. It can be seen that the stress difference is small at 125 ℃ and increases linearly with the decreasing temperature and reaches maximum at 25 ℃. The standard deviations in Table. 8.1 is relatively large due to several factors. First, the piezoresistive coefficients π_D at various temperatures are average values (Fig. 3.12) and were assumed to be the same for each specimen. However, they are different from specimen to specimen. Since the SiC chip is attached on the DIP manually, the location and angle of the SiC chip is not identical for each specimen. Additionally, the thickness of the die attachment is difficult to control. More accurate and stable results require better consistency of packaging process and accurate piezoresistive coefficient of each sample.

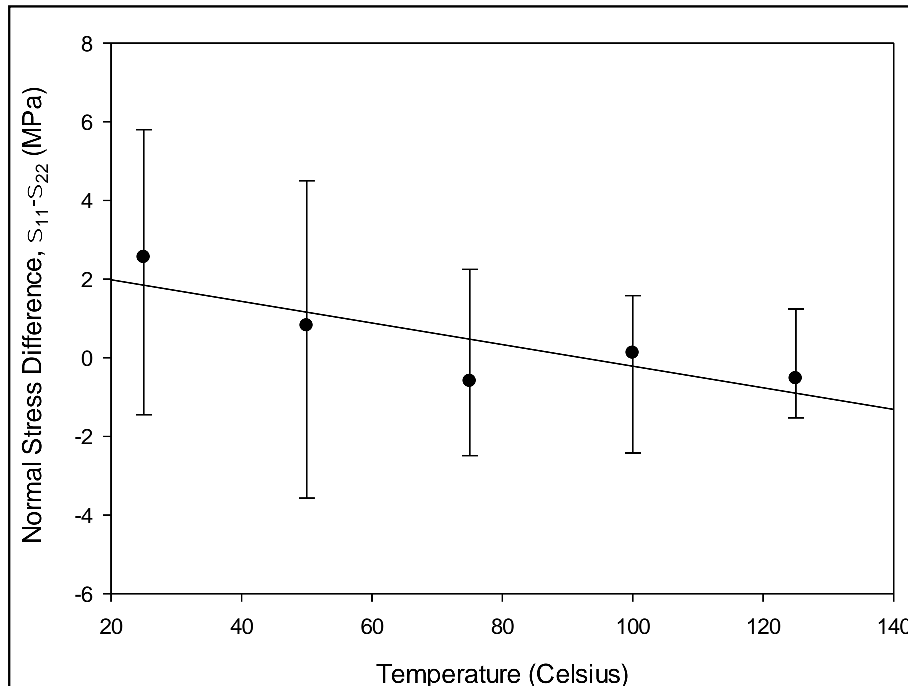

Figure 8.6: Normal Stress Difference vs. Temperature for n^+ VDP

The results for n^+ VDP measurement present in Fig. 8.6. It can be observed that the stress difference is around 2.5 MPa at 25℃ and starts to fluctuate near 0 MPa. Also, the sign of stress is changing and there is no obvious trend of the stress change.

8.3 FEA Simulation

The finite element simulation was performed using ANSYS 18.2. Fig. 8.7 shows the quarter model of the ceramic DIP package with encapsulated SiC chip. A schematic drawing of the package is shown in Fig. 8.8 with dimensions of all the components. Fig. 8.9 shows the developed mesh and finer mesh is applied to the volume of interest (near the SiC chip) as shown in Fig, 8.10.

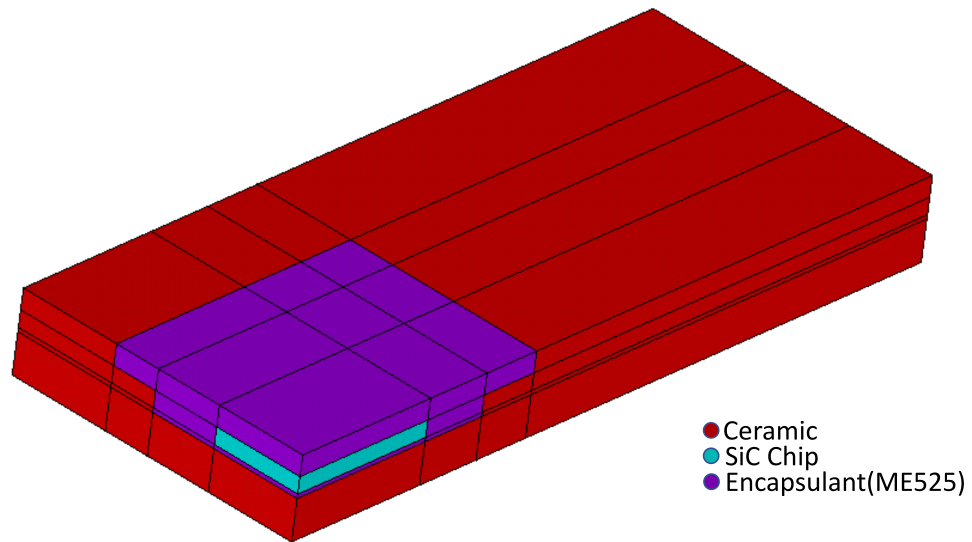

Figure 8.7: Quarter Model of Ceramic DIP

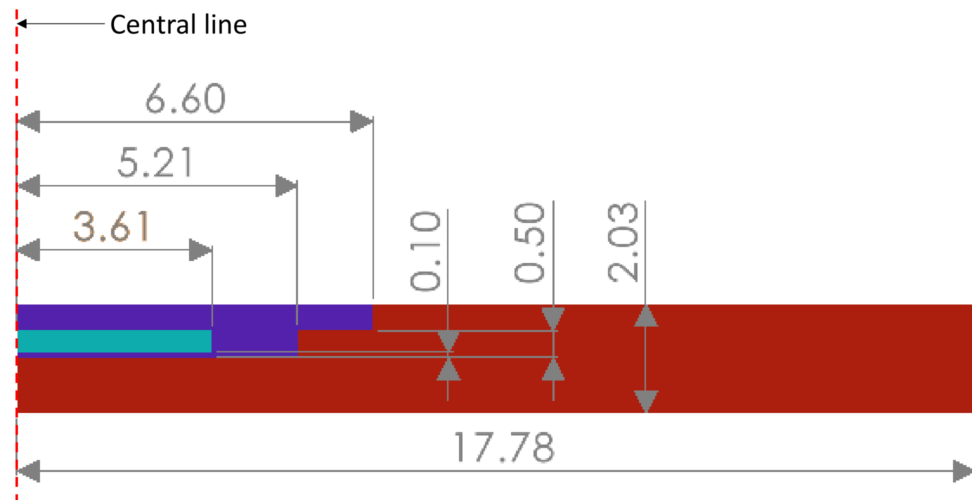

Figure 8.8: Dimensions of DIP in Millimeters

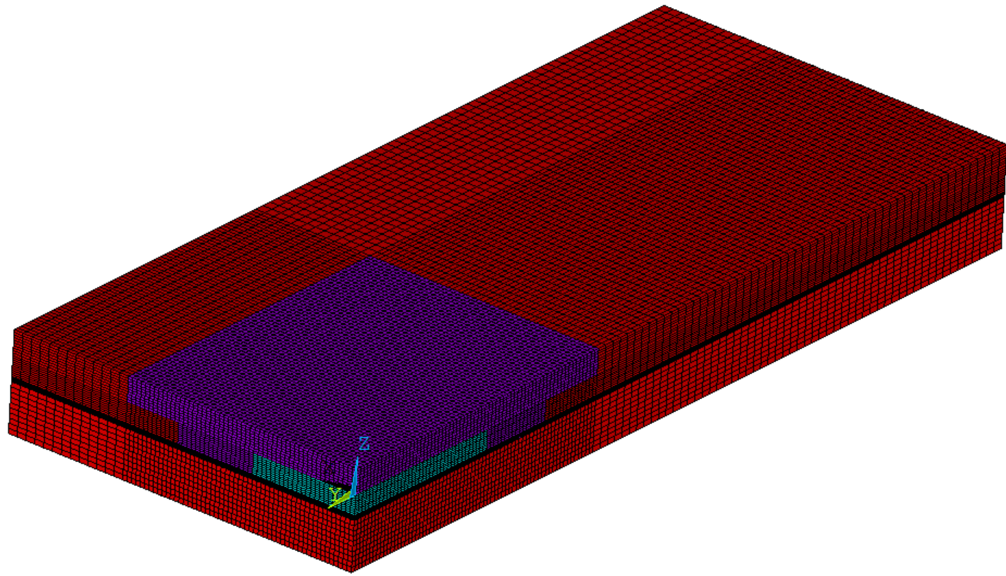

Figure 8.9: Meshed Quarter Model

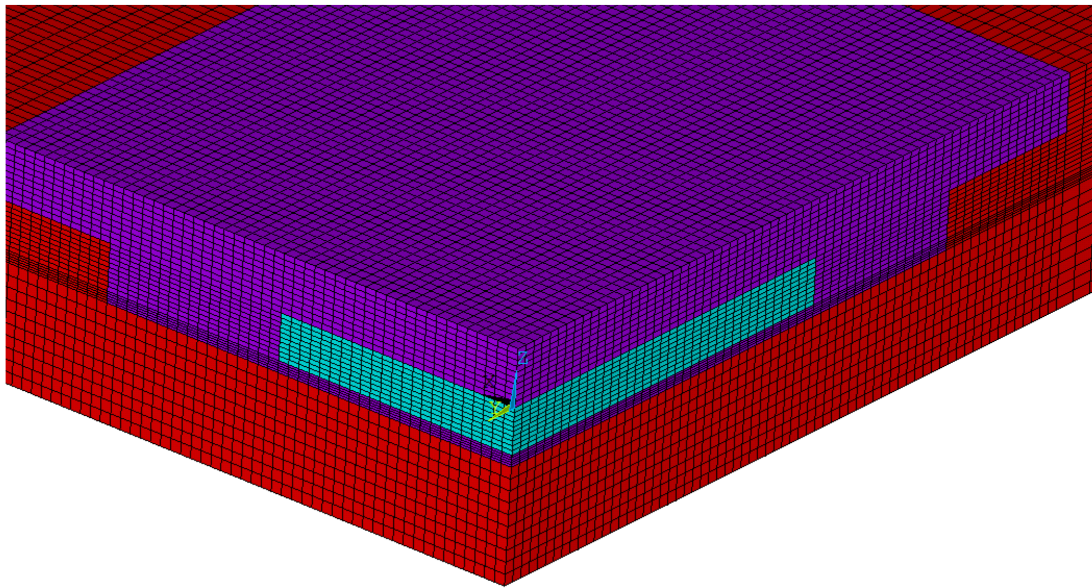

Figure 8.10: Detailed View of Mesh Near the Chip

To perform the simulation, elastic modulus, Poisson's ratio and the coefficient of thermal expansion (CTE) of each component are required.

As discussed in Chapter 7, the SiC is a transversely isotropic material and the elastic constants used for this study are from [114], which are shown in Table 7.5. The CTE of 4H-SiC is temperature and orientation dependent according to Li [125]. The CTE of 4H-SiC along a-axis (in-plane) and c-axis(out-of-plane) (Fig. 3.1) are expressed by the second-order polynomials:

$$a_{11} = 3.21\times10^{-6} + 3.56\times10^{-9}T - 1.62\times10^{-12}T^2 \ (1/^\circ C) \tag{8.1}$$

for the a-axis, and

$$a_{33} = 3.09\times10^{-6} + 2.63\times10^{-9}T - 1.08\times10^{-12}T^2 \ (1/^\circ C) \tag{8.2}$$

for the c-axis. They are illustrated in Fig. 8.11.

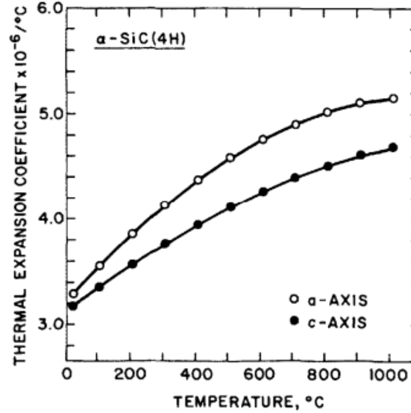

Figure 8. 11: The CTE of 4H-SiC, Reprinted From [125].

Chang [126] measured the elastic modulus change with temperature from 25 to 125 ℃. Fig. 8.12 shows the measured data and fitted curve and equation.

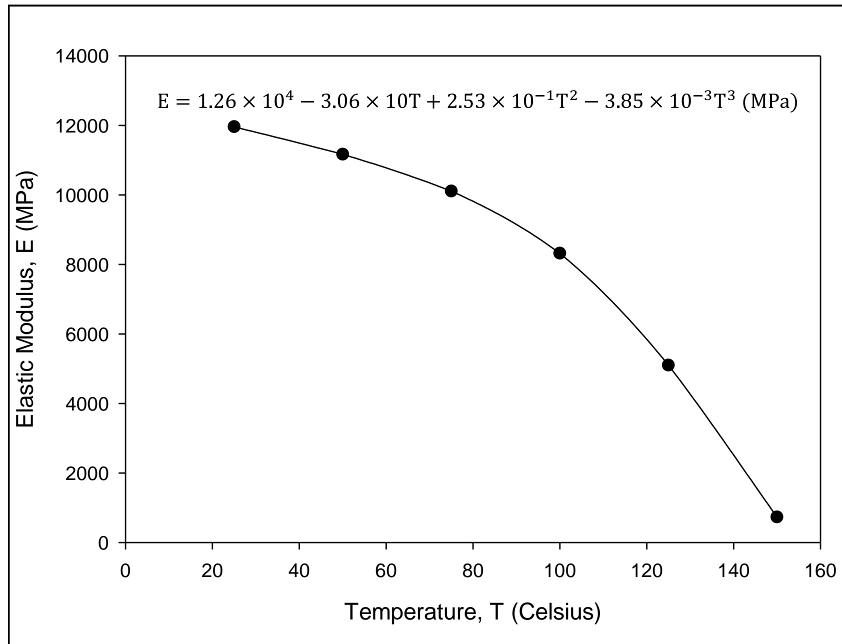

Figure 8.12: Elastic Modulus of Encapsulant at Different Temperatures

Poisson's ratio of ME525 is assumed to be 0.3 and temperature independent in this study. Chang also measured the CTE of the ME525 and the results are shown in Fig. 8.13. The glass transition temperature marks the boundary between the two regions, and CTE is 18.59 ppm/℃ and 72.61 ppm/℃, respectively, when the temperature is below and above the Tg.

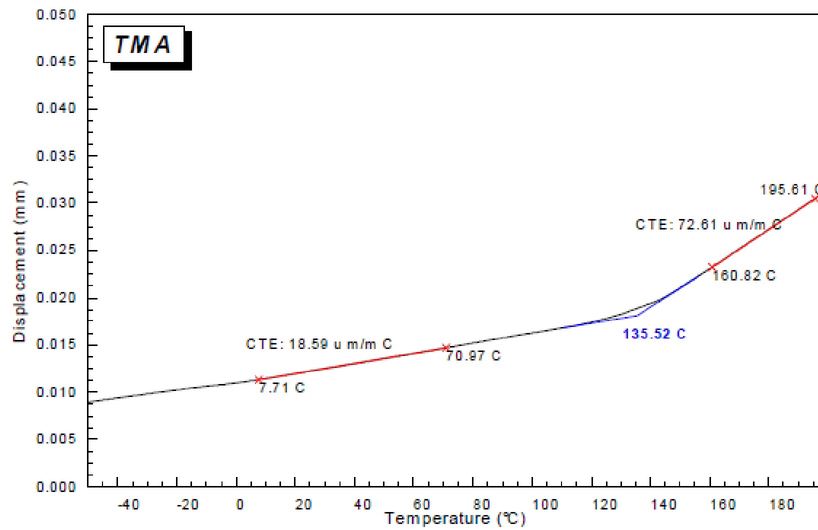

Figure 8.13: TMA Test Results for ME 525, Borrowed From [126].

The ceramic is considered to be an isotropic material and the elastic modulus and Poisson's ratio are 295 GPa and 0.23, respective. Comparing to ME525, ceramic has a much lower CTE of 5 ppm/℃.

Once the material properties are defined, a nonlinear FEA simulation is performed. The package is cooling from stress-free state at 150 ℃ to the room temperature at 25 ℃. Fig. 8.14-Fig. 8.18 shows the thermal stress developed on the die surface. In order to illustrate the stress change with decreasing temperature, the scale for each plot stays the same.

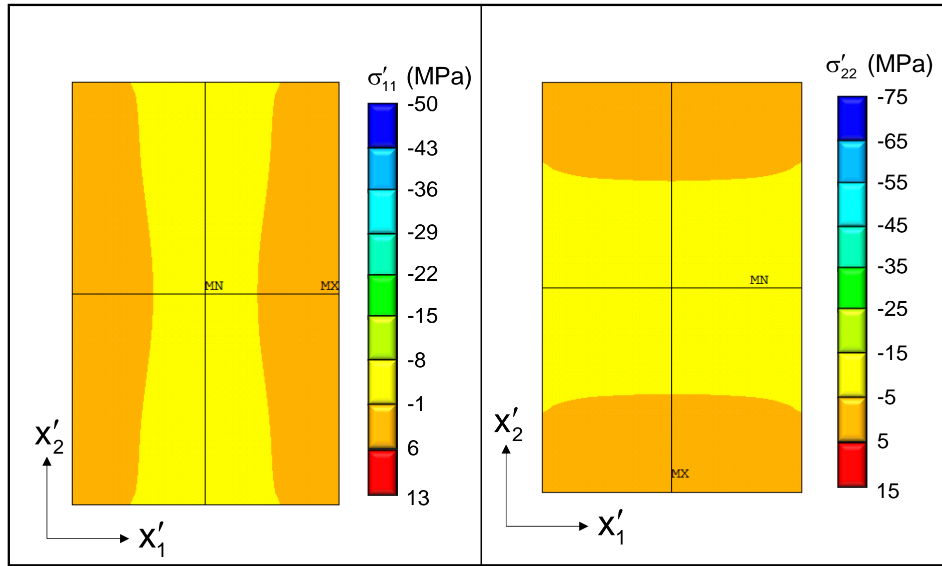

Figure 8.14: Simulation Results for σ'_{11} and σ'_{22} at 125 °C

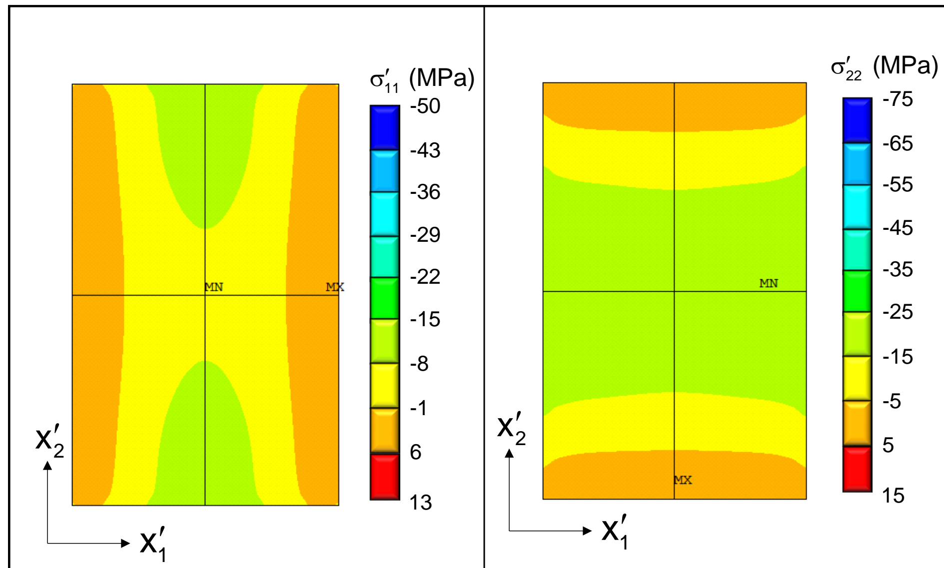

Figure 8.15: Simulation Results for σ'_{11} and σ'_{22} at 100 °C

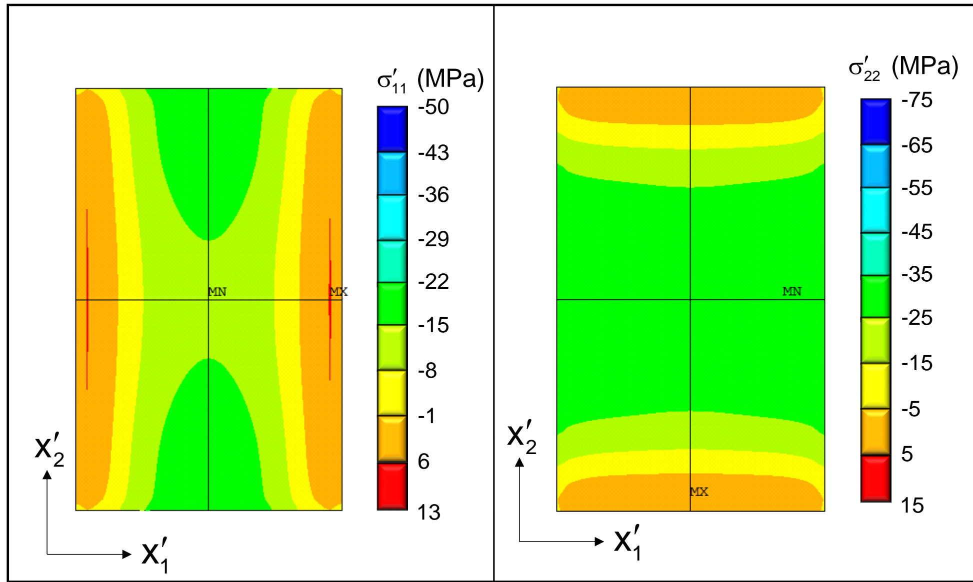

Figure 8.16: Simulation Results for σ'_{11} and σ'_{22} at 75 ℃

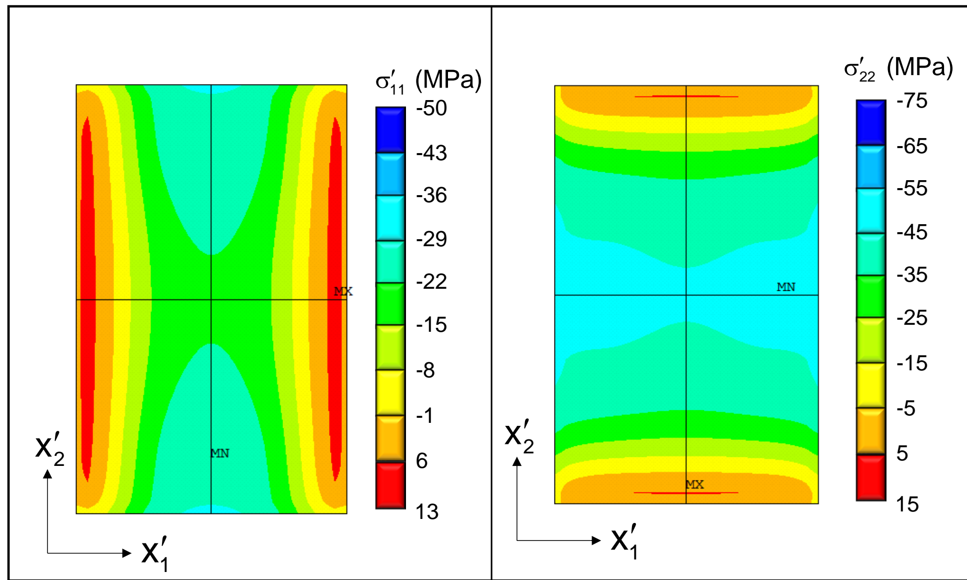

Figure 8.17: Simulation Results for σ'_{11} and σ'_{22} at 50 ℃

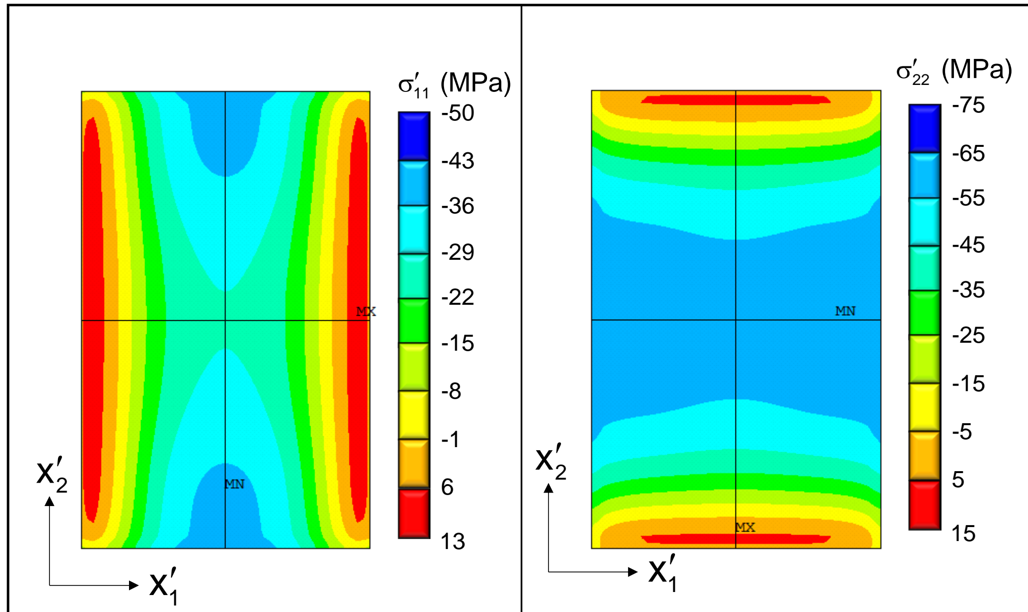

Figure 8.18: Simulation Results for σ'_{11} and σ'_{22} at 25 ℃

As expected, increases in the stress magnitudes were observed when the temperature was decreasing. Since SiC and ceramic have similar CTE, the thermal stress is mainly caused by encapsulant material. Fig. 8.14 shows that the die stress levels are very low when the temperature is near the glass transition temperature of the encapsulant.

The following figures show the correlation between the experimental measurements and finite element predictions for the stress difference $\sigma'_{11} - \sigma'_{22}$. The contours are the stress distributions predicted by the finite element model. Each of small squares within these contours locates a VDP sensor and the color of the square represents the experimental value of stress in the same scale with the finite element contour.

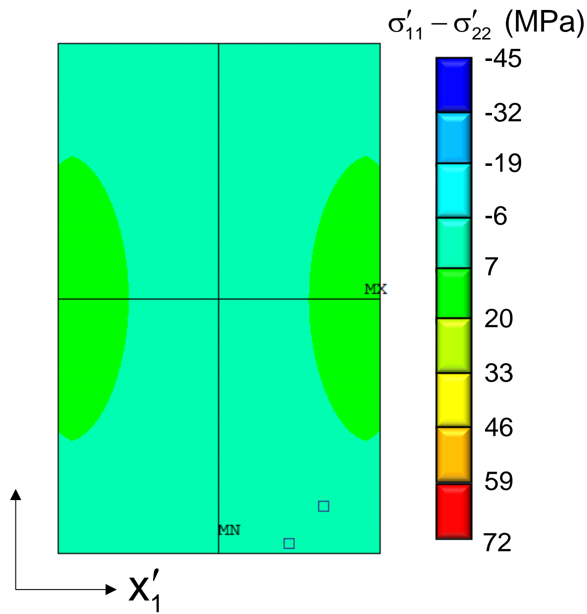

Figure 8.19: Stress Difference ($\sigma'_{11} - \sigma'_{22}$) Correlations at 125 ℃

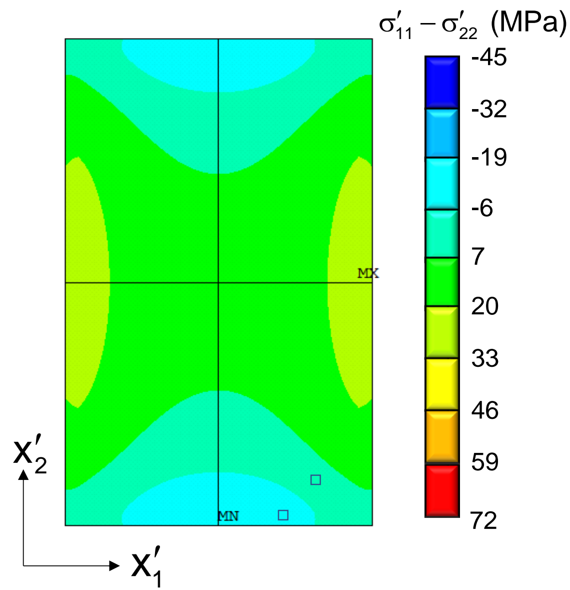

Figure 8.20: Stress Difference ($\sigma'_{11} - \sigma'_{22}$) Correlations at 100 ℃

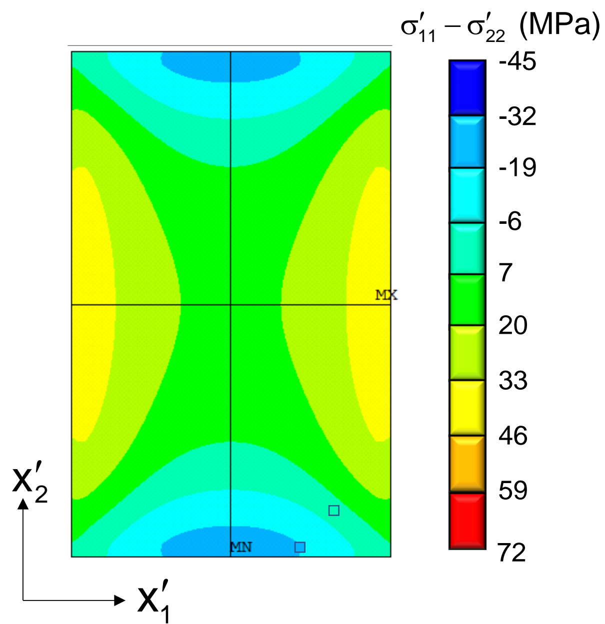

Figure 8.21: Stress Difference ($\sigma'_{11} - \sigma'_{22}$) Correlations at 75 °C

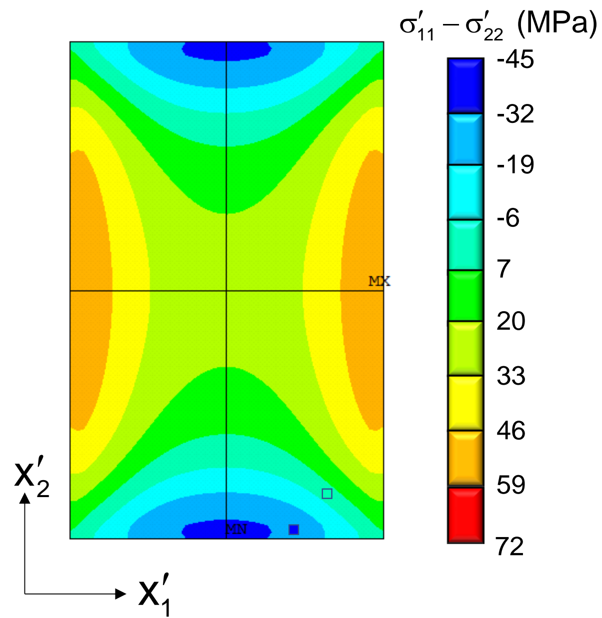

Figure 8.22: Stress Difference ($\sigma'_{11} - \sigma'_{22}$) Correlations at 50 °C

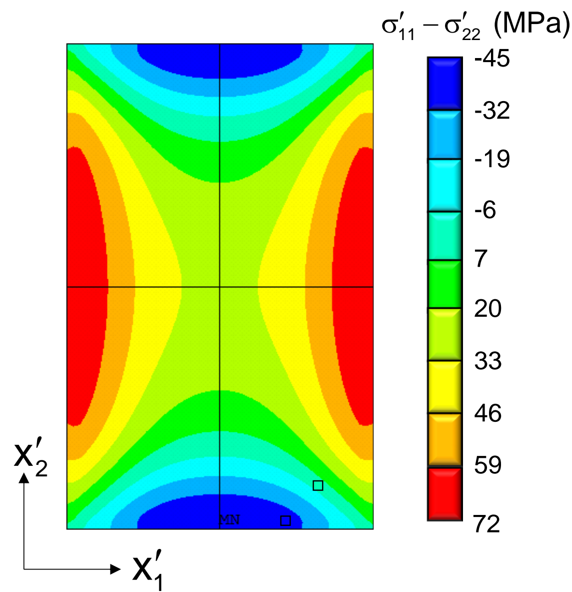

Figure 8.23: Stress Difference ($\sigma'_{11} - \sigma'_{22}$) Correlations at 25 ℃

Fig. 8.24 and Fig. 8.25 compare the simulated stress values at sensor locations and experimental results. Note that only the experimental results have the error bar, which shows upper and lower limits of the measured stress. It can be seen that the stress difference changes almost linearly with the temperature based on the simulation results. The finite element predictions for the normal stress difference are in good agreement with the experimental results of p^+ VDP sensors. Even though the standard deviations are relatively large, the averages of the measurements still provide good results, especially at 25 ℃.

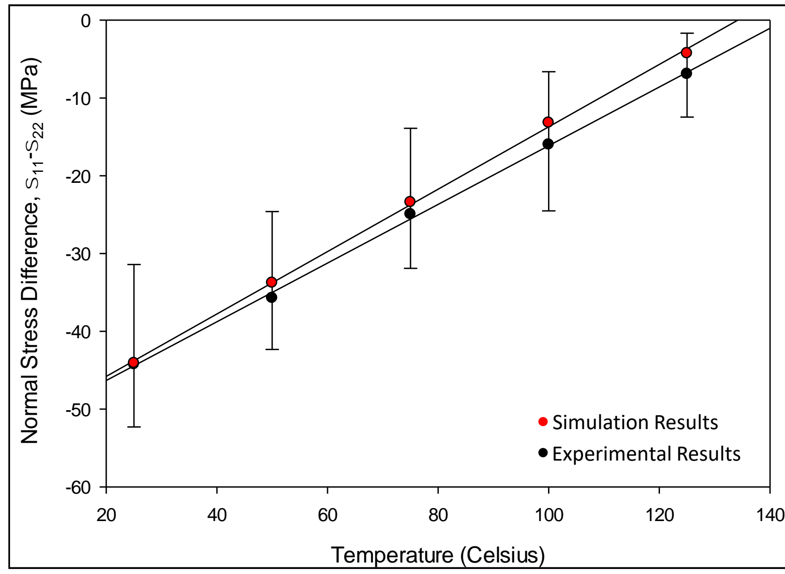

Figure 8.24: Comparison Between Simulation and Experimental Results for p^+ VDP

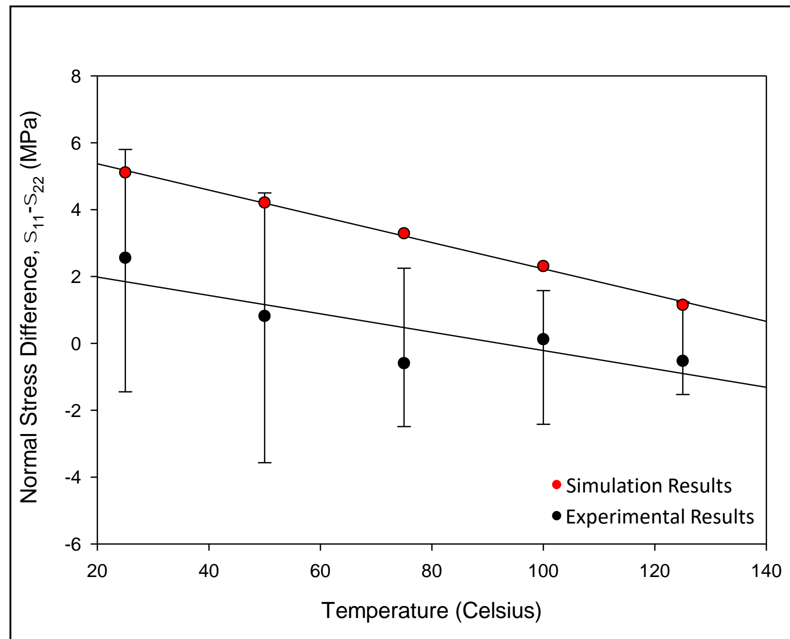

Figure 8.25: Comparison Between Simulation and Experimental Results for n^+ VDP

The simulation shows that the stress difference values at the n+ VDP location are small and positive and keep decreasing with increasing temperature. However, the average values of the measured stress fluctuate and change signs during the experiment. The stress sensors may have reached the resolution limit of the experimental method. Another reason could be that the n+ sensor is positioned on the boundary between positive and negative stresses. In Fig. 8.26, the green square shows the position of n+ sensor on the die surface and non-uniform stress contours are applied to better present the stress values near the sensor. A slight change of position makes a large difference in stress values.

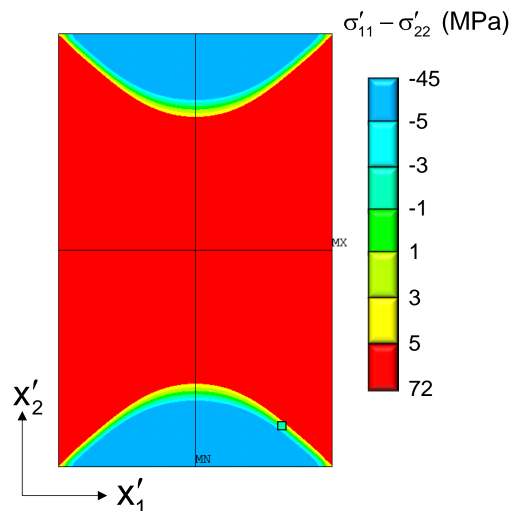

Figure 8.26: Stress Distributions near the n+ Sensor at 25°C

8.4 Summary

In this work, both n+ and p+ VDP sensors were used to characterize the variation of die stress during the encapsulant process at different temperatures. The temperature compensated stress component $(\sigma'_{11} - \sigma'_{22})$ is calculated using the measured resistance change before and after encapsulation and the piezoresistive coefficients calibrated in early

chapters. Five sets of measurement were performed and the results from p^+ VDP sensor show that the stress difference $(\sigma'_{11} - \sigma'_{22})$ increased linearity with decreasing temperature. Also, relatively large standard deviations between samples were observed because of piezoresistive coefficients variations and the manually controlled packaging process. If each sensor was carefully calibrated prior to experiment and packaging process was well controlled, better accuracy should be achieved. The measured stress values from the n^+ sensor are small and very sensitive to exact positions of the sensors.

Three-dimensional nonlinear finite element simulation was also performed. The results show that the normal stress difference $(\sigma'_{11} - \sigma'_{22})$ has a negative value near the top and bottom edges of the chip and positive value near the side edges. The experimental stress results from p^+ sensors were in good agreement with the finite element predictions. At 25 °C, the simulated stress value for the n^+ sensor is 5 MPa, which is relatively low and might approach the resolution limits of the SiC sensors. Also, the n^+ sensor is located in the “changing sign” region and small misalignment of the assembly may cause changes in signs.

Chapter 9

SUMMARY AND FUTURE WORK

9.1 Summary

This work has developed general expressions for the stress dependence of resistors and van der Pauw devices on standard 4H-SiC wafer. The theoretical results present the similarities and differences relative to the stress sensors on (100) silicon: only four of the six components of the stress state can be measured; a four-element element rosette design exists for measuring the in-plane stress components; two stress quantities can be measured in a temperature compensated manner. However, the piezoresistance of 4H-SiC in (0001) plane is isotropic and only one combined coefficient is required for temperature compensated stress measurements. For a free top surface, the three individual in-plane stresses can also be resolved, but the extraction is no longer temperature independent. The VDP devices exhibit the expected 3.16 times higher stress sensitivity than standard resistor rosettes.

A four-point-bending technique has been used to calibrate the basic lateral and transverse piezoresistance coefficients at different temperatures. It has been found that the sensitivity goes down linearly with increasing temperature from 25 to 180 ℃. Compared to silicon, 4H-SiC possesses smaller piezoresistive coefficients. However, with excellent mechanical strength, thermal stability and electrical conductivity, 4H-SiC sensors are still promising for harsh environment applications.

The out-of-plane normal stress can be measured with a resistive rosette, which requires out-of-plane piezoresistive coefficients π_{13} for both n and p type resistors. hydrostatic calibration was used to obtain π_{13} in this study. Prior to the calibration, the TCR values were characterized. The extracted π_{13} is -80 /TPa for p^+ VDP, but the pressure induced resistance change for n+ VDP is not observable, due to its low reference resistance.

The theory for stress dependence of NMOS transistors on 4H-SiC was developed. The stress model considers both mobility and threshold voltage changes. At low values of gate drive, the threshold voltage terms in the stress model becomes significant and can no longer be ignored. The measured piezoresistive coefficients are relatively small but can become large at low gate drives. Similar to resistive sensors, a four-element NMOS stress sensor was proposed that can measure two temperature compensated stress quantities.

The impact of tilted wafer plane on the sensor calibration was discussed. The 4 degree tilted angle for our samples was determined by electron backscattering diffraction analysis. The errors induced by the tilted wafer plane are found to be small if all piezoresistive coefficients for 4H-SiC have similar values. The off-axis effect on silicon sensors was also studied and a case study was performed. The theoretical results show that the errors are highly dependent on the off-axis angle and the stress distributions.

Since the mechanical properties may change after the micro-electronical fabrication process (e.g., annealing after ion implantation), we also investigate the elastic properties of 4H-SiC using four-point bending, strain gauge, and nano-indentation methods. Using the coordination transformation, we found the elastic property within the (0001) plane is

identical, which means 4H-SiC is a transversely isotropic material. The measured elastic modulus and Poisson's ratio are eventually compared with other studies.

Finally, SiC chips were encapsulated in a ceramic dual-in line package and the thermal stress was monitored with VDP sensors. A non-linear finite-element analysis was performed. Good agreement was achieved between the experiment and the simulation.

9.2 Recommendations for Future Work

The current study discussed the basic theory for embedded 4H-SiC piezoresistive stress sensors and there are several opportunities for future work:

The calibration temperature range for the current study is limited by the flex circuit. If a test strip can be redesigned using zero-insertion force (ZIF) connectors [39], calibration at much higher temperature can be achieved.

The off-axis errors are strongly dependent on the value of basic piezoresistive coefficients. Hence, it is worth to discover all fundamental piezoresistive coefficients, based on which new stress sensors can be developed. Additionally, it can help optimizing the current MEMS sensors by using higher piezoresistive components. Also, we can explore whether other isotropic planes exist in 4H-SiC.

The coefficients of NMOS reported in this study are relatively small for large gate drive. To achieve higher sensitivity, the transistor sensors can be directly implemented with a multi-terminal inversion-layer van der Pauw structure. The out-of-plane piezoresistive coefficients of NMOS can be extracted using the hydrostatic calibration. Also, the piezoresistive effects on PMOS have not been investigated.

In this work, we only measured the normal stress difference at two locations. By placing different stress sensors at different locations on the die surface, more stress components at more

positions can be measured. The stress distribution on packaged chips can be monitored in harsh environments using a well-designed test chip.

REFERENCES

[1] Elasser, A., and Chow, T. P., "Silicon Carbide Benefits and Advantages for Power Electronics Circuits and Systems," *Proceedings of the IEEE*, 90(6), pp. 969-986, 2002.

[2] Zolper, J. C., "Emerging Silicon Carbide Power Electronics Components," *In Twentieth Annual IEEE Applied Power Electronics Conference and Exposition*, pp. 11-17, 2005.

[3] Rabkowski, J., Peftitsis, D., and Nee, H. P., "Silicon Carbide Power Transistors: A new Era in Power Electronics is Initiated," *IEEE Industrial Electronics Magazine*, 6(2), pp. 17-26, 2012.

[4] She, X., Huang, A. Q., Lucía, Ó., and Ozpineci, B., "Review of Silicon Carbide Power Devices and Their Applications," *IEEE Transactions on Industrial Electronics*, 64(10), pp. 8193-8205, 2017.

[5] Kassakian, J. G., and Jahns, T. M., "Evolving and Emerging Applications of Power Electronics in Systems," *IEEE Journal of Emerging and Selected Topics in Power Electronics*, 1(2), pp. 47–58, 2013.

[6] J. D. Van Wyk and F. C. Lee, "On a Future for Power Electronics," *IEEE Journal of Emerging and Selected Topics in Power Electronics*, 1(2), pp. 59–72, 2013.

[7] Seal, S., and Mantooth, H. A., "High Performance Silicon Carbide Power Packaging—Past Trends, Present Practices, and Future Directions," *Energies*, 10(3), pp. 341, 2017.

[8] Hÿtch, M., Houdellier, F., Hüe, F., and Snoeck, E., "Nanoscale Holographic Interferometry for Strain Measurements in Electronic Devices," *Nature*, 453(7198), pp. 1086-1089, 2008.

[9] Miller, M. R., Mohammed, I., and Ho, P. S., "Quantitative Strain Analysis of Flip-chip Electronic Packages Using Phase-shifting Moiré Interferometry," *Optics and Lasers in Engineering*, 36(2), 127-139, 2001.

[10] Zou, Y., Suhling, J. C., Johnson, R. W., and Jaeger, R. C., "Complete Stress State Measurements in Chip on Board Packages," *International Conference on Multichip Modules and High-Density Packaging*, Cat. No. 98EX154, pp. 405-415, 1998.

[11] Zou, Y., Suhling, J. C., Johnson, R. W., Jaeger, R. C., and Mian, A. K. M., "In-situ Stress State Measurements During Chip-on-board Assembly," *IEEE Transactions on Electronics Packaging Manufacturing*, 22(1), pp. 38-52, 1999.

[12] Palczynska, A., Prisacaru, A., Gromala, P. J., Han, B., Mayer, D., and Melz, T. "Towards Prognostics and Health Monitoring: The Potential of Fault Detection by Piezoresistive Silicon Stress Sensor," *EuroSimE*, pp. 1-8,2016.

[13] Prisacaru, A., Palczynska, A., Theissler, A., Gromala, P., Han, B., and Zhang, G. Q., "In-Situ Failure Detection of Electronic Control Units Using Piezoresistive Stress Sensor," *IEEE Transactions on Components Packaging and Manufacturing Technology*, 8(5), pp. 750-763, 2018.

[14] Fraga, M. A., Furlan, H., Pessoa, R. S., and Massi, M., "Wide Bandgap Semiconductor Thin Films for Piezoelectric and Piezoresistive MEMS Sensors Applied at High Temperatures: an Overview," *Microsystem technologies*, 20(1), pp. 9-21, 2014.

[15] Mehregany, M., and Zorman, C. A., "SiC MEMS: Opportunities and Challenges for Applications in Harsh Environments," *Thin solid films*, 355, pp. 518-524, 1999.

[16] Sarro, P. M., "Silicon Carbide as a New MEMS Technology," *Sensors and Actuators A: Physical*, 82(1-3), pp. 210-218, 2000.

[17] Azevedo, R. G., Jones, D. G., Jog, A. V., Jamshidi, B., Myers, D. R., Chen, Pisano, A. P., "A SiC MEMS Resonant Strain Sensor for Harsh Environment Applications," *IEEE Sensors Journal*, 7(4), pp. 568-576, 2007.

[18] Wright, N. G., Horsfall, A. B.,Vassilevski, K., "Prospects for SiC Electronics and Sensors," *Materials Today*, 11(1-2), pp. 16-21, 2008.

[19] Backes, W. H., Bobbert, P. A., and Van Haeringen, W., "Energy-band Structure of SiC Polytypes by Interface Matching Of Electronic Wave Functions," *Physical Review B*, 49(11), pp. 7564, 1994.

[20] Thomson, W. XIX., "On the Electro-dynamic Qualities of Metals: Effects of Magnetization on the Electric Conductivity of Nickel and of Iron," *Proceedings of the Royal Society of London*, (8), pp. 546-550, 1857.

[21] Tomlinson, H., "On The Increase In Resistance to The passage Of an Electric Current Produced on Wires By Stretching," *Proc. R. Soc. London*, 25, pp. 451–453, 1876.

[22] Tomlinson, H., "The Influence of Stress and Strain on the Action of Physical Forces," *Philos. Trans. R. Soc. London*, 174, pp. 1–172, 1883.

[23] Bardeen, J., and Shockley, W.,"Deformation Potentials and Mobilities in Non-polar Crystals," *Physical Review*, 80(1), 72, 1950.

[24] Smith, C. S., "Piezoresistance Effect in Germanium and Silicon," *Physical Review*, 94(1), 42, 1954.

[25] Mason, W. P., and Thurston, R. N., "Use of Piezoresistive Materials in the Measurement of Displacement, Force, and Torque," *The Journal of the Acoustical Society of America*, 29(10), pp. 1096-1101, 1957.

[26] Hoerni, J. A., "Planar Silicon Diodes and Transistors," *In 1960 International Electron Devices Meeting*, pp. 50-50, 1960.

[27] Barlian, A. A., Park, W. T., Mallon, J. R., Rastegar, A. J., and Pruitt, B. L., "Semiconductor Piezoresistance for Microsystems," *Proceedings of the IEEE*, 97(3), pp. 513-552, 2009.

[28] Bittle, D. A., Suhling, J. C., Beaty, R. E., Jaeger, R. C., and Johnson, R. W., "Piezoresistive Stress Sensors for Structural Analysis of Electronic Packages," *J. Electron. Packag.*, pp. 203-215, 1991.

[29] Suhling, J. C., and Jaeger, R. C., "Silicon Piezoresistive Stress Sensors and Their Application in Electronic Packaging," *IEEE Sensors Journal*, 1(1), pp. 14-30, 2001.

[30] Edwards, D., Heinen, K., Groothuis, S., and Martinez, J., "Shear Stress Evaluation of Plastic Packages," *IEEE Transactions on Components, Hybrids, and Manufacturing Technology*, 10(4), pp. 618-627, 1987.

[31] Edwards, D., Heinen, G., Bednarz, G., and Schroen, W., "Test Structure Methodology of IC Package Material Characterization," *IEEE Transactions on Components, Hybrids, and Manufacturing Technology*, 6(4), pp. 560-567, 1983.

[32] Spencer, J. L., Schroen, W. F., Bednarz, G. A., Bryan, J. A., Metzgar, T. D., Cleveland, R. D., and Edwards, D. R., "New Quantitative Measurements of IC Stress Introduced by Plastic Packages," *In 19th International Reliability Physics Symposium*, pp. 74-80, 1981.

[33] Beaty, R. E., Suhling, J. C., Moody, C. A., Bittle, D. A., Johnson, R. W., Butler, R. D., and Jaeger, R. C., "Calibration Considerations for Piezoresistive-based Stress Sensors," *In 40th Conference Proceedings on Electronic Components and Technology*, pp. 797-806, 1990.

[34] Natarajan, B., and Bhattacharyya, B., "Die Surface Stresses in a Molded Plastic Package," *Proceedings of the 36th IEEE Electronic Components Conference*, pp. 544-551, 1986.

[35] Gee, S. A., Akylas, V. R., and Van Den Bogert, W. F., "The Design and Calibration of a Semiconductor Strain Gauge Array," *Proceedings of the 1988 IEEE International Conference on Microelectronic Test Structures*, pp. 185-191, 1988.

[36] Gee, S. A., Van Den Bogert, W. F., and Akylas, V. R., "Strain-Gauge Mapping of Die Surface Stresses," *IEEE Transactions on Components, Hybrids, and Manufacturing Technology*, 12(4), pp. 587-593, 1989.

[37] Tufte, O. N., and Stelzer, E. L., "Piezoresistive Properties of Silicon Diffused Layers," *Journal of Applied Physics*, 34(2), pp. 313-318, 1963.

[38] Tufte, O. N., and Stelzer, E. L., "Piezoresistive Properties of Heavily Doped n-type Silicon," *Physical Review*, 133(6A), A1705, 1964.

[39] Gharib, H. M. H., "An Investigation of Using n-Si Piezoresistive Behavior to Develop a Three-Dimensional Stress Sensing Rosette," *PhD Dissertation*, University of Alberta, 2013.

[40] Mian, A. K. M., Suhling, J. C., and Jaeger, R. C., "The van der Pauw Stress Sensor," *IEEE Sensors Journal*, 6(2), pp. 340-356, 2006.

[41] Ramani, R., "Piezoresistive Behaviour of MOSFET and FET-based Stress Sensor Circuits," *PhD Dissertation*, Auburn University, 1996.

[42] Bradley, A. T., "Piezoresistive Behavior of MOSFETs and MOS Circuits," *PhD Dissertation*, Auburn University, 1999.

[43] Jaeger, R. C., Suhling, J. C., Ramani, R., Bradley, A. T., and Xu, J., "CMOS Stress Sensors on [100] Silicon," *IEEE Journal of Solid-state Circuits*, 35(1), pp. 85-95, 2000.

[44] Hussain, S., Jaeger, R. C., and Suhling, J. C., "Current Dependence of the Piezoresistive Coefficients of CMOS FETs on (100) silicon," *In 2014 44th European Solid State Device Research Conference*, pp. 74-77, 2014.

[45] Jaeger, R. C., and Suhling, J. C., "First and Second Order Piezoresistive Characteristics of CMOS FETs: Weak Through Strong Inversion," *In 2018 48th European Solid-State Device Research Conference*, pp. 126-129, 2018.

[46] Baumann, M., Gieschke, P., Lemke, B., and Paul, O., "CMOS Sensor Chip with A 10 by 10 Array of Unit Cells for Mapping Five Stress Components and Temperature," *In 2010 IEEE 23rd International Conference on Micro Electro Mechanical Systems,* pp. 604-607, 2010.

[47] Verma, A.R. and Krishna, P., *Polymorphism and Polytypism in Crystals*, John Wiley and Sons, Inc., 1966.

[48] Cheng, C., Needs, R.J. and Heine, V., "Inter-layer Interactions and the Origin of SiC Polytpes," *Journal of Physics C: Solid State Physics,* 21(6), pp. 1049, 1988.

[49] Denteneer, P.J.H. and van Haeringen, W., "Ground-state Properties of Polytypes of Silicon Carbide," *Physical Review B,* 33(4), pp. 2831, 1986.

[50] Fisher, G. R., and Barnes, P., "Towards a Unified View of Polytypism in Silicon Carbide," *Philosophical Magazine B*, 61(2), pp. 217-236, 1990.

[51] Tsunenobu K., James, A., C., *Fundamentals of Silicon Carbide Technology: Growth, Characterization, Devices and Applications*, Wiley-IEEE Press, 2014.

[52] Wijesundara, M., Azevedo, R., "Silicon Carbide Microsystems for Harsh Environments," *Springer Science and Business Media*, 22, 2011.

[53] Cheung, R., *Silicon Carbide Microelectromechanical Systems for Harsh Environments*, World Scientific, 2006.

[54] Cimalla, V., Pezoldt, J., and Ambacher, O., "Group III Nitride and SiC Based MEMS and NEMS: Materials Properties," *Technology and Applications. Journal of Physics D: Applied Physics*, 40(20), pp. 6386, 2007.

[55] Choyke, W. J., Matsunami, H., Pensl, G., "Silicon Carbide: Recent Major Advances," *Springer Science and Business Media*, 2013.

[56] Cho, S., Chasiotis, I., Friedmann, T. A., and Sullivan, J. P., "Young's Modulus, Poisson's Ratio and Failure Properties of Tetrahedral Amorphous Diamond-like Carbon for MEMS Devices," *Journal of Micromechanics and Microengineering*, 15(4), pp. 728, 2005.

[57] Nakamura K., Toriyama, T., and Sugiyama S., "Analysis on Piezoresistive Property of Silicon Carbide on the Basis of First-principles Calculation," *In Proc. 27th Sensor Symp. Sensors, Micromach., Appl.Syst*., pp. 1–6, 2010.

[58] Akiyama, T., Briand, D., De Rooij, N. F., "Design-dependent Gauge Factors of Highly Doped n-type 4H-SiC Piezoresistors," *Journal of Micromechanics and Microengineering*, 22(8), 085034, 2012.

[59] Okojie, R. S., Lukco, D., Nguyen, V., Savrun, E., "4H-SiC Piezoresistive Pressure Sensors at 800 C with Observed Sensitivity Recovery," *IEEE Electron Device Letters*, 36(2), pp. 174-176, 2014.

[60] Nguyen, T. K., Phan, H. P., Dinh, T., Han, J., Dimitrijev, S., Tanner, P., Dao, D. V., "Experimental Investigation of Piezoresistive Effect in p-type 4H–SiC," *IEEE Electron Device Letters*, 38(7), pp. 955-958, 2017.

[61] Nguyen, T. K., Phan, H. P., Dinh, T., Foisal, A. R. M., Nguyen, N. T., and Dao, D. V., "High-temperature Tolerance of the Piezoresistive Effect in p-4H-SiC for Harsh Environment Sensing," *Journal of Materials Chemistry C*, 6(32), pp. 8613-8617, 2018.

[62] Smith, C.S., "Macroscopic Symmetry and Properties of Crystals," *Solid State Physics*, 6, pp. 175-249, 1958.

[63] Jaeger, R. C., Motalab, M., Hussain, S., and Suhling, J. C., "Four-wire Bridge Measurements of Silicon van der Pauw Stress Sensors," *Journal of Electronic Packaging*, 136(4), 041014, 2014.

[64] Jaeger, R. C., Suhling, J. C., Chen, J., "Diagonal Mode van der Pauw Stress Sensors: Proof of Diagonal-Mode Conjecture," *Journal of Electronic Packaging*, 140(4), 044501, 2018.

[65] Asada, S., Suda, J., Kimoto, T., "Analytical Formula for Temperature Dependence of Resistivity in p-type 4H-SiC with Wide-range Doping Concentrations," *Japanese Journal of Applied Physics*, 57(8), 088002, 2018.

[66] Dinh, T, Nguyen, T K, Phan, H P., "Thermoresistance of p-Type 4H-SiC Integrated MEMS Devices for High-Temperature Sensing," *Advanced Engineering Materials*, 21(3), 1801049, 2019.

[67] Yonggang, C., "CMOS Stress Sensor Circuit," *PhD Dissertation*, Auburn University, 2006.

[68] Colman, D., Bate, R. T., Mize, J. P., "Mobility Anisotropy and Piezoresistance in Silicon p-Type Inversion Layers," *Journal of Applied Physics*, 39(4), pp. 1923-1931, 1968.

[69] Dorey, A. P., and Maddern, T. S.,"The Effect of Strain on MOS Transistors," *Solid-State Electronics*, 12(3), pp. 185-189. 1969.

[70] Mikoshiba, H., "Stress-sensitive Properties of Silicon-gate MOS Devices," *Solid-State Electronics*, 24(3), pp. 221-232, 1981.

[71] Hamada, A., Furusawa, T., Saito, N., and Takeda, E., "A New Aspect of Mechanical Stress Effects in Scaled MOS Devices," *IEEE Transactions on Electron Devices*, 38(4), pp. 895-900, 1991.

[72] Wanga, Z. Z., Suski, J., Collard, D., Dubois, E., "Piezoresistivity Effects in N-MOSFET Devices," *Sensors and Actuators A: Physical*, 34(1), pp. 59-65, 1992.

[73] Miura, H., and Nishimura, A., "Device Characteristic Changes Caused by Packaging Stress," *Applied Mechanics Division,* 195, pp. 101-109, 1994.

[74] Jaeger, R. C., Ramani, R., Suling, J. C., "Effects of Stress-induced Mismatches on CMOS Analog Circuits," *In 1995 International Symposium on VLSI Technology, Systems, and Applications*, pp. 354-360, 1995.

[75] Bastos, J., Steyaert, M. S., Pergoot, A., and Sansen, W. M., "Influence of Die Attachment on MOS Transistor Matching," *IEEE Transactions on Semiconductor Manufacturing*, 10(2), pp. 209-218, 1997.

[76] Jaeger, R. C., Bradley, A. T., Suhling, J. C., Zou, Y., "FET Mobility Degradation and Device Mismatch Due to Packaging Induced Die Stress," *In Proceedings of the 23rd European Solid-State Circuits Conference*, pp. 272-275, 1997.

[77] Ali, H., "Stress-induced Parametric Shift in Plastic Packaged Devices," *IEEE Transactions on Components, Packaging, and Manufacturing Technology: Part B*, 20(4), pp. 458-462, 1997.

[78] Thompson, S., Anand, N., Armstrong, M., Auth, C., Arcot, B., Alavi, M., Bohr, M., "A 90 nm Logic Technology Featuring 50 nm Strained Silicon Channel Transistors 7 Layers of Cu Interconnects, Low k ILD, and 1/spl mu/m/sup 2/SRAM Cell," *In Digest. International Electron Devices Meeting*, pp. 61-64, 2002.

[79] Mistry, K., Armstrong, M., Auth, C., Cea, S., Coan, T., Ghani, T., Bohr, M., "Delaying Forever: Uniaxial Strained Silicon Transistors in a 90nm CMOS

Technology," *In Digest of Technical Papers. 2004 Symposium on VLSI Technology*, pp. 50-51, 2004.

[80] Tsividis, Y., *Operation and Modeling of the MOS Transistor,* Oxford University Press, 2010.

[81] Jaeger, R. C., *Microelectronic Circuit Design 6E*, McGraw-Hill Education, 2022.

[82] Mikoshiba, H., "Stress-sensitive Properties of Silicon-gate MOS Devices," *Solid-State Electronics*, 24(3), pp. 221-232, 1981.

[83] Sun, Y., Thompson, S. E., Nishida, T., "Physics of Strain Effects in Semiconductors and Metal-Oxide-Semiconductor Field-Effect Transistors," *Journal of Applied Physics*, 101(10), 104503, 2007.

[84] Fruett, F., "The Piezojunction Effect in Silicon, its Consequences and Applications for Integrated Circuits and Sensors," *PhD Dissertation*, Delft University of Technology, 2001.

[85] Creemer, J. F., Fruett, F., Meijer, G. C., French, P. J., "The Piezojunction Effect in Silicon Sensors and Circuits and its Relation to Piezoresistance," *IEEE Sensors Journal*, 1(2), 98, 2001.

[86] Creemer, J. F., "The Effect of Mechanical Stress on Bipolar Transistor Characteristics," *PhD Dissertation,* Delft University of Technology, 2002.

[87] Jaeger, R. C., Hussain, S., Suhling, J. C., Gnanachchelvi, P., Wilamowski, B. M., and Hamilton, M. C. "Impact of Mechanical Stress on Bipolar Transistor Current Gain and Early Voltage," *SENSORS*, pp. 1-4., 2013.

[88] Dhar, S., Haney, S., Cheng, L., Ryu, S. R., Agarwal, A. K., Yu, L. C., Cheung, K. P., "Inversion Layer Carrier Concentration and Mobility in 4H–Sic Metal-Oxide-Semiconductor Field-Effect Transistors," *Journal of Applied Physics*, 108(5), 054509, 2010.

[89] Yoshioka, H., Senzaki, J., Shimozato, A., Tanaka, Y., Okumura, H., "Effects of Interface State Density on 4H-SiC n-Channel Field-Effect Mobility," *Applied Physics Letters*, 104(8), 083516, 2014.

[90] Bartholomeyczik, J., Brugger, S., Ruther, P., Paul, O., "Multidimensional CMOS In-plane Stress Sensor," *IEEE Sensors Journal*, 5(5), pp. 872-882, 2005.

[91] Bartholomeyczik, J., Doelle, M., Ruther, P., Paul, O., "The Continuous Spinning Current (CSC) Stress Sensor Method for the Extraction of Two Stress Components in an Offset Compensated Manner," *Sensors and Actuators A: Physical*, 127(2), pp. 255-260, 2006.

[92] Brander, R. W., Sutton, R. P., "Solution Grown SiC pn Junctions," *Journal of Physics D: Applied Physics*, 2(3), 309, 1969.

[93] Ikeda, M., Hayakawa, T., Yamagiwa, S., Matsunami, H., Tanaka, T., "Fabrication of 6H-SiC Light-emitting Diodes by a Rotation Dipping Technique:

Electroluminescence Mechanisms," *Journal of Applied Physics*, 50(12), pp. 8215-8225, 1979.

[94] Jennings, V. J., Sommer, A., Chang, H. C., "The Epitaxial Growth of Silicon Carbide," *Journal of the Electrochemical Society*, 113(7), 728, 1966.

[95] Campbell, R. B., Chu, T. L., "Epitaxial Growth of Silicon Carbide by the Thermal Reduction Technique," *Journal of The Electrochemical Society*, 113(8), 825, 1966.

[96] Muench, W. V., Pfaffeneder, I., "Epitaxial Deposition of Silicon Carbide From Silicon Tetrachloride and Hexane," *Thin Solid Films*, 31(1-2), pp. 39-51, 1976.

[97] Yoshida, S., Sakuma, E., Okumura, H., Misawa, S., Endo, K., "Heteroepitaxial Growth of SiC Polytypes," *Journal of Applied Physics*, 62(1), pp. 303-305, 1987.

[98] Ueda, T., Nishino, H., and Matsunami, H., "Crystal Growth of SiC by Step-controlled Epitaxy," *Journal of Crystal Growth*, 104(3), pp. 695-700, 1990.

[99] Kong, H. S., Glass, J. T., & Davis, R. F., "Chemical Vapor Deposition and Characterization of 6H-SiC Thin Films on Off-Axis 6H-SiC Substrates," *Journal of Applied Physics*, 64(5), pp. 2672-2679, 1988.

[100] Itoh, A., Akita, H., Kimoto, T., Matsunami, H., "High-quality 4H-SiC Homoepitaxial Layers Grown by Step-controlled Epitaxy," *Applied Physics Letters*, 65(11), pp. 1400-1402, 1994.

[101] Kimoto, T., Itoh, A., Akita, H., Urushidani, T., Jang, S., and Matsunami, H., "Step-Controlled Epitaxial Growth of α-SiC and Application to High-voltage Schottky Rectifiers," *In Conference Series-institute of Physics*, 141, pp. 437-437, 1995.

[102] Raghunathan, R., Alok, D., Baliga, B. J., "High Voltage 4H-SiC Schottky Barrier Diodes," *IEEE Electron Device Letters*, 16(6), pp. 226-227, 1995.

[103] Baba-Kishi, K. Z., "Review Electron Backscatter Kikuchi Diffraction in the Scanning Electron Microscope for Crystallographic Analysis," *Journal of Materials Science*, 37(9), pp. 1715-1746, 2002.

[104] Qin, G., Liu, H., Guo, Y., Dang, M., Ma, J., Ma, Z., Luo, T., "On the Performance Characterization of Silicon MOSFETS On 4° Off-Axis Substrate," *IEICE Electronics Express*, 13(17), pp. 20160634-20160634, 2016.

[105] Fischer, R., Morkoc, H., Neumann, D. A., Zabel, H., Choi, C., Otsuka, N., Erickson, L. P., "Material Properties of High-quality GaAs Epitaxial Layers Grown on Si Substrates," *Journal of Applied Physics*, 60(5), pp. 1640-1647, 1986.

[106] Nguyen, N. D., Wang, G., Brammertz, G., Leys, M., Waldron, N., Winderickx, G., Caymax, M., "Selective Epitaxial Growth of III-V Semiconductor Heterostructures on Si Substrates for Logic Applications," *ECS Transactions*, 33(6), pp. 933, 2010.

[107] Kataria, H., Metaferia, W., Junesand, C., Zhang, C., Julian, N., Bowers, J. E., Lourdudoss, S., "Simple Epitaxial Lateral Overgrowth Process as a Strategy for

Photonic Integration on Silicon," *IEEE Journal of Selected Topics in Quantum Electronics*, 20(4), pp. 380-386, 2013.

[108] Wang, G., Leys, M. R., Nguyen, N. D., Loo, R., Brammertz, G., Richard, O., Caymax, M., "Growth of High Quality InP Layers in STI Trenches on Miscut Si (001) Substrates," *Journal of Crystal Growth*, 315(1), pp. 32-36, 2011.

[109] Ohata, A., Bae, Y., Cristoloveanu, S., Signamarcheix, T., Widiez, J., Ghyselen, B., and Clavelier, L., "Deep-amorphization and Solid-phase Epitaxial Regrowth Processes for Hybrid Orientation Technologies in SOI MOSFETs with Thin Body," *Microelectronics Reliability*, 52(11), pp. 2602-2608, 2012.

[110] Cerutti, L., Rodriguez, J. B., and Tournié, E., "GaSb-Based Laser, Monolithically Grown on Silicon Substrate, Emitting at 1.55 μm at Room Temperature," *IEEE Photonics Technology Letters*, 22(8), pp. 553-555, 2010.

[111] Jaeger, R. C., Suhling, J. C., and Ramani, R., "Errors Associated with the Design, Calibration and Application of Piezoresistive Stress Sensors in (100) Silicon," *IEEE Transactions on Components*, *Packaging, and Manufacturing Technology: Part B,* 17(1), pp. 97-107, 1994.

[112] McSkimin, H. J., "Pulse Superposition Method for Measuring Ultrasonic Wave Velocities in Solids," *The Journal of the Acoustical Society of America*, 33(1), pp. 12-16, 1961.

[113] Damzen, M. J., Vlad, V., Mocofanescu, A., Babin, V., *Stimulated Brillouin Scattering: Fundamentals and Applications*, CRC Press, 2003.

[114] Iuga, M., Steinle-Neumann, G., Meinhardt, J., "Ab-initio Simulation of Elastic Constants for Some Ceramic Materials," *The European Physical Journal B*, 58(2), pp. 127-133, 2007.

[115] Gibson, R. F., *Principles of Composite Material Mechanics*. CRC Press, 2016.

[116] Nye, J. F., *Physical Properties of Crystals: Their Representation by Tensors and Matrices.* Oxford University Press, 1985.

[117] Lekhnitskii, S. G., *Anisotropic Plates*, Gordon and Breach, 1968.

[118] Kang, Y., "Piezoresistive Stress Sensors for Advanced Semiconductor Materials," *PhD Dissertation*, Chap. 9, pp. 258-266, Auburn University, 1997.

[119] Oliver W. C., Pharr, G. M., "An Improved Technique for Determining Hardness and Elastic-modulus Using Load and Displacement Sensing Indentation Experiments," *Journal of Materials Research*, 7(6), pp. 1564-1583, 1992.

[120] Ko, S. H., Kim, Y. D., Shin N. Y., Park, H. C., and Lee., K. H., "On the Mechanical Properties of Transversely Isotropic Material Using the Nanoindentation," *In Advanced Materials Research*, 33, pp. 987-992, 2008.

[121] Prasad, K. E., and Ramesh, K. T., "Hardness and Mechanical Anisotropy of Hexagonal SiC Single Crystal Polytypes.", *Journal of Alloys and Compounds*, 770, pp. 158-165, 2019.

[122] Pizzagalli, L., "Stability and Mobility of Screw Dislocations in 4H, 2H and 3C Silicon Carbide.", *Acta Materialia*, 78, pp. 236-244, 2014.

[123] Kamitani, K., Grimsditch, M., Nipko, J. C., Loong, C. K., Okada, M., Kimura, I., "The Elastic Constants of Silicon Carbide: a Brillouin-scattering Study of 4H and 6H SiC Single Crystals," *Journal of Applied Physics*, 82(6), pp. 3152–3154, 1997.

[124] Nuruzzaman, M., Islam, M. A., Alam, M. A., Shah, M. H., and Karim, A. M. T., "Structural, Elastic and Electronic Properties of 2H- and 4H-SiC," *International Journal of Engineering Research and Applications*, 5(5), pp. 48-52, 2015.

[125] Li, Z., Bradt, R. C., "Thermal Expansion of the Hexagonal (4 H) Polytype of SiC," *Journal of Applied Physics*, 60(2), pp. 612-614, 1986.

[126] Chang, L., "The Effects of Isothermal Aging on the Mechanical Behavior of Underfill Encapsulants," *PhD Dissertation*, Auburn University, 2010.